Spin-fluctuation mediated superconductivity and magnetic order in the cuprate $\mathbf{La_{1.88}Sr_{0.12}CuO_4}$

by

Astrid Tranum Rømer

PhD thesis in Physics

Supervisors: Brian Møller Andersen, Henrik M. Rønnow and Kim Lefmann

Niels Bohr Institute
University of Copenhagen

July 2015

Abstract

High-temperature superconductivity in cuprates emerges as one out of many electronic phases when doping the antiferromagnetic Mott insulator $\mathrm{La_2CuO_4}$ away from half filling. The description of the superconducting phase is therefore complicated by intertwined electronic orders that compete with superconductivity. However, it is possible that the tendency towards additional ordering phenomena is a necessary condition for unconventional superconductivity to develop. Indeed most superconductors discovered throughout the last 29 years, including also the recently discovered class of iron-based superconductors, show a very rich electronic phase diagram. A common feature that characterizes both cuprates, heavy fermions, and iron pnictides is the proximity to magnetic order. Therefore, the idea of spin-fluctuation mediated pairing is a popular paradigm proposed for unconventional superconductivity. A fingerprint of the pairing mechanism is found in the superconducting gap symmetry. Therefore the study of gap symmetries constitutes one of the most important parts of resolving the superconducting puzzle.

This thesis consists of a theoretical and an experimental part. In the theoretical part, we address spin-fluctuation mediated pairing in the weak-coupling limit by a systematic study of the one-band Hubbard model. We consider the problem of spin-fluctuation mediated pairing in a paramagnetic system, as well as a system in which spin-density wave order is well-established. In addition, we describe how disorder locally affects the spin susceptibility and its implications on the local superconducting gap.

In the experimental part, we use neutron scattering experiments to investigate magnetic order and low-energy spin fluctuations in the cuprate superconductor $\mathrm{La_{1.88}Sr_{0.12}CuO_4}$. This crystal is superconducting with $T_c = 27$ K and shows incommensurate magnetic order as well as spin fluctuations which are "stripe-like" and distinct from the antiferromagnetic order of the parent compound $\mathrm{La_2CuO_4}$. Yet some remnant features of the original $\mathrm{La_2CuO_4}$ spin order remain. For instance, we find that despite the glassy nature of the low-energy spin fluctuations in $\mathrm{La_{1.88}Sr_{0.12}CuO_4}$, the spectrum supports small anisotropy gaps similar to the observations of anisotropy gaps in the parent compound as well as stripe-ordered $\mathrm{La_{1.875}Ba_{0.125}CuO_4}$.

Contents

Acknowledgments

I am grateful to Brian Møller Andersen for the everyday guidance, good ideas and encouragements. Also I would like to thank Kim Lefmann for teaching me the technique of neutron scattering and for his enthusiasm and support. I have benefited greatly from the valuable discussions with Niels Bech Christensen, Andreas Kreisel, Shantanu Mukherjee, Maria Navarro Gastiasoro, Morten Holm Christensen, Henrik M. Rønnow, and Johan Chang. Also, I would also like to thank Ilya Eremin and Peter J. Hirschfeld for many enlightening discussions.

I am grateful to the valuable help of all the people from the experimental group in Copenhagen, Pia Jensen Ray, Linda Udby, Henrik Jacobsen, Mads Bertelsen and Sonja Lindahl Holm, who have been present in some of the experiments when I was unable. I thank Johan Chang for letting me "inherit" his raw data on low-energy fluctuations in $La_{1.88}Sr_{0.12}CuO_4$.

Thank you to Maria Navarro Gastiasoro for the good office spirit and for everyday private lessons in Spanish (and Basque). Finally, I thank Torsten, Clara and Simon for the spoken and unspoken never-failing support.

Astrid Tranum Rømer
Copenhagen, July 2015.

Chapter 1

Introduction

The problem of high-temperature superconductivity is tightly connected to the problem of a complex electronic phase diagram with a whole zoo of exotic ordering phenomena occuring at comparable ordering temperatures. In many cases, one might describe the different ordering phenomena as competing, since they are fighting for the same electrons. Indeed, coexistence at a microscopic scale is usually quite rare, and when it occurs, one order usually acts to suppress the other. Nevertheless, it is not unlikely that the electrons are able to multitask in the sense that one of the "competing" orders in fact provides the prerequisites for onset of superconductivity.

In the case of the cuprates, we are dealing with the spectacular mystery of the Mott insulating system La_2CuO_4, that becomes superconducting by electron- or hole doping of the CuO_2 layers. The Cu atoms each have one unpaired electron, giving them an effective spin of 1/2. The three-dimensional antiferromagnetic order of the Mott insulating phase disappears rapidly as a function of doping. Hole doping is particularly detrimental for the antiferromagnetic order, but magnetic order survives in the form of an incommensurate spin-density wave order in a range of hole dopings. Electron doping is less damaging for antiferromagnetism, and there is evidence for coexistence of superconductivity and antiferromagnetic order in electron-doped cuprates, although this is still an issue of debate [1, 2]. A schematic overview of the phase diagram is given in Fig. 1.1, where the regions of magnetic and charge order are depicted, as well as the intriguing pseudogap phase, which encloses most of the phase diagram. A recent controversial claim [2] for electron-doped crystals is that removal of all apical oxygen ions causes superconductivity all the way down to zero doping.

For the more recently discovered iron-based superconductors, superconductivity also emerges in dome-like shapes upon electron- or hole doping of the parent compounds. In these materials, the parent compound is not a Mott insulator but a metal displaying itinerant magnetism. In parts of the phase diagram, additional rotational symmetry breaking nematic order has been the focus of intense research, and these compounds also host a number of different magnetic structures.

For sufficient electron- or hole doping a superconducting dome appears. For the cuprates, it was established at an early stage [3] that the charge carriers are electron pairs as revealed by flux quantization measurements. In this aspect, the superconducting phase in the cuprates resembles conventional superconductivity. Combining the electrons into pairs was one of the very important steps towards the understanding of conventional superconductors, as described by the most succesful theory of Bardeen, Cooper and Schrieffer in 1957. The BCS theory came as a milestone of theoretical physics after almost 50 years of many unsuccesful attempts to describe the microscopic origin of superconductivity. The major advances came in steps initiated by the realization, that electrons living in a solid can become effectively attractive. As a consequence, two electrons can form a stable bound state regardless of how weak the attractive force, thereby causing an instability of the Fermi surface. Finally, these bound states, the Cooper pairs, form a coherent many-body wave function which adequately describes the astonishing features of the superconducting phase. In fact, once the idea of Cooper pairs was established, the BCS theory provided a quite simple framework for describing the superconducting phase. The simplicity of

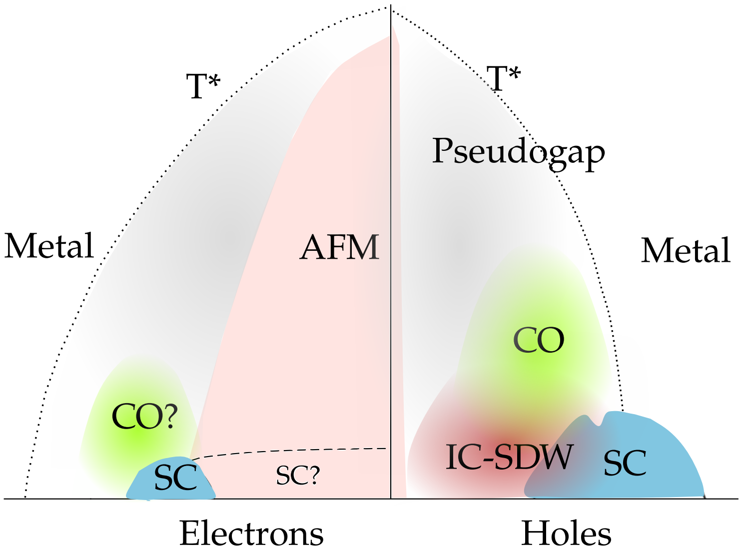

Figure 1.1: Schematic phase diagram of the cuprates showing ordering temperatures as a function of electron and hole doping. At half filling the system is an antiferromagnetic insulator. The commmensurate antiferromagnetic region (AFM) expands for large electron dopings as a spin-density wave which might coexist with superconductivity (SC). On the contrary, antiferromagnetic order dies off extremely fast upon hole doping and in this case, incommensurate spin-density wave order (IC-SDW) order takes over at intermediate hole dopings. Note also the pseudo gap phase on both sides of the phase diagram. In either case the origin of the pseudogap is still controversial. Recently, charge order (CO) has been confirmed in a number of hole doped cuprates, and in one class of electron-doped systems. In hole-doped systems, there is compelling evidence for a $d_{x^2-y^2}$ superconducting gap [7, 8]. Recent experimental advances seem to agree on a $d_{x^2-y^2}$ gap also on the electron-doped side [1].

conventional BCS theory relies on two main aspects of conventional superconductors; 1) the normal state is an usual metal, which is well-described by a Fermi gas of non-interacting electrons, and 2) the Cooper pairs are built from two electrons which effectively attract each other due to phonons of the underlying lattice.

Evidence of phonon-mediated pairing was found from the so-called isotope effect; BCS theory predicts that the superconducting transition temperature changes with the mass of the ions in the crystal, M, as $T_c \propto M^{-0.5}$. This prediction found experimental support in some of the conventional superconductors, e.g. Hg and Pb [4]. Furthermore, BCS theory predicted the existence of a temperature dependent energy gap at the Fermi level, which satisfies $\frac{2\Delta(0)}{k_B T_c} = 3.53$, where $\Delta(0)$ is the gap at zero temperature. Also this prediction found strong support from experimental observations.

The structure of the phonon-mediated interaction is well approximated by an onsite attraction in real space, or a **k**-independent attractive constant in reciprocal space. The phonons and electrons are only very weakly coupled with an effective vertex that scales with $\sqrt{\frac{m}{M}} \sim 10^{-2} - 10^{-4}$, where m is the effective electron mass and M is the mass of the ions in the crystal. This is called Migdal's theorem. The smallness of the effective vertex justifies the treatment of electrons and phonons separately. In other words, compared to the fast-moving electrons, phonons can be considered slowly varying ionic vibrations of the crystal, which are roughly insensitive to the presence of the electrons.

The BCS theory was further developed by Eliashberg to account for the retarded nature of the phonon-induced interaction and the effect of electrons on the phonon spectrum to order m/M. This enabled a more detailed comparison between experiment and theory. McMillan [5] found that the electron-phonon coupling constant depends primarily on the phonon frequencies rather than the electronic properties of the metal, and predicted a maximum critical temperature due to phonon-mediated pairing of the order

$\sim 30 - 40$ K. However, it is noted that the prediction is limited to certain classes of superconductors, and should not be understood as a rigorous upper bound on T_c for phonon-mediated superconductors.[1]

The discovery of superconductivity in the ceramic oxide $\mathrm{La_{2-x}Ba_xCuO_4}$ by Bednorz and Müller in 1986 started a new era of superconductivity. The first surprise of $\mathrm{La_{2-x}Ba_xCuO_4}$ was not so much because of a high critical temperature ($T_c \sim 35$ K), but more due to the fact that superconductivity emerged from the Mott insulator $\mathrm{La_2CuO_4}$ by substituting a certain percentage of $\mathrm{La^{3+}}$ by $\mathrm{Ba^{2+}}$, thereby effectively hole doping the system. Among the members of the cuprate family, $\mathrm{Bi_2Sr_2CaCu_2O_{8+\delta}}$ and $\mathrm{YBa_2Cu_3O_7}$ have superconducting temperatures around 80 K, which is above the boiling point of nitrogen, an important advance for application purposes. Until very recently, the critical temperature record holder was a cuprate, $\mathrm{HgBa_2Ca_2Cu_3O_{8+x}}$, with $T_c = 164$ K (under pressure).

In the cuprates, as well as the iron-based superconductors and heavy fermion systems, we are quite far from the simplifying condition number 1) mentioned above; the normal phase is *not* well-described by a Fermi sea of non-interacting electrons. On the contrary, electron-electron interactions give rise to a number of different ordering phenomena. Therefore, an adequate description of unconventional superconductivity has to take into account the more complex underlying electronic structure and the electron-electron interactions. Also, condition number 2) of a phonon-mediated pairing glue is unlikely; for instance $\mathrm{YBa_2Cu_3O_7}$ shows zero isotope effect, and also in many cases, T_c is larger than what is expected from a purely phonon-mediated interaction. The problem of the pairing glue is perhaps the most challenging problem of unconventional superconductivity. If the lattice does not produce the glue, then the natural suggestion is, that the glue is provided by the electrons themselves. In this respect, it becomes even more crucial to address the details of the electronic structure that characterizes the system.

A common feature that characterizes both cuprates, heavy fermions, and iron pnictides is the proximity to magnetic order. The spin-spin correlations are quantified by the magnetic susceptibility, $\chi_0(\mathbf{q}, i\omega_n)$. In the random phase approximation (RPA) screening of the bare electron-electron interaction is taken into account and hereby the susceptibility takes the form:

$$\chi_{\mathrm{RPA}}(\mathbf{q}, i\omega_n) = \frac{\chi_0(\mathbf{q}, i\omega_n)}{1 - U\chi_0(\mathbf{q}, i\omega_n)}. \tag{1.1}$$

The onset of magnetic order is characterized by the static Stoner criteria;

$$1 - URe\chi_0(\mathbf{q}, 0) = 0. \tag{1.2}$$

This means that when the spin-spin correlation increases as a function of e.g. temperature or doping, we may obtain a situation where $URe\chi_0(\mathbf{q}, 0) \to 0$ and this is manifested by a divergent real part of the RPA susceptibility at zero energy. The imaginary part of the RPA susceptibility is a measure of the spin fluctuation intensity, and this is likewise enhanced by an increase in the spin-spin correlations at small energies, given that the imaginary part arising from dissipative processes is small. In simple terms, a system on the verge of magnetic order is characterized within RPA by intense low-energy magnetic fluctuations, and a large (eventually divergent) real part of the susceptibility at zero energy. The latter is in fact a manifestation of the Goldstone mode appearing in the ordered phase.

Now, a straight-forward suggestion for the pairing glue in the unconventional superconductors is to use the intense low-energy magnetic fluctuations present in the proximity of magnetic order. In this way, the same mechanism which renders the system magnetic could in principle just as well lead to superconductivity. This is in its essence the idea behind spin-fluctuation mediated pairing. Of course, once the system has entered a symmetry broken phase, this has implications on the spin fluctuations, and must be considered as feedback effects on the pairing mechanism.

With the above motivation, we are left with the minimal model that contains all the important

---

[1] A very recent and controversial finding of $T_c = 203$ K in $\mathrm{H_2S}$ under high pressure, presumably mediated by high-frequency phonons, has been reported in Ref. [6].

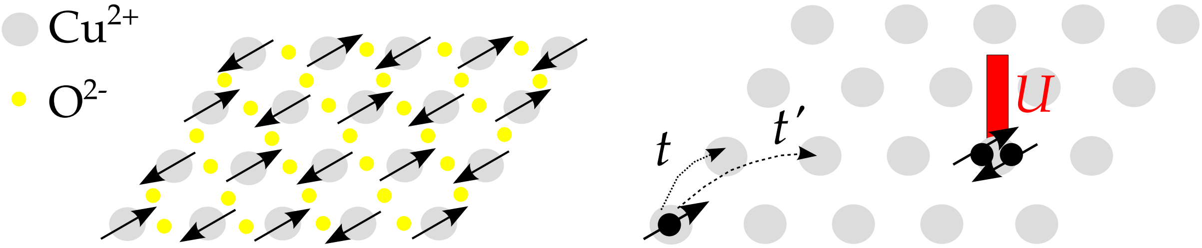

Figure 1.2: (**left:**) Schematic drawing of a CuO_2 plane depicting the antiferromagnetic order of the electronic spin at the Cu atoms. (**right:**) Illustration of the Hubbard model with hopping constants t and t' and onsite Coulomb repulsion U.

ingredients. In the Hubbard model

$$H = -\sum_{i,j,\sigma} t_{i,j} c^{\dagger}_{i\sigma} c_{j\sigma} + U \sum_{i} n_{i\uparrow} n_{i\downarrow} - \mu \sum_{i,\sigma} n_{i\sigma}, \tag{1.3}$$

$c^{\dagger}_{i\sigma}$ creates an electron on site i with spin σ, which can hop between neighboring and next-neighboring sites with an associated energy of t and t', respectively. The interaction term U denotes the energy cost associated with having two electrons on the same site and the average electron density is controlled by the chemical potential, μ. The Coulomb interaction provides the tendency towards magnetic order, when it is sufficiently large compared to the hopping energies, but it also brings about the superconducting glue by higher order interaction processes. The CuO_2 plane and the schematics of the one-band Hubbard model is depicted in Fig. 1.2.

The Stoner criteria, Eq. (1.2), selects a certain wave vector $\mathbf{q}$ which characterizes the structure of the magnetic phase, but also decides the symmetry of the superconducting gap. In the commensurate antiferromagnet, the ordering vector is $\mathbf{Q} = (\pi, \pi)$, which in turn supports $d_{x^2-y^2}$ superconductivity. Close to half filling and for small next-nearest hoppings t', the Hubbard model accomodates both types of order. In this way it captures some of the important features of the CuO_2 planes in the cuprates. The ferromagnet is characterized by an ordering vector $\mathbf{q} = (0, 0)$, which is realized when the density of states at the Fermi level becomes large. This is most prominent if a van Hove singularity crosses the Fermi level marked by a change of the Fermi surface topology. A spin susceptibility peak at $\mathbf{q} = (0, 0)$ supports the development of triplet superconductivity. In general, the spin susceptibility structure is tightly connected to the Fermi surface, and this has implications on the superconducting gap symmetry if superconductivity is mediated by spin fluctuations.

In this thesis, we perform a comprehensive study of the weak-coupling limit of the Hubbard model, Eq. (1.3), to map out the spin-fluctuation mediated superconducting pairing instability in the paramagnetic and the spin-density wave phase. We include a large region of parameter space, also regions of intermediate fillings and large t' where the pairing instabilities are largely unknown. One of our main questions is the implications of well-established magnetic order prior to the onset of superconductivity. In this case, the normal state Fermi surface is no longer that of a simple metal, and also, the spin fluctuation spectrum is changed including now a Goldstone mode of the magnetic order. This requires a reformulation of the standard approach to spin-fluctuation mediated pairing commonly addressed in the literature.

Another important aspect of spin-fluctuation mediated pairing in cuprate superconductors is the fact that doping not only alters the chemical potential, but also introduces random impurities into the system. This calls for a theoretical approach that treats the microscopic physics in a real space manner, allowing for local variations of the electronic structure, in particular the spin fluctuations and the superconducting gap. We pose the question of how the presence of disorder alters the superconducting gap locally. Within spin-fluctuation mediated pairing this is of course tightly connected to the local variations of the spin susceptibility.

From the experimental point of view, it is important to map out the nature of the underlying electronic structure and the occurrence of magnetic ordering tendencies. In the cuprates, more than 30 years of research have lead to a vast amount of literature addressing magnetic order and spin fluctuations as a function of doping, temperature and applied magnetic field. In this thesis, we continue the experimental quest by addressing two questions; 1) what is the nature of the magnetic order that coexists with superconductivity in hole-doped $La_{1.88}Sr_{0.12}CuO_4$, and 2) what is the effect of an applied magnetic field on the magnetic order in the same system. To answer these questions, we have performed elastic and inelastic neutron scattering experiments, one of the most powerful techniques to study bulk magnetism and low-energy magnetic fluctuations.

Chapter 2

Spin-fluctuation mediated pairing in the homogeneous and paramagnetic state

Some of material discussed in this chapter has been submitted to Phys. Rev. B and is available at arXiv:1506.03593v1. We study the spin-fluctuation mediated superconducting pairing gap in a weak-coupling approach to the Hubbard model for a two dimensional square lattice in the paramagnetic state. Performing a comprehensive theoretical study of the phase diagram as a function of filling, we find that the superconducting gap exhibits transitions from p-wave at very low electron fillings to $d_{x^2-y^2}$*-wave symmetry close to half filling in agreement with previous reports. At intermediate filling levels, different gap symmetries appear as a consequence of the changes in the Fermi surface topology and the associated structure of the spin susceptibility. In particular, the vicinity of a van Hove singularity in the electronic structure close to the Fermi level has important consequences for the gap structure in favoring the otherwise sub-dominant triplet solution over the singlet d-wave solution. By solving the full gap equation, we find that the energetically favorable triplet solutions are chiral and break time reversal symmetry. Finally, we also calculate the detailed angular gap structure of the quasi-particle spectrum, and show how spin-fluctuation mediated pairing leads to significant deviations from the first harmonics both in the singlet* $d_{x^2-y^2}$ *gap as well as the chiral triplet gap solution.*

2.1 Pairing mediated by spin fluctuations

The idea of an effective interaction between electrons mediated by spin fluctuations dates back to Kohn and Luttinger, who proposed a "new mechanism for superconductivity" in their paper from 1965 [9]. In the paper, Kohn and Luttinger argued that even though electrons repel each other, higher order interactions can give rise to an effective attractive interaction between two electrons, whereby the formation of Cooper pairs can take place. In its essence, this effect is due to Friedel oscillations; the susceptibility evaluated at $q = 2k_F$, where k_F is the Fermi momentum diverges. This gives rise to a long-range oscillatory force in real space at low temperatures, where the Fermi surface is sharp [9]. Intrinsic to this model is the spatial structure of the Cooper pairs; the superconducting gap symmetry carry a finite angular momentum, i.e. standard onsite s-wave superconductivity cannot be realized by purely repulsive interactions. The Friedel oscillations are derived from the screening of the bare Coulomb repulsion. These can be drawn by bubble diagrams. Kohn and Luttinger proposed another type of diagrams as an important player for the new mechanism of superconductivity, namely the exchange diagrams which can be drawn by ladder diagrams. The nature of the two types of interactions are quite distinct. The exchange interaction is a spin flip interaction, whereas the screening interaction is more innocent; in the paramagnetic system it is weaker than the exchange interaction and does not give rise to a spin flip. The higher order interactions as derived from the special classes of diagrams mentioned above, i.e. the bubble and ladder diagrams, can be expressed in terms of spin and charge fluctuations of the system. It is the spin fluctuations which dominate the interaction, therefore the name "spin-fluctuation mediated pairing". In the paramagnetic system, the screening interaction and the exchange interaction act in concert to generate a superconducting phase. If the system is magnetically ordered, they will in some cases in fact counteract each other by supporting different symmetries of the superconducting gap. We shall return to this in chapter 5.

Shortly after the work by Kohn and Luttinger, Berk and Schrieffer [10] addressed the model in the context of ^{3}He, which displays ferromagnetic spin fluctuations. ^{3}He atoms are neutral spin-1/2 fermions, and superfluidity in ^{3}He is particularly interesting because phonon-mediated pairing is not possible. Since there is no underlying lattice, the pairing interaction has to arise directly from the helium atoms. It was therefore natural to search for a pairing interaction arising due to the spins. However, Berk and Schrieffer argued that such an effective interaction would cause a suppression of singlet superfluidity. At this point it was believed that the superfluid phase of ^{3}He was most adequately described by a singlet spin pairing mechanism. However, at a later point it was realized that the superfluid state of ^{3}He is in fact a triplet state, and as a matter of fact, ferromagnetic fluctuations support triplet superfluidity. This was realized much later [11, 12, 13]. So interestingly, the first disappointment of Berk and Schrieffer regarding the idea that spin fluctuations could consitute the pairing glue in ^{3}He was turned into a strong support for spin fluctuations as the good candidate for the glue that connects ^{3}He atoms together in the superfluid phase.

In the year 1986, the same year the first cuprate superconductor $\mathrm{La}_{2-x}\mathrm{Ba}_x\mathrm{CuO}_4$ was discovered by Bednorz and Müller, a new and very important feature of spin-fluctuation mediated pairing was pointed out by Scalapino *et al.* [12] and Miyake *et al.* [14] with relevance for cuprates and heavy fermions, respectively. In both works it was pointed out, how the proximity to a quantum critical point (QCP) of a competing order can cause a strengthing of the effective interaction. This might lead to superconductivity of a particular symmetry which bears a fingerprint of the competing order. In Refs. [12, 14] the proximity to antiferromagnetic spin-density-wave (SDW) order was shown to give rise to strong $d_{x^2-y^2}$ superconductivity.

The idea of the work of Scalapino *et al.* [12] is the following. Two electrons residing on the same site of a lattice repel each other by the bare Coulomb repulsion. Higher order interactions through the Fermi sea (screening) or repeated interactions between the same two electrons (exchange) give longer range interactions. Expressed in terms of the electron momentum $\mathbf{k}$ appropriate to a homogeneous system, the singlet spin interaction remains purely repulsive. Therefore a solution to the superconducting gap equation is possible only if the gap changes sign between pairs of $\mathbf{k}$ and $\mathbf{k}'$ which are strongly interacting through higher order processes. This implies that they must be connected by a nesting vector of the underlying Fermi surface. For triplet spin pairing, the higher order interaction becomes attractive for certain pair scattering processes, but a standard onsite s-wave solution to the gap equation is prevented due to the triplet character, i.e. the gap must be odd under inversion ($\mathbf{k} \to -\mathbf{k}$).

Based on the ideas of the pairing glue in unconventional superconductors put forward in Refs. [12, 14] it has been an ongoing quest to search for magnetic fluctuations and order in the vicinity of the superconducting phases. In recent years, not only spin fluctuations, but also charge fluctuations as well as nematic fluctuations have entered the game. The basic idea is the same as the original; if the system has a tendency towards some kind of order, we can expect strong fluctuations of the corresponding susceptibility. Depending on the details of the order, these fluctuations will be the glue that supports a particular superconducting phase. The symmetry of the superconductivity is thus tightly connected to the susceptibility structure. The antiferromagnetically ordered phase and superconductivity of $d_{x^2-y^2}$ symmetry consitutes an example of this, which will be the main focus of this thesis. We shall also discuss gap symmetries, which are not related to antiferromagnetism.

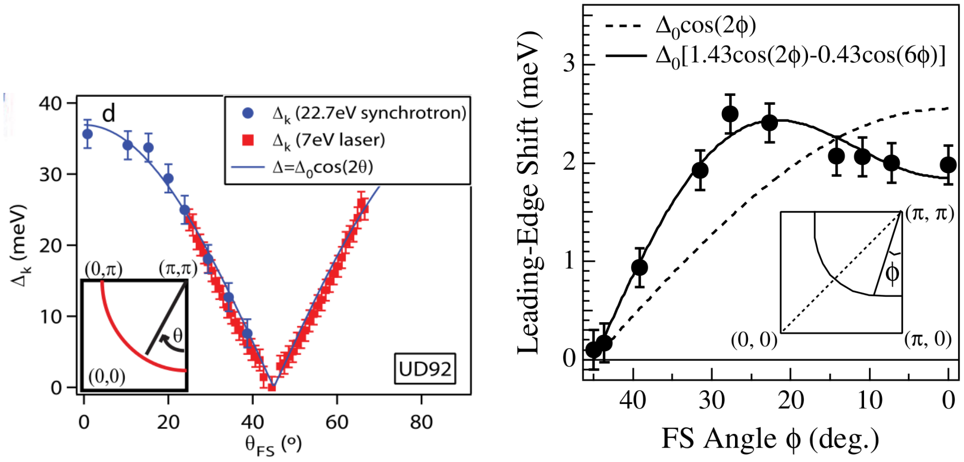

Figure 2.1: (**left:**) Superconducting gap of measured by ARPES in $\mathrm{Bi_2Sr_2CaCu_2O_{8+\delta}}$ (hole doping of 14 %). Note that ARPES is insensitive to the sign of the gap. Adapted from Vishik *et al.*, Ref. [17]. (**right:**) Superconducting gap of measured by ARPES in the electron-doped cuprate $\mathrm{Pr_0.89LaCe_0.11CuO_4}$. Note the deviation from the first harmonic. Adapted from Matsui *et al.*, Ref. [18].

2.2 Experimental studies of the superconducting gap in cuprates

In the cuprates there is substantial evidence for a $d_{x^2-y^2}$-wave gap structure with nodes along the zone diagonals $k_x = \pm k_y$ [15, 16]. In Fig. 2.1 the ARPES result for hole-doped $\mathrm{Bi_2Sr_2CaCu_2O_{8+\delta}}$ and electron-doped $\mathrm{Pr_0.89LaCe_0.11CuO_4}$ is shown. In both systems the nodal structure is clearly visible. Some experiments find evidence that the gap form does not follow the simplest form as given by $\Delta_k = \Delta(\cos(k_x) - \cos(k_y))$, as in the case of $\mathrm{Pr_0.89LaCe_0.11CuO_4}$ shown in Fig. 2.1. Away from the nodes, the gap does not follow a monotonic behaviour towards the antinodes, but the maximum gap value is obtained in-between the antinode ($\phi = 0$) and the node ($\phi = 45°$). The deviation from the first harmonic has also been reported by Raman scattering in the compound NCCO [19], where it was highlighted that the position of maximum gap is found at the position of the hot spots, i.e. segments of the Fermi surface which are connected by $\mathbf{Q} = (\pi, \pi)$. This points towards a pairing interaction mediated by antiferromagnetic spin fluctuations in which case we expect the largest gaps to be located at pairs of $\mathbf{k}$ and $\mathbf{k}'$ that are separated by $\mathbf{Q}$. The same scenario was also discussed in the theoretical work by Parker and Balatsky [20], who argued that there is a quantitative evidence for spin-fluctuation mediated pairing due to this higher order content of the gap function, both in electron- and hole-doped systems. In the case of hole-doped systems, the non-monotonicity of the gap function is seen by a gap enhancement at the position of the antinodes, i.e. where the first order gap function is maximal. However, the situation is complicated by the presence of an energy gap at the antinodal positions, which is present at temperatures above the superconducting transition temperature, the so-called ”pseudogap”. Therefore, the non-monotonicity might not be entirely due to the superconducting gap, but could arise from a combination of the two gaps (superconducting and pseudo) coexisting. As shown in Fig. 2.2(left) for the case of $\mathrm{Bi_2Sr_2CaCu_2O_{8+\delta}}$, the deviations from the first harmonic d-wave is mostly seen in the underdoped regime [16]. Since the pseudogap is observed in the underdoped regime, this points towards an interpretation of the enhancement effect due to the pseudogap only. However, one report on $\mathrm{La_{2-x}Sr_xCuO_4}$ with hole doping of 15 %, [21] which is close to the optimal doping, also found strong non-monoticity of the superconducting gap, see Fig. 2.2(right). This indicates that the effect might not be intimately related to the presence of a pseudogap, and there could be different effects leading to gap enhancements in the antinodal regions. One of these may be pairing due to spin fluctuations.

Previously, the importance of hot spots when pairing is mediated by spin-fluctuations was also discussed by Khodel *et al.* [22] in relation to electron-doped cuprates. In this work it was shown that the

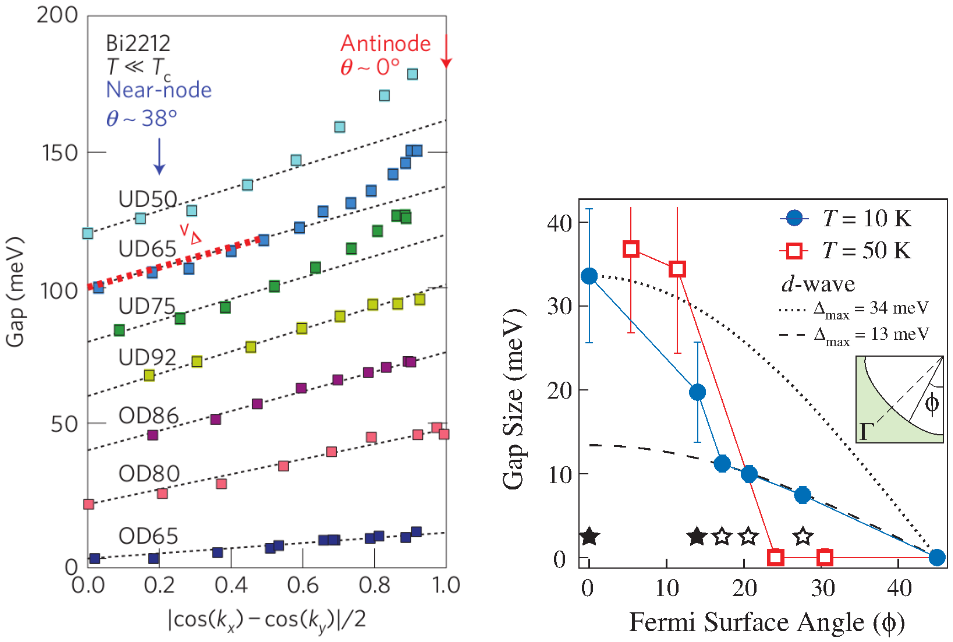

Figure 2.2: (**left:**) Deviation from the $\cos k_x - \cos k_y$ form of the energy gap in $Bi_2Sr_2CaCu_2O_{8+\delta}$. Adapted from Hashimoto *et al.*, Ref. [16]. (**right:**) Energy gap as a function of angle measured by ARPES in $La_{2-x}Sr_xCuO_4$ of $x = 0.15$ above and below the superconducting transition temperature. Adapted from Terashima *et al.*, Ref. [21].

$d_{x^2-y^2}$ solution becomes suppressed upon heavy electron doping because the hot spots are brought into close vicinity of the nodes. As a consequence of this, it was argued that electron-doped cuprates are expected to display a transition from $d_{x^2-y^2}$ to a different gap symmetry. In Ref. [22] triplet p-wave is proposed, but the underlying pairing mechanism is not settled.

2.3 Previous results on the pairing coupling strength

The effective pairing vertex due to spin fluctuations have been studied extensively in context of the one-band Hubbard model:

$$H = -\sum_{i,j,\sigma} t_{i,j} c^\dagger_{i\sigma} c_{j\sigma} + U \sum_i n_{i\uparrow} n_{i\downarrow} - \mu \sum_{i,\sigma} n_{i\sigma}. \tag{2.1}$$

Here $c^\dagger_{i\sigma}$ creates an electron on site i with spin σ. The electrons can hop between neighboring and next-neighboring sites with an associated energy of t and t', respectively. The interaction term U denotes the energy cost associated with having two electrons on the same site and the average electron density is controlled by the chemical potential, μ.

The effective pairing vertex is derived from higher order interactions in U, and the resulting superconducting pairing instabilities have been a subject of a number of previous reports. Here we will review the work of Hlubina [23], Guinea *et al.* [24] and Raghu *et al.* [25]. The approach in Refs. [23] and [24] is based on a projection of the pairing vertex onto different possible gap symmetries, and gives a measure of the coupling strength in the different symmetry channels. Their procedure is closely related to the method of Scalapino [12], and we adopt a similar approach in section 2.7. Hlubina and Guinea express the effective pairing to second order in U due to the exchange interaction, and Hlubina considers the limit of very small U and a range of t' hopping integrals, while Guinea *et al.* focus on a particular

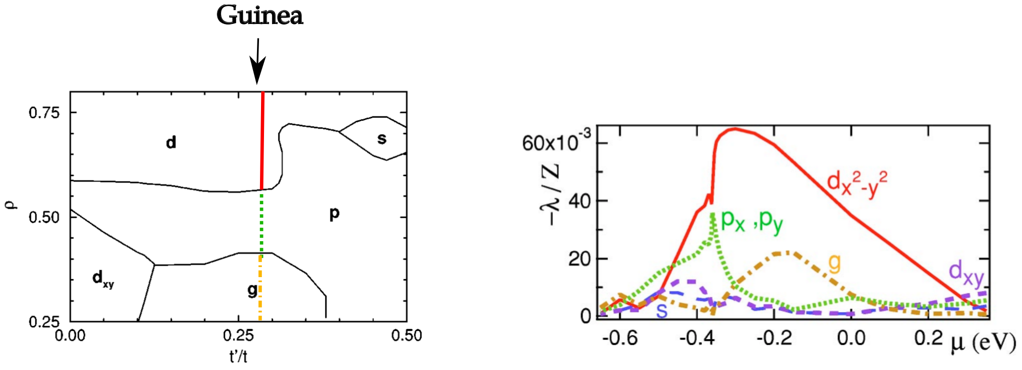

Figure 2.3: (**left:**) Coupling strength λ as a function of filling, ρ, and t' for $U \to 0$. Adapted from Hlubina, Ref. [23]. A line of results from Guinea *et al.*, Ref. [24], has been drawn at $|t'| = 0.276$ to vizualize the agreement between Ref. [23] and [24]. (**right:**) Coupling strength λ as a function of chemical potential for $U/t = 6$ and $t'/t = -0.276$. Note that the sign convention: the dominating instability has largest negative value of λ. Adapted from Guinea *et al.*, Ref. [24]. In both works, the gap functions are expressed in terms of an angle ϕ around the Fermi surface, and the gap function solutions are truncated to 15 harmonics in ϕ.

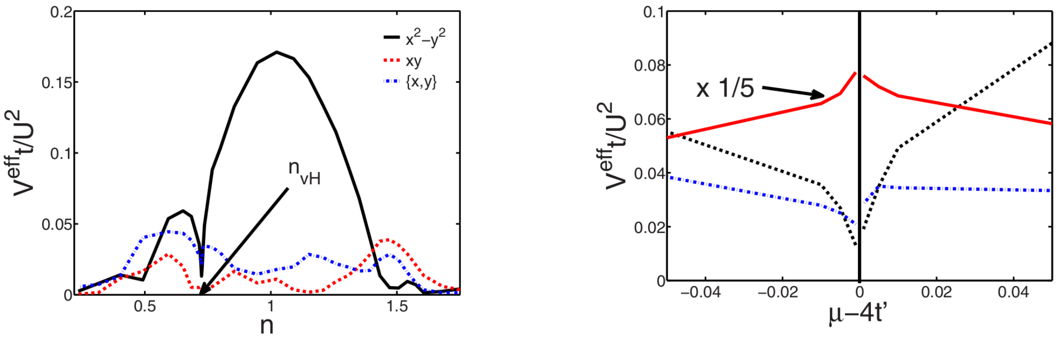

Figure 2.4: (**left:**) Pairing strength as a function of filling for $t' = -0.3$. $\mathrm{n_{vH}}$ is the density for which the van Hove singularity occurs at the Fermi level. (**right:**) Pairing strength as a function of $\mu - 4t'$. At $\mu - 4t' = 0$ the van Hove singularity resides at the Fermi level. For $t' = -0.05$, the red curve shows the pairing in the $d_{x^2-y^2}$ channel. For $t' = -0.3$ the dashed black line shows the pairing in the $d_{x^2-y^2}$ channel and blue dashed line shows the pairing in the p_x/p_y triplet channel. Note that in the latter case, the triplet solution is favored very close to the van Hove critical density, $\mathrm{n_{vH}}$. Adapted from Raghu *et al.*, Ref. [25].

band with $t'/t = -0.276$ and $U = 6$. The main results of the two papers is shown in Fig. 2.3. The phase diagram is presented by the coupling strength of the pairing interaction in five different symmetry channels. In both cases the expected $d_{x^2-y^2}$ is found close to half filling. In addition, Hlubina finds a large region of triplet superconductivity around $\langle n \rangle = 0.5$ for all t' values in a range from $t'/t = 0$ to $t'/t = 0.5$. Also, small regions of s (not the standard onsite, but a higher order nodal s-wave), a d_{xy} solution and a g-wave solution is found in different regimes of the phase diagram. The results of Guinea *et al.*, Fig. 2.3(right), has been plotted on top of the phase diagram of Hlubina, Fig. 2.3(left), to visualize the agreement between the two papers.

The effect of ferromagnetic fluctuations on spin-fluctuation mediated pairing was discussed first by Berk and Schrieffer [10] as mentioned above. These fluctuations are enhanced when a van Hove singularity is close to the Fermi level. Emphasis on the pairing strengths close to the doping for which the van Hove singularity resides at the Fermi level was discussed by Raghu *et al.* in Ref. [25]. In this work, analytical arguments were given for whether the $\mathbf{q} = (0, 0)$ or the $\mathbf{Q} = (\pi, \pi)$ structure dominates the susceptibility. When t' is small the $\mathbf{Q}$ structure is always dominant close to half filling, due to the close-to-perfect nesting of the Fermi surface (perfect nesting occurs for $t' = 0.0$). At larger values of t', the logarithmic divergence of the susceptibility at $\mathbf{q} = (0, 0)$ dominates, which will favor triplet pairing. We obtain similar features in our numerical approach as we will show in the following sections.

2.4 Derivation of the effective interaction Hamiltonian

In this section, we derive the pairing interaction due to bubble diagrams (screening effects) and ladder diagrams (exchange interactions) relevant of a paramagnetic, homogeneous system, which can be described by the one-band Hubbard model. We lay emphasis on the exact momentum space structure of the pairing interaction. In the literature, less care is usually taken considering the sign between the momentum of each Cooper pair $\mathbf{k}$ and $\mathbf{k}'$, where the pair scattering vertex is a function of either $\mathbf{k} - \mathbf{k}'$ or $\mathbf{k} + \mathbf{k}'$ in the translationally invariant system. As we shall show below, it is usually due to the fact that in the singlet channel it is of no importance whether the effective pairing interaction is written as a function of $\mathbf{k} - \mathbf{k}'$ or $\mathbf{k} + \mathbf{k}'$. However, in the triplet channel it is of great importance to keep track of the detailed momentum dependence and for a fully consistent formulation of the spin-fluctuation mediated pairing in both the singlet and triplet channels care should be given to this.

When we derive the interaction Hamiltonian for the effective pairing interaction between two electrons we start by the bare interaction due to the onsite Coulomb repulsion. This is the interaction part of the one-band Hubbard Hamiltonian, Eq. (2.1):

$$H_{\text{int}} = U \sum_{i} n_{i\uparrow} n_{i\downarrow} \tag{2.2}$$

We consider the effective interaction between opposite spin electrons derived from higher order interactions in U. This interaction vertex contains both a spin singlet and a spin triplet channel. On the contrary, the pairing between same spin electrons contains is a pure spin triplet. In the paramagnetic phase, where spin rotation symmetry is preserved, both of the same spin triplet channels (↑↑ and ↓↓) give the same result as the opposite spin triplet channel (↑↓ + ↓↑). Thus, all information about the superconducting instabilities the paramagnetic phase is contained in the interaction Hamiltonian of opposite spin electrons. However, for completeness we shall briefly discuss pairing of same spin electrons in section 2.4.3.

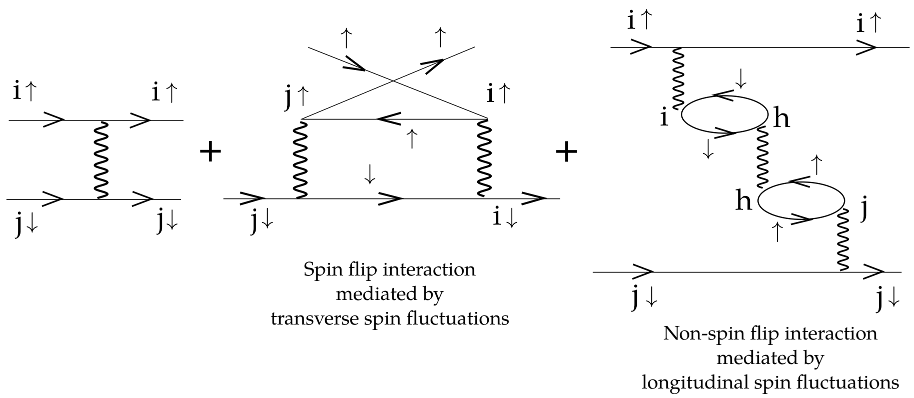

Figure 2.5: Representation of the interaction diagrams in real space. Straight lines are the electronic propagators. Wavy lines represent the bare interaction U. The ladder diagram represents an effective spin flip interaction, while the bubble diagram is a non-spin flip vertex.

In the following we derive the interaction vertices arising from the bubble and ladder (maximally crossed) diagrams. First we draw the lowest order diagrams in real space in Fig. 2.5. From inspection of the real space interaction diagrams it is seen that ladder diagrams represent spin-flip processes. By a spin-flip process we mean that the electron located at site j start as a spin down electron before the interaction, and becomes a spin up electron afterwards, while at site i the electron start as spin up electron and becomes as spin down electron after the interaction. This is illustrated in Fig. 2.5(middle). The electronic part of this interaction vertex is characterized by two Green's functions of opposite spin. This can be expressed in terms of a transverse spin susceptibility:

$$\begin{aligned}\chi_0^{+-}(\mathbf{r}_i,\mathbf{r}_j,\tau) &= \langle T_\tau S_i^+(0)S_j^-(\tau)\rangle \\ &= \langle T_\tau c_{i\uparrow}^\dagger(0)c_{i\downarrow}(0)c_{j\downarrow}^\dagger(\tau)c_{j\uparrow}(\tau)\rangle \\ &= -\langle T_\tau c_{j\uparrow}(\tau)c_{i\uparrow}^\dagger(0)\rangle\langle T_\tau c_{i\downarrow}(0)c_{j\downarrow}^\dagger(\tau)\rangle \\ &= -G_\uparrow(j,i,\tau)G_\downarrow(i,j,-\tau) \qquad (2.3)\end{aligned}$$

Thus, ladder diagrams depict spin-flip interactions mediated by transverse spin fluctuations.

The bubble diagram represents a spin preserving interaction. As shown in Fig. 2.5(right), the electron at site j stays spin down, and the electron at site i stays spin up before and after the interaction takes place. In this case, the electronic part of the interaction Hamiltonian is given by bubbles made from two Green's functions of same spin. These are related to the longitudinal spin susceptibility, since

$$\chi_0^{zz}(\mathbf{r}_i,\mathbf{r}_j,\tau) = \langle T_\tau S_i^z(0)S_j^z(\tau)\rangle = -G_\uparrow(j,i,\tau)G_\uparrow(i,j,-\tau) - G_\downarrow(j,i,\tau)G_\downarrow(i,j,-\tau) \qquad (2.4)$$

Therefore, the bubble diagrams represent non-spin flip interactions mediated by longitudinal spin fluctuations.

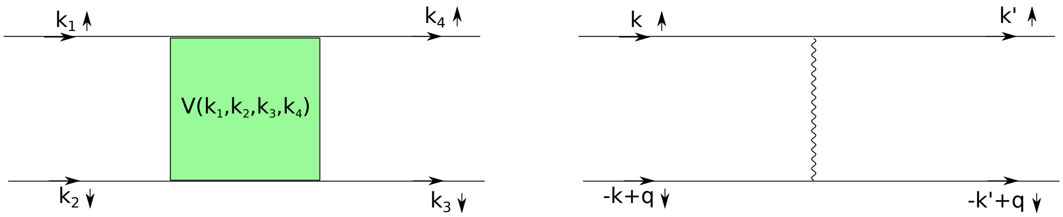

Figure 2.6: (**left**:) Bare U interaction diagram. (**right**:) General interaction vertex diagram. The spin indices is maintained in the same order as for the bare vertex, i.e. a "non-spin flip" vertex.

In a homogeneous system we express the interaction Hamiltonian by the Fourier transformed version of Eq. (2.2). Thus, we have a general form of the interaction Hamiltonian:

$$H_{\text{int}} = \sum_{\mathbf{k}_1,\mathbf{k}_2,\mathbf{k}_3,\mathbf{k}_4} V(\mathbf{k}_1,\mathbf{k}_2,\mathbf{k}_3,\mathbf{k}_4)c_{\mathbf{k}_4\uparrow}^\dagger c_{\mathbf{k}_3\downarrow}^\dagger c_{\mathbf{k}_2\downarrow}c_{\mathbf{k}_1\uparrow} + h.c. \qquad (2.5)$$

We draw the general interaction vertex of Eq. (2.5) as shown in Fig. 2.6(left). In all drawings of higher order diagrams it is important to keep the momentum labels in the drawing consistent with the order stated in Eq. (2.5). In this way we ensure that all higher order interaction Hamiltonians reduce correctly to the first order interaction Hamiltonian Eq. (2.2) in the limit $V_{\text{higher order}} = U$. Due to momentum conservation, we have only three free momenta. The specific relabeling of $\mathbf{k}_1$, $\mathbf{k}_2$, $\mathbf{k}_3$ and $\mathbf{k}_4$ in the case of bubble or ladder diagrams will be shown explicitly below.

The bare interaction vertex is shown in Fig. 2.6(right) and is given by:

$$H_{bare} = \frac{1}{2N}\sum_{\mathbf{k},\mathbf{k}',\mathbf{q}} Uc_{\mathbf{k}'\uparrow}^\dagger c_{-\mathbf{k}'+\mathbf{q}\downarrow}^\dagger c_{-\mathbf{k}+\mathbf{q}\downarrow}c_{\mathbf{k}\uparrow} + h.c. \qquad (2.6)$$

This is simply the bare repulsive Hubbard Hamiltonian as stated in Eq. (2.2) written in its Fourier transformed form.

2.4.1 Bubble diagrams

The interaction Hamiltonian related to bubble diagrams can be written as:

$$H_{lo/ch} = \frac{1}{2N} \sum_{\mathbf{k},\mathbf{k}',\mathbf{q}} V_{\text{long}}(\mathbf{k},\mathbf{k}',\mathbf{q}) c^{\dagger}_{\mathbf{k}'\downarrow} c^{\dagger}_{-\mathbf{k}'+\mathbf{q}\downarrow} c_{-\mathbf{k}+\mathbf{q}\downarrow} c_{\mathbf{k}\uparrow} + h.c. \tag{2.7}$$

This form of the interaction Hamiltonian with the labeling of the c-operators settles the way we draw the interaction vertex shown in Fig. 2.7. Note that the first vertex of "bubble"-type which connects opposite spin electrons has *two* bubbles. This is due to the constraint that the bare interaction U only connects opposite spin electrons. Evaluation of the vertex drawn in Fig. 2.7 gives:

$$\begin{aligned} -V_{\text{long}}(\mathbf{k},\mathbf{k}',\mathbf{q}) &= (-U)^3 \sum_{\mathbf{p}} G_{\uparrow}(\mathbf{p}+(\mathbf{k}-\mathbf{k}'),\tau) G_{\uparrow}(\mathbf{p},-\tau) \sum_{\mathbf{p}'} G_{\downarrow}(\mathbf{p}'+(\mathbf{k}-\mathbf{k}'),\tau') G_{\downarrow}(\mathbf{p}',-\tau') \\ &= -U^3[\chi_0^z(\mathbf{k}-\mathbf{k}')]^2. \end{aligned} \tag{2.8}$$

Here we have used that in the paramagnetic phase, $\sum_{\mathbf{p}} G_{\uparrow}(\mathbf{p}+\mathbf{q},\tau)G_{\uparrow}(\mathbf{p},-\tau) = \sum_{\mathbf{p}} G_{\downarrow}(\mathbf{p}+\mathbf{q},\tau)G_{\downarrow}(\mathbf{p},-\tau)$, and we have defined the longitudinal susceptibility by the Lindhard function:

$$\begin{aligned} \chi_0^z(\mathbf{q},\tau) &= -\sum_{\mathbf{p}} G(\mathbf{p}+\mathbf{q},\tau)G(\mathbf{p},-\tau) \\ \chi_0^z(\mathbf{q},i\omega_n) &= -\frac{1}{N}\sum_{\mathbf{p}} \frac{f(\xi_{\mathbf{p}+\mathbf{q}})-f(\xi_{\mathbf{p}})}{i\omega_n+\xi_{\mathbf{p}}-\xi_{\mathbf{p}+\mathbf{q}}}, \end{aligned} \tag{2.9}$$

The longitudinal/charge interaction Hamiltonian to third order has the form:

$$H_{lo/ch} = \frac{1}{2N} \sum_{\mathbf{k},\mathbf{k}',\mathbf{q}} U^3[\chi_0^z(\mathbf{k}-\mathbf{k}')]^2 c^{\dagger}_{\mathbf{k}'\uparrow} c^{\dagger}_{-\mathbf{k}'+\mathbf{q}\downarrow} c_{-\mathbf{k}+\mathbf{q}\downarrow} c_{\mathbf{k}\uparrow} + h.c. \tag{2.10}$$

For the higher order bubble diagrams, we are restricted to an even number of bubbles. We perform a summation to all orders in U:

$$\begin{aligned} -V_z(\mathbf{k}-\mathbf{k}') &= (-U)^3[\chi_0^z(\mathbf{k}-\mathbf{k}')]^2 + (-U)^5[\chi_0^z(\mathbf{k}-\mathbf{k}')]^4 + (-U)^7[\chi_0^z(\mathbf{k}-\mathbf{k}')]^6 + \cdots \\ &= (-U)^3[\chi_0^z(\mathbf{k}-\mathbf{k}')]^2[1+U^2[\chi_0^z(\mathbf{k}-\mathbf{k}')]^2 + U^4[\chi_0^z(\mathbf{k}-\mathbf{k}')]^4+\cdots] \\ &= -\frac{U^3[\chi_0^z(\mathbf{k}-\mathbf{k}')]^2}{1-U^2[\chi_0^z(\mathbf{k}-\mathbf{k}')]^2}. \end{aligned} \tag{2.11}$$

In conclusion, the interaction by longitudinal fluctuations can be rewritten in two terms in the following way:

$$V_z(\mathbf{k}-\mathbf{k}') = \frac{U^3\chi_0^z(\mathbf{k}-\mathbf{k}')^2}{1-U^2[\chi_0^z(\mathbf{k}-\mathbf{k}')]^2} = \frac{U^2}{2}\Big[\underbrace{\frac{\chi_0^z(\mathbf{k}-\mathbf{k}')}{1-U\chi_0^z(\mathbf{k}-\mathbf{k}')}}_{\chi^{sp}(\mathbf{k}-\mathbf{k}')} - \underbrace{\frac{\chi_0^z(\mathbf{k}-\mathbf{k}')}{1+U\chi_0^z(\mathbf{k}-\mathbf{k}')}}_{\chi^{ch}(\mathbf{k}-\mathbf{k}')}\Big]. \tag{2.12}$$

Usually, this type of interaction is referred to as the screening of the bare Coulomb interaction [9].

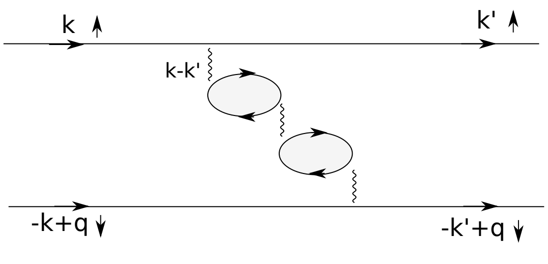

Figure 2.7: Bubble interaction diagram third order.

2.4.2 Ladder diagrams

Now we turn to the ladder diagrams. The exchange interaction to second order in U is shown in Fig. 2.8. The corresponding interaction Hamiltonian is given by the form:

$$H_{tr} = \frac{1}{2N} \sum_{\mathbf{k},\mathbf{k}',\mathbf{q}} V_{\mathrm{tr}}(\mathbf{k},\mathbf{k}',\mathbf{q}) c^{\dagger}_{\mathbf{k}'\uparrow} c^{\dagger}_{-\mathbf{k}'+\mathbf{q}\downarrow} c_{-\mathbf{k}\downarrow} c_{\mathbf{k}+\mathbf{q}\uparrow} + h.c. \tag{2.13}$$

Evaluation of the interaction vertex gives:

$$\begin{aligned} -V_{tr}(\mathbf{k},\mathbf{k}',\mathbf{q}) &= (-U)^2 \sum_{p} G_{\uparrow}(\mathbf{k}'-\mathbf{p},\tau) G_{\downarrow}(-\mathbf{k}-\mathbf{p},-\tau) \\ &= U^2 \sum_{\mathbf{p}} G_{\uparrow}(\mathbf{p}+\mathbf{k}',\tau) G_{\downarrow}(\mathbf{p}-\mathbf{k},-\tau) \\ &= -U^2 [-\sum_{\mathbf{p}} G_{\uparrow}(\mathbf{p}+(\mathbf{k}+\mathbf{k}'),\tau) G_{\downarrow}(\mathbf{p},-\tau)] \\ &= -U^2 \chi^0_{+-}(\mathbf{k}+\mathbf{k}') \end{aligned} \tag{2.14}$$

where in the paramagnetic phase, the bare susceptibility is given by the Lindhard function:

$$\chi_0^{+-}(\mathbf{q}, i\omega_n) = -\frac{1}{N} \sum_{\mathbf{p}} \frac{f(\xi_{\mathbf{p}+\mathbf{q}}) - f(\xi_{\mathbf{p}})}{i\omega_n + \xi_{\mathbf{p}} - \xi_{\mathbf{p}+\mathbf{q}}}, \tag{2.15}$$

The interaction Hamiltonian to second order reads:

$$H_{tr} = \frac{1}{2N} \sum_{\mathbf{k},\mathbf{k}',\mathbf{q}} U^2 \chi^0_{+-}(\mathbf{k}+\mathbf{k}') c^{\dagger}_{\mathbf{k}'\uparrow} c^{\dagger}_{-\mathbf{k}'+\mathbf{q}\downarrow} c_{-\mathbf{k}\downarrow} c_{\mathbf{k}+\mathbf{q}\uparrow} + h.c. \tag{2.16}$$

We sum all ladder type of diagrams to infinite order and end up with:

$$\begin{aligned} -V_{tr}(\mathbf{k}+\mathbf{k}') &= (-U)^2[-\chi^0_{+-}(\mathbf{k}+\mathbf{k}')] + (-U)^3[-\chi^0_{+-}(\mathbf{k}+\mathbf{k}')]^2 + (-U)^4[-\chi^0_{+-}(\mathbf{k}+\mathbf{k}')]^3 + \cdots \\ &= -U^2\chi^0_{+-}(\mathbf{k}+\mathbf{k}')[1 + U\chi^0_{+-}(\mathbf{k}+\mathbf{k}') + U^2[\chi^0_{+-}(\mathbf{k}+\mathbf{k}')]^2 + \cdots] \\ &= -\frac{U^2\chi^0_{+-}(\mathbf{k}+\mathbf{k}')}{1 - U\chi^0_{+-}(\mathbf{k}+\mathbf{k}')}. \end{aligned} \tag{2.17}$$

In conclusion, spin-fluctuation mediated pairing for two opposite spin electrons can be captured by the interaction vertices given by:

$$V_{lo}(\mathbf{q}) = \frac{U^2}{2}\Big[\frac{\chi_0^z(\mathbf{q})}{1 - U\chi_0^z(\mathbf{q})} - \frac{\chi_0^z(\mathbf{q})}{1 + U\chi_0^z(\mathbf{q})}\Big] \tag{2.18}$$

$$V_{tr}(\mathbf{q}) = \frac{U^2\chi^0_{+-}(\mathbf{q})}{1 - U\chi^0_{+-}(\mathbf{q})} \tag{2.19}$$

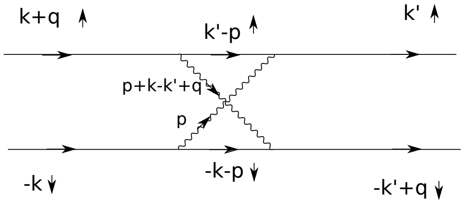

Figure 2.8: Ladder interaction diagram second order. Labelling of interaction vertices corresponds to the form of the interaction Hamiltonian stated in Eqn. (C.11).

where in the paramagnetic phase $\chi_0^z = \chi_0^{+-}$ are both given by the Lindhard function, Eq. (2.15). The final expression for the interaction Hamiltonian in which opposite spin electrons interact through transverse and longitudinal spin fluctuations can be written as:

$$H_{\text{int}} = \frac{1}{2N} \sum_{\mathbf{k},\mathbf{k}',\mathbf{q}} [V_{lo}(\mathbf{k}-\mathbf{k}') + V_{tr}(\mathbf{k}+\mathbf{k}')] c^\dagger_{\mathbf{k}'\uparrow} c^\dagger_{-\mathbf{k}'\downarrow} c_{-\mathbf{k}\downarrow} c_{\mathbf{k}\uparrow} + h.c. \tag{2.20}$$

In both forms, we have taken into account only $\mathbf{q} = (0,0)$ Cooper pairs. Now, we have spent some time discussing the details of the interaction Hamiltonian with emphasis on momentum indices $\mathbf{k}-\mathbf{k}'$ or $\mathbf{k}+\mathbf{k}'$. This is of great importance in unconventional superconductivity, where the momentum structure of the pairing interaction plays a decisive role for the superconducting state.

2.4.3 Same spin triplet interaction

In the derivation above we have only been concerned with the interaction of opposite spin electrons. Same spin electrons can interact, but only through effective interaction vertices which contain an *odd* number of bubbles. Therefore, in this case the interaction is solely mediated by longitudinal fluctuations. The procedure is similar to the one stated above for the longitudinal part of the opposite spin electron interaction; we simply sum up all diagrams containing an odd number of bubbles.

$$\begin{aligned} V_{ss}(\mathbf{k}-\mathbf{k}') &= -\frac{U^2\chi_0(\mathbf{k}-\mathbf{k}')}{1-U^2\chi_0^2(\mathbf{k}-\mathbf{k}')} \\ &= -\frac{U^2}{2}\left[\chi^{sp}(\mathbf{k}-\mathbf{k}') + \chi^{ch}(\mathbf{k}-\mathbf{k}')\right] \quad \text{(Odd number of bubbles for same spin (ss) interaction)} \end{aligned} \tag{2.21}$$

This interaction Hamiltonian takes the form

$$H_{ss} = \; = \frac{1}{2N} \sum_{\mathbf{q},\mathbf{k},\mathbf{k}'} \sum_{\sigma} V_{ss}(\mathbf{k}-\mathbf{k}') c^\dagger_{\mathbf{k}'\sigma} c^\dagger_{-\mathbf{k}'+q\sigma} c_{-\mathbf{k}+\mathbf{q}\sigma} c_{\mathbf{k}\sigma} \tag{2.22}$$

Here we cannot verify the form of the interaction Hamiltonian by taking the limit $V_{ss} = U$ and compare to the original Hubbard Hamiltonian, because all electron operators have same spin. The way to confirm the correctness of the form of the interaction Hamiltonian above, is to compare it to the opposite spin triplet case in the paramagnetic phase, where all triplet gaps should be identical. This check we will perform in the next section after the discussion of the formulation of the singlet and triplet interaction channel.

2.5 Singlet and triplet gap equations

In the previous section the interaction Hamiltonian was derived for a certain classes of interaction diagrams to infinite order. The way to proceed now is to derive the superconducting gap equation. First we write the interaction Hamiltonian in the BCS mean field form, and then we derive the self-consistent equation for the superconducting gap in the singlet and triplet channel. The Hamiltonian is given by:

$$H = \sum_{\mathbf{k}\sigma} \xi_{\mathbf{k}} c^\dagger_{\mathbf{k}\sigma} c_{\mathbf{k}\sigma} + H_{\text{int}} \tag{2.23}$$

with

$$\xi_{\mathbf{k}} = -2t(\cos k_x + \cos k_y) - 4t' \cos k_x \cos k_y - \mu \tag{2.24}$$

and the interaction part as derived in Eq. (2.20). Now we perform a mean field decoupling in the Cooper channel:

$$\begin{aligned}
H_{\text{int}} &= \frac{1}{2N}\sum_{\mathbf{k},\mathbf{k}'}\underbrace{[V_z(\mathbf{k}-\mathbf{k}')+V_{tr}(\mathbf{k}+\mathbf{k}')]}_{V(\mathbf{k},\mathbf{k}')}[c^\dagger_{\mathbf{k}'\uparrow}c^\dagger_{-\mathbf{k}'\downarrow}c_{-\mathbf{k}\downarrow}c_{\mathbf{k}\uparrow}+c^\dagger_{\mathbf{k}'\downarrow}c^\dagger_{-\mathbf{k}'\uparrow}c_{-\mathbf{k}\uparrow}c_{\mathbf{k}\downarrow}] \\
&\simeq \frac{1}{2N}\sum_{k,k'}V(\mathbf{k},\mathbf{k}')\Big[\langle c^\dagger_{\mathbf{k}'\uparrow}c^\dagger_{-\mathbf{k}'\downarrow}\rangle c_{-\mathbf{k}\downarrow}c_{\mathbf{k}\uparrow} \\
&\qquad\qquad +c^\dagger_{\mathbf{k}'\uparrow}c^\dagger_{-\mathbf{k}'\downarrow}\langle c_{-\mathbf{k}\downarrow}c_{\mathbf{k}\uparrow}\rangle \\
&\qquad\qquad +\langle c^\dagger_{\mathbf{k}'\downarrow}c^\dagger_{-\mathbf{k}'\uparrow}\rangle c_{-\mathbf{k}\uparrow}c_{\mathbf{k}\downarrow}] \\
&\qquad\qquad +c^\dagger_{\mathbf{k}'\downarrow}c^\dagger_{-\mathbf{k}'\uparrow}\langle c_{-\mathbf{k}\uparrow}c_{\mathbf{k}\downarrow}\rangle\Big] \\
&= \frac{1}{2N}\sum_{\mathbf{k},\mathbf{k}'}V(\mathbf{k},\mathbf{k}')\Big[\langle c^\dagger_{\mathbf{k}'\uparrow}c^\dagger_{-\mathbf{k}'\downarrow}\rangle c_{-\mathbf{k}\downarrow}c_{\mathbf{k}\uparrow}+\langle c^\dagger_{\mathbf{k}'\downarrow}c^\dagger_{-\mathbf{k}'\uparrow}\rangle c_{-\mathbf{k}\uparrow}c_{\mathbf{k}\downarrow} \\
&\qquad\qquad +\langle c_{-\mathbf{k}\downarrow}c_{\mathbf{k}\uparrow}\rangle c^\dagger_{\mathbf{k}'\uparrow}c^\dagger_{-\mathbf{k}'\downarrow}+\langle c_{-\mathbf{k}\uparrow}c_{\mathbf{k}\downarrow}\rangle c^\dagger_{\mathbf{k}'\downarrow}c^\dagger_{-\mathbf{k}'\uparrow}\Big] \\
&= \frac{1}{4N}\sum_{\mathbf{k},\mathbf{k}'}\Big[V(\mathbf{k},\mathbf{k}')\Big[\langle c^\dagger_{\mathbf{k}'\uparrow}c^\dagger_{-\mathbf{k}'\downarrow}\rangle-\langle c^\dagger_{\mathbf{k}'\downarrow}c^\dagger_{-\mathbf{k}'\uparrow}\rangle\Big][c_{-\mathbf{k}\downarrow}c_{\mathbf{k}\uparrow}-c_{-\mathbf{k}\uparrow}c_{\mathbf{k}\downarrow}] \\
&\qquad +V(\mathbf{k},\mathbf{k}')\Big[\langle c^\dagger_{\mathbf{k}'\uparrow}c^\dagger_{-\mathbf{k}'\downarrow}\rangle+\langle c^\dagger_{\mathbf{k}'\downarrow}c^\dagger_{-\mathbf{k}'\uparrow}\rangle\Big][c_{-\mathbf{k}\downarrow}c_{\mathbf{k}\uparrow}+c_{-\mathbf{k}\uparrow}c_{\mathbf{k}\downarrow}] \\
&\qquad +h.c.\Big] \qquad (2.25)
\end{aligned}$$

We hereby split the interaction Hamiltonian into two separate channels which do not mix; the singlet and triplet channel. The superconducting instability will occur in one of these channels. For the two dimensional square lattice, the gap symmetry can be classified according to the five irreducible representations of the D_{4h} group that are even under reflection through the horizontal plane, i.e. extended s-wave (s^*), $d_{x^2-y^2}$, d_{xy}, g and the triplet solution, p_x/p_y, which is a two dimensional representation and thus doubly degenerate:

$$A_{1g}:\quad s^*=\cos(k_x)+\cos(k_y), \qquad (2.26a)$$

$$A_{2g}:\quad g=[\cos(k_x)-\cos(k_y)]\sin(k_x)\sin(k_y), \qquad (2.26b)$$

$$B_{1g}:\quad d_{x^2-y^2}=\cos(k_x)-\cos(k_y), \qquad (2.26c)$$

$$B_{2g}:\quad d_{xy}=\sin(k_x)\sin(k_y), \qquad (2.26d)$$

$$E_u:\quad p=\sin(k_x)\quad / \quad \sin(k_y). \qquad (2.26e)$$

As shown above, the singlet and triplet mean field Hamiltonians are given by:

$$H^{sing/trip}_{MF} = \frac{1}{4N}\sum_{\mathbf{k},\mathbf{k}'}\Big[V(\mathbf{k},\mathbf{k}')\Big[\langle c^\dagger_{\mathbf{k}'\uparrow}c^\dagger_{-\mathbf{k}'\downarrow}\rangle\mp\langle c^\dagger_{\mathbf{k}'\downarrow}c^\dagger_{-\mathbf{k}'\uparrow}\rangle\Big]\big(c_{-\mathbf{k}\downarrow}c_{\mathbf{k}\uparrow}\mp c_{-\mathbf{k}\uparrow}c_{\mathbf{k}\downarrow}\big)+h.c.\Big]. \qquad (2.27)$$

Now we proceed by determining the gap equation arising from the mean field Hamiltonian Eq. (2.27). For the singlet channel we have:

$$\begin{aligned}
H^{sing}_{MF} &= \sum_{\mathbf{k}\sigma}\xi_{\mathbf{k}}c^\dagger_{\mathbf{k}\sigma}c_{\mathbf{k}\sigma}+\frac{1}{4N}\sum_{\mathbf{k},\mathbf{k}'}\Big[V(\mathbf{k},\mathbf{k}')\Big[\langle c^\dagger_{\mathbf{k}'\uparrow}c^\dagger_{-\mathbf{k}'\downarrow}\rangle-\langle c^\dagger_{\mathbf{k}'\downarrow}c^\dagger_{-\mathbf{k}'\uparrow}\rangle\Big]\big(c_{-\mathbf{k}\downarrow}c_{\mathbf{k}\uparrow}-c_{-\mathbf{k}\uparrow}c_{\mathbf{k}\downarrow}\big) \\
&\qquad +V(\mathbf{k},\mathbf{k}')\Big[\langle c_{-\mathbf{k}'\downarrow}c_{\mathbf{k}'\uparrow}\rangle-\langle c_{-\mathbf{k}'\uparrow}c_{\mathbf{k}'\downarrow}\rangle\Big]\big(c^\dagger_{\mathbf{k}\uparrow}c^\dagger_{-\mathbf{k}\downarrow}-c^\dagger_{\mathbf{k}\downarrow}c^\dagger_{-\mathbf{k}\uparrow}\big)\Big] \\
&= \sum_{\mathbf{k}\sigma}\xi_{\mathbf{k}}c^\dagger_{\mathbf{k}\sigma}c_{\mathbf{k}\sigma}-\sum_{\mathbf{k}}\Big[\Delta_{\mathbf{k}}\big(c_{-\mathbf{k}\downarrow}c_{\mathbf{k}\uparrow}-c_{-\mathbf{k}\uparrow}c_{\mathbf{k}\downarrow}\big)+\Delta^*_{\mathbf{k}}\big(c^\dagger_{\mathbf{k}\uparrow}c^\dagger_{-\mathbf{k}\downarrow}-c^\dagger_{\mathbf{k}\downarrow}c^\dagger_{-\mathbf{k}\uparrow}\big)\Big],
\end{aligned}$$

$$(2.28)$$

with

$$\begin{aligned} V(\mathbf{k},\mathbf{k}') &= U + \frac{1}{2}[V_z(\mathbf{k}-\mathbf{k}') - V_c(\mathbf{k}-\mathbf{k}')] + V_{+-}(\mathbf{k}+\mathbf{k}'), \tag{2.29} \\ & \tag{2.30} \end{aligned}$$

and each of the pairing contributions are given by the RPA expressions:

$$\begin{aligned} V_z(\mathbf{k}-\mathbf{k}') &= \frac{U^2\chi_0^z(\mathbf{k}-\mathbf{k}')}{1-\bar{U}\chi_0^z(\mathbf{k}-\mathbf{k}')}, \tag{2.31} \\ V_c(\mathbf{k}-\mathbf{k}') &= \frac{U^2\chi_0^z(\mathbf{k}-\mathbf{k}')}{1+\bar{U}\chi_0^z(\mathbf{k}-\mathbf{k}')}, \tag{2.32} \\ V_{+-}(\mathbf{k}+\mathbf{k}') &= \frac{U^2\chi_0^{+-}(\mathbf{k}+\mathbf{k}')}{1-\bar{U}\chi_0^{+-}(\mathbf{k}+\mathbf{k}')}. \tag{2.33} \\ & \tag{2.34} \end{aligned}$$

Here $\bar{U} = U/z$ is a renormalized Coulomb interaction. We will mostly use $z = 1$ corresponding to the usual RPA, but when solving the full gap equation we use a renormalization ($z = 2, 3$) to achieve a larger pairing strength for numerical convergence. The bare susceptibility in the paramagnetic phase is given by the Lindhard function

$$\chi_0(\mathbf{q},\omega) = \frac{1}{N}\sum_{\mathbf{k}} \frac{f(\xi_{\mathbf{k}+\mathbf{q}}) - f(\xi_{\mathbf{k}})}{\omega + \xi_{\mathbf{k}} - \xi_{\mathbf{k}+\mathbf{q}} + i\eta}, \tag{2.35}$$

The strength of the interaction is given by the real part of the vertex functions Eqs. (2.31-2.33) evaluated at zero energy. We neglect the energy dependence of the interactions.

The gap is defined as

$$\begin{aligned} \Delta_{\mathbf{k}} &= -\frac{1}{4N}\sum_{\mathbf{k}'} V(\mathbf{k},\mathbf{k}')\Big[\langle c^{\dagger}_{\mathbf{k}'\uparrow}c^{\dagger}_{-\mathbf{k}'\downarrow}\rangle - \langle c^{\dagger}_{\mathbf{k}'\downarrow}c^{\dagger}_{-\mathbf{k}'\uparrow}\rangle\Big] \tag{2.36} \\ \Delta^*_{\mathbf{k}} &= -\frac{1}{4N}\sum_{\mathbf{k}'} V(\mathbf{k},\mathbf{k}')\Big[\langle c_{-\mathbf{k}'\downarrow}c_{\mathbf{k}'\uparrow}\rangle - \langle c_{-\mathbf{k}'\uparrow}c_{\mathbf{k}'\downarrow}\rangle\Big] \tag{2.37} \end{aligned}$$

Rewriting the Hamiltonian in matrix form we have:

$$\begin{aligned} H^{sing}_{MF} &= \sum_{\mathbf{k}} [c^{\dagger}_{\mathbf{k}\uparrow}\ c_{-\mathbf{k}\downarrow}] \begin{bmatrix} \xi_{\mathbf{k}} & -\Delta^*_{\mathbf{k}} \\ -\Delta_{\mathbf{k}} & -\xi_{\mathbf{k}} \end{bmatrix} \begin{bmatrix} c_{\mathbf{k}\uparrow} \\ c^{\dagger}_{-\mathbf{k}\downarrow} \end{bmatrix} + [c^{\dagger}_{-\mathbf{k}\uparrow}\ c_{\mathbf{k}\downarrow}] \begin{bmatrix} 0 & -\Delta^*_{\mathbf{k}} \\ -\Delta_{\mathbf{k}} & 0 \end{bmatrix} \begin{bmatrix} c_{-\mathbf{k}\uparrow} \\ c^{\dagger}_{\mathbf{k}\downarrow} \end{bmatrix} \\ &= \sum_{\mathbf{k}} [c^{\dagger}_{\mathbf{k}\uparrow}\ c_{-\mathbf{k}\downarrow}] \begin{bmatrix} \xi_{\mathbf{k}} & -(\Delta^*_{\mathbf{k}} + \Delta^*_{-\mathbf{k}}) \\ -(\Delta_{\mathbf{k}} + \Delta_{-\mathbf{k}}) & -\xi_{\mathbf{k}} \end{bmatrix} \begin{bmatrix} c_{\mathbf{k}\uparrow} \\ c^{\dagger}_{-\mathbf{k}\downarrow} \end{bmatrix} \\ &= \sum_{\mathbf{k}} [c^{\dagger}_{\mathbf{k}\uparrow}\ c_{-\mathbf{k}\downarrow}] \begin{bmatrix} \xi_{\mathbf{k}} & -\Delta^{s*}_{\mathbf{k}} \\ -\Delta^s_{\mathbf{k}} & -\xi_{\mathbf{k}} \end{bmatrix} \begin{bmatrix} c_{\mathbf{k}\uparrow} \\ c^{\dagger}_{-\mathbf{k}\downarrow} \end{bmatrix}, \tag{2.38} \end{aligned}$$

with the singlet gap defined as:

$$\Delta^s_{\mathbf{k}} = -\frac{1}{4N}\sum_{k'} (V(\mathbf{k},\mathbf{k}') + V(-\mathbf{k},\mathbf{k}'))\Big[\langle c^{\dagger}_{\mathbf{k}'\uparrow}c^{\dagger}_{-\mathbf{k}'\downarrow}\rangle - \langle c^{\dagger}_{\mathbf{k}'\downarrow}c^{\dagger}_{-\mathbf{k}'\uparrow}\rangle\Big]. \tag{2.39}$$

The eigenvalues are:

$$\Omega^s_{\mathbf{k}} = \pm\sqrt{\xi^2_{\mathbf{k}} + |\Delta^s_{\mathbf{k}}|^2}. \tag{2.40}$$

The problem is diagonalized by a Bogoliubov transformation which is given by:

$$\begin{bmatrix} c_{\mathbf{k}\uparrow} \\ c^{\dagger}_{-\mathbf{k}\downarrow} \end{bmatrix} = \begin{bmatrix} u_{\mathbf{k}} & v_{\mathbf{k}} \\ -v_{\mathbf{k}} & u_{\mathbf{k}} \end{bmatrix} \begin{bmatrix} \gamma_{\mathbf{k}\uparrow} \\ \gamma^{\dagger}_{-\mathbf{k}\downarrow} \end{bmatrix}. \tag{2.41}$$

To obtain the final self-consistent expression for the superconducting gap, we must express the mean fields of Eq. (2.39) in terms of the new dispersion, $\Omega^s_{\mathbf{k}}$.

$$\begin{aligned}\langle c^\dagger_{\mathbf{k}\uparrow} c^\dagger_{-\mathbf{k}\downarrow}\rangle &= -\langle c^\dagger_{\mathbf{k}\downarrow} c^\dagger_{-\mathbf{k}\uparrow}\rangle = u_{\mathbf{k}} v_{\mathbf{k}}[1-2f(\Omega_{\mathbf{k}})] = u_{\mathbf{k}} v_{\mathbf{k}} \tanh\Big(\frac{\Omega_{\mathbf{k}}}{2k_BT}\Big) && (2.42)\\ \langle c^\dagger_{\mathbf{k}\uparrow} c^\dagger_{-\mathbf{k}\downarrow}\rangle - \langle c^\dagger_{\mathbf{k}\downarrow} c^\dagger_{-\mathbf{k}\uparrow}\rangle &= 2\frac{\Delta^s_{\mathbf{k}}}{2\Omega_{\mathbf{k}}}\tanh\Big(\frac{\Omega_{\mathbf{k}}}{2k_BT}\Big) && (2.43)\end{aligned}$$

The final form of the singlet gap equation is therefore:

$$\Delta^s_{\mathbf{k}} = -\frac{1}{4N}\sum_{k'}[V(\mathbf{k},\mathbf{k}') + V(-\mathbf{k},\mathbf{k}')]\frac{\Delta^s_{\mathbf{k}}}{\Omega^s_{\mathbf{k}}}\tanh\Big(\frac{\beta\Omega^s_{\mathbf{k}}}{2}\Big). \tag{2.44}$$

If we perform the exact same exercise with the triplet channel of the interaction Hamiltonian, i.e. the lower sign of Eq. (2.27) we get the final form of the triplet gap equation:

$$\Delta^t_{\mathbf{k}} = -\frac{1}{4N}\sum_{k'}[V(\mathbf{k},\mathbf{k}') - V(-\mathbf{k},\mathbf{k}')]\frac{\Delta^t_{\mathbf{k}}}{\Omega^t_{\mathbf{k}}}\tanh\Big(\frac{\beta\Omega^t_{\mathbf{k}}}{2}\Big). \tag{2.45}$$

From Eqs. (2.44) and (2.45) it is seen that the gap equation contains an explicit symmetrization/antisymmetrization of the pairing potential to the singlet/triplet channel. This means that for each channel, the effective pairing interaction is

$$\begin{aligned}V^{sing}(\mathbf{k},\mathbf{k}') &= \frac{1}{2}[V(\mathbf{k},\mathbf{k}') + V(-\mathbf{k},\mathbf{k}')]\\ &= \frac{1}{2}\Big[2U + \frac{3}{2}U^2\chi_s(\mathbf{k}-\mathbf{k}') - \frac{1}{2}U^2\chi_c(\mathbf{k}-\mathbf{k}') + \frac{3}{2}U^2\chi_s(\mathbf{k}+\mathbf{k}') - \frac{1}{2}U^2\chi_c(\mathbf{k}+\mathbf{k}')\Big], && (2.46)\\ V^{trip}(\mathbf{k},\mathbf{k}') &= \frac{1}{2}[V(\mathbf{k},\mathbf{k}') - V(-\mathbf{k},\mathbf{k}')]\\ &= \frac{1}{2}\Big[-\frac{1}{2}U^2\chi_s(\mathbf{k}-\mathbf{k}') - \frac{1}{2}U^2\chi_c(\mathbf{k}-\mathbf{k}') + \frac{1}{2}U^2\chi_s(\mathbf{k}+\mathbf{k}') + \frac{1}{2}U^2\chi_c(\mathbf{k}+\mathbf{k}')\Big]. && (2.47)\end{aligned}$$

It is these momentum structures that has to be considered in the determination of the superconducting gap, and not the structure derived directly from the diagrammatics. Furthermore, it is now evident that we obtain the same effective pairing interaction in the triplet channel of same spin and opposite spin electrons, compare Eq. (2.47) with the antisymmetrizated version of Eq. (2.21). Since in the paramagnetic phase there is no breaking of spin rotation symmetry, this is of course to be expected. On the contrary, in the SDW phase, we cannot expect all triplet gap equations to be identical. This will be discussed further in chapter 5.

For the moment we will concentrate on the momentum structures of the effective interactions as given in Eqs. (2.46) and (2.47). Some important differences between the structure of the pairing in the singlet and triplet channel allows us deduce which one will be favored over the other already at this point. First, we note that the strength of the charge part of the potential is usually much weaker than the spin part. It is the proximity to a magnetic instability, i.e. $URe\chi_0 \to 1$ which drives the superconducting transition. Therefore, we can focus the attention to the spin contributions of Eqs. (2.46) and (2.47). In conventional superconductors, the phonon-mediated interaction $V_{\mathbf{k},\mathbf{k}'}$ is simply approximated by a negative constant, $V_{\mathbf{k},\mathbf{k}'} = -V$, for $\mathbf{k}$ and $\mathbf{k}'$ in a thin energy shell around the Fermi level. This negative potential is referred to as an attractive potential. For unconventional superconductivity we keep the same nomenclature, i.e. an attractive potential contribution refers to a negative value of $V_{\mathbf{k},\mathbf{k}'}$, whereas a repulsive interaction is given by a positive value of $V_{\mathbf{k},\mathbf{k}'}$. Note that the superconducting gap equation is unsolvable if $V_{\mathbf{k},\mathbf{k}'}$ is constant (i.e. momentum independent) and positive (repulsive). But as pointed out in e.g. Ref. [26] a peaked momentum structure at some momentum vector $\mathbf{q}_{pair}$ combined with a gap solution that changes sign between $\mathbf{k}$ and $\mathbf{k}' = \mathbf{k} + \mathbf{q}_{pair}$, purely repulsive pairing potentials can give rise to a superconducting phase. In the case of $d_{x^2-y^2}$ the pairing vector is $\mathbf{q}_{pair} = (\pi, \pi)$ and this is particularly relevant for a system close to an antiferromagnetic instability, where the Fermi surface displays pronounced nesting properties at this wave vector. However, the property is completely general and a similar scenario could in principle take place for other susceptibility structures as well, in this case favoring a different superconducting gap symmetry. A close look on the gap equations, Eqs. (2.44) and (2.45) reveals that a negative potential contribution $V(\mathbf{k}, \mathbf{k}') < 0$ will favor the same sign of the gap for $\Delta_{\mathbf{k}}$ and $\Delta_{\mathbf{k}'}$. On the contrary, a positive potential contribution $V(\mathbf{k}, \mathbf{k}') > 0$ will favor opposite signs of $\Delta_{\mathbf{k}}$ and $\Delta_{\mathbf{k}'}$. This is the main focus of the next section where we will study the case of dopings far away from the half filled region where the antiferromagnetic instability and thus the $d_{x^2-y^2}$ pairing symmetry dominates.

But before we turn to a thorough investigation of the one-band case for spin-fluctuation mediated pairing we would like to address one very important difference between the effective potential in the singlet and triplet channel. This difference relies on the fact that there is a different sign between the term $\frac{U^2}{2}\chi_s(\mathbf{k} - \mathbf{k}')$, which is repulsive in the singlet channel, but *attractive* in the triplet channel. This has important consequences for the competition between singlet and triplet superconductivity. In fact, it was first discussed in 1966 by Berk and Schrieffer [10] in relation to superfluidity in ^{3}He. In 1966 it was believed that the superfluid phase o ^{3}He was a spin singlet $l = 2$ phase. At the same time it was argued that the spin susceptibility was peaked at $\mathbf{q} = (0, 0)$, and from this is was inferred that spin fluctuations actually suppress superfluidity in ^{3}He. Remember that in the singlet channel the potential contribution $\frac{U^2}{2}\chi_s(\mathbf{k} - \mathbf{k}')$, provides a repulsive interaction for $\mathbf{k} = \mathbf{k}'$. It was later found out that the superfluid phase of ^{3}He is in fact of a triplet form, and this falls very nicely in place along the lines of a spin fluctuation mediated interaction, since a $\mathbf{q} = (0, 0)$ peak in the spin susceptibility actually provides an attraction for $\mathbf{k} = \mathbf{k}'$, as seen from the term $-\frac{U^2}{2}\chi_s(\mathbf{k} - \mathbf{k}')$. As a very general feature of spin fluctuation mediated pairing, we can conclude just by considering the potential forms stated in Eqs. (2.46) and (2.47) that a $\mathbf{q} = (0, 0)$ peak in the spin susceptibility will suppress singlet superconductivity, and support development of a triplet superconducting phase.

2.6 Linearized gap equation and projection

We have derived expressions for the superconducting gaps in Eqs. (2.44) and (2.45) above. These equations must be solved self-consistently since $\Delta_{\mathbf{k}}$ enters the dispersion of the quasiparticle spectrum $\Omega_{\mathbf{k}}$. There exists, however, a commonly used simplified way of attacking the problem. The idea is to consider the solution of the gap in the case where the temperature is just below the superconducting transition temperature. Here we expect the mean field order parameter $\Delta_{\mathbf{k}}$ to be very small. Therefore we can invoke an approximation $\Omega_{\mathbf{k}} = \sqrt{\xi_{\mathbf{k}}^2 + |\Delta_{\mathbf{k}}|^2} \sim |\xi_{\mathbf{k}}|$. For simplicity we have suppressed the singlet/triplet index, but the derivation holds in both cases. Using this approximation we have:

$$\Delta_{\mathbf{k}} = -\frac{1}{2N}\sum_{\mathbf{k}'}[V(\mathbf{k}, \mathbf{k}') \pm V(-\mathbf{k}, \mathbf{k}')]\frac{\Delta_{\mathbf{k}'}}{2|\xi_{\mathbf{k}'}|}\tanh\Big(\frac{|\xi_{\mathbf{k}'}|}{2k_BT}\Big). \tag{2.48}$$

If we define $G(\mathbf{k},\mathbf{k}') = -\frac{1}{2N}[V(\mathbf{k},\mathbf{k}') \pm V(-\mathbf{k},\mathbf{k}')]\Delta_{\mathbf{k}'}$ and $F(\xi_{\mathbf{k}'}) = \frac{\tanh(\frac{|\xi_{\mathbf{k}'}|}{2k_BT_c})}{2|\xi_{\mathbf{k}'}|}$ we have the following equation:

$$\begin{aligned}
\Delta_{\mathbf{k}} &= \sum_{\mathbf{k}'} F(\xi_{\mathbf{k}'})G(\mathbf{k},\mathbf{k}') \\
&= \frac{N}{(2\pi)^2}\int d\mathbf{k}' F(\xi_{\mathbf{k}'})G(\mathbf{k},\mathbf{k}') \\
&= \frac{N}{(2\pi)^2}\int_{FS} d\mathbf{k}' \int d\xi\,\delta(\xi-\xi_{\mathbf{k}'})F(\xi_{\mathbf{k}'})G(\mathbf{k},\mathbf{k}') \\
&= \frac{N}{(2\pi)^2}\int_{FS} \frac{d\mathbf{k}'}{|v_{\mathbf{k}'}|}G(\mathbf{k}')\int d\xi F(\xi) \qquad \text{(invoke energy cutoff, } \xi_c) \\
&= \frac{N}{(2\pi)^2}\Big[-\frac{1}{2N}\int_{FS}\frac{d\mathbf{k}'}{|v_{\mathbf{k}'}|}[V(\mathbf{k},\mathbf{k}') \pm V(-\mathbf{k},\mathbf{k}')]\Delta_{\mathbf{k}'}\Big]\int_{-\xi_c}^{\xi_c} d\xi \frac{1}{2|\xi|}\tanh(\frac{|\xi|}{2k_BT_c}) \qquad (2.49)
\end{aligned}$$

The Fermi velocity is given by $v_{\mathbf{k}} = \frac{d\xi_{\mathbf{k}}}{d\mathbf{k}}$. This is easily obtained analytically for the simple one-band case. The energy integral is solved approximately in the limit where $\xi_c < k_BT_c$. We get

$$\int_{-\xi_c}^{\xi_c} d\xi \frac{1}{2|\xi|}\tanh(\frac{|\xi|}{2k_BT_c}) = \int_0^{\xi_c} d\xi \frac{1}{|\xi|}\tanh(\frac{|\xi|}{2k_BT_c}) \sim \ln\Big[\frac{1.13\xi_c}{k_BT_c}\Big]. \qquad (2.50)$$

The remaining part of the linearized gap equation is expressed as an eigenvalue problem, where we convert the Fermi surface integral into a sum of k values on the Fermi surface:

$$\begin{aligned}
\frac{N}{(2\pi)^2}\Big[-\frac{1}{2N}\int_{FS}\frac{d\mathbf{k}'}{|v_{\mathbf{k}'}|}[V(\mathbf{k},\mathbf{k}') \pm V(-\mathbf{k},\mathbf{k}')]\Delta_{\mathbf{k}'}\Big] &= \lambda\Delta(\mathbf{k}) \qquad (2.51) \\
&\Updownarrow \\
\Big[-\frac{1}{2(2\pi)^2}\int_{FS}\frac{d\mathbf{k}'}{|v_{\mathbf{k}'}|}[V(\mathbf{k},\mathbf{k}') \pm V(-\mathbf{k},\mathbf{k}')]\Big]\Delta_{k'} &= \lambda\Delta(\mathbf{k}) \qquad (2.52) \\
&\Updownarrow \\
-\frac{1}{2(2\pi)^2}\sum_{\mathbf{k}'}\frac{l_{\mathbf{k}'}}{|v_{\mathbf{k}'}|}[V(\mathbf{k},\mathbf{k}') \pm V(-\mathbf{k},\mathbf{k}')]\Delta(\mathbf{k}') &= \lambda\Delta(\mathbf{k}) \qquad (2.53)
\end{aligned}$$

When converting the integral to a sum, we introduce $l_{\mathbf{k}'}$, which denotes the length of the Fermi surface path represented by the point $\mathbf{k}'$.

We diagonalize the matrix, $M_{\mathbf{k},\mathbf{k}'}$:

$$M_{\mathbf{k},\mathbf{k}'} = -\frac{1}{2(2\pi)^2}\frac{l_{\mathbf{k}'}}{|v_{\mathbf{k}'}|}[V(\mathbf{k},\mathbf{k}') \pm V(-\mathbf{k},\mathbf{k}')]. \qquad (2.54)$$

The diagonalization gives both positive and negative eigenvalues. The results must be related to Eq. (2.49). Thereby we get:

$$\Delta_{\mathbf{k}} = \lambda\Delta_{\mathbf{k}}\underbrace{\int_{-\xi_c}^{\xi_c} d\xi \frac{1}{2|\xi|}\tanh(\frac{|\xi|}{2k_BT_c})}_{\alpha}. \qquad (2.55)$$

Here we note that α must be positive, because the integrant is positive. Therefore, the only valid solutions of the diagonalization must have positive λ. We identify the largest eigenvalues λ and the corresponding eigenvectors, $g(\mathbf{k})$. After diagonalization we are left with the independent equations for each eigenvector of the problem:

$$\begin{aligned}
\Delta_{\mathbf{k}} &= \lambda\Delta_{\mathbf{k}}\ln\Big[\frac{1.13\xi_c}{k_BT_c}\Big] \\
\Leftrightarrow k_BT_c &= 1.13\xi_c e^{-\frac{1}{\lambda}} \qquad (2.56)
\end{aligned}$$

From this it is seen that the largest eigenvalue, λ^*, with the corresponding eigenvector, $\Delta^*_{\mathbf{k}}$, will give the dominant superconducting instability, since λ^* gives rise to the largest superconducting transition temperature (negative values of λ do not provide a valid solution).

All solutions to the gap equation can be classified into one of the five classes listed in Eqs. (2.26a)-(2.26e) according to its symmetry properties. Note that there is only one triplet class. This means that all triplet gap solutions transform like the p-wave under the symmetry transformations of the lattice. In the following, we will pay special attention to the higher order solution:

$$p' = [\cos(k_x) - \cos(k_y)] \sin(k_x). \tag{2.57}$$

In the literature on $\mathrm{Sr_2RuO_4}$ the p' solution is sometimes called $f_{x^2-y^2}$-wave [27], which derives from the fact that it is a higher order triplet solution that have common nodes to the singlet $d_{x^2-y^2}$. The two triplet solutions p and p' are sketched in Fig. 2.9. Note the important difference that the p-wave solution has $\mathrm{sgn}(\Delta_{\mathbf{k}+\mathbf{Q}}) = -\mathrm{sgn}(\Delta_{\mathbf{k}})$, whereas the p'-wave solution has $\mathrm{sgn}(\Delta_{\mathbf{k}+\mathbf{Q}}) = \mathrm{sgn}(\Delta_{\mathbf{k}})$. Due to this, the p-wave solution will be favored in cases where the potential $V(\mathbf{k},\mathbf{k}')$ is repulsive for a momentum difference of $\mathbf{k}-\mathbf{k}' = \mathbf{Q}$, while the p'-wave solution is favored if this interaction contribution is attractive. We shall return to this in section 2.10.

We are interested a determination of the leading instability. Our first approach is to look for the leading instability between a number of well-defined gap functions, like e.g. the lowest order solutions given in Eqs. (2.26a-2.26e) and the higher order triplet gap in Eq. (2.57). In order to do so we follow the procedure of Scalapino *et al.* [12] and calculate the projection of the interaction vertex onto the basis functions. In this approach we rank the different gap symmetries by a comparison of the pairing strength as given by:

$$\lambda_\alpha = -\int_{FS} \frac{d\mathbf{k}}{|v_{\mathbf{k}}|} \int_{FS} \frac{d\mathbf{k}'}{|v'_{\mathbf{k}}|} g_\alpha(\mathbf{k}) \Gamma^{s/t}_{\mathbf{k},\mathbf{k}'} g_\alpha(\mathbf{k}') \Big/ \int_{FS} \frac{d\mathbf{k}}{|v_{\mathbf{k}}| g^2_\alpha(\mathbf{k})}, \tag{2.58}$$

with g_α being one of the functions stated in Eqs. (2.26a)-(2.26e) and (2.57). The quantity defined in Ref. (2.58) is derived from the linearized gap equation, Eq. (2.49), by setting $\Delta_{\mathbf{k}}$ equal to a specific basis

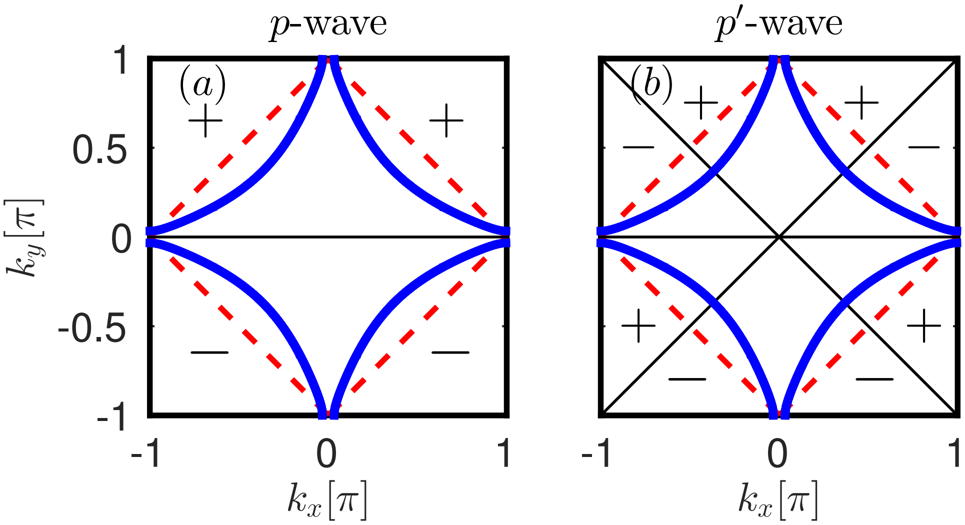

Figure 2.9: Illustration of the triplet gaps p-wave (a) and p'-wave (b). The latter is favored in the doping regime where the spin susceptibility has a peak or plateau at $\mathbf{Q} = (\pi,\pi)$. The magnetic zone boundary is indicated by the a dashed red line. Nodal lines in the two cases are shown by full black lines.

function, $g_\alpha(\mathbf{k})$ and identifying $\frac{1}{2(2\pi)^2}\int_{-\xi_c}^{\xi_c} d\xi \frac{1}{2|\xi|}\tanh(\frac{|\xi|}{2k_BT_c}) = \frac{1}{\lambda_\alpha}$, where it is noted that λ_α is positive. We then have:

$$
\begin{aligned}
g_\alpha(\mathbf{k}) &= -\int_{FS}\frac{d\mathbf{k}'}{|v_{\mathbf{k}'}|}[V(\mathbf{k},\mathbf{k}') \pm V(-\mathbf{k},\mathbf{k}')]g_\alpha\mathbf{k}'\frac{1}{\lambda_\alpha} \quad \Leftrightarrow \\
\int_{FS}\frac{d\mathbf{k}}{|v_{\mathbf{k}}|}g_\alpha(\mathbf{k})^2 &= -\int_{FS}\frac{d\mathbf{k}}{|v_{\mathbf{k}}|}\int_{FS}\frac{d\mathbf{k}'}{|v_{\mathbf{k}'}|}g_\alpha(\mathbf{k})[V(\mathbf{k},\mathbf{k}') \pm V(-\mathbf{k},\mathbf{k}')]g_\alpha(\mathbf{k}')\frac{1}{\lambda_\alpha} \quad \Leftrightarrow \\
\lambda_\alpha &= -\int_{FS}\frac{d\mathbf{k}}{|v_{\mathbf{k}}|}\int_{FS}\frac{d\mathbf{k}'}{|v_{\mathbf{k}'}|}g_\alpha(\mathbf{k})[V(\mathbf{k},\mathbf{k}') \pm V(-\mathbf{k},\mathbf{k}')]g_\alpha(\mathbf{k}')/\int_{FS}\frac{d\mathbf{k}}{|v_{\mathbf{k}}|}g_\alpha^2(\mathbf{k})
\end{aligned}
\tag{2.59}
$$

As in the case of the linearized gap equation, if the projection method yields a negative solution for a given gap basis function $g_\alpha(\mathbf{k})$, this means that the gap symmetry is not supported by the pairing potential. The largest value of λ_α provides the leading instability. This projection procedure has the limitation that it only shows the leading solution among the functions that we project onto, and it does not include possible higher order solutions. Thus one should be aware that in some cases it can be misleading, as a higher order solution might in fact dominate in some regions of the phase diagram. In order to address this, we also solve the linearized gap equation as stated in Eq. (2.54) to determine the leading solution among all possible higher order harmonics. We classify the solution according to its transformation properties into one of the four singlet solutions $s*$, $d_{x^2-y^2}$, d_{xy}, g or triplet.

As stated explicitly in Eq. (2.59), the pairing potential enters in its (anti)symmetrized form. In the literature, this is almost never the case, e.g. Refs. [12, 24, 23]. However, since the potential is projected onto the basis functions, this does not change a lot for the obtained results. However, when solving the linearized or full gap equation, it is crucial that the potential is correctly (anti)symmetrized.

Now we will turn to a presentation of the results obtained by the three different approaches presented above; the projection method of Eq. (2.59), the linearized gap equation, Eq. (2.54) and the full self-consistent gap equation, Eq. (2.44)/(2.45).

2.7 Results from the projection method

In this section, we show the results of projecting the pairing potential onto the basis functions in Eqs. (2.26a)-(2.26e) and (2.57). We first restrict to the case of $t' = 0$. This is a particle-hole symmetric band and therefore, we obtain the same results in the case of electron and hole doping, respectively. The results obtained in this case is similar to the original work of Scalapino [12] in the three dimensional case. As seen in Fig. 2.10, the $d_{x^2-y^2}$ solution becomes clearly dominant close to half filling. At intermediate fillings, the d_{xy} symmetry dominates and at very small fillings the p-wave is in fact favored, although this is not very easily seen from the figure. At very large dopings, all solutions provide very small pairing strengths which is a consequence of very weak Fermi surface nesting when the Fermi surface becomes (almost) circular.

Now, we will discuss in further details the case of $t' = -0.35$, which is relevant for the cuprates. In Fig. 2.11 (k-t) the Fermi surfaces at different electron fillings are shown. Note the transition of the Fermi surface between Fig. 2.11 (n) and Fig. 2.11 (o). In the latter case, the Fermi surface has "split up" at the antinodal positions $(\pi, 0)$ and $(0, \pi)$. This splitting occurs when the van Hove singularities at $(\pm\pi, 0)$ and $(0, \pm\pi)$ cross the Fermi level for a chemical potential of $\mu = 4t'$. For $t' = -0.35$ this happens at the van Hove critical density, $\langle n\rangle_{vH} = 0.66$.

The spin susceptibilities at the different doping levels are shown in Fig. 2.11 (a-j). At very large dopings the susceptibility shows a diffuse peak around $\mathbf{q} = (0, 0)$, Fig. 2.11 (a) and (j), which develops into peaks at $(\pm\pi, 0)$, $(0, \pm\pi)$ as doping is decreased, as seen for $\langle n\rangle = 0.35$ in Fig. 2.11(b). At intermediate doping levels the peaks at $(\pm\pi, 0)$, $(0, \pm\pi)$ move inwards and develop a quartet of peaks at $(\pi \pm \delta, \pi)$ and $(\pi, \pi \pm \delta)$, as shown in Fig. 2.11(c), where δ decreases as the system gets closer to half filling. A special feature is observed at the filling $\langle n\rangle = 0.65$, Fig. 2.11 (d) which is close to the van Hove density. At this

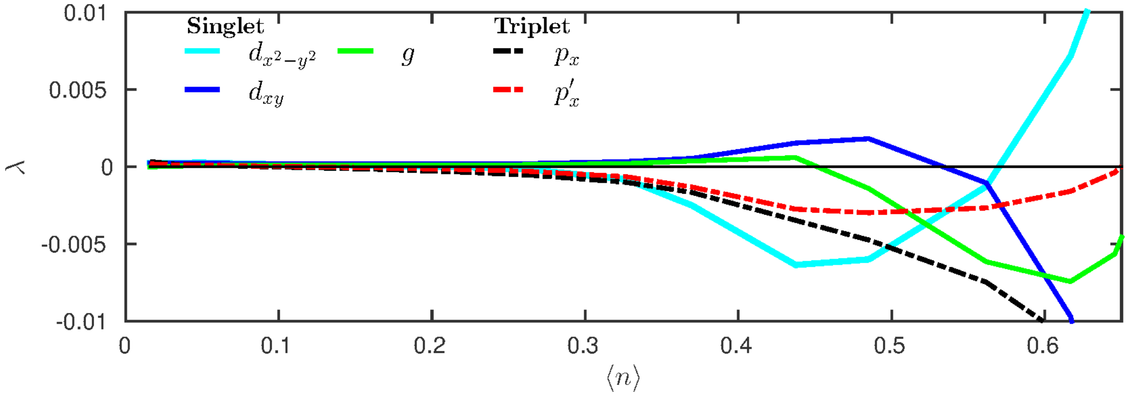

Figure 2.10: Projection of the spin-fluctuation-mediated pairing potential on gap basis functions Eqs. (2.26b-2.57) for $t' = 0$, $U = 3.25$ and $k_BT = 0.02$. The projection of the s-wave solution is negative at all filling levels in this range.

doping level a $\mathbf{q} = (0, 0)$ peak develops as a direct consequence of the large density of states at the Fermi level. Close to half filling a clear peak plateau builds up around $\mathbf{Q} = (\pi, \pi)$ as shown Fig. 2.11(e-g). At very large fillings, the spin susceptibility becomes almost structure-less, see Fig. 2.11(h-j) with weak intensity around $\mathbf{q} = (0, 0)$ at very large electron dopings.

We have chosen the Coulomb interaction $U = 1.75$. While this choice leads to small values of λ, it allows us to avoid the instability to long range magnetic order over the entire phase diagram. At very large hole and electron dopings, the peaks in the spin susceptibility are weak in intensity and, as a direct consequence, the projected pairing strengths are relatively small compared to half filling. This doping regime has a leading triplet p-wave solution, which for the hole doped case is visible from the left inset of Fig. 2.11. This is in agreement with the result of the $t' = 0$ band [12]. In the filling regime $\langle n \rangle \sim 0.2-0.4$, the g-wave solution is favored, whereas none of the lowest harmonic solutions are supported in the filling regime around $\langle n \rangle = 0.45$. It is important to note that the projection method does not take into account possible higher order solutions. These might dominate in some regions. For instance, the absence of a positive λ for $\langle n \rangle \sim 0.45$ indicates that the leading solution in this region is a higher order solution. For the more general solution we determine the leading solution to be a higher order s^*-wave in this case, as we shall see below.

Close to half filling the $d_{x^2-y^2}$ solution is clearly dominant. When the system is hole doped away from half filling, the $d_{x^2-y^2}$ solution becomes increasingly strong as the van Hove critical density, $\langle n \rangle_{vH} = 0.66$, is approached. However, an abrupt change occurs very close to the van Hove critical density, where the $d_{x^2-y^2}$ solution becomes unstable. This is manifested by a sharp dip of the cyan curve in Fig. 2.11(u). The $d_{x^2-y^2}$ solution becomes unfavorable due to the development of the peak at $\mathbf{q} = (0, 0)$ in the susceptibility. This gives rise to a large repulsive interaction between neighboring momenta $\mathbf{k}$ and $\mathbf{k}'$ in the singlet channel, and will cause a suppression of all singlet solutions, in this case the $d_{x^2-y^2}$ solution. Such a suppression of singlet superconductivity due to the $\mathbf{q} = (0, 0)$ peak in the spin susceptibility was originally discussed by Berk and Schrieffer [10] in their pioneering work on spin-fluctuation mediated pairing. As clearly visible in Fig. 2.11(u) the sharp dip of the singlet solution around the van Hove critical density is accompanied by an increase in the triplet solution p' shown by the red line. Thus, the $\mathbf{q} = (0, 0)$ susceptibility peak not only suppresses the singlet solution, but actually supports the development of a triplet gap because it gives rise to an effective attraction for neighboring $\mathbf{k}$ and $\mathbf{k}'$ at the Fermi surface. In the absence of additional structures in the spin susceptibility the p-wave solution is favored, as in the case of very small filling shown in the inset of Fig. 2.11(u). However, if the spin susceptibility shows additional peaks as in the case of fillings close to the van Hove critical density, Fig. 2.11 (d), higher order triplet solutions will be favored. The detailed structure of the potential turns

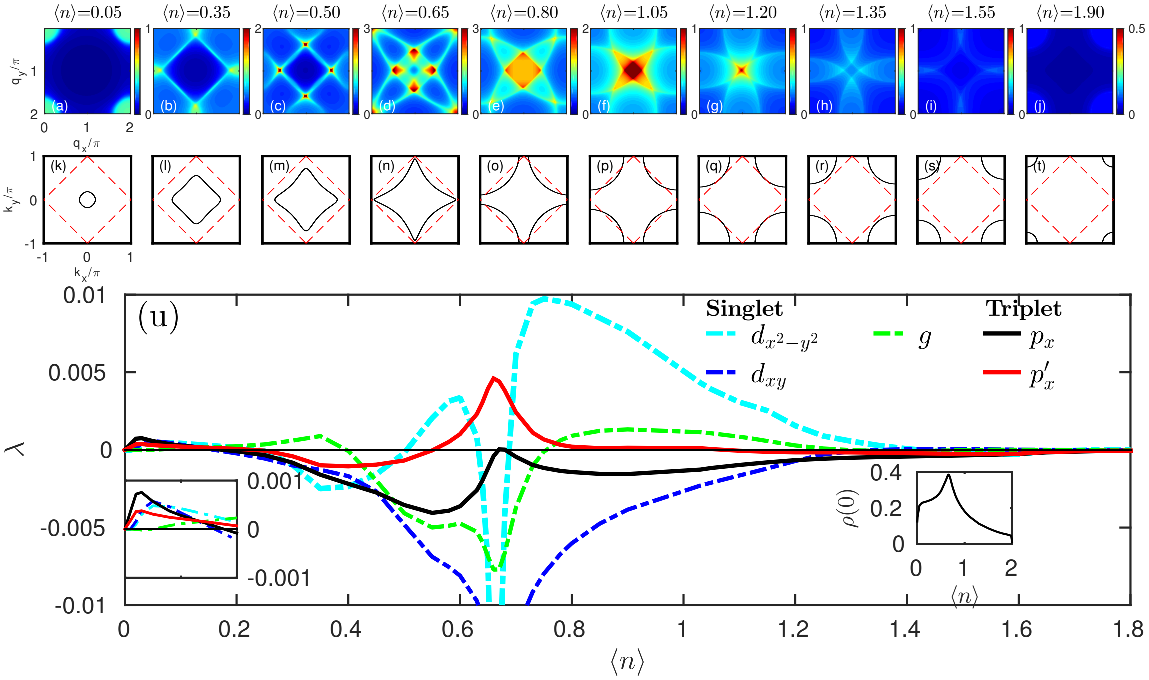

Figure 2.11: (color online) (a-j) Spin susceptibility in the RPA approximation and (k-q) Fermi surfaces for fillings $\langle n\rangle = 0.05, 0.35, 0.50, 0.65, 0.80$ and $\langle n\rangle = 1.05, 1.2, 1.35, 0.55, 0.90$ with $t' = -0.35$ and $U = 1.75$. The antiferromagnetic zone boundary is shown by the dashed red line. Note the different colorbar range for each susceptibility plot. (u) Phase diagram for λ as stated in Eq. (2.58) for a band with $t' = -0.35$ and $U = 1.75$. The temperature is $k_BT = 0.015$. Projection onto $s*$-wave $(\cos k_x + \cos k_y)$ gives a negative value of λ at all fillings. The inset shows the density of states at the Fermi level, $\rho(0)$, as a function of filling. Note that the at the filling for which $\rho(0)$ is maximal the triplet p' solution is the leading instability. This we refer to as the van Hove density. For $t' = -0.35$ the van Hove critical density is $\langle n\rangle_{vH}$=0.66.

out to favor a six node p'-wave gap, see Eq. (2.57) and Fig. 2.9. We will return to this is section 2.10.

The importance of the van Hove singularity crossing the Fermi level was clearly seen in the sharp features of the phase diagram shown in Fig. 2.11 around a filling of $\langle n\rangle = 0.66$, where the singlet solution was completely suppressed and the triplet p'-wave solution becomes the dominating instability. Previously, it has been discussed that the presence of a van Hove singularity close to the Fermi level might enhance the superconducting gap[28]. This effect was discussed in connection with d-wave superconductors in a model with the pairing interaction consisting of a constant nearest neighbor attraction. A larger superconducting gap was found as a consequence of an additional number of states available for Cooper pairing[28]. In our case, the role of the van Hove singularity is twofold. Besides the effect considered in Ref. [28], the strength and structure of the pairing interaction is also affected by the presence of a van Hove singularity close to the Fermi level. We can in fact trace the appearence of the triplet solution by the position of the van Hove critical density, $\langle n\rangle_{vH}$, as we will discuss next two sections.

2.8 Fermi surface evolution and the van Hove critical density

We derive the criteria for the chemical potential μ_{vH} for which the van Hove singularity resides at the Fermi level. The corresponding filling level is what we denote the van Hove critical density. First we determine the position of the van Hove singularities. The energy band of the paramagnetic one-band

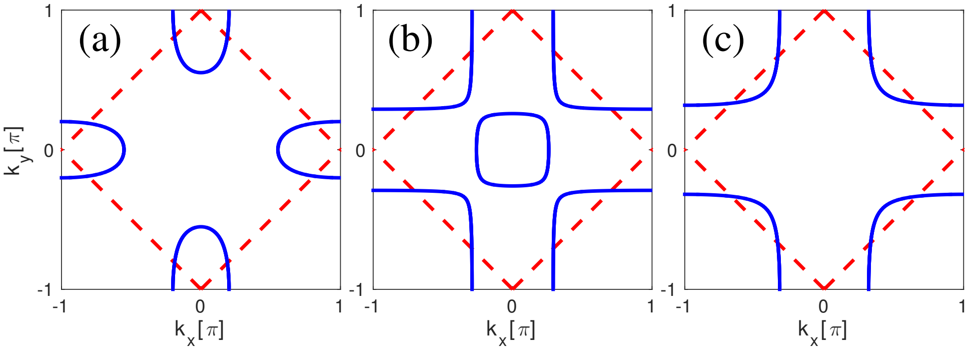

Figure 2.12: Fermi surfaces for $t' = -0.8$ at three fillings. (a) At small fillings, $\langle n \rangle = 0.3$, the Fermi surface consists of four electron pockets centered at $(\pm\pi, 0)$ and $(0, \pm\pi)$. (b) For a filling above the van Hove critical density, $\langle n \rangle = 9$, a hole pocket is centered at $(0, 0)$ and four hole pockets are centered at $(\pm\pi, \pm\pi)$ and $(\pm\pi, \mp\pi)$. (c) At larger fillings, the central hole pocket is removed from the Fermi surface.

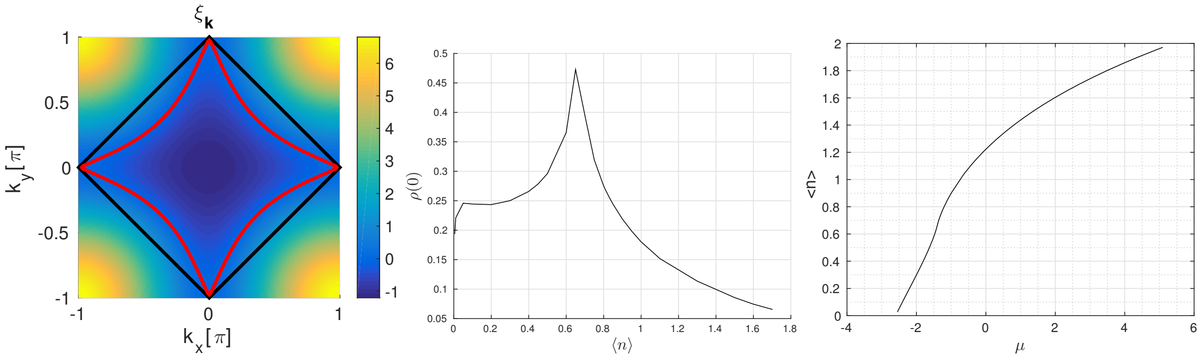

Figure 2.13: (**left:**) Band at the transition $\langle n \rangle_{vH} = 0.66$ for $t' = -0.35$. (**middle:**) Density of states at the Fermi level for the $t' = -0.35$ band as a function of filling. (**right:**) Filling as a function of chemical potential. The transition occurs at $\mu = -1.4025 = 4t'$.

Hubbard Hamiltonian with nearest and next-nearest neighbors is given by:

$$\xi_{\mathbf{k}} = -2t(\cos k_x + \cos k_y) - 4t' \cos k_x \cos k_y - \mu \tag{2.60}$$

In the following, we set $t = 1$. The van Hove singularity is obtained by minimizing the energy band with respect to k_x and k_y simultanously. In this way we find band extrema at $(0, 0)$ and (π, π), and van Hove singularities at the positions and $(0, \pi)$ and $(\pi, 0)$ as well as for $\cos(k_x) = \cos(k_y) = \frac{t}{2t'}$. We are interested in the chemical potentials for which the van Hove singularity is located at the Fermi level. For $|t'/t| < 0.5$ this occurs at the positions $(0, \pi)$ and $(\pi, 0)$ and gives the condition $4t' - \mu_{vH} = 0$. For $|t'/t| > 0.5$ the Fermi surface takes an unusual form, which is less discussed in the literature. This is mainly because in the cuprates, the next-nearest neighbor hoppings are estimated to be smaller than $|0.5t|$. However, this limit might be of relevance in the soon-to-be constructions of the Hubbard model in optical lattices, and we therefore include these in the discussion.

The Fermi surface at three different fillings for $t' = -0.8$ is shown in Fig. 2.12. At small fillings, the Fermi surface consists of four electron pockets centered at $(\pm\pi, 0)$ and $(0, \pm\pi)$. For a filling above the van Hove critical density, a hole pocket is centered at $(0, 0)$ and four hole pockets are centered at $(\pm\pi, \pm\pi)$ and $(\pm\pi, \mp\pi)$, and for even larger fillings, the central hole pocket is removed from the Fermi surface.

When $|t'/t| > 0.5$ the van Hove singularities appear at $\cos(k_x) = \cos(k_y) = \frac{t}{2t'}$, which cross the Fermi level at $\mu_{vH} = t^2/|t'|$. For the special case of $|t'/t| = 0.5$ the van Hove singularity resides at the bottom

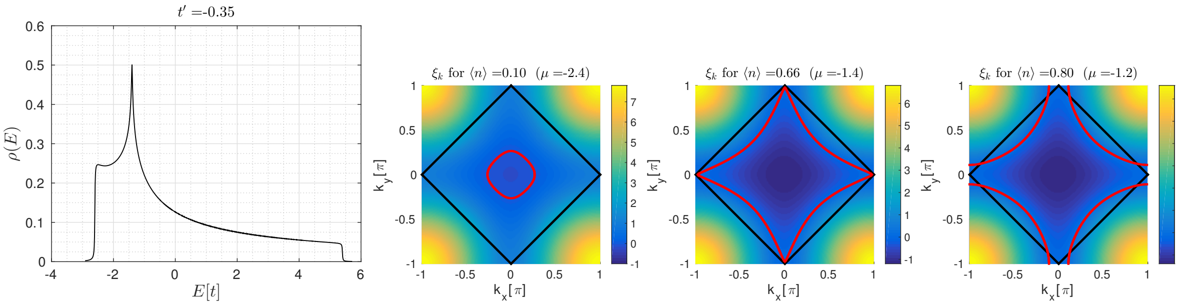
$t' = -0.35$

ξ_k for $\langle n\rangle = 0.10$ ($\mu = -2.4$)

ξ_k for $\langle n\rangle = 0.66$ ($\mu = -1.4$)

ξ_k for $\langle n\rangle = 0.80$ ($\mu = -1.2$)

Figure 2.14: Density of states, $\rho(E)$, for the $t' = -0.35$ band and energy band and Fermi surface at different fillings $\langle n\rangle = 0.10, 0.66, 0.80$ for $t' = -0.35$.

of the energy band.

When the van Hove singularity crosses the Fermi level, the geometry of the Fermi surface changes. In the special electron-hole symmetric case when $t' = 0$, the the transition occurs at half filling, where the total density of spin up and spin down electrons is $\langle n\rangle = 1$. For $t' = -0.35$ the Fermi surface at the transition is depicted in Fig. 2.13 (left). At this filling, there is a peak in the density of states at the Fermi level, which is a signature of the crossing of the van Hove singularity. This is also visible from the drastic change in filling that occurs for small changes in the chemical potential right around the filling of the transition, $\langle n\rangle_{vH} = 0.66$, as visualized in Fig. 2.13 (right).

To see how the Fermi surface for the $t' = -0.35$ evolves as a function of doping, we plot in Fig. 2.14 the Fermi surface at fillings of $\langle n\rangle = 0.10, 0.66, 0.80$. The Fermi surface is an electron pocket centered at the zone center $(k_x, k_y) = (0, 0)$ for fillings $\langle n\rangle < \langle n\rangle_{vH} = 0.66$. For fillings $\langle n\rangle > \langle n\rangle_{vH}$ the Fermi surface becomes a hole pocket centered at $(k_x, k_y) = (\pi, \pi)$. For completeness we also show the density of states, $\rho(E)$ for the $t' = -0.35$. For $t' = -0.5$ the van Hove singularity resides at the bottom of the band, as shown in Fig. 2.15 (left). In this case, there is no change of Fermi surface geometry as a function of doping.

A special feature of the spin susceptibility is related to the presence of a van Hove singularity at the Fermi level. Around this doping level, a $\mathbf{q} = (0, 0)$ peak develops. The density of states at the Fermi

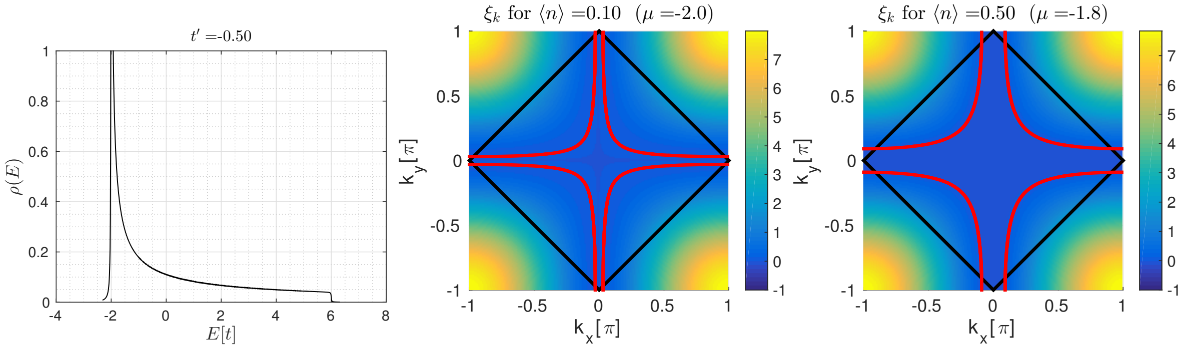
$t' = -0.50$

ξ_k for $\langle n\rangle = 0.10$ ($\mu = -2.0$)

ξ_k for $\langle n\rangle = 0.50$ ($\mu = -1.8$)

Figure 2.15: Density of states, $\rho(E)$, for the $t' = -0.5$ band and energy band and Fermi surface at different fillings $\langle n\rangle = 0.10, 0.50$ for $t' = -0.5$.

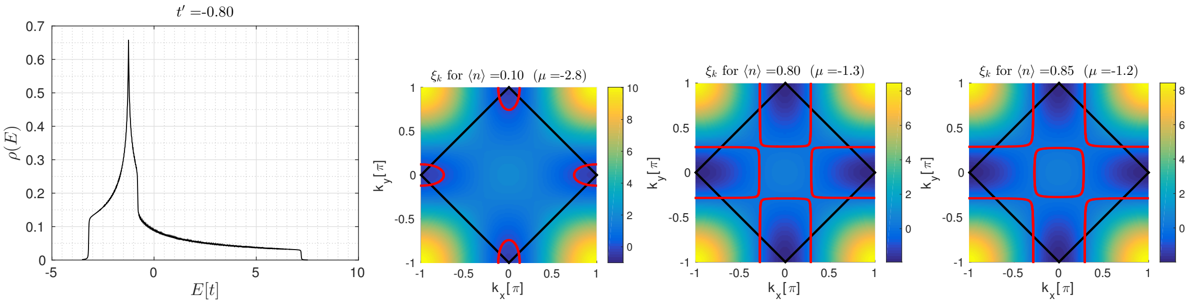

Figure 2.16: Density of states,$\rho(E)$, for the $t' = -0.8$ band. Energy band and Fermi surface at different fillings $\langle n\rangle = 0.10, 0.80, 0.85$ for the $t' = -0.8$ band is also shown.

level is related to the susceptibility in the following way:

$$\begin{aligned}
\chi(\mathbf{q}\to 0, \omega = 0) &= \lim_{\mathbf{q}\to 0}\int \frac{d\mathbf{k}}{(2\pi)^2}\frac{f(\xi_{\mathbf{k}+\mathbf{q}}) - f(\xi_{\mathbf{k}})}{\xi_{\mathbf{k}} - \xi_{\mathbf{k}+\mathbf{q}}} \\
&\simeq \int \frac{d\mathbf{k}}{(2\pi)^2}\frac{(\xi_{\mathbf{k}+\mathbf{q}} - \xi_{\mathbf{k}})\frac{d}{d\xi_{\mathbf{k}}}f(\xi_{\mathbf{k}})}{\xi_{\mathbf{k}} - \xi_{\mathbf{k}+\mathbf{q}}} \\
&= \int \frac{d\mathbf{k}}{(2\pi)^2}\delta(\xi_{\mathbf{k}}) \\
&= DOS(0)
\end{aligned} \tag{2.61}$$

A divergence of the density of states at the Fermi level gives a $\mathbf{q} = (0,0)$ peak at the van Hove critical density. We can trace the $\mathbf{q} = (0,0)$ peak in the bare susceptibility as a function of t' and doping. We find in accordance with our expectations that the occurrence of a peak at $\mathbf{q} = (0,0)$ exactly follows the points $(\langle n\rangle, t')$ for which the van Hove singularity crosses the Fermi level. This is shown in Fig. 2.17. In the next section we shall discuss this further.

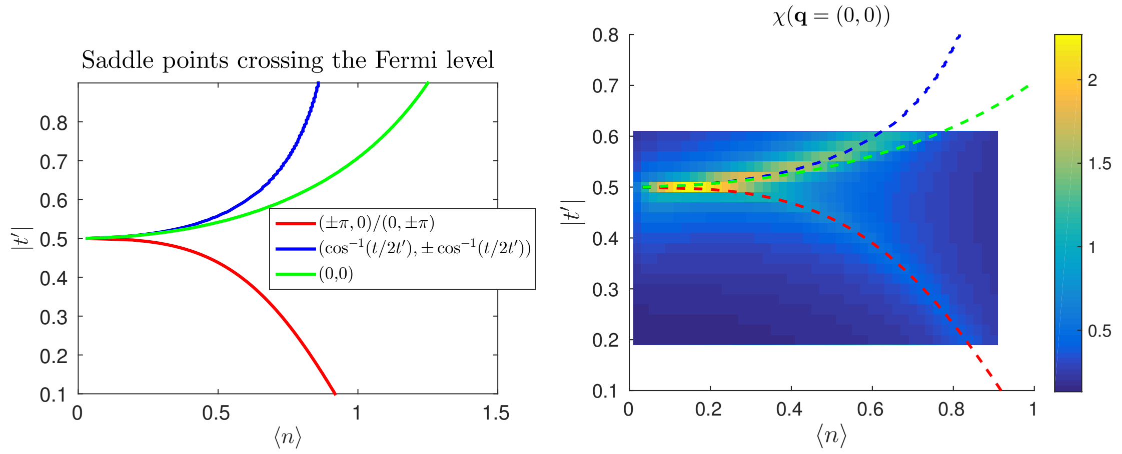

Figure 2.17: (**left:**)Positions of band parameters, $\langle n\rangle$ and t', for which a saddle point or local band maximum at $(0,0)$ crosses the Fermi level. The green line corresponds to the position where a the local band maximum at $(0,0)$ crosses the Fermi level at which point a hole pocket is removed from the Fermi surface. (**right:**) Bare susceptibility evaluated at $\mathbf{q} = (0,0)$ as a function of $\langle n\rangle$ and t'.

2.9 Linear gap equation: Phase diagram as a function of doping and t'

In order to further investigate the generality of the results obtained by projection in Fig. 2.11 we turn to a solution of the (non-projected) linearized gap equation, Eq. (2.54), for different next-nearest neighbor hopping strengths $|t'|$ in the range $0 - 1.5$. These results have been obtained in collaboration with Andreas Kreisel.

In contrast to the projection method, this general procedure determines the leading solution amongst all possible higher order harmonics. The solution is classified according to its transformation properties into one of the four singlet solutions s^*, $d_{x^2-y^2}$, d_{xy}, g or triplet. Note that in general solutions may correspond to higher order harmonics and have additional nodes compared to the leading harmonics given in Eqs. (2.26a-2.26e). For instance, the triplet solutions are all named "p" even though they might be really of the form given in Eq. (2.57), or yet a third different function. We shall discuss the triplet solutions in detail in section 2.10.

For each point in the phase diagram $(\langle n\rangle, t')$ we solve Eq. (2.54) and adjust the value of U such that the leading eigenvalue is $\lambda = 0.1$. The result of this procedure is shown in Fig. 2.18, where the leading superconducting instability for fillings and next-nearest neighbor hopping strengths in the range $0 - 1.5$ is shown. This procedure is justified as follows. Since we cover a large range of different Fermi

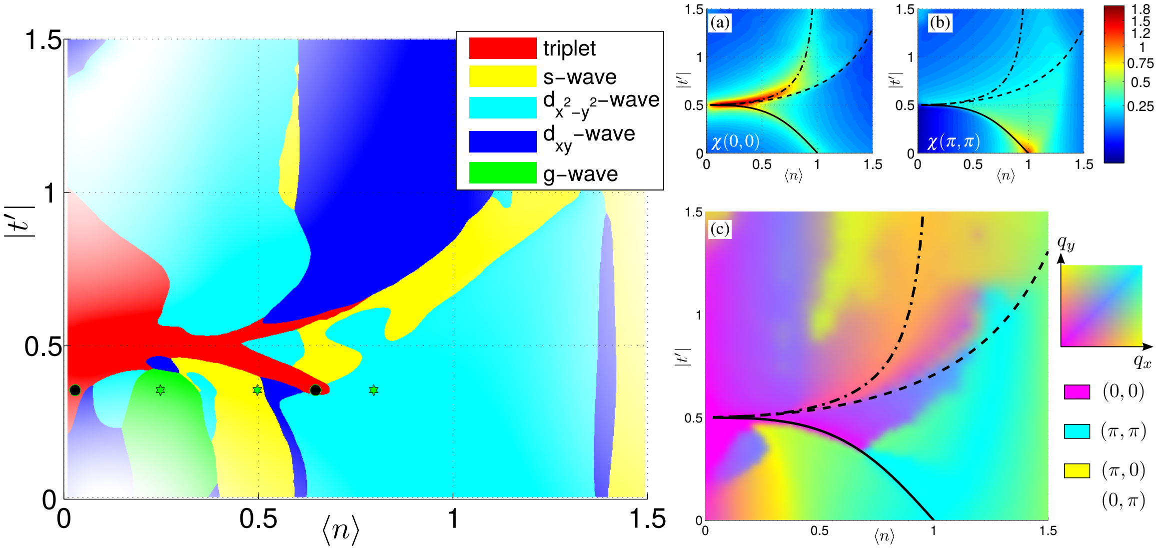

Figure 2.18: **(right:)** Phase diagram of the leading superconducting instability as a function of electron filling $\langle n\rangle$ and next-nearest neighbor hopping constant $|t'|$. Throughout, the value of U is adjusted such that the leading eigenvalue is $\lambda = 0.1$. For values of $U < 3$, the eigenvalue is shown in full color. For large U values in the range $3 - 8$ the eigenvalue is shown with brighter color in order to indicate this. We include only fillings $\langle n\rangle \leq 1.5$ since the instability is negligible for higher electron dopings for $U < 8$. The two black filled circles mark the position for which we solve the full (non-linearized) gap equation in the triplet channel, Figs. 2.26 and 2.27. **(left:)** (a) Spin susceptibility Re $\chi_0(\mathbf{q}, \omega = 0)$ at the wave vector $\mathbf{q} = (0, 0)$ as a function of filling, $\langle n\rangle$ and next-nearest hopping constant t'. The full black line and the black dashed dotted line show where the van Hove singularity crosses the Fermi level at the positions $(\pm\pi, 0)/(0, \pm\pi)$ and $(k, \pm k)$, with $k = \pm\cos^{-1}(\frac{1}{2|t'|})$, respectively. The dashed line shows where a hole pocket is removed from the Fermi surface. (b) Spin susceptibility weight at the wave vector $\mathbf{Q} = (\pi, \pi)$. (c) The wave vector $\mathbf{q}$, for which the bare spin susceptibility achieve its maximum value (color indicates $\mathbf{q}$ according to inset), plotted as a function of filling $\langle n\rangle$ and next-nearest hopping constant t'. This figure is made by Andreas Kreisel.

surface structures, a fixed value of the Coulomb interaction of e.g. $U = 2$ will cause a break-down of the paramagnetic RPA formalism due to the instability to long range magnetic order. By allowing for a variation in U this is avoided, and at the same time we discuss only instabilities with a non-negligible critical temperature. Note that this approach is different than some previous reports, where the genuinely weak-coupling approach $U \to 0$ limit was taken [23]. Nevertheless, our results show some qualitatively agreement with Ref. [23]; a g-wave and a (small) d_{xy} region appear in the filling regime of $\langle n \rangle = 0.25 - 0.4$ for $|t'| < 0.5$ and at fillings around $\langle n \rangle = 0.7$ a $d_{x^2-y^2}$ region dominates at all $|t'| < 0.4$, whereas a s-wave domain takes over for $0.4 < |t'| < 0.5$ in this filling regime. In our approach, the region of triplet solutions has substantially shrunk compared to Ref. [23], with different higher order singlet solutions taking over in the regime of small t' close to a filling of $\langle n \rangle = 0.5$. In the case of large electron dopings, where the spin susceptibility shows only very weak structure, U must be very large to obtain a leading instability of $\lambda = 0.1$ and we omit this regime in Fig. 2.18. Further, regions for which $U > 3$ the colors are less saturated to indicate this.

The structure of the spin susceptibility plays a decisive role for the gap symmetry, and this is very tightly connected to the geometry of the Fermi surface. As discussed in the previous section, two different regimes of t' give rise to very different Fermi surface geometries. The correlation between the van Hove singularity at the Fermi level and the appearance of spin susceptibility weight at the wave vector $\mathbf{q} = (0, 0)$ is shown in Fig. 2.18(a). Here the value of the spin susceptibility at $\mathbf{q} = (0, 0)$ is shown as a function of $\langle n \rangle$ and t'. We also show where the van Hove singularity crosses the Fermi level, indicated by the full black line in the case of $|t'| < 0.5$ and the dashed-dotted line for the $|t'| > 0.5$ case. The black dashed line shows where a hole pocket is removed from the Fermi surface. In Fig. 2.18(b) the spin susceptibility weight at the wave vector $\mathbf{Q} = (\pi, \pi)$ is depicted. As expected, the signatures of a strong peak at $\mathbf{Q}$ is clearly visible near half filling and $t' = 0$. The weight at $\mathbf{Q}$ expands in a doping region around half filling for $|t'| < 0.5$. In addition, it shows a clear correlation with the van Hove critical density shown by the full black line. This explains why the $d_{x^2-y^2}$ solution is increasingly favored upon hole doping away from half filling for $t' = -0.35$, as observed in Fig. 2.11(u).

By a comparison of the red regions in Fig. 2.18(left) and Fig. 2.18(a), we observe that the two triplet solution branches that expand from the low filling regime in Fig. 2.18(left) are explained by the weight at $\mathbf{q} = (0, 0)$ in the spin susceptibility, which is correlated with the van Hove critical densities. This is in agreement with the expectations that a $\mathbf{q} = (0, 0)$ peak in the pairing interaction favors triplet superconductivity. The reason why we see a shift from triplet to singlet ($d_{x^2-y^2}$) superconductivity at the lower red branch around $\langle n \rangle \sim 0.6$ is because the $\mathbf{Q}$ peak becomes dominant in this regime. This transition from triplet to $d_{x^2-y^2}$ superconductivity is most clearly visible in Fig. 2.18(c), where we capture the dominating structure of the spin susceptibility at every position $(\langle n \rangle, t')$ of the phase diagram, by plotting the wave vector $\mathbf{q}$ for which the bare spin susceptibility achieve its maximum value. Note how the structure of the spin susceptibility transforms from being dominated by a $\mathbf{q} \sim (0, 0)$ peak in the regime of the triplet branch, to being dominated by the $\mathbf{Q}$ peak. Also, from the large magneta region in Fig. 2.18(c) we see why triplet superconductivity governs the phase diagram in an extended regime around $|t'| = 0.5$ for small fillings. As expected, a $\mathbf{Q}$ peak dominates in the region around half filling. In other regions of the phase diagram where we observe a different type of singlet superconductivity, other $\mathbf{q}$ structures of the susceptibility become dominant, as seen in Fig. 2.18(c). Note, however, that subdominant features in the susceptibility which might influence the gap equation, are not visible from this figure. The large region of d_{xy} superconductivity, which occurs at small to moderate hole dopings and small electron dopings for $|t'| > 0.5$ is correlated with spin susceptibility peaks near $(\pi, 0)$ and $(0, \pi)$.

Now, we turn to the manifestations of the different symmetry solutions in the regime of $|t'| < 0.5$ and hole doping. In Fig. 2.19 we show the three leading solutions for the band with $t' = -0.35$ at three filling levels. For $\langle n \rangle = 0.03$ the p-wave solution dominates, and in this regime the solution is the first order harmonic as stated in Eq. (2.26e). This solution is doubly generate; the other solution (not shown) has a nodal line along k_y. The two subleading solutions, d_{xy}, and $d_{x^2-y^2}$ are also shown in Fig. 2.19(first row).

At a larger filling of $\langle n \rangle = 0.20$, the singlet g-wave solution dominates, as seen from Fig. 2.19(middle

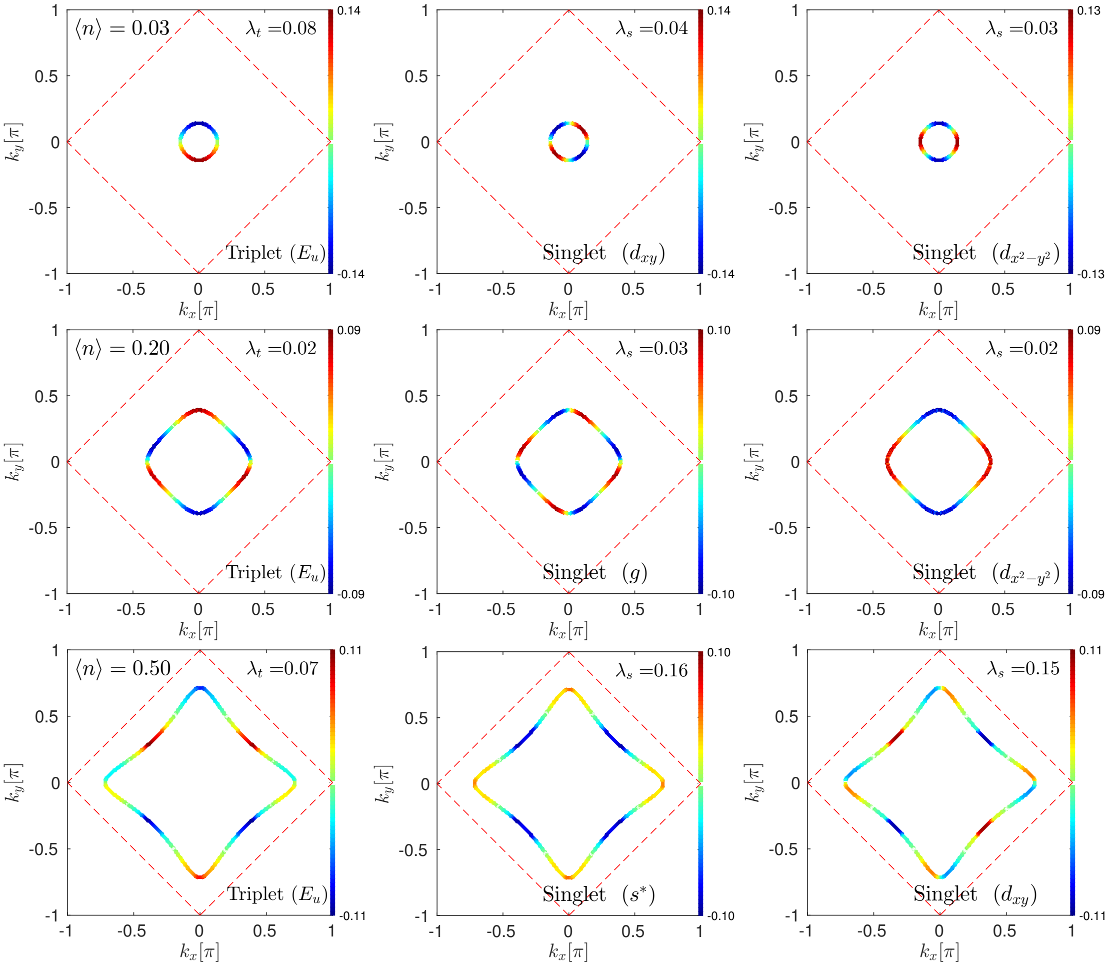

Figure 2.19: Three leading solutions to the linearized gap equation Eq. (2.54) for $t' = -0.35$ and small fillings indicated by black dots in Fig. 2.18. For $\langle n \rangle = 0.03, 0.20$ we set $U = 2.5$. For $\langle n \rangle = 0.5$ we set $U = 1.75$. Temperature is $k_B t = 0.015$.

row). The nodal structure of the solution is the same as the basis function stated in Eq. (2.26b). Note that the p'-wave, Eq. (2.57), as well as the $d_{x^2-y^2}$ are very closeby. In Ref. [23] a g-wave solution was also found in this region. We have found that the results obtained in regions where the susceptibility structure is not very strong, the results for leading and subleading λ might depend on the value of U. This lead us to the procedure of adjusting U such that the leading λ is 0.1. In the previous work by Hlubina[23], and Guinea *et al.*[24], the pairing interaction is calculated to second order in U, where $U \to 0$ or $U = 6$, repectively. This might give rise to some discrepancies in the phase diagram in regions where several solutions are almost degenerate. Another clear difference from our approach and the previous approach of Ref. [23] and Ref. [24] is that the basis functions are truncated to the first 15 harmonics expressed in terms of angle around the Fermi surface, whereas we have the eigenvector $g(\mathbf{k})$ being a completely general function of $\mathbf{k}$. We are only limitated by the resolution of the Fermi surface. Usually, we use a system size of 300×300 grid points and the Fermi surface is resolved by $100 - 800$ $\mathbf{k}$ points depending on the size of the Fermi surface. We actually do find some discrepancies between our phase diagram Fig. 2.18(c) and the phase diagram of Hlubina Fig. 2.3(left), which are most likely due to these small differences in the approaches. However, the phase diagrams do agree in most of the main features.

At $\langle n \rangle = 0.5$ the singlet solutions are clearly dominating, as seen from Fig. 2.19(last row). We find the dominating solution to be s-wave, with the d_{xy} being the subleading solution in this regime. The s-wave solution extends in a large region for fillings around $\langle n\rangle = 0.5$ and $|t'| < 0.5$, observed as a large yellow region in Fig. 2.18(left). Intriguingly, this region is classified by a triplet solution in Ref. [23]. Also Ref. [24] claims this region to be triplet. We suspect that the discrepancy of the two approaches arises from truncation of the gap functions mentioned above, since we do not get the expanded triplet region even when taking the same parameters as in Reg. [24]; i.e. $t' = -0.276$, $U = 6$ and the pairing potential $V(\mathbf{k},\mathbf{k}') = U + U^2\chi_0(\mathbf{k}+\mathbf{k}')$ (i.e. the exchange interaction from the ladder diagrams only to second order in U), see Fig. 2.20.

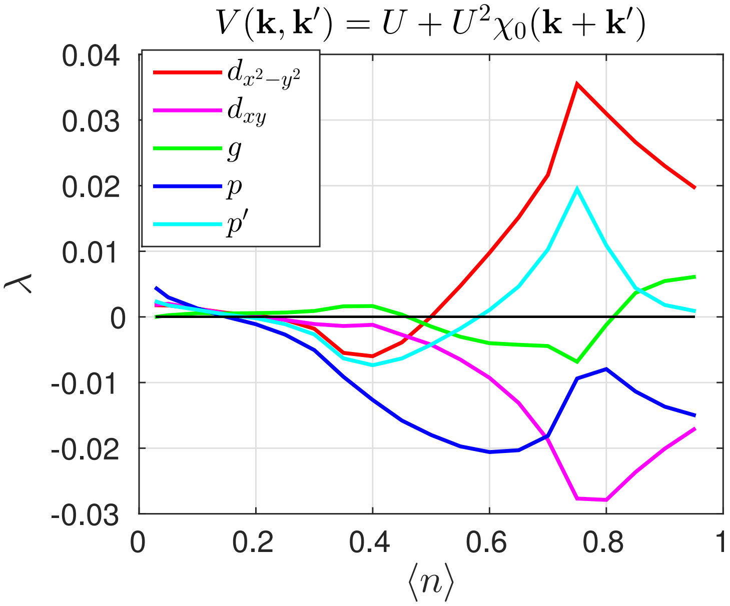

Figure 2.20: Coupling strength, λ, calculated by projection to the basis functions Eqs. (2.26a-2.26e) and (2.57), for $V(\mathbf{k},\mathbf{k}') = U + U^2\chi_0(\mathbf{k}+\mathbf{k}')$ (i.e. the exchange interaction from the ladder diagrams only to second order in U), with $U = 6$ and $t' = -0.276$. To be compared with the results of the coupling strength in Fig. 4 of Ref. [24].

When we approach half filling, the $d_{x^2-y^2}$ becomes dominant for a large regime of $|t'| < 0.5$. The $d_{x^2-y^2}$ solution of the one-band Hubbard model is commonly discussed in this region, due to the relevance for cuprates. From the phase diagram in Fig. 2.18, we observe that there is in fact another large region of the phase diagram for which a $d_{x^2-y^2}$ solution dominates corresponding to $|t'| > 0.5$ where the Fermi surface topology is quite different. In order to show a solution in both regimes, we plot in Fig. 2.21 the $d_{x^2-y^2}$ solution in the case of $t' = -0.35$, $\langle n\rangle = 0.8$ and $t' = -0.8$, $\langle n\rangle = 0.5$. Note that even though the Fermi surface of the $t' = -0.8$ band has no Fermi surface weight along the zone diagonals, which are the nodal lines of the simple harmonic d-wave, it displays more nodes at the Fermi surface than the solution for the $t' = -0.35$ band, namely eight nodes instead of four.

A closer inspection of the $d_{x^2-y^2}$ solution for the band with $t' = -0.35$ indicates deviations from the simple form of $\Delta[\cos k_x - \cos k_y]$ due to the presence of higher harmonics, i.e. longer range superconducting pairing interaction. The maximum gap value is not achieved at the antinodal points, but shifted towards the nodal direction. This effect has been discussed previously as a signature of spin-fluctuation-mediated pairing [19, 22, 24, 20, 31]. In previous work special attention was drawn to the hot spot effect in which the gap maximum occurs at the $\mathbf{k}$ position of the hot spot. In Fig. 2.22 we show the singlet gap as calculated by the full (non-linearized) gap equation, Eq. (2.44). In the figure we also show the position of the hot spot, i.e. the angle at which the Fermi surface intersects the magnetic zone boundary. This is shown by the vertical lines in Fig. 2.22. It is seen that the non-monotonicity of the gap is not directly related to the hot spot effect, since the hot spot position moves towards $\phi = 0$, but the strong gap enhancement moves closer to the nodal direction. Upon increased hole doping towards the van Hove critical density, the higher harmonic content of the gap function becomes more pronounced. This tendency was also pointed out in Ref. [24]. Note that proximity of the van Hove singularity leads to an increase in the number of states participating in the formation of Cooper pairs, but the corresponding formation of additional nesting peaks in the susceptibility at small $\mathbf{q}_{vH} = (\delta, \delta)$, see Fig. 2.11(e), in fact work against the $d_{x^2-y^2}$ solution, favoring nodes along the zone axes. This will act in favor of the p' solution in the triplet channel.

In the regime of $|t'| > 0.5$ the d_{xy} solution is dominating in a large region close to half filling. In Fig. 2.23 we show the d_{xy} solutions in the case of $|t'| < 0.5$ (Fig. 2.23(a)) and $|t'| > 0.5$ (Fig. 2.23(b)). Due to the difference in Fermi surface topology, the appearance of the d_{xy} solution is quite different in the two cases. For $t' = -1.2$ the d_{xy} solution has the same nodes as the simplest harmonic stated in Eq. (2.26d), i.e. four nodes per electron pocket (there is two electron pocket per Brillouin zone). For $t' = -0.35$ the d_{xy} is a higher order solution with twelve nodes at the electron pocket, centered at $(k_x, k_y) = (0, 0)$.

2.10 Triplet gap at the van Hove critical density

In the section above we saw how the suppression of singlet superconductivity and concurrently, the development of a triplet gap is intimately related to a $\mathbf{q} = (0, 0)$ peak in the susceptibility which occurs at the van Hove critical density. Now we turn to a more detailed investigation of the structure of the pairing potential and the consequences for the favored gap symmetries. In our model two contributions are important for the pairing structure: 1) the hot spot effect, which for most filling levels is more accurately described as a plateau around $\mathbf{Q}$ rather than a sharp peak at $\mathbf{Q}$ as seen e.g. from Fig. 2.11(f), 2) the van Hove effect with pairing contributions arising due to the appearance of a quartet of peaks at the diagonal corners at $\mathbf{q}_{vH} = (\delta, \delta)$ where $\delta \to 0$ as the van Hove singularity crosses the Fermi level (in the case of $|t'| < 0.5$). The peaks at $\mathbf{q}_{vH}$ are visible in Fig. 2.11(e) and appear as a purple region in Fig. 2.18(c) when hole doping is increased towards the van Hove critical doping, shown by the full black line in Fig. 2.18(c). To visualize the hot spot effect and the van Hove effect explicitly, we plot the pairing potential for the band with $t' = -0.35$ and fillings $\langle n \rangle = 0.80$ and $\langle n \rangle = 0.65$ in Fig. 2.24(a) and 2.24(b), respectively. In the case of $\langle n \rangle = 0.80$, the largest pairing potential is found due to the hot spot effect, as seen by the red curve close to the angles $\theta = \frac{\pi}{2}$ and $\theta = \frac{3\pi}{4}$ in Fig. 2.24(a). A smaller signature due to the van Hove effect is seen in the red curve close to $\theta = 0$ and $\theta = \pi$. As the hole doping is

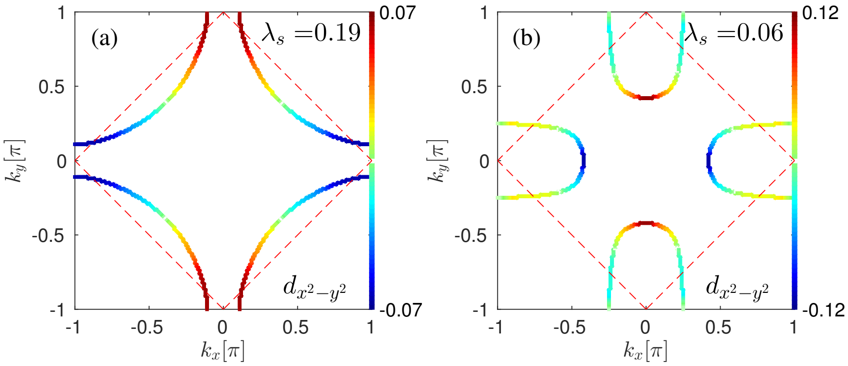

Figure 2.21: (a) $d_{x^2-y^2}$ solution to the linearized gap equation as stated in Eq. (2.54) for a band with $t' = -0.35$ and $U = 1.75$ at a filling of $\langle n \rangle = 0.8$. (b) $d_{x^2-y^2}$ solution to the linearized gap equation as stated in Eq. (2.54) for a band with $t' = -0.8$ and $U = 1.75$ at a filling of $\langle n \rangle = 0.5$. The magnetic zone boundary is indicated by the red dashed line.

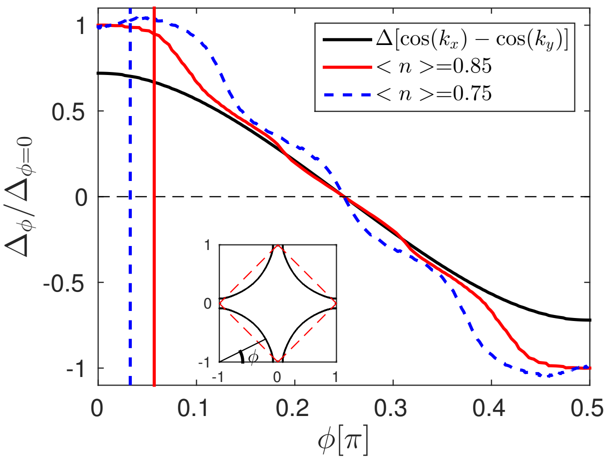

Figure 2.22: Solution to the full gap equation Eq. (2.44) with singlet pairing interaction for $t' = -0.35$ at filling levels $\langle n \rangle = 0.85$ (full red line) and $\langle n \rangle = 0.75$ (dashed blue line) at temperature $k_BT = 0.01$. The renormalized Coulomb interaction is $\bar{U} = 2, 1.88$, respectively and the Coulomb renormalization is $z = 3$. The energy cut-off is set to $\epsilon_c = 0.015$, and the gap value at the antinodes is $\Delta_{\phi=0} = 0.01$ in both cases. The angle ϕ is defined in the Fermi surface inset. The vertical lines show the position of the hot spots for the $\langle n \rangle = 0.85$ (full red line) and $\langle n \rangle = 0.75$ (dashed blue line). Note that there is a clear correlation between the position of the hot spot and enhancement of the superconducting gap away from a simple harmonic gap function in the case of $\langle n \rangle = 0.85$. However, at $\langle n \rangle = 0.75$, which is closer to the van Hove critical density, the higher harmonic angular dependence of the gap function is not directly related to the position of the hot spot.

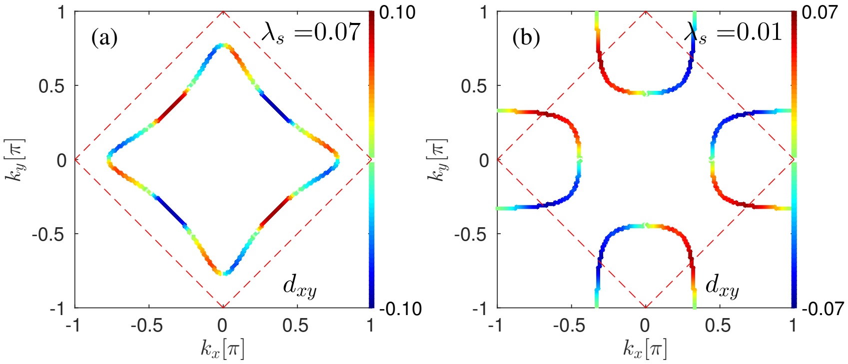

Figure 2.23: (a) d_{xy} solution to the linearized gap equation as stated in Eq. (2.54) for a band with $t' = -0.35$ and $U = 1.5$ at a filling of $\langle n \rangle = 0.55$. (b) d_{xy} solution to the linearized gap equation as stated in Eq. (2.54) for a band with $t' = -1.2$ and $U = 1.5$ at a filling of $\langle n \rangle = 0.65$. The magnetic zone boundary is indicated by the red dashed line.

increased, the van Hove effect becomes more pronounced, and very close to the van Hove critical density at $\langle n \rangle_{vH} = 0.66$, we observe sharp peaks at $\theta = 0$ and $\theta = \pi$ in the red dashed curve in Fig. 2.24(b). These peaks are responsible for suppression of the singlet solution. At the same time the van Hove effect gives rise to attractive potentials in the triplet channel, as seen in from the full blue line at $\theta = \frac{\pi}{4}$ and the full red line at $\theta = 0$.

At very small fillings, the triplet solution has the simple p-wave form as stated in Eq. (2.26e), but away from the small filling regime, the triplet solution is represented by higher order harmonics. One of these solutions is the p' solution given in Eq. (2.57). The main difference between the p-wave and

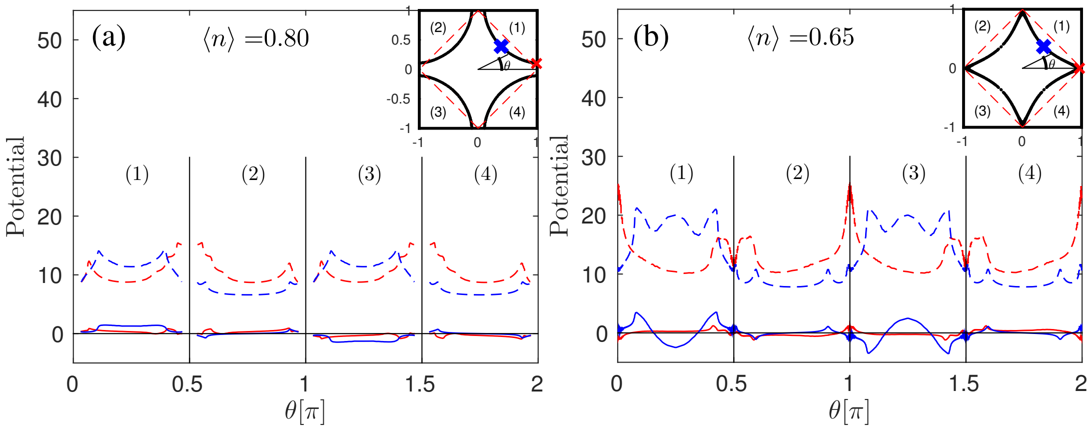

Figure 2.24: Singlet (dashed lines) and triplet (full lines) pairing interaction, $\Gamma^{s/t}_{k,k'} \pm \Gamma^{s/t}_{-k,k'}$, see Eqs. (2.46) and (2.47) for filling (a) $\langle n \rangle = 0.80$ and (b) $\langle n \rangle = 0.65$. Two different positions of the momentum $\mathbf{k}$ has been chosen, as shown by the crosses in the Fermi surface inset. The pairing between $\mathbf{k}$ and all $\mathbf{k}'$ in region (1), (2), (3) and (4) of the Fermi surface are shown in the main panels with the position of $\mathbf{k}'$ being parametrized by the angle θ measured with respect to the x axis. The next-nearest neighbor hopping is $t' = -0.35$ and the Coulomb interaction is $U = 1.75$.

the p'-wave was shown in Fig. 2.9; whereas p'-wave obeys $\text{sgn}[\Delta_{\mathbf{k}+\mathbf{Q}}] = \text{sgn}[\Delta_{\mathbf{k}}]$, the p-wave solution has $\text{sgn}[\Delta_{\mathbf{k}+\mathbf{Q}}] = -\text{sgn}[\Delta_{\mathbf{k}}]$. When the susceptibility has a peak or a plateau at $\mathbf{Q} = (\pi, \pi)$, it is favorable for the triplet gap to display the same sign at $\mathbf{k}$ and $\mathbf{k}'$ displaced by $\mathbf{Q}$, since the triplet pairing potential contains the term $-\frac{U^2}{2}\chi(\mathbf{k} - \mathbf{k}')$. Therefore the p'-wave gap will be favored in the filling regime where the susceptibility shows a $\mathbf{q} = (0, 0)$ peak as well as a peak or plateau structure around $\mathbf{Q} = (\pi, \pi)$. In the more general case of a quartet peak structure around $\mathbf{Q}$ as seen in Fig. 2.11(d) the triplet gap will resemble the structure of p', as visible from Fig. 2.25. In this figure, we show explicitly the two degenerate solutions. The eigenvalues of the two triplet solutions differ on the third decimal which is a numerical artifact due to the construction of the Fermi surface, which is not completely C_4 symmetric.

The fact that all triplet solutions found in the linearized approach are two-fold degenerate suggests that a TRSB solution might be favored; if two solutions of the same symmtry class are allowed (e.g. p_x and p_y), then solutions of the form $p_x \pm ip_y$ are also allowed. A direct superposition, $p_x \pm p_y$ would break four fold rotation symmetry and is therefore not allowed. A solution of the form $p_x \pm ip_y$ breaks time reversal symmetry, since the superconducting condensate of this form will have an overall magnetic moment associated with the orbital part of the wave function [29]. We must solve the full gap equation, Eq. (2.45), in order to investigate if the preferred triplet solution is chiral.

2.11 Time reversal symmetry broken triplet gaps

The full gap equation in the triplet channel is stated in Eq. (2.45). We consider two special fillings of $\langle n \rangle = 0.03$ (see Fig. 2.26) and $\langle n \rangle = 0.65$ (see Fig. 2.27) where in both cases $t' = -0.35$. Numerically, in order to stabilize a TRSB solution, we initiate the calculation by a complex gap and solve Eq. (2.45) self-consistently with this initial guess. If the self-consistent calculation is initialized by complex gap, then a complex (TRSB) solution is always found. On the other hand, if we start the self-consistency loop with a real gap, the final solution is also real. A way of checking if the TRSB solution is favored over the real gap solution, is to compare the energies of the real and complex converged gap solutions. For that purpose, we need an expression of the mean field energy calculated in the triplet channel. The details of the calculation is given in appendix A. Here we simply state the final result of for mean field

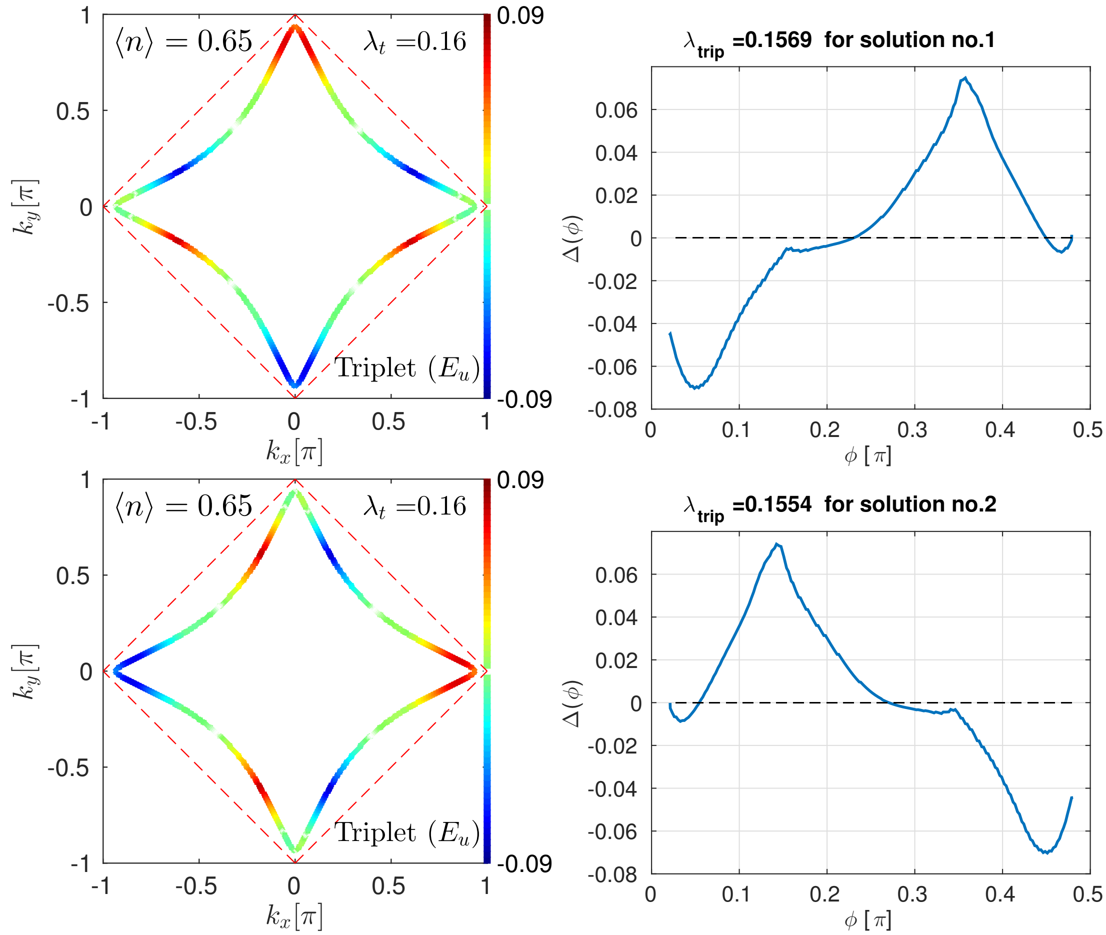

Figure 2.25: Leading solution to the linearized gap equation Eq. (2.54) for $t' = -0.35$ close to the van Hove critical density for $\langle n \rangle = 0.65$ we set $U = 1.75$. The solution is twofold degenerate. Due to numerical inaccuracy there is a difference in the values of λ on the third decimal.

energy $\langle H \rangle$ in the singlet (s) and triplet (t) channel:

$$\langle H \rangle = \sum_{\mathbf{k}} E_{\mathbf{k}}^{s/t} f(E_{\mathbf{k}}^{s/t}) - \frac{|\Delta_{\mathbf{k}}^{s/t}|}{E_{\mathbf{k}}^{s/t}} \tanh\Big(\frac{E_{\mathbf{k}}^{s/t}}{2k_B T}\Big), \tag{2.62}$$

and the free energy is

$$\langle H \rangle = \sum_{\mathbf{k}} E_{\mathbf{k}}^{s/t} f(E_{\mathbf{k}}^{s/t}) - \frac{|\Delta_{\mathbf{k}}^{s/t}|}{E_{\mathbf{k}}^{s/t}} \tanh\Big(\frac{E_{\mathbf{k}}^{s/t}}{2k_B T}\Big) + k_B T \Big[f(E_{\mathbf{k}}^{s/t}) \ln[f(E_{\mathbf{k}}^{s/t})] + f(-E_{\mathbf{k}}^{s/t}) \ln[f(-E_{\mathbf{k}}^{s/t})]. \Big] \tag{2.63}$$

For our purposes, where temperatures are very low, the entropy term is much smaller than the contribution from $\langle H \rangle$. The numerical approach to the full gap equation is to calculate the superconducting gaps within a small energy cutoff close to the Fermi surface. The energy cutoff is put in "by hand", since there is no obvious energy cutoff related to the spin fluctuation pairing mechanism. We can also do the full gap equation with no energy cutoff. In this case we note that the contributions from **k** points far from the Fermi surface will contribute less in the **k**-sum of Eq. (2.45), since $|\xi_{\mathbf{k}}| >> \Delta_{\mathbf{k}}$ for these points.

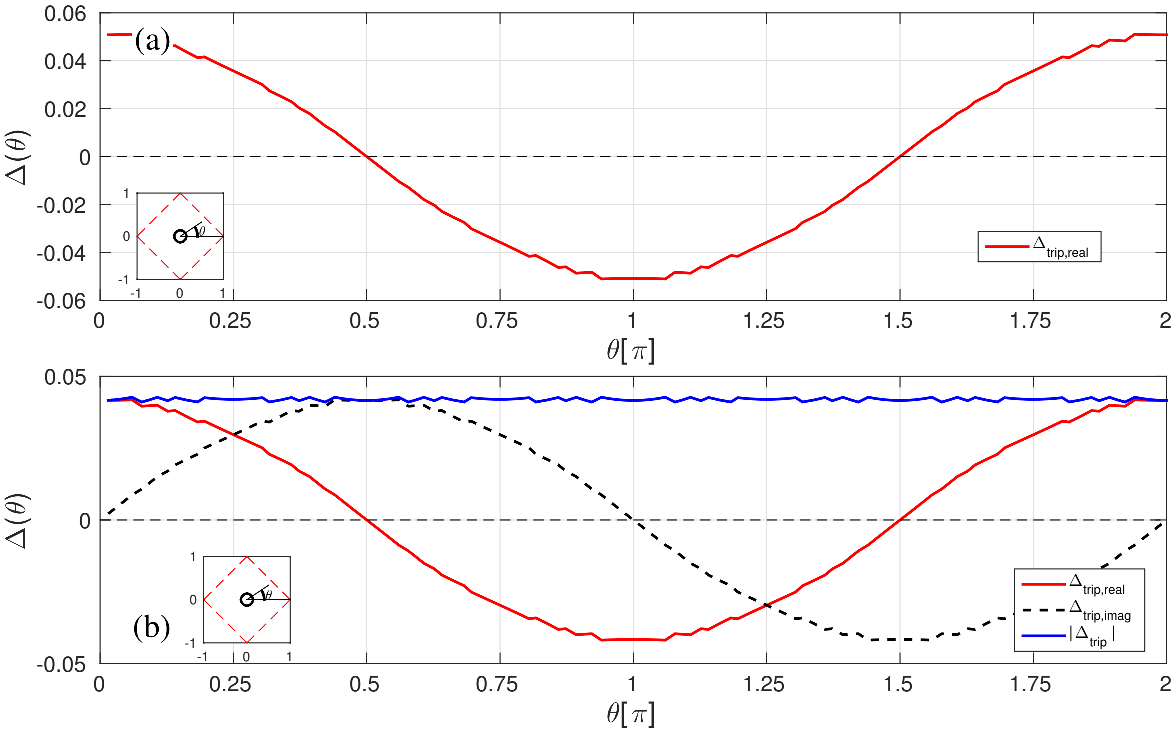

Figure 2.26: (a) Real gap solution and (b) complex gap solution to the full gap equation Eq. (2.45) with the bare Coulomb interaction $U = 10.5$ renormalized to $\bar{U} = 3.5$. The filling level is $\langle n \rangle = 0.03$ and energy cut-off is set to $\epsilon_c = 0.012$. Real (full red line) and imaginary (black dashed line) part of the chiral p-wave gap as a function of angle θ defined in the Fermi surface inset. The absolute value of the gap $|\Delta(\theta)|$ is shown by the full blue line. The next-nearest neighbor hopping is $t' = -0.35$ and temperature is $k_B T = 0.01$.

When we solve the gap equation with an energy cutoff, ϵ_c, we evaluate the energy as stated in Eq. (2.62) with the $\mathbf{k}$-sum restricted to the $\mathbf{k}$-points for which $\xi_{\mathbf{k}} \in [-\epsilon_c, \epsilon_c]$. The restriction of the $\mathbf{k}$-sum means that we will miss out the energy contribution from the states further away from the Fermi level. However, since the superconducting gap only modifies the energy band close to the Fermi level this additional contribution can be safely omitted, since it is independent on the superconducting gap solution. In order to test this numerical procedure we do the energy calculation for several values of the energy cutoff, to make sure that the results does not change qualitative when the size of the energy cutoff is changed. When this is ensured we rely on this procedure to correctly conclude which superconducting state will have the lowest energy, and we always find that the triplet channel provides TRSB (complex) solutions.

At very low filling, the susceptibility only displays a weak structure around $\mathbf{q} = (0, 0)$ as seen in Fig. 2.11(a). In this case the p-wave triplet solution is favored. If the gap is real, the p-wave solution has two nodes at the Fermi level, along one of the zone axes as visible from Fig. 2.26(a). The TRSB solution is shown in Fig. 2.26(b), revealing a nodeless TRSB gap of the form $p_x \pm ip_y$. In this filling regime, strong Coulomb interactions are required to achieve a superconducting instability due to the weak structure of the spin susceptibility. We invoke a bare Coulomb interaction of $U = 10.5$ which is renormalized in the RPA expressions to $\bar{U} = 3.5$. At higher fillings, the spin susceptibility becomes more structure-full and provides a superconducting gap with a bare Coulomb interaction $U = 5.7$ renormalized to $\bar{U} = 1.9$. For this band, the real gap solution is depicted in Fig. 2.27(a). Note that the solution displays six nodes at the Fermi level, similar to the p'-wave solution, Eq. (2.57). But only two of the six nodes at positioned

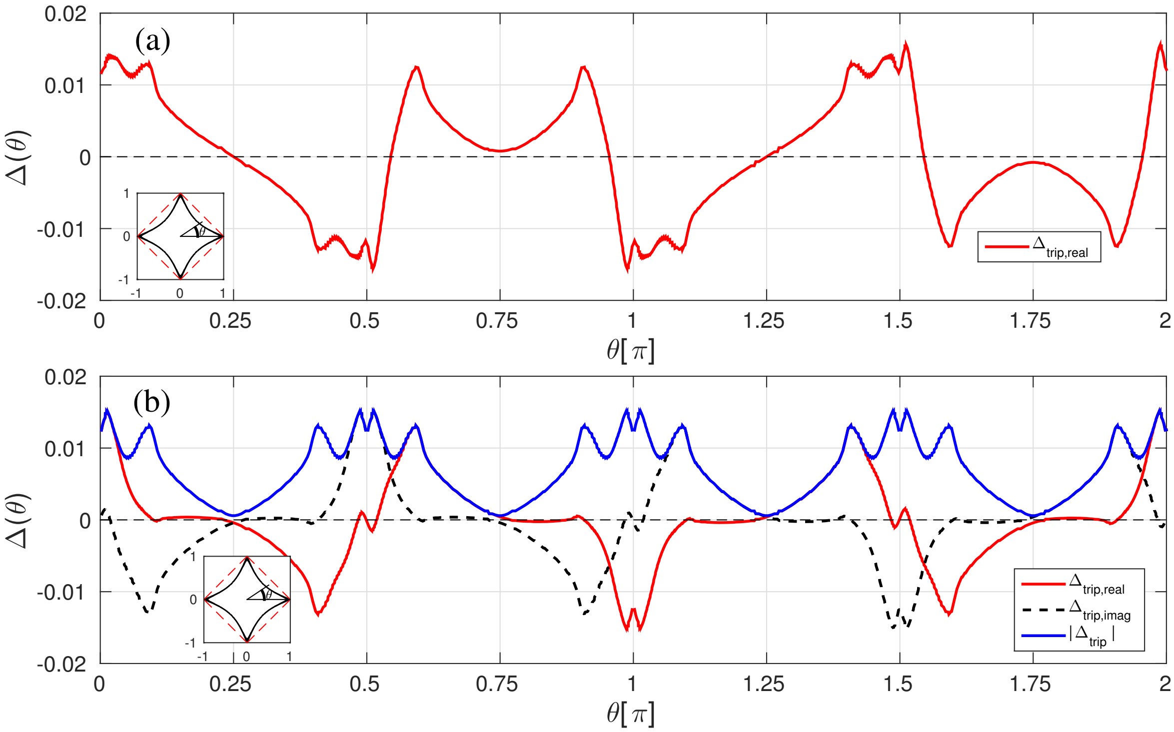

Figure 2.27: (a) Real gap solution and (b) complex gap solution to the full gap equation Eq. (2.45). We have invoked the triplet potential for the band with next-nearest neighbor hopping constant $t' = -0.35$ and a filling level of $\langle n \rangle = 0.65$. This is close to the van Hove critical density, $\langle n \rangle_{vH} = 0.66$. The bare Coulomb interaction $U = 5.7$ renormalized to $\bar{U} = 1.9$ and energy cut-off is set to $\epsilon_c = 0.012$. Real (full red line) and imaginary (black dashed line) part of the gap solution is plotted as a function of angle θ defined in the Fermi surface inset. The absolute value of the gap $|\Delta(\theta)|$ is shown by the full blue line. The temperature is $k_B T = 0.01$.

along the zone diagonal, $\theta = \frac{\pi}{4}$ and $\theta = \frac{5\pi}{4}$, and thus the real gap solutions differs significantly from the simple p'-wave form. It turns out that also at this doping, the preferred solution is a complex (TRSB) solution. If the TRSB solution had been of the form $p'_x \pm ip'_y$ only the nodes along the zone axes k_x and k_y would become lifted with the four nodes along the zone diagonals preserved. In this case, since only two of the six nodes are lifted, the gain in condensation energy of the TRSB solution compared to one of the solutions, p'_x or p'_y, would be limited. However, as seen already in the case of the real gap solution in Fig. 2.27(a), the simple p'-wave form is replaced by a more complicated gap structure. This is also observed for the real and imaginary part of the gap solution shown in Fig. 2.27(b). Note that at this doping, the spin susceptibility has in addition to the $\mathbf{q} = (0, 0)$ peak also a quartet of peaks around $\mathbf{Q}$. Therefore the simple form $p'_x \pm ip'_y$ is replaced by a more complicated gap solution. In fact, due to this the TRSB solution does become fully gapped. From the angular gap dependence shown in Fig. 2.27(b), strong effects due to the susceptibility structure are clearly visible from the absolute value of the gap, $|\Delta_{\text{trip}}(\theta)|$ as shown by the full blue line. The maximum of the gap achieved close to $\theta = 0$ and $\frac{\pi}{2}$ is due to the van Hove effect, and the peaked feature at $\theta \sim \pi/8$ is related to the quartet of peaks around the $\mathbf{Q}$ vector in the susceptibility as shown in Fig. 2.11(d). This underlines again the strong connection between the Fermi surface structure, spin susceptibility, and the detailed angular dependence of the superconducting gap. Lastly, we note that the gap minimum of this higher order triplet solution is achieved at $\theta = \frac{\pi}{4}$, which is at the position of the nodal lines of the $d_{x^2-y^2}$ structure.

2.12 Discussion

In Ref. [24] the changes in gap symmetry as a function of electron- and hole doping within spin fluctuation mediated pairing to second order in $U = 6t$ were discussed. The pairing potential was $V(\mathbf{k}, \mathbf{k}') = U + U^2\chi(\mathbf{k} + \mathbf{k}')$, and the next-nearest hopping constant fixed at $t'/t = -0.276$. The $d_{x^2-y^2}$ solution dominates at all moderate doping levels, also at the van Hove critical density, in agreement with our findings. However, in contrast to our results, Ref. [24] reports a regime of triplet superconductivity at smaller fillings. As mentioned above, Ref. [23] also reports an extended region of triplet superconductivity which is unrelated to the van Hove critical density. We suspect this discrepancy to arise from the details of procedure; in Refs. [23] and [24] gap solutions was truncated to the first 15 harmonics, whereas in our case we do not invoke any restrictions on the gap functions.

In a recent work by Deng *et al.*, [30] the emergence of pairing for the paramagnetic liquid was also addressed in a numerical study of the two-dimensional Hubbard model with $t' = 0$. They reported a transition from p-wave superconductivity at small fillings through a d_{xy} gap at intermediate filling levels to a $d_{x^2-y^2}$ symmetry close to half filling. For small values of U, a higher order triplet gap with six nodes was also found for fillings at $\langle n \rangle \simeq 0.55$. This triplet solution is thus unrelated to the van Hove critical density, and we do not find a similar solution at $t' = 0$ in our case. Their findings, however, agrees with the results in Ref. [23] which report the $U \to 0$ case. The disagreement might arise from the difference in strength of U.

2.13 Interactions through longer range Coulomb repulsion

In the study discussed in this chapter, we have been concerned only with onsite bare Coulomb repulsion and higher order interactions derived from this. We now discuss how the effective interaction would modify in the case where a (smaller) nearest neighbor Coulomb repulsion, $V > 0$, is taken into account. The interaction Hamiltonian takes the form:

$$H_{\text{int2}} = V \sum_{i\delta,\sigma,\sigma'} n_{i\sigma} n_{i+\delta,\sigma'}. \tag{2.64}$$

Here the δ sum runs over the four nearest neighbors. Since the repulsion is between electrons on neighboring sites, there is no restriction on the spins σ and σ'. These can be same or opposite, both cases are allowed. By a Fourier transformation we get the bare interaction Hamiltonian of the form:

$$H_{\text{int2}} = \sum_{\mathbf{k},\mathbf{k}'\mathbf{q}} \sum_{\sigma,\sigma'} \underbrace{2V[\cos(k_x - k_x') + \cos(k_y - k_y')]}_{V(\mathbf{k}-\mathbf{k}')} c^\dagger_{\mathbf{k}'\sigma} c^\dagger_{-\mathbf{k}'+\mathbf{q}\sigma'} c_{-\mathbf{k}+\mathbf{q}\sigma'} c_{\mathbf{k}\sigma} \tag{2.65}$$

The main difference from the interaction Hamiltonian invoking the onsite Coulomb repulsion U is the fact, that the interaction vertex, $V(\mathbf{q}) = V(\cos k_x + \cos k_y)$ has internal structure, i.e. it depends explicitly on $\mathbf{q}$. The bare interaction diagram is drawn as: For interactions of same spin as well as opposite spin electrons, bubble diagrams can now be constructed from the first order diagram in Fig. 2.28, and as

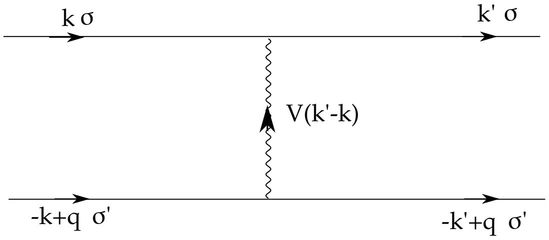

Figure 2.28: Bare interaction diagram for nearest neighbor repulsion.

opposed to the previous case of onsite repulsion U, we are in this case not restricted to the number of bubbles being even or odd. Thus, in both the cases $\sigma = \sigma'$ and $\sigma = -\sigma'$ we get the effective interaction vertex:

$$-V_{\text{eff2,bub}}(\mathbf{k},\mathbf{k}') = V^2(\mathbf{k}-\mathbf{k}')\chi_0(\mathbf{k}-\mathbf{k}') - V^3(\mathbf{k}-\mathbf{k}')\chi_0^2(\mathbf{k}-\mathbf{k}') + V^4(\mathbf{k}-\mathbf{k}')\chi_0^3(\mathbf{k}-\mathbf{k}') + \cdots \Leftrightarrow \tag{2.66}$$

$$V_{\text{eff2,bub}}(\mathbf{k},\mathbf{k}') = \frac{-V^2(\mathbf{k}-\mathbf{k}')\chi_0(\mathbf{k}-\mathbf{k}')}{1+V(\mathbf{k}-\mathbf{k}')\chi_0(\mathbf{k}-\mathbf{k}')} \tag{2.67}$$

with $V(\mathbf{k}-\mathbf{k}') = 2V[\cos(k_x-k_x') + \cos(k_y-k_y')]$. The potential form in Eq. (2.67) resembles a charge susceptibility, which usually does not bring about very significant contributions to the pairing. However, we should keep in mind that $V(\mathbf{k}-\mathbf{k}')$ becomes negative for some pairs $(\mathbf{k},\mathbf{k}')$. Let us consider the case of a system close to an antiferromagnetic instability. This means that the susceptibility $U\chi_0(\mathbf{q}) \to 1$ for $\mathbf{q} = \mathbf{Q} = (\pi,\pi)$. For a pair scattering with $\mathbf{k}-\mathbf{k}' = \mathbf{Q}$ then $V(\mathbf{k}-\mathbf{k}') = -4V$ and if V is of the order $U/4$ then the pairing potential contribution in Eq. (2.67) becomes significant. Now, the overall sign of $V_{\text{eff2,bub}}(\mathbf{k},\mathbf{k}')$ means that the contribution to the effective pairing will be an *attractive* pair scattering for $\mathbf{k}$ and $\mathbf{k}'$ displaced by $\mathbf{Q}$. This will favor a superconducting gap for which $\Delta_{\mathbf{k}}$ and $\Delta_{\mathbf{k}+\mathbf{Q}}$ has the same sign. It will therefore act against the $d_{x^2-y^2}$ solution supported by the singlet potential arising from the onsite repulsion, U, stated in Eq. (2.46). On the contrary, the contribution from $V_{\text{eff2,bub}}(\mathbf{k},\mathbf{k}')$ will act in concert with the triplet potential which was derived from U in Eq. (2.47), and this would support the p' triplet gap, as discussed in relation to Fig. 2.9.

In order to include ladder diagrams the calculation becomes more involved. In this case summation is complicated by the explicit momentum dependence of the bare interaction vertex. In fact, a different approach is needed in order to sum up the vertices. In this approach, real space information of the interaction is kept partly intact [33, 34, 35]. The full FLEX treatment with inclusion of the offsite V repulsion was discussed for the square lattice by Onari *et al.*, Ref. [34]. The explicit momentum dependence of the bare vertex becomes more complex, with all vertices as well as susceptibilities becoming matrices of dimension $(z+1)\times(z+1)$ [34], where z is the lattice coordination number. Upon this generalization it might happen that spin and charge pairing potential achieve different momentum structures. As pointed out in Ref. [34] the charge fluctuations will promote triplet pairing provided that the peak structure of the spin and charge pairing potential are similar. This conclusion is very similar to the simple picture derived in terms of the new bubble diagram contribution derived above.

Chapter 3

Local pairing from spin fluctuations

Part of the material in this chapter has been presented in Phys. Rev. B **86***, 054507 (2012) and Journal of Superconductivity and Novel Magnetism* **26***, 1729 (2013). We present a self-consistent real space formulation of spin-fluctuation mediated d-wave pairing. By calculating all relevant inhomogeneous spin and charge susceptibilities in real space within the random phase approximation (RPA), we obtain the effective pairing interaction and study its spatial dependence near both local potential and hopping impurities. A remarkably large enhancement of the pairing interaction may be obtained near the impurity site.*

3.1 Local modulations of the superconducting gap in cuprate superconductors

Scanning tunneling spectroscopy (STS) experiments on surfaces of several high-T_c materials[36] have discovered that the electronic structure of at least some of the cuprate superconductors is strongly inhomogeneous in real space. Modulations observed include checkerboard local density of states (LDOS) patterns which peak at biases near the local pseudogap energy, together with strong gap modulations on nanometer length scales[37, 38, 39, 40, 41, 42, 43]. While the latter modulations appear to be random in character and driven by disorder, the STS conductance maps contain important correlations of gaps with other physical observables. For example, the size of the local gap was found to be positively correlated with atomic scale defects, thought to be interstitial oxygen dopants [44]. Correlations between the oxygen position $O(\mathbf{r})$ and the superconducting gap magnitude $\Delta(\mathbf{r})$ was quantified by the cross-correlation function:

$$C(O,\Delta,\mathbf{R}) \quad \propto \quad \int d\mathbf{r}[O(\mathbf{r})-\langle O(\mathbf{r})\rangle]\times[\Delta(\mathbf{r}+\mathbf{R})-\langle\Delta(\mathbf{r})\rangle] \tag{3.1}$$

and it was found that positive correlations occur in a range of $R \simeq 0-15$ Å i.e. the superconducting gap apparently becomes larger in the vicinity of the impurity. The images showing $O(\mathbf{r})$ and $\Delta(\mathbf{r})$ for three different samples, as well as an image of the cross-correlation function $C(\mathbf{R})$ is reproduced from Ref. [44] in Fig. 3.1. In addition to the correlation of $O(\mathbf{r})$ and $\Delta(\mathbf{r})$, it was observed that the coherence peak height decreases as the peak energy (Δ) grows, see Fig. 3.1(D). The observations of Ref. [44] inspired a reexamination of the effect of an impurity in the oxygen-doped systems, since it had been anticipated that an oxygen, which donates two holes to the CuO_2 plane, would locally overdope the system and lead to a smaller gap in the neighborhood of such a dopant impurity.

Nunner *et al.*[45] proposed a phenomenological model, where the effect of the impurities was assumed to cause local enhancement of the superconducting pairing mechanism. In this approach, the local impurity strength *as well as* the pairing interaction was assumed to be modulated by the phenomenological

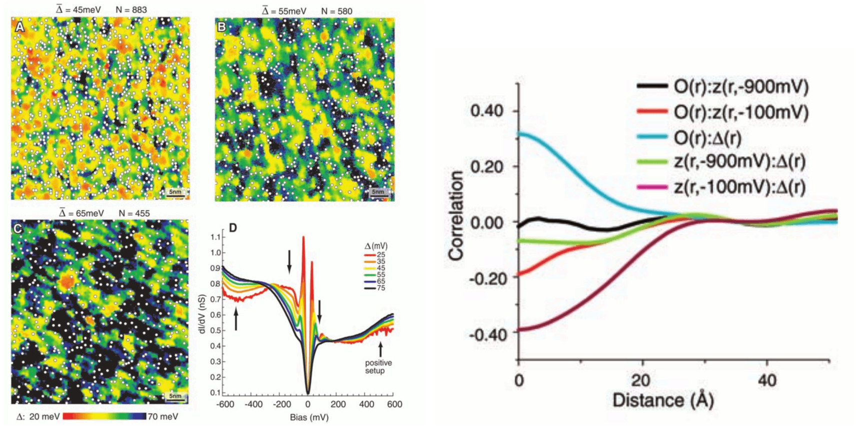

Figure 3.1: (**left:**) Map of the local gap size at the surface of $Bi_2Sr_2CaCu_2O_8$. The oxygen positions are determined by a peak in the density of states, $O(r) = LDOS(E = –0.96eV, r)$. These positions are shown by white dots and the number N denotes the number of white spots in each image. (**right:**) Correlation function as defined in Eq. (3.1). Adapted from Ref. [44].

form $f_i = \sum_s \frac{e^{-r_{is}/\lambda}}{r_{is}}$, where i is the site index, and s denotes the impurity sites. This form gives rise to a strong onsite repulsion occuring at the impurity sites, but in addition the attractive nearest-neighbor interaction is boosted at the impurity site as well as in the close vicinity of an impurity. It maybe does not come as a big surprise that such a modulation of the pairing interaction produces a positive correlation between the impurity position and local gap value. However, the model is able to explain a number of additional experimental findings. For example, it correctly reproduces the anti-correlation of coherence peak height and peak energy, the correlation of impurity position with gap size, and the detailed frequency dependence of the O:LDOS(ω) correlation. Some key findings is reproduced in Fig. 3.2.

We want to pursue this finding further, to investigate from a microscopic approach, if impurities can lead to a local strengthening of the effective pairing interaction. In this chapter, we formulate the full

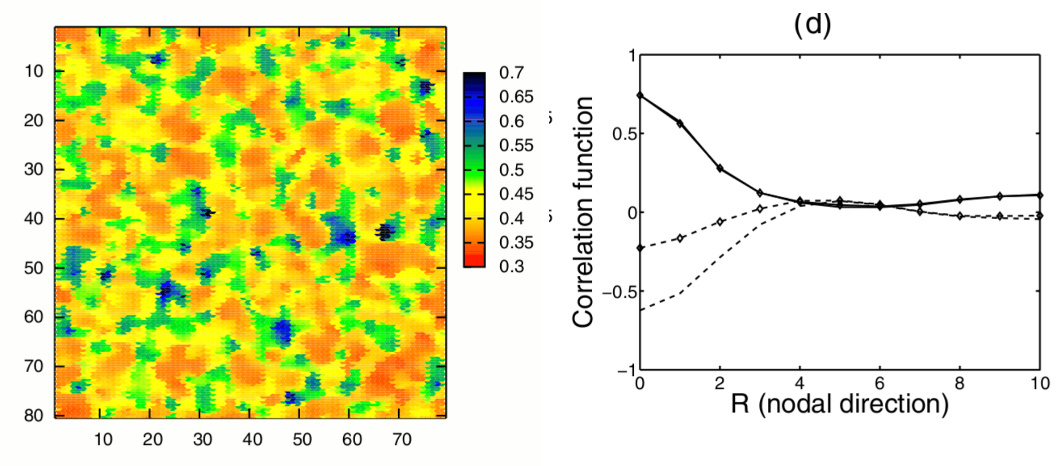

Figure 3.2: (**left:**) Map of the local gap size as generated numerically. (**right**:) Correlation function between the gap map and the dopant atoms (solid line), and the gap map and the peak height map (dashed line). Adapted from Ref. [45].

RPA particle-particle vertex in real space for a general inhomogeneous system. Since we a dealing with a non-translationally invariant system, the pairing interaction is expressed in large real space matrices and thus appear somewhat more complicated compared to the usual form [10, 65] which was discussed in detail in chapter 2. We derive the pairing arising from bubble and ladder diagrams, corresponding to interactions due to longitudinal and transverse spin fluctuations, respectively.

We will show the derivation of the pairing interaction and mean field gap Hamiltonian of the superconducting phase. We have not included feedback from superconductivity, but calculate the effective pairing in the normal phase. The discussion of feedback effects we will return to in chapter 4, where we will show that feedback causes a general weakening of the spin-fluctuation mediated pairing.

3.2 Effective pairing interaction in real space

We derive the interaction Hamiltonian arising from the bare onsite Coulomb repulsion by drawing the bubble and ladder diagrams in real space. In general, the interaction Hamiltonian is given by

$$H_{\text{int}} = \sum_{a,b,c,d} V_{\text{eff}}(a,c;b,d)\big(c^{\dagger}_{b\uparrow}c^{\dagger}_{d\downarrow}c_{c\downarrow}c_{a\uparrow} + H.c.\big), \tag{3.2}$$

where $a, ..d$ are real space points. We define the noninteracting spin-dependent susceptibility of the normal phase as

$$\chi^{\sigma\sigma'}_{ab}(\tau) = -\mathcal{G}_{ab,\sigma}(\tau)\mathcal{G}_{ba,\sigma'}(-\tau). \tag{3.3}$$

Note the sign convention. The effective interaction in real space is evaluated directly from the real space version of the standard spin-fluctuation diagrams. Since the Coulomb interaction is local both in space and time, it connects fermions at the same site and of opposite spin. Omitting the external fermion lines and evaluating the interaction part from the bubble diagrams shown in Fig. 3.3 gives

$$\begin{aligned} V^{(1)}_{\text{eff}}(a,c;b,d) &= U\delta_{ab}\delta_{cd}\delta_{ad} + \\ U^3\sum_{e}\delta_{ab}\delta_{cd}&\mathcal{G}_{ae,\downarrow}\mathcal{G}_{ea,\downarrow}\mathcal{G}_{ed,\uparrow}\mathcal{G}_{de,\uparrow} + \cdots \end{aligned} \tag{3.4}$$

The pairing interaction is dependent only on two spatial variables since U is onsite. We get

$$\begin{aligned} V^{(1)}_{\text{eff}}(a,c;b,d) &= \delta_{ab}\delta_{cd}[U\delta_{ad} + U^3\sum_{e}\chi^{\downarrow\downarrow}_{ae}\chi^{\uparrow\uparrow}_{ed} \\ &\quad + U^5\sum_{e,f,g}\chi^{\downarrow\downarrow}_{ae}\chi^{\uparrow\uparrow}_{ef}\chi^{\downarrow\downarrow}_{fg}\chi^{\uparrow\uparrow}_{gd} + \cdots] \\ &= \delta_{ab}\delta_{cd}[U\hat{1} + U^3\chi^{\downarrow\downarrow}\chi^{\uparrow\uparrow} + U^5(\chi^{\downarrow\downarrow}\chi^{\uparrow\uparrow})^2 + \cdots]_{ad} \\ &= \delta_{ab}\delta_{cd}\left(U\hat{1}_{ad} + \frac{U^3\chi^{\downarrow\downarrow}\chi^{\uparrow\uparrow}}{\hat{1} - U^2\chi^{\downarrow\downarrow}\chi^{\uparrow\uparrow}}\Big|_{ad}\right). \end{aligned} \tag{3.5}$$

Similarly, in the case of the ladder diagrams shown in Fig. 3.4 we get

$$\begin{aligned} V^{(2)}_{\text{eff}}(a,c;b,d) &= \delta_{ad}\delta_{bc}[U\chi^{\uparrow\downarrow}_{ab} + U^3\sum_{e}\chi^{\uparrow\downarrow}_{ae}\chi^{\uparrow\downarrow}_{eb} + U^5\sum_{e,f}\chi^{\uparrow\downarrow}_{ae}\chi^{\uparrow\downarrow}_{ef}\chi^{\uparrow\downarrow}_{fb} + \cdots] \\ &= \delta_{ad}\delta_{bc}[U^2\chi^{\uparrow\downarrow} + U^3(\chi^{\uparrow\downarrow})^2 + U^5(\chi^{\uparrow\downarrow})^4 + \cdots]_{ab} \\ &= \delta_{ad}\delta_{bc}\left(\frac{U^2\chi^{\uparrow\downarrow}}{\hat{1} - U\chi^{\uparrow\downarrow}}\Big|_{ab}\right). \end{aligned} \tag{3.6}$$

The interaction Hamiltonian now becomes

$$\begin{aligned} H_{\text{int}} &= \sum_{a,b,c,d} V^{(1)}_{\text{eff}}(a,c;b,d)\big(c^{\dagger}_{b\uparrow}c^{\dagger}_{d\downarrow}c_{c\downarrow}c_{a\uparrow} + H.c.\big) + V^{(2)}_{\text{eff}}(a,c;b,d)\big(c^{\dagger}_{b\uparrow}c^{\dagger}_{d\downarrow}c_{c\downarrow}c_{a\uparrow} + H.c.\big) \\ &= \sum_{ad} V^{(1)}_{\text{eff}}(a,d;a,d)\left(c^{\dagger}_{a\uparrow}c^{\dagger}_{d\downarrow}c_{d\downarrow}c_{a\uparrow} + H.c.\right) + \sum_{ab} V^{(2)}_{\text{eff}}(a,b;b,a)\left(c^{\dagger}_{b\uparrow}c^{\dagger}_{a\downarrow}c_{b\downarrow}c_{a\uparrow} + H.c.\right). \end{aligned} \tag{3.7}$$

From this it is apparent that the first part corresponds to spin-conserving processes while the second describes a spin-flip interaction.

3.3 Mean field Hamiltonian in the real space approach

The result for the effective interaction derived in Eq. (3.7) is treated in a mean-field approach. We consider only the singlet channel

$$\begin{aligned} H_{\text{int}} &= 2\sum_{i,j} V_{\text{eff}}^{(1)} c_{i\uparrow}^\dagger c_{j\downarrow}^\dagger c_{j\downarrow} c_{i\uparrow} - \sum_{i,j} V_{\text{eff}}^{(2)} (c_{i\downarrow}^\dagger c_{j\uparrow}^\dagger c_{j\downarrow} c_{i\uparrow} + c_{i\uparrow}^\dagger c_{j\downarrow}^\dagger c_{j\uparrow} c_{i\downarrow}) \\ &= H_{\text{int}}^{(1)} + H_{\text{int}}^{(2)}, \end{aligned} \tag{3.8}$$

where we have used that the interactions are symmetric with respect to interchange of spatial indices. We define two gaps which are respectively symmetric (s) and anti-symmetric (a) under interchange of spatial indices

$$\begin{aligned} \Delta_{(1),ij}^{s/a} &= \frac{V_{\text{eff}}^{(1)}}{2} \left(\langle c_{j\downarrow} c_{i\uparrow} \rangle \pm \langle c_{j\uparrow} c_{i\downarrow} \rangle \right), \\ \Delta_{(2),ij}^{s/a} &= \frac{V_{\text{eff}}^{(2)}}{2} \left(\langle c_{j\downarrow} c_{i\uparrow} \rangle \pm \langle c_{j\uparrow} c_{i\downarrow} \rangle \right). \end{aligned} \tag{3.9}$$

Here we have used that $V_{\text{eff}}^{(1)}$ and $V_{\text{eff}}^{(2)}$ are both even under exchange of spatial indices $i \leftrightarrow j$. For the first term in the interaction Hamiltonian, we get by a standard mean field decoupling

$$\begin{aligned} H_{\text{int}}^{(1)} &= 2\sum_{i,j} V_{\text{eff}}^{(1)} c_{i\uparrow}^\dagger c_{j\downarrow}^\dagger c_{j\downarrow} c_{i\uparrow} \\ &\simeq \sum_{i,j} V_{\text{eff}}^{(1)} \left(\langle c_{i\uparrow}^\dagger c_{j\downarrow}^\dagger \rangle c_{j\downarrow} c_{i\uparrow} + c_{i\uparrow}^\dagger c_{j\downarrow}^\dagger \langle c_{j\downarrow} c_{i\uparrow} \rangle \right) \\ &= \sum_{ij} \frac{1}{2} \Big[\Delta_{(1),ij}^{s^*} (c_{j\downarrow} c_{i\uparrow} - c_{j\uparrow} c_{i\downarrow}) + \Delta_{(1),ij}^{s} (c_{i\uparrow}^\dagger c_{j\downarrow}^\dagger - c_{i\downarrow}^\dagger c_{j\uparrow}^\dagger) \\ &\qquad + \Delta_{(1),ij}^{a^*} (c_{j\downarrow} c_{i\uparrow} + c_{j\uparrow} c_{i\downarrow}) + \Delta_{(1),ij}^{a} (c_{i\uparrow}^\dagger c_{j\downarrow}^\dagger + c_{i\downarrow}^\dagger c_{j\uparrow}^\dagger) \Big]. \end{aligned}$$

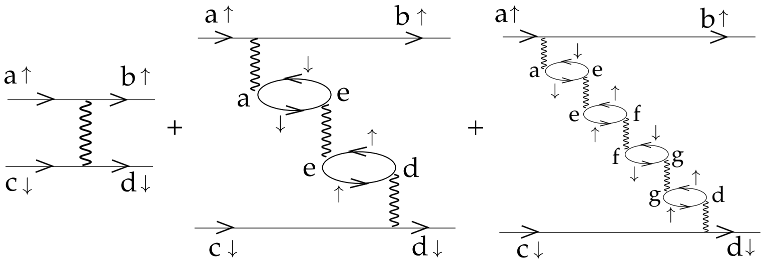

Figure 3.3: Real space diagrams for longitudinal spin fluctuations to fifth order in U.

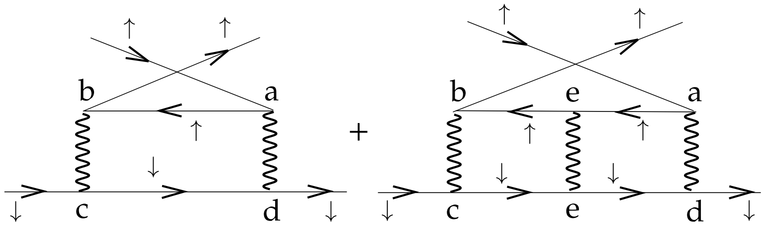

Figure 3.4: Real space diagrams for transverse spin fluctuations to third order.

The second term gives

$$
\begin{aligned}
H^{(2)}_{\text{int}} &= -\sum_{i,j} V^{(2)}_{\text{eff}}(c^\dagger_{i\downarrow}c^\dagger_{j\uparrow}c_{j\downarrow}c_{i\uparrow} + c^\dagger_{i\uparrow}c^\dagger_{j\downarrow}c_{j\uparrow}c_{i\downarrow}) \\
&= -\sum_{i,j}\frac{V^{(2)}_{\text{eff}}}{2}\Big[\langle c^\dagger_{i\downarrow}c^\dagger_{j\uparrow}\rangle c_{j\downarrow}c_{i\uparrow} + \langle c^\dagger_{i\uparrow}c^\dagger_{j\downarrow}\rangle c_{j\uparrow}c_{i\downarrow} \\
&\qquad + c^\dagger_{i\downarrow}c^\dagger_{j\uparrow}\langle c_{j\downarrow}c_{i\uparrow}\rangle + c^\dagger_{i\uparrow}c^\dagger_{j\downarrow}\langle c_{j\uparrow}c_{i\downarrow}\rangle\Big] \\
&= \sum_{ij}\frac{1}{2}\Big[\Delta^{s^*}_{(2),ij}(c_{j\downarrow}c_{i\uparrow} - c_{j\uparrow}c_{i\downarrow}) + \Delta^{s}_{(2),ij}(c^\dagger_{i\uparrow}c^\dagger_{j\downarrow} - c^\dagger_{i\downarrow}c^\dagger_{j\uparrow}) \\
&\qquad + \Delta^{a^*}_{(2),ij}(c_{j\downarrow}c_{i\uparrow} + c_{j\uparrow}c_{i\downarrow}) + \Delta^{a}_{(2),ij}(c^\dagger_{i\uparrow}c^\dagger_{j\downarrow} + c^\dagger_{i\downarrow}c^\dagger_{j\uparrow})\Big].
\end{aligned}
$$

Adding these results, we obtain the final effective mean field Hamiltonian in the singlet channel

$$
H^{\text{MF}}_{\text{singlet}} = \frac{1}{2}\sum_{i,j}\left[\Delta^{s*}_{ij}(c_{j\downarrow}c_{i\uparrow} - c_{j\uparrow}c_{i\downarrow}) + \Delta^{s}_{ij}(c^\dagger_{i\uparrow}c^\dagger_{j\downarrow} - c^\dagger_{i\downarrow}c^\dagger_{j\uparrow})\right], \tag{3.10}
$$

where

$$
\Delta^s_{ij} = \frac{V_{\text{eff}}(i,j)}{2}\big(\langle c_{j\downarrow}c_{i\uparrow}\rangle - \langle c_{j\uparrow}c_{i\downarrow}\rangle\big). \tag{3.11}
$$

Here, the total effective pairing interaction $V_{\text{eff}}(i,j)$ is the sum of the effective interactions $V^{(1)}_{\text{eff}}$ and $V^{(2)}_{\text{eff}}$ derived in Eqs. (3.5) and (3.6). Thus, the effective pairing is given by the real space matrix

$$
\begin{aligned}
V_{\text{eff}}(i,j) &= V^{(1)}_{\text{eff}}(i,j) + V^{(2)}_{\text{eff}}(i,j) \\
&= U\hat{1}_{i,j} + \frac{U^3\chi^{\downarrow\downarrow}\chi^{\uparrow\uparrow}}{\hat{1} - U^2\chi^{\downarrow\downarrow}\chi^{\uparrow\uparrow}}\Big|_{i,j} + \frac{U^2\chi^{\uparrow\downarrow}}{\hat{1} - U\chi^{\uparrow\downarrow}}\Big|_{i,j},
\end{aligned} \tag{3.12}
$$

which reduces to the usual expression in the translationally invariant case.

In the initial step of the calculation of the effective real space pairing potential, we obtain the electronic densities calculated self-consistently in the normal state using a mean-field approximation to the one-band Hubbard model

$$
\begin{aligned}
H_0 &= \sum_{i,j,\sigma} t_{i,j}c^\dagger_{i\sigma}c_{j\sigma} + \sum_{i\sigma}(U\langle n_{i\sigma}\rangle - \mu)n_{i\bar{\sigma}} \\
&\quad + \sum_{i\sigma} V_{\text{imp}}\delta(r_i - r_{\text{imp}})n_{i\sigma}.
\end{aligned} \tag{3.13}
$$

Here, $c^\dagger_{i\sigma}$ refers to creation of an electron with spin σ at lattice site i, and $n_{i\sigma}$ is the number operator of spin σ particles at site i. The hoppings $t_{i,j}$ are included to nearest $t = 1$, and next-nearest neighbor sites $t' = -0.3$. Note that this Hamiltonian also contains the impurity potential V_{imp} at a site placed at position $r_{i_{\text{imp}}}$. A diagonalization of Eq.(3.13) allows us to obtain the effective interaction $V_{\text{eff}}(i,j)$ as given in Eq. (3.12). The susceptibilities entering Eq.(3.12) are real space matrices and given by

$$\chi_{ij}^{\sigma\sigma'} = \sum_{m,n} u_{mi\sigma} u_{mj\sigma} u_{nj\sigma'} u_{ni\sigma'} \frac{f(E_{m\sigma}) - f(E_{n\sigma'})}{E_{n\sigma'} - E_{m\sigma} + i\eta}, \tag{3.14}$$

in terms of the eigenvectors $u_{m\sigma}$ and eigenvalues $E_{m\sigma}$ obtained in the diagonalization of Eq.(3.13).

It is useful now to consider the partial Fourier transform of the susceptibility with respect to relative coordinate $\mathbf{r} = \mathbf{r}_i - \mathbf{r}_j$, leaving explicit dependence on one spatial variable, $\mathbf{r}_i$

$$\chi(\mathbf{q}, \mathbf{r}_i) = \sum_{\mathbf{r}_j} e^{i\mathbf{q}\cdot(\mathbf{r}_i - \mathbf{r}_j)} \chi(\mathbf{r}_i, \mathbf{r}_j). \tag{3.15}$$

Note that Eq. (3.12) reduces to the usual form in the case of translational invariance, $\chi(\mathbf{q}, \mathbf{r}_i) = \chi(\mathbf{q})$. In addition, it is worth remarking that the convention used here is slightly different from other works, e.g. Ref. [70] where the mixed susceptibility is a function of the center of mass variable $(\mathbf{r}_i + \mathbf{r}_j)/2$. After the calculation of the effective spin-fluctuation mediated pairing, the densities $\langle n_{i\sigma} \rangle$ and superconducting gap values $\Delta_{i,j}$ are calculated self-consistently from Eq.(3.13) with the addition of a standard BCS singlet pairing term, i.e. from the Hamiltonian

$$H_{\text{SC}} \quad = \quad H_0 + \sum_{i,j} \left[\frac{\Delta_{i,j}}{2} (c_{i\uparrow}^\dagger c_{j\downarrow}^\dagger - c_{i\downarrow}^\dagger c_{j\uparrow}^\dagger) + H.c. \right], \tag{3.16}$$

where $\Delta_{i,j} = \frac{V_{\text{eff}}(i,j)}{2} \langle c_{j\downarrow} c_{i\uparrow} - c_{j\uparrow} c_{i\downarrow} \rangle$. The factors of 1/2 arises from the restriction to the singlet pairing channel.

Now we turn to a discussion of how the presence of a single impurity modulates the local change density and effective pairing strength with special attention on the effective attraction between electron on nearest neighbor sites, since this is the interaction responsible for a $d_{x^2-y^2}$ gap. We will consider three different species of impurities; point-like potential impurities which are either non-magnetic or magnetic, and an impurity that diminishes all hopping integrals to a specific impurity site of the lattice. We show how the pairing modulations lead to large enhancements of the gap close to the impurity site, and show how the characteristic shape of the pairing modulation near a strong impurity is reflected in the LDOS pattern observable by STM. We relate the pairing modulation to local changes in the spin susceptibility.

3.4 Point-like nonmagnetic impurity

In this section we will discuss the effects of placing a nonmagnetic impurity in an otherwise homogeneous system characterized by the nearest neighbor ($t = 1$) and next-nearest neighbor ($t' = -0.3$) hopping integrals and moderate values of onsite Coulomb repulsion $U \sim 2$, for which the system stays paramagnetic. The direct consequence of the impurity is visible from the changes in the local density of states throughout the system. In Fig. 3.5 we show how the density of states is suppressed at the impurity site, with the electrons moving primarily to the nearest neighbor sites. We plot also the density of states at an energy $E = 0.78$, which shows a distinct spatial pattern. We will return to this below. But first we describe the modulations of electron density and effective nearest neighbor attraction, which occurs in the vicinity of the impurity. In Fig. 3.6(a) we show the normal state electron density, $n_i = \langle n_{i\uparrow} + n_{i\downarrow} \rangle$ as a function of site i around a single nonmagnetic point-like impurity. In the single impurity case, we do not observe any induced local magnetization. This contrasts the situation of the superconducting case, and is due to the fact that the normal state does not have an impurity bound state near the Fermi level.[66, 67, 68, 69]

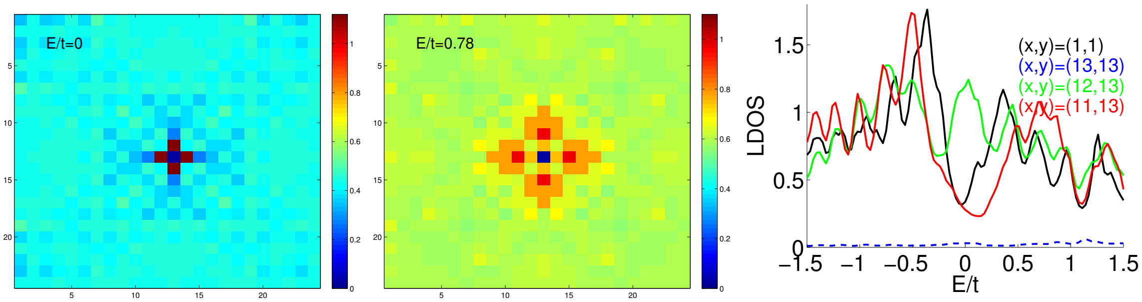

Figure 3.5: LDOS for all sites at energies $E/t = 0, 0.78$, for the 15 % hole doped system with $t' = -0.3$ and $U = 2.2$, as well as LDOS as a function of energy for the impurity site $(13, 13)$, neighbor site $(12, 13)$ and in the bulk $(1, 1)$.

The effective pairing interaction between the nearest neighbor sites is shown in Fig. 3.6(b), where we at each site show the average interaction to the four nearest neighbors:

$$V_{\mathrm{sc}}(i) = \frac{1}{4}\sum_j V_{\mathrm{eff}}(i,j), \qquad j \in \{i \pm \hat{x}, i \pm \hat{y}\} \tag{3.17}$$

It is seen that the effective pairing interaction is suppressed at the impurity site, but enhanced on a quartet of small regions close to the impurity. The response of the system to a perturbation is dominated by the peaks in the homogeneous susceptibility, although because the perturbation is space dependent all wave vectors are coupled. The strength of the pairing interaction is given by the real part of V_{eff} (Eq. (3.12)) at $\omega = 0$. Note that since we are restricted to the paramagnetic phase, there is no difference between the longitudinal and transverse susceptibility. In the present band structure of 15 % hole doping, the real part of the spin susceptibility in a homogeneous system displays a plateau around (π, π). The corners of this plateau is a quartet of peaks at incommensurate wave vectors $\mathbf{Q} + \Delta\mathbf{q}$, where $\mathbf{Q} = (\pi, \pi)$ and $\Delta\mathbf{q} \simeq (\pm 0.5\pi, 0), (0, \pm 0.5\pi)$. The susceptibility plot of Fig. 3.6(c) is obtained with a larger resolution, since it is calculated for the homogeneous system, and suggests that $\Delta\mathbf{q}$ is slightly smaller. However, in real space we are limited by a poorer resolution and only rough estimates for the extension of the

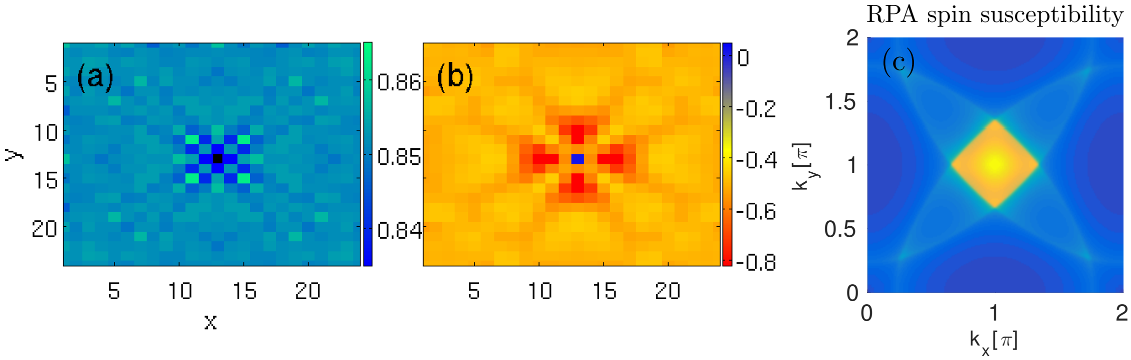

Figure 3.6: (a) Local charge density n_i in the normal phase prior to calculation of the effective pairing interaction. For the results presented here the parameters are: $U = 2.2$, $t' = -0.3$ (all energies are given in units of t) and doping $x = 0.15$. A strong point-like nonmagnetic impurity ($V_{\mathrm{imp}} = 10$) is situated at site $(x_{\mathrm{imp}}, y_{\mathrm{imp}}) = (13, 13)$. (b) Effective pairing interaction between nearest neighbors for the same system as in (a). For each site the average potential to the four nearest neighbors is plotted. (c) High-resolution plot of the RPA spin susceptibility for $t' = -0.3$ and 15 % hole doping.

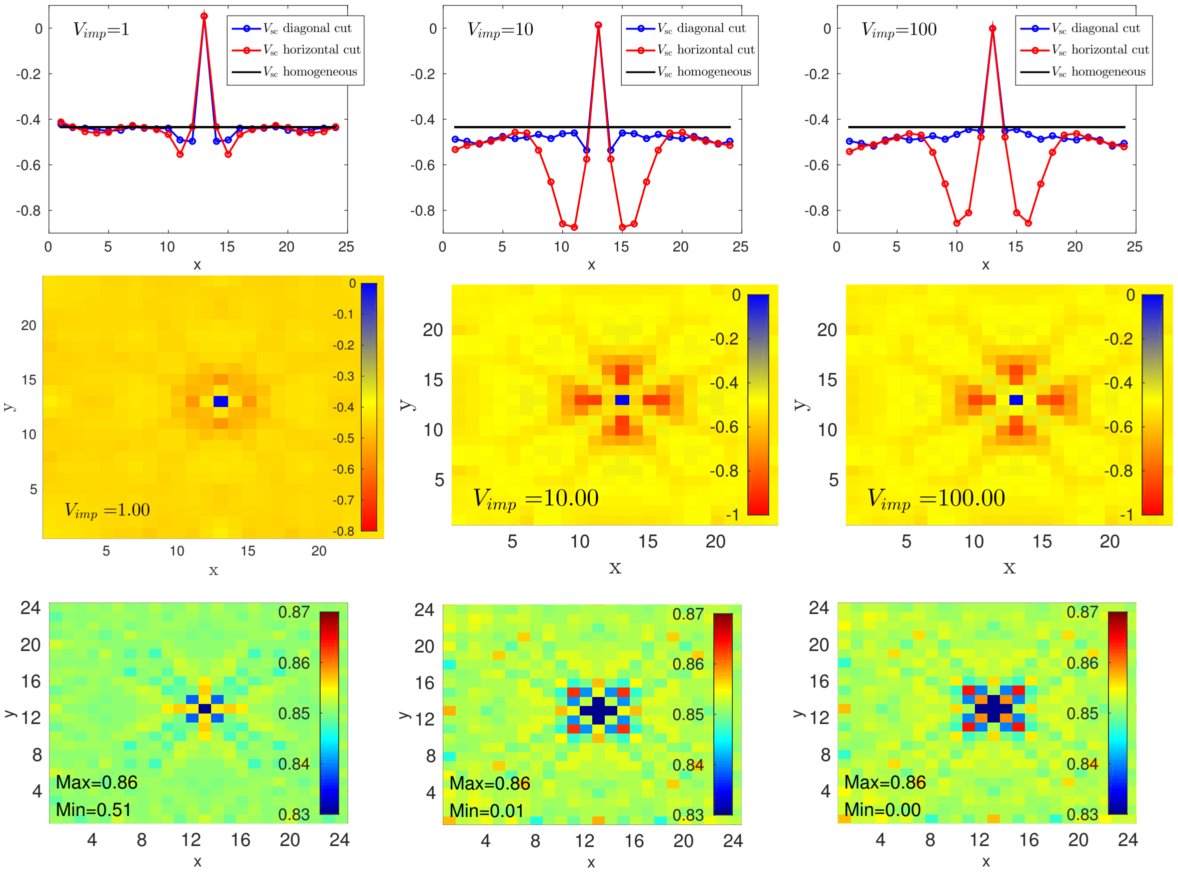

Figure 3.7: (**First and second row:**) Modulation effective nearest neighbor pairing for three different impurity strengths ($V_{imp} = 1, 10, 100$) of a non-magnetic impurity in a system with $t' = -0.3$, $U = 2.2$, and 15 % hole doping. Note the different color scale for the weak impurity case. (**Third row:**) Local density of states in the three cases.

peak plateau can be made. We relate the spatial modulation of the nearest neighbor pairing shown in Fig. 3.6(b) to $\mathbf{\Delta q}$ which roughly is 1/4 of a reciprocal lattice unit $\frac{2\pi}{a}$. Therefore this structure of the susceptibility is expected to give rise to the quartet of peaks at roughly four lattice spacings from the impurity site oriented along the nearest neighbor bonds, as observed in Fig. 3.6(b). Higher resolution calculations is likely to give a slightly larger extension of the real space enhancement structure. The extension of the modulation is primarily a feature of the underlying band, and not very dependent the strength of the impurity V_{imp}. This is shown in Fig. 3.7, where the modulation is plotted for three different impurity strengths. The magnitude of the pairing modulation *is*, however, dependent on the impurity strength and as seen from the middle and right-most figure in Fig. 3.7 the potential enhancement is saturated for an impurity strength of $V_{imp} = 10$. This is tied to the fact that the local density modulation does almost not change from the strong impurity case of $V_{imp} = 10$, to the "infinite" impurity strength case of $V_{imp} = 100$, the latter corresponding to completely blocking any hopping onto the impurity site.

In the spatially inhomogeneous system, the effective chemical potential is site and spin dependent. For spin up electrons, the effective chemical potential is defined as $\mu_{\mathrm{eff,i},\uparrow} = \mu - U\langle n_{i\downarrow}\rangle$ and visa versa for spin down electrons. If no magnetic order is present, as in the present case, the effective chemical potential

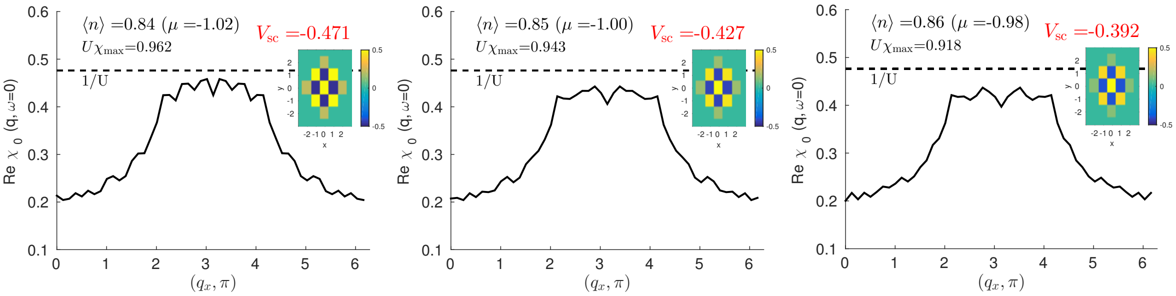

Figure 3.8: Susceptibility of the homogeneous system, $\chi(q_x, \pi)$ at three different filling levels, $\langle n \rangle = 0.84, 0.85, 0.86$ with corresponding spatially homogeneous chemical potential values of $\mu = -1.02, -1.00, -0.98$, respectively. In the three different filling cases, the corresponding real space pairing interaction for the twelve nearest neighbors is shown in the inset. The dominating interactions are a large onsite repulsion, a nearest neighbor attraction V_{sc} (the value is stated explicitly in red in the figures), and the next-nearest neighbor repulsion, which is of the same order of magnitude as V_{sc}, but *repulsive*. Notice that the smallest filling level, $\langle n \rangle = 0.84$, which corresponds to the smallest chemical potential gives the largest nearest neighbor attraction. This is caused by a rise in the susceptibility plateau, due to the proximity of the van Hove singularity, which is located at $\mu_{vH} = -1.20$.

is simply *site-dependent*. Local changes in the effective chemical potential arising from the density mean field, i.e. $U\langle n_{i\sigma}\rangle$ in Eq. (3.13), will cause the local structure of the pairing potential through the spin susceptibility. A larger occupation number compared to the average occupation $\langle n \rangle$ at one site i gives rise to an effectively smaller chemical potential at this site. At the same time, the neighboring sites will usually display the opposite, i.e. smaller occupation number than the average and thus a larger chemical potential. Since we are primarily concerned with a quantity that connects a site with its neighboring sites, namely the nearest neighbor effective attraction (which we call V_{sc}), it is hard to give a simple picture where we relate the observations to the homogeneous susceptibility. We will nevertheless illustrate how a hole doped *homogeneous* system with a fixed value of t' and U behave for different filling levels in order to get a hint for the underlying reason for the local pairing enhancement. In the simplest case of $t' = 0$, approaching the half filled system, i.e. $\mu = 0$, will cause an increase in the (π, π) peak as the Stoner instability of commensurate antiferromagnetic order is approached $(URe\chi_0(\mathbf{q}) \to 1)$. For the hole doped system this means that a larger chemical potential would give an increase the pairing interaction, i.e. the largest pairing for small hole dopings compared to large hole dopings. Naïvely, one could expect the same thing to happen for finite t'. However, another effect is at play in this case, which is related to the discussion in Chap. 2, section 2.8. For $t' = -0.3$ the dominating structure of the spin susceptibility is a broad plateau around (π, π), as shown in Fig. 3.6 (c). In this band, the van Hove singularity is located at $\mu_{vH} = -1.2$, and when the hole doping is such that $\mu \to \mu_{vH}$, $(\langle n \rangle_{vH} = 0.73)$, an increase of the plateau arises due to the proximity of the van Hove singularity. This is illustrated in Fig. 3.8. This is in fact quite opposite to the aforementioned effect of the proximity to a SDW instability close to half filling, since the pairing actually increases as the hole doping is *increased*. This trend was also illustrated for the $t' = -0.35$ band in the homogeneous system discussed in Chap. 2 section 2.7, where the $d_{x^2-y^2}$ solution monotonically increased upon increasing the hole doping, until the $\mathbf{q} = (0, 0)$ peak of the van Hove density causes an abrupt decrease of the singlet superconductivity. In the spatially inhomogeneous system, a local increase of the occupation number leads to an decrease of the chemical potential locally through $\mu_{\text{eff}} = \mu - U\langle n_{i\downarrow}\rangle$. In the discussion of the homogeneous system above, we saw that a decrease of the chemical potential leads to a larger pairing in the $t' = -0.3$ band. This leads us to speculate a trend towards increased pairing V_{sc} at sites with a larger occupation number compared to the bulk, where $\langle n \rangle = 0.85$. For the weak impurity case $(V_{imp} = 1)$ this trend is visible, see Fig. 3.7 (left column); note that the largest local occupation is at the sites $(0, \pm 2)$ and $(\pm 2, 0)$ away from the impurity site, and these coincide with the positions of the largest pairing interaction. However, as these sites are surrounded by sites with a locally larger effective chemical potential, the picture is not that simple. Especially for stronger impurities, the local density modulation becomes more complex, and in this case it is even harder to make a simple connection from the density modulations to the pattern of the effective pairing attraction. What we can do is to make a local Fourier transform of the site dependent spin susceptibility as defined in Eq. (3.15). Thereby we obtain the picture shown in Fig. (3.9), where the spatially-dependent variations in the pairing interaction is simply related to the (π, π) peak plateau of the bare transverse spin susceptibility. We Fourier transform the real space susceptibility to obtain $\chi_{\uparrow\downarrow}(\mathbf{q}, \mathbf{r}_i)$ for all sites r_i of the lattice. Hereby we map out the change in the magnitude of the susceptibility plateau near $\mathbf{Q}$ as a function of site $\mathbf{r}_i$. To account for the broadening of the peak and to minimize finite-size effects, we average over a region containing $\mathbf{Q}$ and the eight closest q-values around $\mathbf{Q}$ to obtain $\langle\chi^0_{\uparrow\downarrow}(\mathbf{Q}, \mathbf{r}_i)\rangle$. The result of this procedure is given in Fig. 3.9. It is seen that due to local variations in the bare transverse spin susceptibility, the quartet of points with enhanced pairing in Figs. 3.6(b) and 3.10(d,f) are characterized by being locally closer to the Stoner instability $U\chi^0_{\uparrow\downarrow}(\mathbf{Q}) \to 1$ than any other sites in the system. This agrees with the more hand waving discussion which relates the local susceptibility changes to the chemical potential dependence of the homogeneous spin susceptibility given above. Specifically, charge density variations due to an impurity act to tune the system closer to the Stoner instability locally which results in the pairing enhancements in the neighboring regions of the impurity.

Now we proceed with a calculation of the superconducting singlet gap in real space, taking into account effective interactions between the twelve nearest neighbor sites j around each site i in $V_{\text{eff}}(i,j)$. Longer range effective interactions are negligible. With the effective pairing interaction given in Eq.(3.12), we can calculate self-consistently the densities $\langle n_{i\sigma}\rangle$ and the superconducting d-wave order parameter $\Delta_{i,j}$ from H_{SC}, see Eq.(3.16). The resulting spatial structure of the density modulations and the superconducting gap variations are shown in Fig. 3.10(b,d). The superconducting order parameter is averaged over the four nearest neighbor sites $\Delta_i = \frac{1}{4}[\Delta_{i,i+\hat{x}} + \Delta_{i,i-\hat{x}} - \Delta_{i,i+\hat{y}} - \Delta_{i,i-\hat{y}}]$. For comparison, we also calculated the densities and the d-wave order parameter in a system containing the same impurity, but with a homogeneous pairing potential calculated from a clean system with the same parameters, giving a nearest neighbor pairing interaction $V_{\text{sc}} = -0.43$. The result is shown in Fig. 3.10(c), where it is seen that no enhancement of the d-wave gap is present, as opposed to the case of spin-fluctuation mediated pairing (Fig. 3.10(d)), where the d-wave gap is locally enhanced and the spatial structure is similar

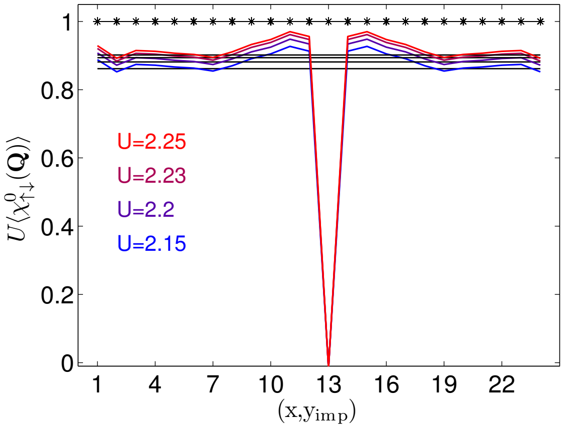

Figure 3.9: Average of $U\chi^0_{\uparrow\downarrow}(\mathbf{Q})$ around $\mathbf{Q} = (\pi, \pi)$ for different values of U as a function of site $\mathbf{r}_i = (x, y_{\text{imp}})$. Black lines are $U\langle\chi^0_{\uparrow\downarrow}(\mathbf{Q})\rangle$ for a homogeneous system whereas colored lines are for systems with a nonmagnetic impurity at $(x_{\text{imp}}, y_{\text{imp}}) = (13, 13)$.

to the structure of the effective pairing potential from Fig. 3.6(b). Note that the scales of the pairing interaction V_{eff} and superconducting gap Δ modulations are similar. As discussed above, the spatial scale of the modulation of the pairing interaction is determined by the extension of the peak plateau around $\mathbf{Q} = (\pi, \pi)$ in the real part of the full susceptibility. It is of the order of a unit cell spacing a. However, calculation of the susceptibility with higher resolution as shown in Fig. 3.6 (c) suggests that the extension is probably slightly larger than a with improved resolution, and the extension is probably slightly underestimated. In the paramagnetic system, the bare susceptibility is insensitive to the strength of U. In our calculations we have used quite large values of U, and this gives an artificially large gap. However, this does not affect the spatial structure of the enhanced gap around the impurity as illustrated in Fig. 3.4 which is confined to the close vicinity of the impurity also in the case of smaller U, i.e. smaller gap magnitudes. The LDOS is suppressed at the impurity site both in the case of a constant effective interaction and in the case of spin-fluctuation mediated pairing, see Fig. 3.10(e,f). However, whereas the LDOS in the case of constant effective interaction is roughly constant for all sites away from the impurity the picture is different when the pairing interaction is due to spin fluctuations. In the latter case, we find significant LDOS enhancements at energies close to the gap value ($\Delta_{max} \simeq 4 \cdot 0.19$) at the same quartet of real space regions seen in Figs. 3.6(b) and 3.10(d).

From Fig. 3.10(d) it is clear how the local enhancement effect on the nearest neighbor pairing interaction discussed previously bears over to the the superconducting gap, which exhibits a local maximum of the superconducting gap at the same sites around the impurity site. In Fig. 3.12 we show how this maximum gap value depends on both the strength of the Coulomb interaction U and the impurity potential V_{imp}. For reference, we have plotted the gap in a homogeneous system which is also enhanced upon increased U. This effect arises simply from the singularity in the RPA susceptibility. Since we tune the

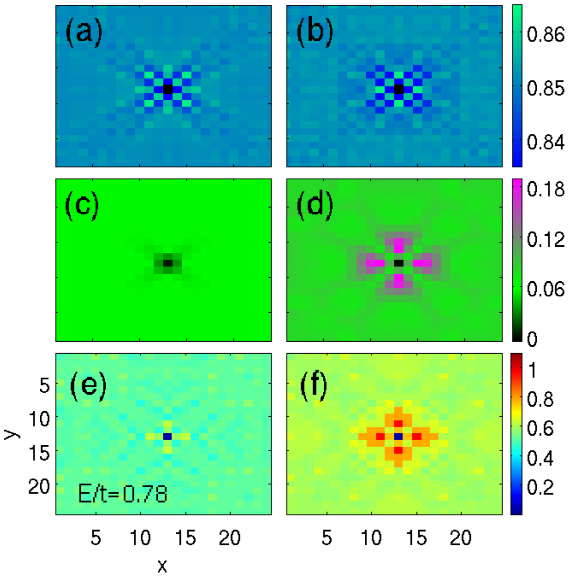

Figure 3.10: (a) Local charge density n_i in a system with a strong nonmagnetic impurity ($V_{\text{imp}} = 10$) and a spatially homogeneous superconducting pairing potential $V_{\text{eff}} = -0.43$. Parameters: $U = 2.2$, $t' = -0.3$ and doping $x = 0.15$. (b) Same as (a) but in the case of the spatially inhomogeneous spin-fluctuation mediated pairing potential $V_{\text{eff}}(i, j)$ from Fig. 3.6(b). (c,d) Local superconducting d-wave order parameter corresponding to the two cases in (a) and (b), respectively. (e,f) Local density of states at energy $E = 0.78$ (close to maximum gap value) corresponding to the two cases in (a) and (b), respectively.

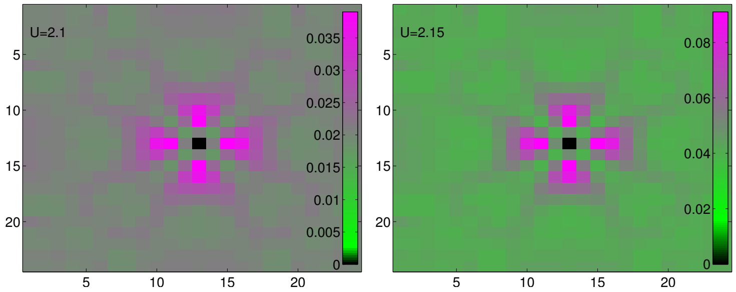

Figure 3.11: Local gap plots Δ_i for two different values of $U = 2.10$ (left) and $U = 2.15$ (right). $t' = -0.3$ and 15 % hole doping. Note the different color scale in the two cases.

system towards the singularity from below in the paramagnetic phase, it is the last term in the effective interaction of Eq.(3.12) which is the most important. In the system containing a single impurity, the gap is strongly enhanced as was shown in Fig. 3.12. The local structure of the gap enhancement is similar for a strong and a weak impurity as seen from the inset in Fig. 3.12 which shows a profile of the d-wave gap through the impurity site. However, the enhancement is much more pronounced in the strong impurity case, as was shown also in Fig. 3.7.

3.5 Point-like magnetic impurity

If the point-like impurity is magnetic, i.e. act as an attractive potential for e.g. spin down electrons, while it is a repulsive potential potential for spin up electrons, local magnetism around the impurity site is induced. This changes the local spin susceptibility such that $URe\chi_0 > 1$ for some sites. This effectively causes a break down of the usual nearest neighbor attraction due to a change of sign in the RPA susceptibility. In a system where long range magnetic order is developed, the Goldstone mode associated

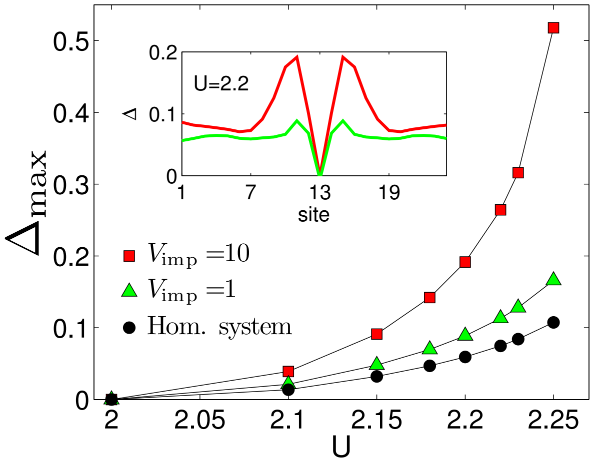

Figure 3.12: Maximum of the superconducting d-wave gap, $\Delta_{\max}$, as a function of Coulomb interaction U for point-like nonmagnetic impurities and a homogeneous system. For all runs the system displays no antiferromagnetic order, since the critical U in this system is $U_{c2} > 2.4$. The inset shows the profile of the d-wave gap as a function of site (x, y_{imp}).

with breaking of spin rotation symmetry develops as transverse (spin-orientational) fluctuations. In this case the spin susceptibilities must be calculated for the longitudinal and transverse channel invoking the presence of a new magnetic order parameter. In this case the effective superconducting pairing is not given directly by the RPA susceptibility, which would suggest an incorrect divergent pairing contributions in the transverse channel. This is an extended discussion which we postpone to Chap. 5 Here we limit ourselves to the single impurity case, where only a small puddle of local magnetization is developed. Prior to the calculation of the effective pairing interaction, the spin densities are calculated self-consistently for a system containing a single point-like magnetic impurity.

In Fig. 3.13 (a-d) the total electron density $\rho_i = \langle n_{i\uparrow}\rangle + \langle n_{i\downarrow}\rangle$ is shown as a function of lattice site. Local density variations occur close to the impurity site, and a small increased charge density is evident at the impurity site caused by a finite magnetization. In Fig. 3.13 (e-h) we show the induced magnetization, $m_i = \langle n_{i\uparrow}\rangle - \langle n_{i\downarrow}\rangle$, as a function of lattice site. Local antiferromagnetism is induced around the impurity, and is most extended because of smaller magnetization induced by weaker impurity potentials.

The effective superconducting pairing interaction is shown in Fig. 3.13 (i-l). The interaction is calculated in real-space from the expression given in Eq. (3.12). We see an enhancement of the pairing interaction at sites around the impurity in a pattern which is very similar to the non-magnetic impurity case discussed in the previous section.

In the limit of very strong magnetic impurities, see Fig. 3.13(h), local antiferromagnetism is essentially confined to the impurity site, and still we find significant local gap enhancement as seen from Fig. 3.13(l). This is consistent with the findings that a local enhancement of the pairing interaction is achieved even though no local antiferromagnetism is induced, i.e. the enhancement effect is not dependent on induced antiferromagnetism and it is local variations of spin densities rather than a difference between spin densities that causes the effect.

However, locally induced magnetism around weak impurities will cause an enhancement of the effect,

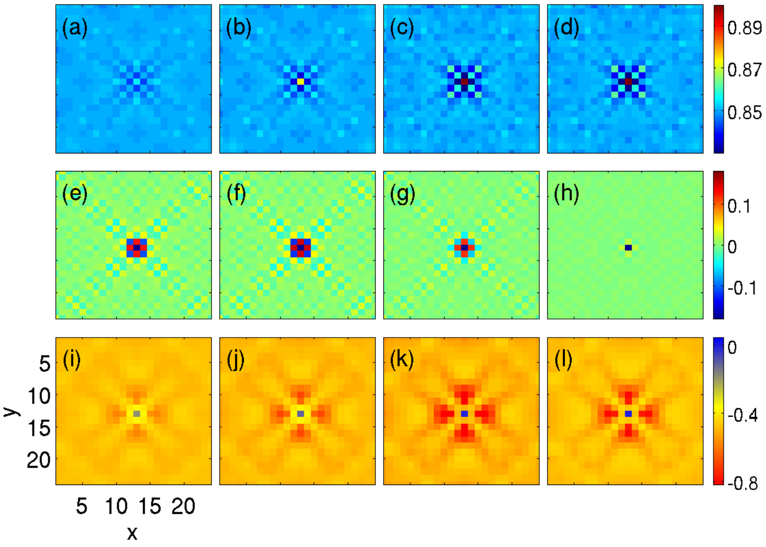

Figure 3.13: (a-d) Local charge density of the normal phase. An impurity is positioned at site $r_{\text{imp}} = (13, 13)$ and the impurity strengths are in units of the nearest neighbor hopping constant t: (a) $V_{\text{imp}} = 0.5$, (b) $V_{\text{imp}} = 1$, (c) $V_{\text{imp}} = 10$ and (d) $V_{\text{imp}} = 100$. For the results presented here the system size is 24×24 and the parameters are: $U = 2.2$, $t' = -0.3$ in units of t, and the doping is $x = 0.15$. In panels (e-h) we show the magnetization, and in (i-l) the average local pairing interaction between nearest neighbors, $V_{\text{sc}}(i) = \frac{1}{4}\sum_j V_{\text{eff}}(i,j)$, $j \in \{i \pm \hat{x}, i \pm \hat{y}\}$, for the same parameters as in (a-d).

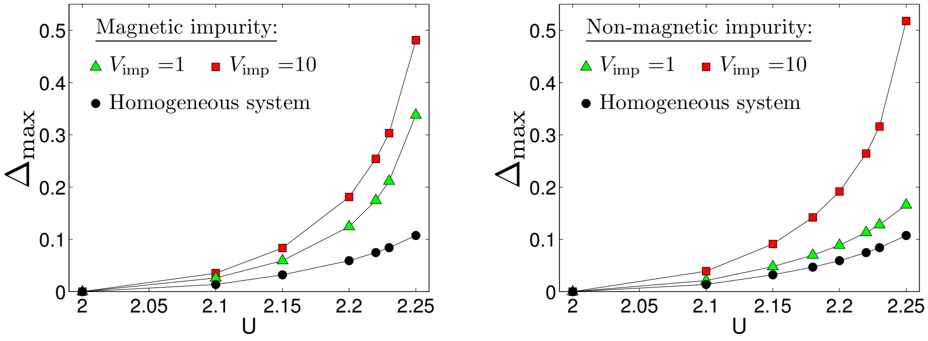

Figure 3.14: Left: Maximum superconducting gap value as a function of Coulomb interaction strength, U, for point-like magnetic impurities of strengths $V_{\text{imp}} = t, 10t$. Also the gap value in the homogeneous system is shown for reference. Right: Maximum superconducting gap value as a function of Coulomb interaction strength, U, for point-like non-magnetic impurities of strengths $V_{\text{imp}} = t, 10t$.

as visible from Fig. 3.14 Including the effective pairing interaction shown in Fig. 3.13 (i-l), we calculate the superconducting gap self-consistently by diagonalization of the mean-field Hamiltonian given in Eq. (3.16). As apparent from Fig. 3.15 (a-h), the total density arrangement around the impurity is roughly unchanged while more antiferromagnetism is induced around the strongest impurity. The superconducting d-wave order parameter is locally enhanced, see Fig. 3.15 (i-l), and the real-space structure

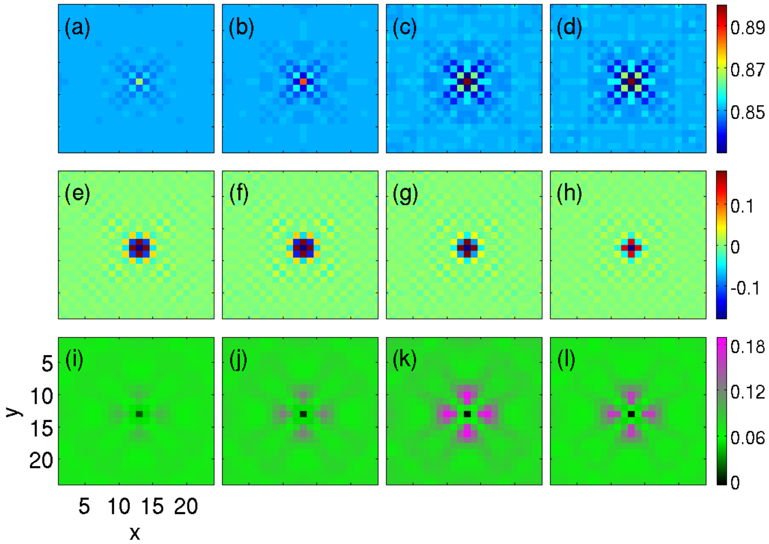

Figure 3.15: (a-d) Local charge density in the superconducting phase. An impurity is positioned at site $r_{\text{imp}} = (13, 13)$ and the impurity strengths are in units of the nearest neighbor hopping constant t: (a) $V_{\text{imp}} = 0.5$, (b) $V_{\text{imp}} = 1$, (c) $V_{\text{imp}} = 10$ and (d): $V_{\text{imp}} = 100$. For the results presented here the system size is 24×24 and the parameters are: $U = 2.2$, $t' = -0.3$ in units of t and doping is $x = 0.15$. (e-h) Local magnetization for the same impurities and parameters as (a-d). (i-l) Magnitude of the local d-wave superconducting order parameter $\Delta_i = \frac{1}{4}[\Delta_{i,i+\hat{x}} + \Delta_{i,i-\hat{x}} - \Delta_{i,i+\hat{y}} - \Delta_{i,i-\hat{y}}]$ for the same impurities and parameters as (a-d).

resembles that of the local pairing potential. The enhancement of the superconducting gap thus occurs at the borders of regions with spin density modulations and the enhancement effect competes locally with antiferromagnetic order. It appears that there exists some optimal intermediate impurity strength at which the gap enhancement becomes strongest, Fig. 3.15 (k).

3.6 Impurity with reduced hopping constants

Finally we turn to the third type of impurity characterized by all hopping constants onto the impurity site being reduced by a certain percentage. In the extreme limit of 100% reduction, we obtain results similar to the case of a strong nonmagnetic potential scatterer as expected (compare e.g. Fig. 3.10(d) and Fig. 3.16(d)). Both magnitude and local structure of the superconducting d-wave gap is similar in these two cases, and in both instances, there is no induced local antiferromagnetic order. In the intermediate regime, however, where the reduction is less than 100%, we find a different local structure of the d-wave gap enhancement, since the enhancement of the local pairing interaction as well as the d-wave gap is maximal *at the impurity site*. As an example, we show in Fig. 3.16(a,c) the effect of reducing the hopping elements by 20%. In this case, the local density and magnetic order is as shown in Fig. 3.17, i.e. weak local antiferromagnetism is induced. A remarkable difference of the local density modulation in this case compared to the results of the point-like impurities, is that the local filling level is smaller than the bulk for a small puddle of sites around the impurity as a consequence of the reduced hopping, see the region of blue-colored sites in Fig. 3.17 (right). Thus, we observe a reduction of $\langle n \rangle$ for a collection of neighboring sites insted of the more checkerboard-like density pattern seen in the case of point-like impurities. This modulation causes enhancement of the (π, π) plateau of spin susceptibility at the impurity site seen from the local Fourier transform of the transverse spin susceptibility shown in Fig. 3.16(e). Note that for the effective pairing interaction shown in Fig. 3.16(a), the spatial structure of the effective interaction and the size of the amplitude modulations are closely comparable to the phenomenological values used in Ref. [45] to model the STS gap variations in optimally doped $Bi_2Sr_2CaCu_2O_8$.

Lastly, we mention that a hopping impurity with increased hopping integrals to the impurity site gives a local increase in the electron density, no magnetic order, and no enhancement of the superconducting gap at or close to the impurity site compared to the bulk.

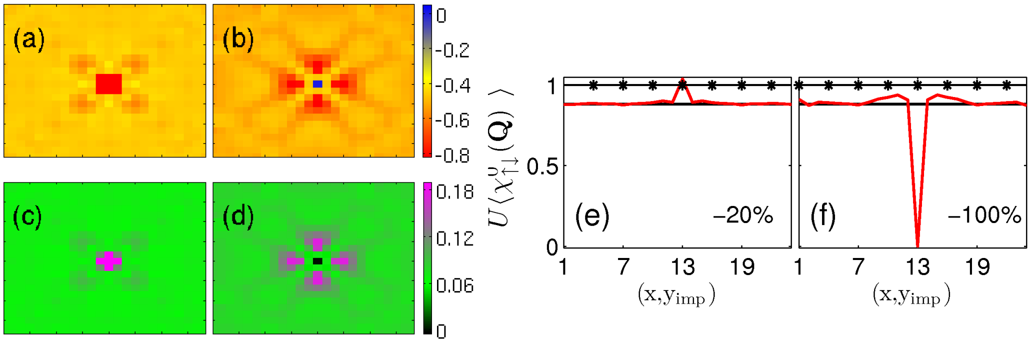

Figure 3.16: (a,b) Effective pairing interaction between nearest neighbors. For the results presented here the parameters are: $U = 2.2$, $t' = -0.3$, doping $x = 0.15$. A reduced hopping impurity of strength -20 % (a) and -100 % (b) is situated at site $(x_{\rm imp}, y_{\rm imp}) = (13, 13)$. (c,d) Local superconducting d-wave order parameter for the two impurity cases. (e,f) Average of $U\chi^0_{\uparrow\downarrow}(\mathbf{Q})$ around $\mathbf{Q} = (\pi, \pi)$ as a function of site $\mathbf{r}_i = (x, y_{\rm imp})$.

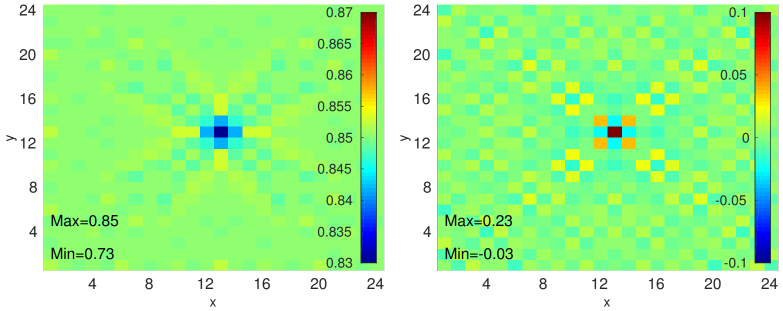

Figure 3.17: Local electron density (left) and local magnetic order (right) in the case of a reduced hopping impurity of strength -20 % for $U = 2.2$, $t' = -0.3$, doping $x = 0.15$.

3.7 Conclusions

We have found that different types of impurities cause local enhancements of the singlet $d_{x^2-y^2}$ superconductivity in a 15 % hole doped system with a finite next-nearest neighbor hopping intergral, $t' = -0.3$. The effect is present both with and without the presence of locally induced magnetic order, and can therefore be ascribed to local changes in the chemical potential. The local structure of the gap enhancement depends on the type of impurity as well as the band, since it is closely related to the spin susceptibility of bulk homogeneous system. We have related the gap modulations to the spin susceptibility by a detailed comparison of the gap pattern with the local Fourier transform. We have discussed the observation of such enhancement effects in relation to STS measurements on the surface of cuprate superconductors.

The results of the local gap enhancements found in this paper gives rise to a number of additional questions for future studies. First, is the LDOS within the present formalism from more realistic many-impurity simulations consistent with the experimental STS data? As shown by Nunner *et al.*[45] the positive correlation between dopant atoms and large gap regions will certainly exist with the presented scenario, but the LDOS evolution with doping, where pseudogap regions become dominant in the underdoped regime cannot be captured within this weak-coupling approach. In addition, several unsolved LDOS issues remain regarding the origin of the so-called extinction of impurity resonances near strong onsite impurity potentials in large-gap regions[73].

In this chapter we have not adressed the situation of a system with many impurities. The reason is that interference of the impurities causes long range density modulations, which makes the system more prone to long range magnetic order. The current formulation of the real space pairing mechanism does not hold in the spin ordered state. The simple expression that was derived in Eq.(3.12) predicts a singularity in the effective pairing interaction as the system develops long range antiferromagnetic order, and the formalism of spin-fluctuation mediated pairing must be reformulated to take into account the presence of a new (magnetic) order parameter. This will be the focus of chapter 5, which is devoted solely a treatment of a *homogeneous* SDW system. The more general formalism in which we allow for both long range magnetic order and spatial inhomogeneity is still not fully established. Such a model would be able to address questions like; what are the thermodynamic consequences of the local enhancements of the gap found above? In particular one might expect a non-trivial evolution of the residual resistivity $\Delta\rho$ and T_c suppression with increasing disorder concentrations. The slow rate of T_c suppression relative to $\Delta\rho$ in the case of strong scatterers such as Zn in cuprates has never been satisfactorily explained, but has been attributed to correlation effects[75]. It will be interesting to find whether inhomogeneous defects or magnetic structures can enhance the critical temperature, as was found in purely phenomenological approaches[76]. This interesting question will be the topic of a future study. The next two chapters will establish some of the prerequisites for this.

Another aspect of the effective pairing interaction which was not discussed in this chapter is the feedback effect on the pairing interaction from superconductivity. We evaluated the pairing vertex only once in the normal phase, and thus the effective pairing vertices did not take into account the presence of anomalous propagators, which appear in the superconducting phase. In a homogeneous system the feedback from superconductivity on the spin-fluctuation mediated pairing was discussed by Pao and Bickers [77], and the feedback effect was dubbed the "pair-weakening effect", since the presence of superconductivity suppresses the spin susceptibilities without altering the momentum space structure. Therefore the gap results remain $d_{x^2-y^2}$ as in the case without feedback, but with smaller gap magnitudes. In the next chapter, we discuss the feedback effect both in the case of a homogeneous system, as established in Ref. [77] and [78] and formulate the feedback effect in real space, relevant for inhomogeneous systems.

Chapter 4

Superconductivity feedback effects on the effective pairing interaction

In this chapter, we derive the feedback effects arising from superconductivity on the spin-fluctuation mediated pairing interaction. The expression is valid in the paramagnetic phase only. First we derive the pairing vertex with feedback effects in a homogeneous system, and thereafter we turn to the feedback effects on the local pairing interaction.

4.1 The pair weakening effect

If the pairing interaction is of electronic origin as in the case of spin fluctuations, then the transition to a superconducting phase is expected to influence the pairing mechanism, because superconductivity affects the spin susceptibilities. Therefore it is likely to find a feedback effect from superconductivity, which is much stronger than in the phonon-driven superconductors, where the phonon modes should be less affected by superconductivity. Due to Migdal's theorem, we know that the electron-phonon coupling is sensitive to the presence of superconductivity through the effective mass of the electrons, but this effect should not be as strong as in the case where electronic modes are responsible for the pairing glue. Now, the question is how this feedback effect would then change the pairing interaction if pairing occurs through purely electronic spin fluctuations. In the case of a homogeneous and paramagnetic system, this question was adressed already in the beginning of the 90ies, and the form of spin-fluctuation mediated pairing including feedback from superconductivity was reported by Pao and Bickers [77] and Monthoux and Scalapino [78]. Superconductivity sets in upon cooling when the spin susceptibility develops signatures of a closelying magnetic instability. This susceptibility structure supports the development of an unconventional superconducting phase, with the gap symmetry closely related to the structure of the spin susceptibility as discussed in detail in chapter 2. When the system enters the superconducting state, magnetic order is prevented because the superconducting order hinders a growth of the spin susceptibility. Since the superconducting pairing is mediated by the spin susceptibility, this naturally affects the superconducting order below T_c. If there is not only a stagnation of the susceptibility, but in fact a decrease of the spin susceptibility peak for $T < T_c$, this leads to a reduction of the zero temperature gap magnitude compared to the simpler model in which the spin susceptibility is calculated in the normal non-superconducting system. This is the so-called pair-weakening effect as first described in Ref. [77].

The aim of this chapter is to derive an expression for the effective pairing including feedback from superconductivity which is valid in an inhomogeneous system. First we derive the expression in the homogeneous system to compare with the result of Ref. [77]. We include higher order diagrams in U by bubble and ladder diagrams with the new possibility of anomalous propagators, which are non-zero in the superconducting phase. Having established the diagrammatic expansion behind the result stated in Ref. [77], we turn to our main goal, which is to derive an expression for the local pairing interaction including feedback effects relevant to the case of inhomogeneous systems. The questions are; is there a local pair weakening effect? And will this local pair weakening effect destroy the impurity enhancement of the local superconducting gap, reported in the previous chapter?

4.2 Feedback effects in a homogeneous and paramagnetic system

First we consider the expression for the effective spin-fluctuation mediated pairing which include feedback effects due to the presence of superconductivity in the homogeneous system. Compared to the original expression as stated in Eqs. (2.46) and (2.47), we now consider the presence of new propagators in the diagrammatic expansion of the pairing interaction. These arise due to the presence of superconductivity. The final expression is very similar to the form of the potential with no feedback effects included:

$$V_{\text{eff}}(\mathbf{k},\mathbf{k}') = U + \Big[\frac{3}{2}\frac{U^2\chi_0^s(\mathbf{k}-\mathbf{k}')}{1-U\chi_0^s(\mathbf{k}-\mathbf{k}')} - \frac{1}{2}\frac{U^2\chi_0^c(\mathbf{k}-\mathbf{k}')}{1+U\chi_0^c(\mathbf{k}-\mathbf{k}')}\Big] \tag{4.1}$$

The importance of the feedback effect is manifested in the definition of the susceptibilities:

$$\begin{aligned}\chi_0^{s,c}(\mathbf{q},i\omega_m) &= -T\sum_{\mathbf{k},n}[G(\mathbf{k}+\mathbf{q},i\omega_n+i\omega_m)G(\mathbf{k},\omega_n) \pm F^\dagger(\mathbf{k}+\mathbf{q},i\omega_n+i\omega_m)F(\mathbf{k},i\omega_n)] \\ &= -[G_\mathbf{q}G \pm F^\dagger_\mathbf{q}F] \end{aligned}\tag{4.2}$$

The susceptibilities are stated in short hand notation:

$$G_\mathbf{q}G = T\sum_{\mathbf{k},n}[G(\mathbf{k}+\mathbf{q},\omega_n+\omega_m)G(\mathbf{k},\omega_n) \quad \text{and} \quad F^\dagger_\mathbf{q}F = T\sum_{\mathbf{k},n}[F^\dagger(\mathbf{k}+\mathbf{q},\omega_n+\omega_m)F(\mathbf{k},\omega_n)] \tag{4.3}$$

In terms of the energy band and superconducting mean field, the spin and charge susceptibilities are given by:

$$\begin{aligned}\chi_0^{\mathrm{s/c}}(\mathbf{q};i\omega_n) &= \frac{1}{2}\sum_\mathbf{k}\Big[1+\frac{\xi_\mathbf{k}\xi_{\mathbf{k+q}} \pm \Delta_\mathbf{k}\Delta_{\mathbf{k+q}}}{E_\mathbf{k}E_{\mathbf{k+q}}}\Big]\frac{f(E_\mathbf{k})-f(E_{\mathbf{k+q}})}{i\omega_n-(E_\mathbf{k}-E_{\mathbf{k+q}})} \\ &+\frac{1}{4}\sum_\mathbf{k}\Big[1-\frac{\xi_\mathbf{k}\xi_{\mathbf{k+q}} \pm \Delta_\mathbf{k}\Delta_{\mathbf{k+q}}}{E_\mathbf{k}E_{\mathbf{k+q}}}\Big]\frac{f(E_\mathbf{k})+f(E_{\mathbf{k+q}})-1}{i\omega_n-(E_\mathbf{k}+E_{\mathbf{k+q}})} \\ &+\frac{1}{4}\sum_\mathbf{k}\Big[1-\frac{\xi_\mathbf{k}\xi_{\mathbf{k+q}} \pm \Delta_\mathbf{k}\Delta_{\mathbf{k+q}}}{E_\mathbf{k}E_{\mathbf{k+q}}}\Big]\frac{1-f(E_\mathbf{k})-f(E_{\mathbf{k+q}})}{i\omega_n+(E_\mathbf{k}+E_{\mathbf{k+q}})} \end{aligned}\tag{4.4}$$

We obtain a measure of the pairing strength by evaluating the susceptibilities at zero energy.

Note that in Eq. (B.1) we have stated the expression which is valid in the singlet channel only, where the internal sign of $\mathbf{k}$ and $\mathbf{k}'$ is optional, because the operator part of the Hamiltonian is even under $\mathbf{k} \to -\mathbf{k}$ and $\mathbf{k}' \to -\mathbf{k}'$ seperately. Therefore, in the following we have suppressed the internal structure of the momentum indices. However, if triplet pairing is to be considered, the derivation should be kept general and the susceptibility dependence on either $\mathbf{k}-\mathbf{k}'$ (bubble diagrams) or $\mathbf{k}+\mathbf{k}'$ (ladder diagrams) must be stated explicitly.

We show the diagrammatic expansion, which leads to the expression Eq. (4.1) for the effective pairing interaction. Expansion to fifth order is shown in appendix B. Below we show the expansion only for the diagrams which are third order in U. We draw the bubble diagrams and ladder diagrams with three diagram species included; those that consists of only normal Green's functions propagators, those with only anomalous propagators and lastly, those containing both normal and anomalous propagators. For

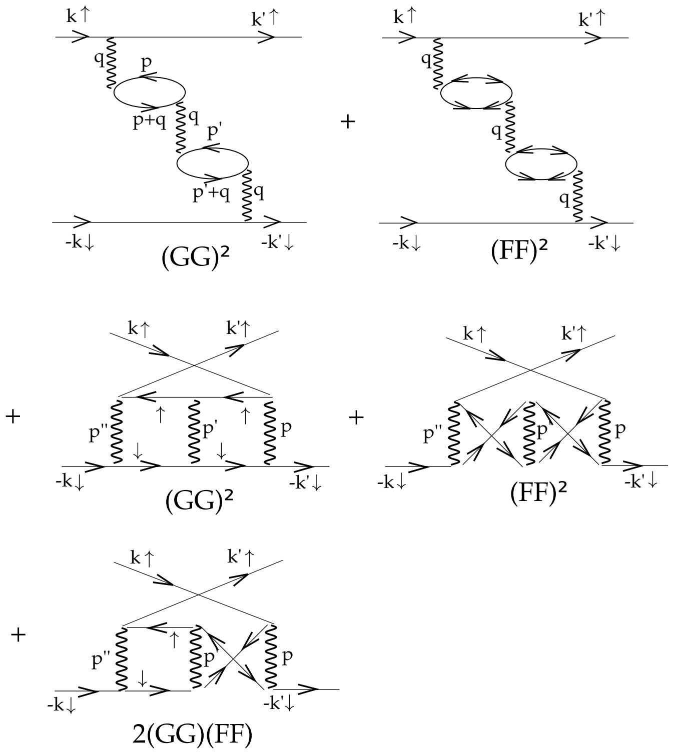

Figure 4.1: Diagrams to third order in U. Due to the restriction of an even number of normal bubbles, no mixed bubble diagrams are allowed.

all diagrams we are restricted to an even number of normal bubbles, due to the fact that U only connects opposite spin propagators. The third order diagrams are shown in Fig. 4.1.
First, the bubble diagrams give:

$$\begin{aligned} -V^{(3)}_{\mathrm{bub}}/(-U)^3 &= (-1)^2 \sum_{p} G(\mathbf{p}+(\mathbf{k}-\mathbf{k}'))G(\mathbf{p}) \sum_{\mathbf{p}'} G(\mathbf{p}'+(\mathbf{k}-\mathbf{k}'))G(\mathbf{p}') \\ &\quad + \sum_{\mathbf{p}} F^{\dagger}(\mathbf{p}+(\mathbf{k}-\mathbf{k}'))F(\mathbf{p}) \sum_{\mathbf{p}'} F^{\dagger}(\mathbf{p}'+(\mathbf{k}-\mathbf{k}'))F(\mathbf{p}'). \end{aligned} \tag{4.5}$$

For the normal ladder we get (note that $-\mathbf{k}' = -\mathbf{k}+\mathbf{p}''+\mathbf{p}'+\mathbf{p}$):

$$\begin{aligned} -V^{(3)}_{\mathrm{lad,norm}}/(-U)^3 &= \sum_{\mathbf{p},\mathbf{p}'} G(\mathbf{k}-\mathbf{p})G(-\mathbf{k}+\mathbf{p}''+\mathbf{p}')G(\mathbf{k}-\mathbf{p}-\mathbf{p}')G(-\mathbf{k}+\mathbf{p}'') \\ &= \sum_{\mathbf{p},\mathbf{p}'} G(\mathbf{k}-\mathbf{p})G(-\mathbf{k}+\mathbf{k}-\mathbf{k}'-\mathbf{p}-\mathbf{p}'+\mathbf{p}')G(\mathbf{k}-\mathbf{p}-\mathbf{p}')G(-\mathbf{k}+\mathbf{k}-\mathbf{k}'-\mathbf{p}-\mathbf{p}') \\ &= \sum_{\mathbf{p},\mathbf{p}'} G(\mathbf{p})G(-\mathbf{k}-\mathbf{k}'+\mathbf{p})G(\mathbf{p}-\mathbf{p}')G(-\mathbf{k}-\mathbf{k}'+\mathbf{p}-\mathbf{p}') \\ &= \sum_{\mathbf{p},\mathbf{p}'} G(\mathbf{p})G(-\mathbf{k}-\mathbf{k}'+\mathbf{p})G(\mathbf{p}')G(-\mathbf{k}-\mathbf{k}'+\mathbf{p}') \\ &= \sum_{\mathbf{p}} G(\mathbf{p}+(\mathbf{k}+\mathbf{k}'))G(\mathbf{p}) \sum_{\mathbf{p}'} G(\mathbf{p}'+(\mathbf{k}+\mathbf{k}'))G(\mathbf{p}'). \end{aligned} \tag{4.6}$$

For the anomalous ladder we get (note that now $-\mathbf{k}' - \mathbf{p}'' + \mathbf{p}' = -\mathbf{k} + \mathbf{p}$):

$$\begin{aligned}
-V^{(3)}_{\text{lad,anom}}/(-U)^3 &= \sum_{\mathbf{p},\mathbf{p}'} F^\dagger(\mathbf{k}-\mathbf{p})F(\mathbf{k}'+\mathbf{p})F^\dagger(\mathbf{k}-\mathbf{p}'')F(\mathbf{k}'+\mathbf{p}'') \\
&= \sum_{\mathbf{p},\mathbf{p}'} F^\dagger(\mathbf{k}-\mathbf{p})F(\mathbf{k}'+\mathbf{p})F^\dagger(\mathbf{k}-(\mathbf{p}'-\mathbf{p}+\mathbf{k}-\mathbf{k}'))F(\mathbf{k}'+\mathbf{p}'-\mathbf{p}+\mathbf{k}-\mathbf{k}') \\
&= \sum_{\mathbf{p},\mathbf{p}'} F^\dagger(\mathbf{k}-\mathbf{p})F(\mathbf{k}'+\mathbf{p})F^\dagger(\mathbf{p}-\mathbf{p}'+\mathbf{k}')F(\mathbf{p}'-\mathbf{p}+\mathbf{k}) \\
&= \sum_{\mathbf{p},\mathbf{p}'} F^\dagger(\mathbf{k}-\mathbf{p})F(\mathbf{k}'+\mathbf{p})F^\dagger(\mathbf{p}'+\mathbf{k}')F(-\mathbf{p}'+\mathbf{k}) \\
&= \sum_{\mathbf{p}} F^\dagger(\mathbf{p}+(\mathbf{k}+\mathbf{k}'))F(-\mathbf{p}) \sum_{\mathbf{p}'} F^\dagger(\mathbf{p}'+(\mathbf{k}+\mathbf{k}'))F(-\mathbf{p}') \\
&= \sum_{\mathbf{p}} F^\dagger(\mathbf{p}+(\mathbf{k}+\mathbf{k}'))F(\mathbf{p}) \sum_{\mathbf{p}'} F^\dagger(\mathbf{p}'+(\mathbf{k}+\mathbf{k}'))F(\mathbf{p}'). \qquad (4.7)
\end{aligned}$$

Lastly, the ladder diagram that contains both normal and anomalous propagators gives (note that $\mathbf{p}'' = \mathbf{p} - \mathbf{p}'$):

$$\begin{aligned}
-V^{(3)}_{\text{lad,mix}}/(-U)^3 &= \sum_{\mathbf{p},\mathbf{p}'} F^\dagger(\mathbf{k}-\mathbf{p})F(\mathbf{k}'+\mathbf{p})G(\mathbf{k}'+\mathbf{p}-\mathbf{p}')G(-\mathbf{k}+\mathbf{p}'') \\
&= \sum_{\mathbf{p},\mathbf{p}'} F^\dagger(\mathbf{k}-\mathbf{p})F(\mathbf{k}'+\mathbf{p})G(\mathbf{k}+\mathbf{p}-\mathbf{p}')G(-\mathbf{k}+\mathbf{p}-\mathbf{p}') \\
&= \sum_{\mathbf{p}} F^\dagger(\mathbf{k}-\mathbf{p})F(\mathbf{k}'+\mathbf{p}) \sum_{\mathbf{p}'} G(\mathbf{k}'+\mathbf{p}')G(-\mathbf{k}+\mathbf{p}') \\
&= \sum_{\mathbf{p}} F^\dagger(\mathbf{p}+(\mathbf{k}+\mathbf{k}'))F(\mathbf{p}) \sum_{\mathbf{p}'} G(\mathbf{p}'+(\mathbf{k}+\mathbf{k}'))G(\mathbf{p}'). \qquad (4.8)
\end{aligned}$$

The same expression as derived in Eq. (4.8) is obtained if we interchange the normal and anomalous propagators of the mixed ladder. In total we get from the diagrammatic expansion above:

$$\begin{aligned}
-V^{(3)}_{\text{eff}}/(-U)^3 &= -V^{(3)}_{\text{bub}}/(-U)^3 - V^{(3)}_{\text{lad,norm}}/(-U)^3 - V^{(3)}_{\text{lad,anom}} - 2V^{(3)}_{\text{lad,mix}}/(-U)^3 \\
&= (-1)^2 G_{(\mathbf{k}-\mathbf{k}')}G \cdot G_{(\mathbf{k}-\mathbf{k}')}G + F^\dagger_{(\mathbf{k}-\mathbf{k}')}F \cdot F^\dagger_{(\mathbf{k}-\mathbf{k}')}F \\
&\quad + G_{(\mathbf{k}+\mathbf{k}')}G_{(\mathbf{k}+\mathbf{k}')} \cdot G_{(\mathbf{k}+\mathbf{k}')}G_{(\mathbf{k}+\mathbf{k}')} + F^\dagger_{(\mathbf{k}+\mathbf{k}')}F \cdot F^\dagger_{(\mathbf{k}+\mathbf{k}')}F + 2F^\dagger_{(\mathbf{k}+\mathbf{k}')}F \cdot G_{(\mathbf{k}+\mathbf{k}')}G. \qquad (4.9)
\end{aligned}$$

Since we are only concerned with the singlet pairing expression, i.e. the Green's functions argument can be written as $\mathbf{k} - \mathbf{k}'$ instead of $\mathbf{k} + \mathbf{k}'$ and we have:

$$V^{(3)}_{\text{eff}}/U^3 = 2G_{(\mathbf{k}-\mathbf{k}')}GG_{(\mathbf{k}-\mathbf{k}')}G + 2F^\dagger_{(\mathbf{k}-\mathbf{k}')}FF^\dagger_{(\mathbf{k}-\mathbf{k}')}F + 2F^\dagger_{(\mathbf{k}-\mathbf{k}')}FG_{(\mathbf{k}-\mathbf{k}')}G. \qquad (4.10)$$

This agrees with the third order term derived from Eq. (B.1);

$$V^{(3)}_{\text{eff}} = U^3[2(G_{\mathbf{q}}G)^2 + 2(F^\dagger_{\mathbf{q}}F)^2 + 2(G_{\mathbf{q}}G)(F^\dagger_{\mathbf{q}}F)] \qquad (4.11)$$

Note that all terms have the same overall sign. This is because all fermion loops enter as a product of two, whereby the signs cancel. In the fourth order expansion, the different susceptibilities come with different weights as shown explicitly in appendix B. Here we only draw the relevant diagrams in Fig. 4.2 and show the final expression:

$$V^{(4)}_{\text{eff}} = -U^4[(G_qG)^3 + 2(F^\dagger_qF)^3 + 6(G_qG)^2(F^\dagger_qF) + 3(G_qG)(F^\dagger_qF)^2], \qquad (4.12)$$

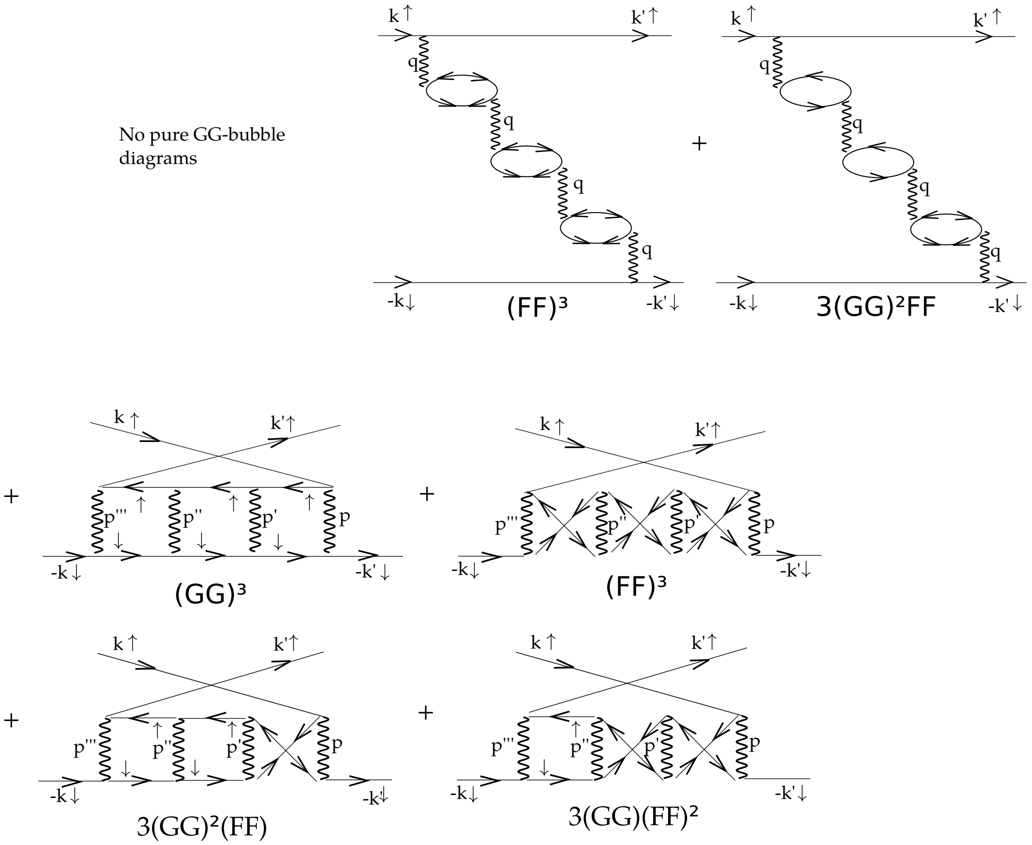

Figure 4.2: Diagrams to fourth order. Note that due to spin conservation it is not possible to construct a bubble diagram consisting of normal propagators only. This causes the unequal weight of contributions from diagrams with normal propagators only compared to those with anomalous propagators only. This arises for all even order diagrams.

which is the same results as obtained from the full expression in Eq. (4.1) expanded to fourth order.

We conclude that the diagrammatic expansion gives the same result as the expression by Pao and Bickers [77] as stated in Eq. (4.1). We have suppressed the internal structure of the momentum indices, since we are only concerned with the singlet channel. However, if triplet pairing is to be considered, the derivation should be kept general and the susceptibility dependence on either $\mathbf{k} - \mathbf{k}'$ (bubble diagrams) or $\mathbf{k} + \mathbf{k}'$ (ladder diagrams) must be stated explicitly.

4.3 Local pairing interaction with feedback from superconductivity

In this section we derive the expression for a spin-fluctuation mediated pairing in real space including the feedback effects. It is important to remember that in the inhomogeneous system, the real space susceptibility matrices do not in general commute. We consider pairing due to transverse fluctuations in section 4.3.1 and pairing in the longitudinal channel in section 4.3.2.

4.3.1 Pairing from transverse spin fluctuations

First we consider the ladder diagrams. As discussed in the previous chapter, this type of electron-electron interaction causes spin-flipping. In order to include feedback effects we define the susceptibilities:

$$\begin{aligned}
\chi_{\uparrow\downarrow}(a,b) &= -G_{\uparrow}(a,b)G_{\downarrow}(b,a) = -\langle T_\tau c_{a\uparrow}(\tau)c^\dagger_{b\uparrow}\rangle\langle T_\tau c_{b\downarrow}c^\dagger_{a\downarrow}(\tau)\rangle, && (4.13)\\
\chi_F(a,b) &= -F^\dagger(a,b)F(a,b) = -\langle T_\tau c^\dagger_{a\downarrow}(\tau)c^\dagger_{b\uparrow}\rangle\langle T_\tau c_{a\uparrow}(\tau)c_{b\downarrow}\rangle, && (4.14)\\
\chi_0^{\mathrm{ts}}(a,b) &= -[G_{\uparrow}(a,b)G_{\downarrow}(b,a) + F^\dagger(a,b)F(a,b)]. && (4.15)
\end{aligned}$$

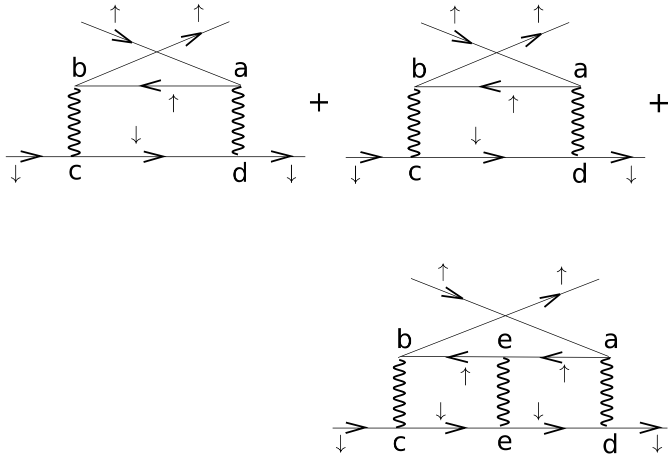

Figure 4.3: Ladder diagrams to third order, where only the normal propagator diagrams are shown. The third order diagrams including anomalous propagators are similar to the diagrams shown in Fig. 4.1.

From all the ladder diagrams we get:

$$\begin{aligned}
V^{\mathrm{ts}}_{\mathrm{eff}}(a,b) &= U^2(\chi_{\uparrow\downarrow}(a,b) + \chi_F(a,b))\\
&\quad + U^3\sum_c[\chi_{\uparrow\downarrow}(a,c)\chi_{\uparrow\downarrow}(c,b) + \chi_F(a,c)\chi_F(c,b) + \chi_{\uparrow\downarrow}(a,c)\chi_F(c,b) + \chi_F(a,c)\chi_{\uparrow\downarrow}(c,b)]\\
&\quad + U^4\sum_{c,d}[\chi_{\uparrow\downarrow}(a,c)\chi_{\uparrow\downarrow}(c,d)\chi_{\uparrow\downarrow}(d,b) + \chi_F(a,c)\chi_F(c,d)\chi_F(d,b)\\
&\qquad + \chi_{\uparrow\downarrow}(a,c)\chi_{\uparrow\downarrow}(c,d)\chi_F(d,b) + \chi_{\uparrow\downarrow}(a,c)\chi_F(c,d)\chi_{\uparrow\downarrow}(d,b) + \chi_F(a,c)\chi_{\uparrow\downarrow}(c,d)\chi_{\uparrow\downarrow}(d,b)\\
&\qquad + \chi_{\uparrow\downarrow}(a,c)\chi_F(c,d)\chi_F(d,b) + \chi_F(a,c)\chi_{\uparrow\downarrow}(c,d)\chi_F(d,b) + \chi_F(a,c)\chi_F(c,d)\chi_{\uparrow\downarrow}(d,b)]\\
&\quad + \dots\\
&= U^2\chi_0^{\mathrm{ts}}(a,b) + U^3(\chi_0^{\mathrm{ts}})^2(a,b) + U^4(\chi_0^{\mathrm{ts}})^3(a,b) + \dots\\
&= \left.\frac{U^2\chi_0^{\mathrm{ts}}}{1-U\chi_0^{\mathrm{ts}}}\right|_{(a,b)} \qquad (4.16)
\end{aligned}$$

The bare susceptibility for transverse spin fluctuations, which was defined in Eq. (4.15), we calculate by use of the Bogoliubov transformation:

$$c_{i\sigma} = \textstyle\sum_n u_{ni\sigma}\gamma_{n\sigma} + v^*_{ni\overline{\sigma}}\gamma^\dagger_{n\overline{\sigma}} \qquad\qquad c^\dagger_{i\sigma} = \textstyle\sum_n u_{ni\sigma}\gamma^\dagger_{n\sigma} + v^*_{ni\overline{\sigma}}\gamma_{n\overline{\sigma}}\ .$$

From the definition we have:

$$\chi_0^{\mathrm{ts}}(i,j;\tau) = -[\langle T_\tau c_{i\uparrow}(\tau)c^\dagger_{j\uparrow}\rangle\langle T_\tau c_{j\downarrow}c^\dagger_{i\downarrow}(\tau)\rangle + \langle T_\tau c^\dagger_{i\downarrow}(\tau)c^\dagger_{j\uparrow}\rangle\langle T_\tau c_{i\uparrow}(\tau)c_{j\downarrow}\rangle]. \qquad (4.17)$$

The first term consisting of normal propagators gives (summing over positive energies only):

$$\begin{aligned}
-\langle T_\tau c_{i\uparrow}(\tau)c^\dagger_{j\uparrow}\rangle\langle T_\tau c_{j\downarrow}c^\dagger_{i\downarrow}(\tau)\rangle \;=\; & \sum_{m,n}[u_{ni\uparrow}u_{nj\uparrow}u_{mj\downarrow}u_{mi\downarrow}(1-f_{n\uparrow})f_{m\downarrow}e^{(E_{m\downarrow}-E_{n\uparrow})\tau} \\
& +v_{ni\downarrow}u_{nj\downarrow}v_{mj\uparrow}v_{mi\uparrow}f_{n\downarrow}(1-f_{m\uparrow})e^{(E_{n\downarrow}-E_{m\uparrow})\tau} \\
& +u_{ni\uparrow}u_{nj\uparrow}v_{mj\uparrow}v_{mi\uparrow}(1-f_{n\uparrow})(1-f_{m\uparrow})e^{-(E_{n\uparrow}+E_{m\uparrow})\tau} \\
& +v_{ni\uparrow}v_{nj\uparrow}u_{mj\downarrow}v_{mi\downarrow}f_{n\downarrow}f_{m\downarrow}e^{(E_{n\downarrow}+E_{m\downarrow})\tau}].
\end{aligned} \tag{4.18}$$

From the second term consisting of the anomalous propagators we get (again summing over positive energies):

$$\begin{aligned}
-\langle T_\tau c^\dagger_{i\downarrow}(\tau)c^\dagger_{j\uparrow}\rangle\langle T_\tau c_{i\uparrow}(\tau)c_{j\downarrow}\rangle \;=\; & \sum_{m,n}[u_{ni\downarrow}v_{nj\downarrow}u_{mi\uparrow}v_{mj\uparrow}f_{n\downarrow}(1-f_{m\uparrow})e^{(E_{n\downarrow}-E_{m\uparrow})\tau} \\
& +u_{ni\downarrow}v_{nj\downarrow}v_{mi\downarrow}u_{mj\downarrow}f_{n\downarrow}f_{m\downarrow}e^{(E_{n\downarrow}+E_{m\downarrow})\tau} \\
& +v_{ni\uparrow}u_{nj\uparrow}u_{mi\uparrow}v_{mj\uparrow}(1-f_{n\uparrow})(1-f_{m\uparrow})e^{-(E_{n\uparrow}+E_{m\uparrow})\tau} \\
& +v_{ni\uparrow}u_{nj\uparrow}v_{mi\downarrow}u_{mj\downarrow}(1-f_{n\uparrow})f_{m\downarrow}e^{(E_{m\downarrow}-E_{n\uparrow})\tau}].
\end{aligned} \tag{4.19}$$

We collect all terms and Fourier transform from imaginary time to Matsubara frequency:

$$\begin{aligned}
\chi_0^{\mathrm{ts}}(i,j;i\omega_n) \;=\; & \sum_{m,n(E_n,E_m>0)}\Big[(u_{ni\uparrow}u_{nj\uparrow}u_{mj\downarrow}u_{mi\downarrow}-v_{ni\uparrow}u_{nj\uparrow}v_{mi\downarrow}u_{mj\downarrow})\frac{f_{n\uparrow}-f_{m\downarrow}}{i\omega_n+E_{m\downarrow}-E_{n\uparrow}} \\
& +(v_{ni\downarrow}v_{nj\downarrow}v_{mj\uparrow}v_{mi\uparrow}-u_{ni\downarrow}v_{nj\downarrow}u_{mi\uparrow}v_{mj\uparrow})\frac{f_{m\uparrow}-f_{n\downarrow}}{i\omega_n+E_{n\downarrow}-E_{m\uparrow}} \\
& +(u_{ni\uparrow}u_{nj\uparrow}v_{mj\uparrow}v_{mi\uparrow}-v_{ni\uparrow}u_{nj\uparrow}u_{mi\uparrow}v_{mj\uparrow})\frac{f_{n\uparrow}+f_{m\uparrow}-1}{i\omega_n-(E_{n\uparrow}+E_{m\uparrow})} \\
& +(v_{ni\downarrow}v_{nj\downarrow}u_{mj\downarrow}u_{mi\downarrow}-u_{ni\downarrow}v_{nj\downarrow}v_{mi\downarrow}u_{mj\downarrow})\frac{1-f_{n\downarrow}-f_{m\downarrow}}{i\omega_n+E_{n\downarrow}+E_{m\downarrow}}\Big],
\end{aligned} \tag{4.20}$$

where the following simplifications have been used:

$$(1-f(E_m))f(E_k)(e^{(E_k-E_m)\beta})-1) \;=\; f(E_m)-f(E_k), \tag{4.21}$$

$$(1-f(E_m))(1-f(E_k))(e^{-(E_m+E_k)\beta})-1) \;=\; f(E_m)+f(E_k)-1, \tag{4.22}$$

$$f(E_m)f(E_k)(e^{(E_m+E_k)\beta})-1) \;=\; 1-f(E_m)-f(E_k). \tag{4.23}$$

From Eq. (4.20) we simplify by the substitutions $v_\downarrow \to u_\uparrow$, $u_\downarrow \to v_\uparrow$ and $E_\downarrow \to -E_\uparrow$. Further we use that $f(-E) = 1 - f(E)$ and get the final expression for the bare transverse susceptibility:

$$\begin{aligned}
\chi_0^{\mathrm{ts}}(i,j;i\omega_n) \;=\; & \sum_{E_n>0,E_m<0}(u_{ni\uparrow}u_{nj\uparrow}v_{mj\uparrow}v_{mi\uparrow}-v_{ni\uparrow}u_{nj\uparrow}u_{mi\uparrow}v_{mj\uparrow})\frac{f_{n\uparrow}-(1-f_{m\uparrow})}{i\omega_n-E_{m\uparrow}-E_{n\uparrow}} \\
& +\sum_{E_n<0,E_m>0}(u_{ni\uparrow}u_{nj\uparrow}v_{mj\uparrow}v_{mi\uparrow}-v_{ni\uparrow}u_{nj\uparrow}u_{mi\uparrow}v_{mj\uparrow})\frac{f_{m\uparrow}-(1-f_{n\uparrow})}{i\omega_n-E_{n\uparrow}-E_{m\uparrow}} \\
& +\sum_{E_n,E_m>0}(u_{ni\uparrow}u_{nj\uparrow}v_{mj\uparrow}v_{mi\uparrow}-v_{ni\uparrow}u_{nj\uparrow}u_{mi\uparrow}v_{mj\uparrow})\frac{f_{n\uparrow}+f_{m\uparrow}-1}{i\omega_n-(E_{n\uparrow}+E_{m\uparrow})} \\
& +\sum_{E_n,E_m<0}(u_{ni\uparrow}u_{nj\uparrow}v_{mj\uparrow}v_{mi\uparrow}-v_{ni\uparrow}u_{nj\uparrow}u_{mi\uparrow}v_{mj\uparrow})\frac{1-(1-f_{n\uparrow})-(1-f_{m\uparrow})}{i\omega_n-E_{n\uparrow}-E_{m\uparrow}} \\
=\; & \sum_{m,n\ (\text{all } E_n,E_m)}\Big[(u_{ni\uparrow}u_{nj\uparrow}v_{mj\uparrow}v_{mi\uparrow}-v_{ni\uparrow}u_{nj\uparrow}u_{mi\uparrow}v_{mj\uparrow})\frac{f_{n\uparrow}+f_{m\uparrow}-1}{i\omega_n-E_{m\uparrow}-E_{n\uparrow}}\Big].
\end{aligned} \tag{4.24}$$

In conclusion the effective pairing interaction arising from transverse spin fluctuations is given by:

$$V_{\text{eff}}^{\text{ts}}(a,b) = \frac{U^2\chi_0^{\text{ts}}}{1-U\chi_0^{\text{ts}}}\Big|_{(a,b)}. \tag{4.25}$$

with

$$\chi_0^{\text{ts}}(i,j;i\omega_n) = -\sum_{m,n}\Big[(u_{ni\uparrow}u_{nj\uparrow}v_{mj\uparrow}v_{mi\uparrow} - v_{ni\uparrow}u_{nj\uparrow}u_{mi\uparrow}v_{mj\uparrow})\frac{1-f_{n\uparrow}-f_{m\uparrow}}{i\omega_n - E_{m\uparrow} - E_{n\uparrow}}\Big] \tag{4.26}$$

4.3.2 Pairing from longitudinal spin fluctuations

We will derive an expression for the longitudinal spin fluctuations which includes feedback effects. As opposed to the translationally invariant case the order of the propagators now becomes important. This complicates the summation procedure. We need to bear in mind that the order of the matrices must be maintained and further we would like to distinguish between spin up and spin down Green's functions. Due to these restrictions we have only succceeded to get a closed expression when the spin-up and spin-down susceptibilities come in pairs. By this approach some diagrams are omitted; those containing an odd number of bubbles (with an even number of normal propagator bubbles), as well as diagrams containing spin-up and spin-down normal bubbles separated by anomalous bubbles. Only when we later relax the explicit spin dependence of the spin susceptibilities, we obtain a full expression for the local pairing including feedback effects. This expression is then only valid in the paramagnetic phase.

As a matter of fact, several additional steps are necessary in the derivation of the effective pairing in a system with broken spin rotation symmetry. We are not yet ready to provide the full theory for an inhomogeneous system. In the next chapter, we will discuss the pairing in the spin rotation symmetry broken state, but restricted to a homogeneous system of commensurate antiferromagnetic order. For now, we are satisfied with a discussion of the feedback effects from superconductivity in a inhomogeneous paramagnetic system.

We introduce a separate expression for the normal and anomalous susceptibilities we have:

$$\chi_{\uparrow\uparrow}(a,b) = -G_\uparrow(a,b)G_\uparrow(b,a) = -\langle T_\tau c_{a\uparrow}(\tau)c_{b\uparrow}^\dagger\rangle\langle T_\tau c_{b\uparrow}c_{a\uparrow}^\dagger(\tau)\rangle, \tag{4.27}$$

$$\chi_{\downarrow\downarrow}(a,b) = -G_\downarrow(a,b)G_\downarrow(b,a) = -\langle T_\tau c_{a\downarrow}(\tau)c_{b\downarrow}^\dagger\rangle\langle T_\tau c_{b\downarrow}c_{a\downarrow}^\dagger(\tau)\rangle, \tag{4.28}$$

and

$$\chi_0^F(a,b) = -\langle T_\tau c_{a\downarrow}(\tau)c_{b\uparrow}\rangle\langle T_\tau c_{b\uparrow}^\dagger c_{a\downarrow}^\dagger(\tau)\rangle. \tag{4.29}$$

Note that the definition of the anomalous susceptibility here differs from the definition used in the case of transverse spin fluctuations, see Eq. (4.14). This is done in order to maintain operator-order with respect to spin. We define the combined susceptibility as:

$$\hat{\chi}_{\text{BUB}}(a,d) = \sum_e[\chi_{\downarrow\downarrow}(a,e)\chi_{\uparrow\uparrow}(e,d) + \chi_0^F(a,e)\chi_0^F(e,d)] \tag{4.30}$$

Now we sum up all diagrams that contain an even number of bubbles in which spin-up and spin-down

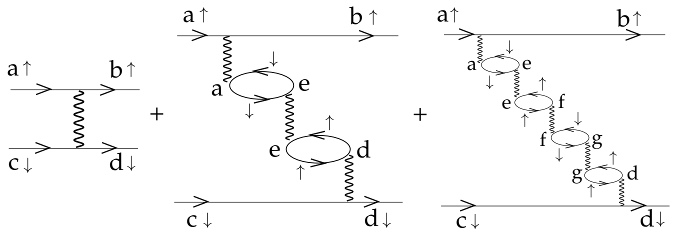

Figure 4.4: Bubble diagrams to fifth order, where only the normal propagator diagrams are shown.

normal bubbles come in pairs.

$$\begin{aligned}
V_{\mathrm{BUB}}(a,d) &= U^3 \sum_e [\chi_{\downarrow\downarrow}(a,e)\chi_{\uparrow\uparrow}(e,d) + \chi_0^F(a,e)\chi_0^F(e,d)] \\
&\quad + U^5 \sum_f \sum_{e,g} [\chi_{\downarrow\downarrow}(a,e)\chi_{\uparrow\uparrow}(e,f) + \chi_0^F(a,e)\chi_0^F(e,f)][\chi_{\downarrow\downarrow}(f,g)\chi_{\uparrow\uparrow}(g,d) + \chi_0^F(f,g)\chi_0^F(g,d)] \\
&\quad + \ldots \\
&= U^3 \hat{\chi}_{\mathrm{BUB}}(a,d) + U^5 \sum_f \hat{\chi}_{\mathrm{BUB}}(a,f)\chi_{\mathrm{BUB}}(f,d) + U^7 \sum_{f,h} \hat{\chi}_{\mathrm{BUB}}(a,f)\chi_{\mathrm{BUB}}(f,h)\chi_{\mathrm{BUB}}(h,d) \\
&\quad + \ldots \\
&= U^3 \hat{\chi}_{\mathrm{BUB}} + U^5 (\hat{\chi}_{\mathrm{BUB}})^2 + U^7 (\hat{\chi}_{\mathrm{BUB}})^3 + \ldots \Big|_{a,d} \\
&= \frac{U^3 \hat{\chi}_{\mathrm{BUB}}}{\hat{1} - U^2 \hat{\chi}_{\mathrm{BUB}}}\Big|_{(a,d)}. \qquad (4.31)
\end{aligned}$$

We can easily sum up all diagrams of an odd number of anomalous bubbles, which gives:

$$\begin{aligned}
V_{\mathrm{F}}(a,d) &= U^2 \chi_0^F(a,d) + U^4 \sum_{e,f} [\chi_0^F(a,e)\chi_0^F(e,f)\chi_0^F(f,d)] + \ldots \\
&= U^2 \chi_0^F + U^4 (\chi_0^F)^3 + U^6 (\chi_0^F)^5 + \ldots \\
&= \frac{U^2 \chi_0^F}{\hat{1} - U^2 (\chi_0^F)^2}\Big|_{(a,d)}. \qquad (4.32)
\end{aligned}$$

It is important to note, that we have left out diagrams containing an odd number of bubbles (with an even number of normal propagator bubbles), as well as diagrams containing spin-up and spin-down normal bubbles separated by anomalous bubbles.

We calculate the susceptibilities involved in the two expressions above, Eqs. (4.31) and (4.32). The method is identical to that performed in the previous section. The susceptibilities defined in Eqs. (4.27) and (4.28) are given by:

$$\chi_{\downarrow\downarrow}(i,k) = -\sum_{mn} v_{mi\uparrow} v_{mk\uparrow} v_{nk\uparrow} v_{ni\uparrow} \frac{f_{n\uparrow} - f_{m\uparrow}}{i\omega_n + E_{m\uparrow} - E_{n\uparrow}}, \qquad (4.33)$$

$$\chi_{\uparrow\uparrow}(i,k) = -\sum_{mn} u_{mi\uparrow} u_{mk\uparrow} u_{nk\uparrow} u_{ni\uparrow} \frac{f_{n\uparrow} - f_{m\uparrow}}{i\omega_n + E_{m\uparrow} - E_{n\uparrow}}. \qquad (4.34)$$

The anomalous susceptibility contribution to the bubble diagrams defined in Eq. (4.29) is given by:

$$\chi_0^F(i,k) = -\sum_{mn} v_{mi\uparrow} u_{mk\uparrow} v_{nk\uparrow} v_{ni\uparrow} \frac{f_{n\uparrow} - f_{m\uparrow}}{i\omega_n + E_{m\uparrow} - E_{n\uparrow}}. \qquad (4.35)$$

In conclusion we have from longitudinal spin fluctuations:

$$\boxed{V_{\text{eff}}^{\text{ls}}(a,d) = \left.\frac{U^3\hat{\chi}_{\text{BUB}}}{\hat{1}-U^2\hat{\chi}_{\text{BUB}}}\right|_{(a,d)} + \left.\frac{U^2\chi_0^F}{\hat{1}-U^2(\chi_0^F)^2}\right|_{(a,d)}}$$

with

$$\hat{\chi}_{\text{BUB}}(a,d) = \sum_e [\chi_{\downarrow\downarrow}(a,e)\chi_{\uparrow\uparrow}(e,d) + \chi_0^F(a,e)\chi_0^F(e,d)] \tag{4.36}$$

and the three susceptibility components given in Eqs. (4.33), (4.34), (4.35). Our expression reduces to the normal state result if the anomalous propagators are zero, as it should. We note that not all diagrams for longitudinal spin fluctuations compared to the homogeneous expression in Eq. (4.1) are included in this real space version. However, as we will see in the next section, a full expression for the effective pairing due to longitudinal spin fluctuations can be achieved if we relax the condition of the spin susceptibilities being different, i.e. we work in the paramagnetic state only.

4.3.3 Complete expression for longitudinal spin-fluctuations in the paramagnetic state

The summation procedure above was complicated due to having non-commuting susceptibilities in real space *and* spin-dependent susceptibilities. However, we can derive the local pairing equivalent to Eq. (4.1) by confining the model to the paramagnetic state. Thus, we relax the condition of spin-dependent susceptibilities, but maintain the non-commutativity. In this case we can sum up all diagrams using same procedure as in section 4.2. We denote the normal phase paramagnetic susceptibility $\chi_G = \chi_{\uparrow\uparrow} = \chi_{\downarrow\downarrow}$. Summing up all bubble diagrams to fourth order in U we get:

$$\begin{aligned} V_{\text{eff}}^{\text{long}}(a,d) &= U + U^2\chi_F(a,d) + U^3\sum_e [\chi_G(a,e)\chi_G(e,d) + \chi_F(a,e)\chi_F(e,d)] \\ &\quad + U^4 \sum_{e,f} [\chi_G(a,e)\chi_G(e,f)\chi_F(f,d) + \chi_F(a,e)\chi_G(e,f)\chi_G(f,d) \\ &\qquad + \chi_G(a,e)\chi_F(e,f)\chi_G(f,d) + \chi_F(a,e)\chi_F(e,f)\chi_F(f,d)] + \ldots \end{aligned} \tag{4.37}$$

We should now pay attention to the structure in this sum. An uneven number of χ_G is prohibited and we must account for this when performing the infinite series. The idea is the following: We consider the normal phase effective pairing expression. In the paramagnetic state this expression can be split into two parts, namely what looks like a spin RPA susceptibility and a charge RPA susceptibility.

$$V_{\text{eff}}^{\text{long}} = \frac{U^3\chi_G^2}{1-U^2\chi_G^2} = \frac{1}{2}\frac{U^2\chi_G}{1-U\chi_G} - \frac{1}{2}\frac{U^2\chi_G}{1+U\chi_G}. \tag{4.38}$$

Now, starting from the right hand side of Eq. (4.38) and expanding each term seperately we see that terms containing an uneven number of χ_G are cancelled out:

$$\begin{aligned} \frac{1}{2}\frac{U^2\chi_G}{1-U\chi_G} - \frac{1}{2}\frac{U^2\chi_G}{1+U\chi_G} &= \frac{1}{2}U^2\chi_G(1 + U\chi_G + U^2\chi_G^2 + U^3\chi_G^3 + \ldots) \\ &\quad - \frac{1}{2}U^2\chi_G(1 - U\chi_G + U^2\chi_G^2 + U^3\chi_G^3 + \ldots). \end{aligned} \tag{4.39}$$

In the superconducting state we want to include the possibility of having both an uneven and even number of anomalous χ_F bubbles while still maintaining the constraint of only even χ_G bubbles. This can be achieved if we use a different definition of the spin and charge susceptibilty. Clearly the normal part must have the same sign due to Eq. (4.39), but the anomalous part get opposite sign for the two different contributions, i.e.:

$$V_{\text{eff}}^{\text{long}} = \frac{1}{2}\frac{U^2\chi_{\text{sp}}}{1-U\chi_{\text{sp}}} - \frac{1}{2}\frac{U^2\chi_{\text{ch}}}{1+U\chi_{\text{ch}}}, \tag{4.40}$$

$$\chi_{\text{sp}} = \chi_G + \chi_F, \tag{4.41}$$

$$\chi_{\text{ch}} = \chi_G - \chi_F. \tag{4.42}$$

This ensures that all terms containing an uneven number of χ_G bubbles is cancelled out. The final expression for the longitudinal spin fluctuations in real space is given by:

$$V_{\text{eff}}^{\text{ls}}(a,d) = U\hat{1}\big|_{(a,d)} + \frac{1}{2}\frac{U^2\hat{\chi}_{\text{sp}}}{\hat{1}-U\hat{\chi}_{\text{sp}}}\bigg|_{(a,d)} - \frac{1}{2}\frac{U^2\hat{\chi}_{\text{ch}}}{\hat{1}+U\hat{\chi}_{\text{ch}}}\bigg|_{(a,d)} \tag{4.43}$$

provided that the system is in a paramagnetic state. The non-commutativity of the real space susceptibilities is accounted for in this expression. The spin susceptibility is the same as in Eq. (4.26) whereas for the charge susceptibility the sign is reversed for the contribution from anomalous propagators:

$$\chi_{\text{sp}}(i,j;i\omega_n) = -\sum_{m,n}\Big[(u_{ni\uparrow}u_{nj\uparrow}v_{mj\uparrow}v_{mi\uparrow} - v_{ni\uparrow}u_{nj\uparrow}u_{mi\uparrow}v_{mj\uparrow})\frac{1-f_{n\uparrow}-f_{m\uparrow}}{i\omega_n - E_{m\uparrow}-E_{n\uparrow}}\Big], \tag{4.44}$$

$$\chi_{\text{ch}}(i,j;i\omega_n) = -\sum_{m,n}\Big[(u_{ni\uparrow}u_{nj\uparrow}v_{mj\uparrow}v_{mi\uparrow} + v_{ni\uparrow}u_{nj\uparrow}u_{mi\uparrow}v_{mj\uparrow})\frac{1-f_{n\uparrow}-f_{m\uparrow}}{i\omega_n - E_{m\uparrow}-E_{n\uparrow}}\Big]. \tag{4.45}$$

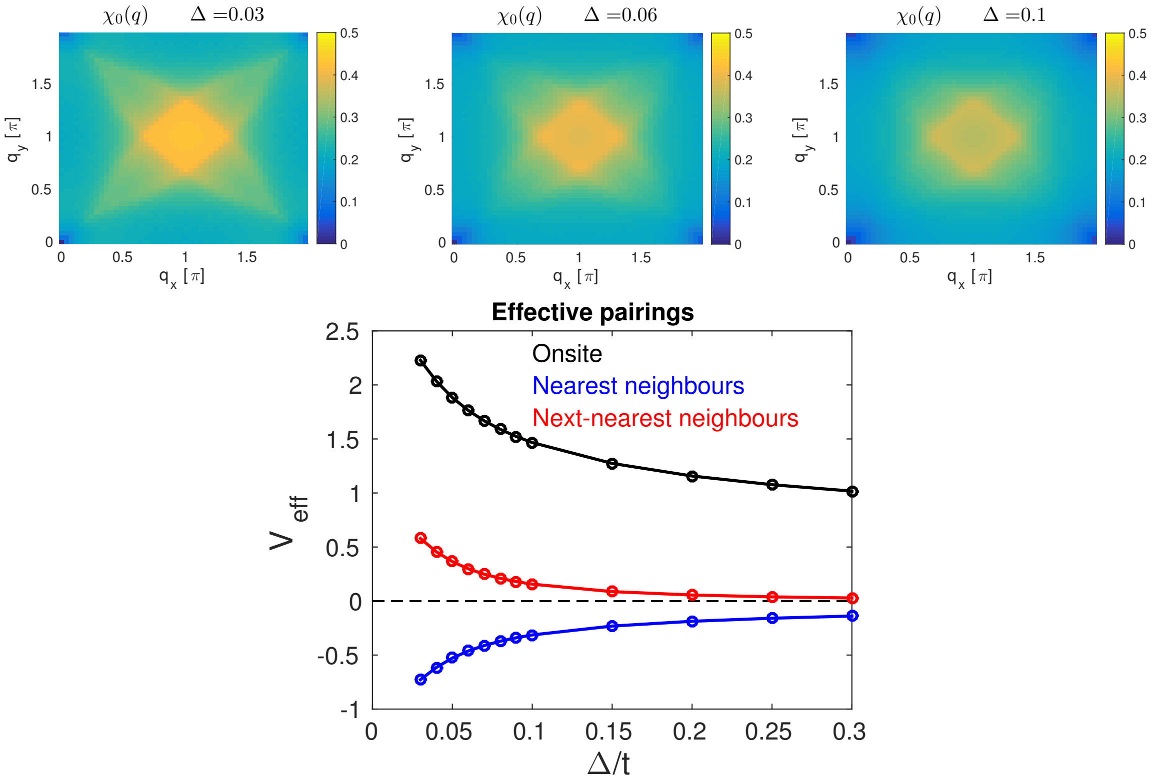

Figure 4.5: Spin susceptibilities as a function of the superconducting order parameter $\Delta = 0.03, 0.06, 0.1$ (from left to right) for a fixed band ($\mu = -1.02$, $t' = -0.3$, and $U = 2.2$). Note how the peak plateau at (π,π) is suppressed as the magnitude of the superconducting order is increased. By Fourier transformation, the onsite (black), nearest (blue) and next-nearest (red) effective interaction is calculated. A larger value of Δ causes a suppression of the effective pairings. In particular, the reduction of the nearest-neighbor attraction is what causes the pair-weakening effect.

4.4 Feedback effects around a single impurity

The final expression for spin-fluctuation mediated pairing including feedback effects is given by

$$V_{\rm eff}(a,d) = U\hat{1}|_{(a,d)} + \frac{3}{2}\frac{U^2\hat{\chi}_{\rm sp}}{\hat{1}-U\hat{\chi}_{\rm sp}}\Big|_{(a,d)} - \frac{1}{2}\frac{U^2\hat{\chi}_{\rm ch}}{\hat{1}+U\hat{\chi}_{\rm ch}}\Big|_{(a,d)} \tag{4.46}$$

where the susceptibilities are given by Eqs. (4.44) and (4.45). Note that this expression is valid only in the paramagnetic phase. The first term is simply the bare interaction. The second term is a summation of the transverse spin fluctuations given in Eq. (4.25) and the spin-part of the longitudinal spin fluctuations given in Eq. (4.43). The third term is the charge-part from the longitudinal spin fluctuations, which quantitatively will turn out to be negligible compared to the second part.

In order to visualize the effect of pair weakening, we first consider a homogeneous system, and use a phenomenological expression for d-wave superconductivity, i.e. $\Delta_{\mathbf{k}} = \Delta(\cos k_x - \cos k_y)$. Then we calculate the effective interactions in real space as a function of the strength of the superconducting order parameter, Δ. In a simple cartoon way we show the effect that a large superconducting gap has on the effective pairing mechanism in Fig. 4.5. As seen from the bare susceptibilities, the effect of an increasing superconducting gap (keeping all other parameters constant) is to suppress the peak at (π,π). The effective pairing interaction in real space is calculated by Fourier transformation and it seen to diminish as a function of Δ, see Fig. 4.5. This is the essence fo the pair weakening first discussed by Pao and Bickers in Ref. [77].

Now, we ask how the result of gap enhancement around a single impurity is affected if feedback effects from superconductivity is taken into account. We know from the above discussion that for fixed parameters, we expect a decrease of the gap magnitude in the homogeneous bulk system. In order to investigate the region close to the impurities, we compare our result obtained when pairing was calculated in the normal phase and the result for the same parameters, when feedback effects are included in the pairing mechanism. As shown in Fig. 4.6 there is a local enhancement structure of the superconducting gap also when feedback effects from superconductivity is taken into account.

In Fig. 4.7 we show the superconducting order parameter for a line cut through the lattice which includes the impurity site. At the impurity site $(13, 13)$, superconductivity is killed. When pairing is calculated in the normal state system, the enhancement effect discussed in the previous chapter is clearly visible, as shown by the full red line of Fig. 4.7. When feedback is included, but all other parameters

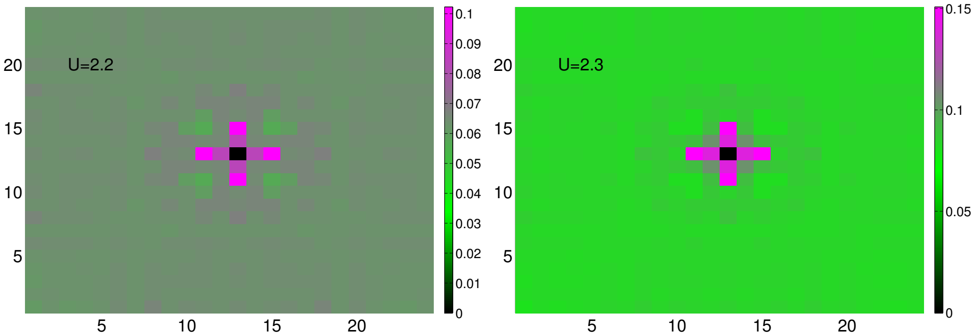

Figure 4.6: Superconducting gap around a single strong ($V_{\rm imp} = 10t$) impurity for Coulomb interaction $U = 2.2$ (left) and $U = 2.3$ (right) and $t' = -0.3$ and doping $x = 0.15$ in a system of dimensions 24×24 to compare with the results discussed in the previous chapter (where the superconducting gap calculated from a normal state pairing interaction strength). No magnetism is induced locally. The enhancement effect shows a similar local structure, but is slightly weaker in the feedback case compared to the calculation where normal state pairing is used.

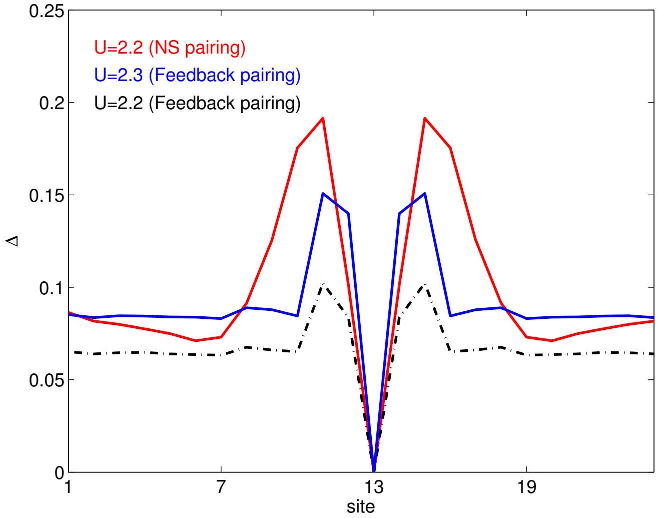

Figure 4.7: Superconducting gap around a single strong ($V_{\mathrm{imp}} = 10t$) impurity for Coulomb interaction $U = 2.2$ and $U = 2.3$, for $t' = -0.3$ and doping $x = 0.15$ in a system of dimensions 24×24. Here we compare the results obtained for normal state pairing and pairing which includes feedback from superconductivity.

kept constant, the superconducting order parameter is smaller in the bulk as well as close to the impurity site, and the enhancement effect around the impurity becomes less pronounced, as seen from the dashed-dotted black line in Fig. 4.7. However, if we increase U slightly from $U = 2.2$ to $U = 2.3$, the bulk gap size becomes comparable to the gap size with normal state pairing, and the effect is comparable to the result obtained without feedback in the pairing mechanism, though the relative enhancement compared to the bulk is a bit smaller when feedback effects are included. This might be expected from the fact, that a stronger local superconducting order will lead to a locally stronger suppression of the pairing interaction.

4.5 Locally induced antiferromagnetic order

A feature that has not yet been elucidated in this chapter or in the previous one, is the induction of local magnetism around an impurity. The emergence of antiferromagnetic order has drastic consequences on the spin-fluctuation mediated pairing and we can no longer rely on the formalism derived in the paramagnetic phase. The problem is that the paramagnetic susceptibility does not describe the spin fluctuations in the ordered state properly. An investigation of the partially Fourier transformed susceptibility by use of the form stated in Eq. (3.15) in chapter 3 shows a break-down of the usual Stoner criteria for magnetism, i.e. $URe\chi_0 \rightarrow 1$. For the sites, where magnetic order is present we have $1 < URe\chi_0$. This is illustrated in Fig. 4.8. In Fig. 4.8 (first row) we show the local magnetic order of the lattice with an impurity residing at $(13, 13)$. In this calculation superconducting order is treated phenomenologically by a constant pairing interaction (not calculated from spin fluctuations). For small values of $U = 2.0$ the magnetic order is induced only very locally around the impurity site. As the Coulomb repulsion is increased, $U = 2.5$, the magnetic order expands further from the impurity site, and eventually, for a large value of the Coulomb repulsion, $U = 3.0$, bulk antiferromagnetism develops. The partial Fourier transformed susceptibility is shown in Fig. 4.8 (second row) as a function of (q_x, π) for the impurity site $(x, y) = (13, 13)$ as shown by the black line, at a bulk site $(x, y) = (1, 1)$ as shown by the blue line, and at the neighbor site of the impurity site $(x, y) = (12, 13)$ as shown in red. We observe a local enhancement of the susceptibility at the neighbor site of the impurity compared to the bulk. In all three cases ($U = 2, 2.5, 3$), the Stoner criteria is exceeded at this site, i.e. $URe\chi_0 > 1$ at the plateau around (π, π). In the last case, for which bulk antiferromagnetism is developed, the partial Fourier transform satisfies $URe\chi_0 > 1$ for almost every site in the system. This is illustrated in Fig. 4.8 (last row).

As mentioned above, our local pairing formalism is unable to handle this situation. When magnetism is present, we must treat the spin fluctuations differently and distinguish between the two different types of spin fluctuations; the transverse fluctuations constituting the Goldstone mode of the ordered state, as well as the longitudinal fluctuations. Especially when many impurities are present, the system becomes more prone towards development of magnetism. Therefore, in order to study the many impurity case, as well as stripe-ordered systems we need to reformulate the theory for spin-fluctuation pairing in a magnetically ordered metallic system. In the next chapter we formulate the theory for pairing by spin fluctuations in a homogeneous spin-density-wave system with commensurate antiferromagnetic order.

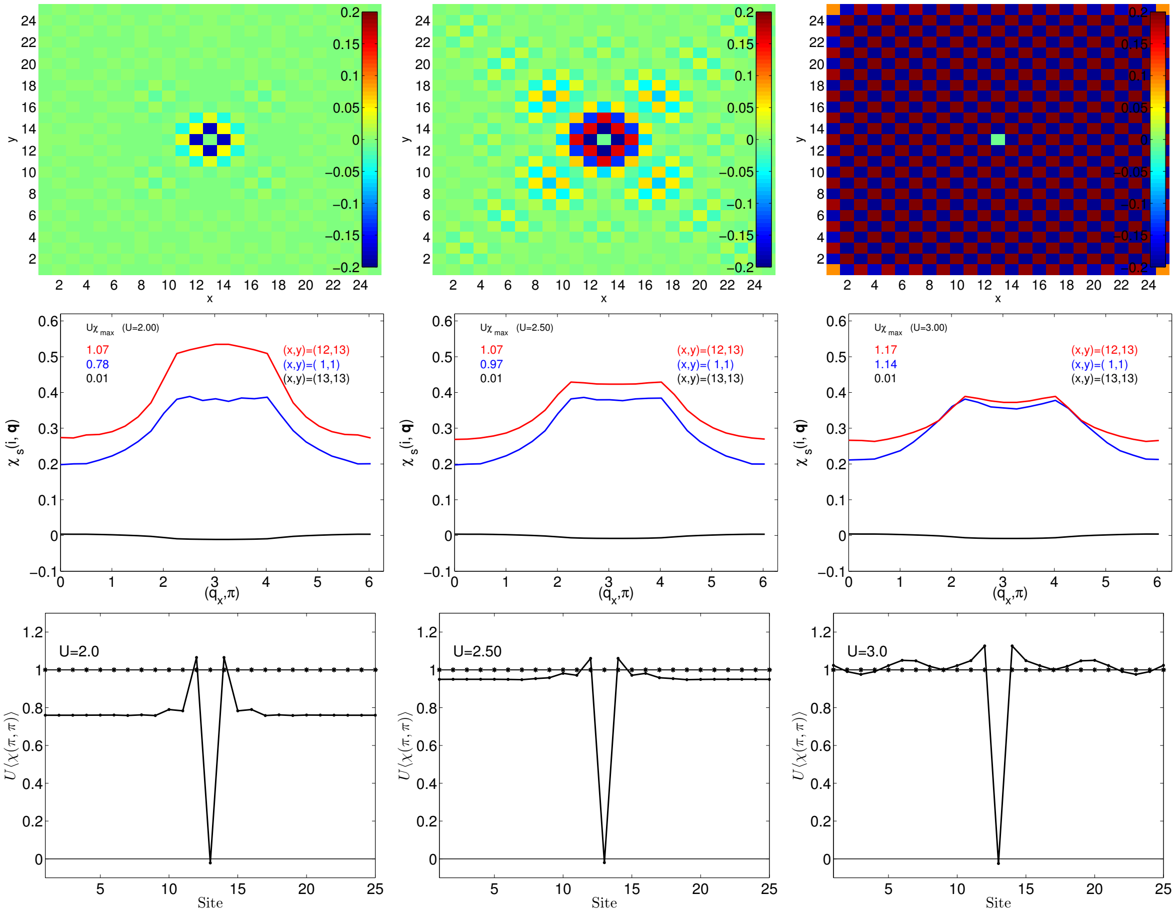

Figure 4.8: **Upper row:** Locally induced magnetism. **Middle row:** Local Fourier transformed bare spin susceptibility, $\chi_s(\mathbf{r}_i, \mathbf{q})$, as a function of $\mathbf{q} = (q_x, \pi)$. The local Fourier transformed is depicted for 3 different sites; bulk $\mathbf{r}_i = (1, 1)$, impurity site $\mathbf{r}_i = (13, 13)$, and neighbour site to the impurity $\mathbf{r}_i = (12, 13)$. **Lower row:** Spin susceptibility average value at $\mathbf{Q} = (\pi, \pi)$; $\langle\chi_s(\mathbf{r}_i, \mathbf{Q})\rangle$ as a function of $\mathbf{r}_i = (x, 13)$. A single strong ($V_{\text{imp}} = 10t$) impurity is placed at site $(13, 13)$. Parameters are $t' = -0.3t$, doping $x = 0.15$, $k_BT = 0.01t$ and Coulomb interactions $U = 2.0, 2.5, 3.0$.

4.6 Conclusions and outlook

We have derived a pairing potential which includes feedback from superconductivity in a local pairing picture, Eq. (4.46). This expression is valid in the paramagnetic phase. We have shown that the local enhancement of the superconducting gap around an impurity which was discussed in chapter 3, is preserved also when feedback from superconductivity is taking into account. However, a small pair weakening effect is observed. This pair weakening has been reported earlier in case of a homogeneous system with spin-fluctuation mediated superconductivity [77, 78].

Since the formalism discussed in this and the previous chapter only applies to the paramagnetic phase, it is not applicable in systems displaying magnetic stripes. However, we can study the effect of charge stripes induced by an underlying periodic potential structure, and investigate if the gap enhancement effect around a single impurity also appears as a general modulation of the gap size when charge order is present. Periodic density modulations will naturally lead to a periodically modulated gap as well with the modulations related to the local structure of the spin fluctuations. If the average gap of a charge modulated system is enhanced compared to the gap in homogeneous system is most likely dependent on the details like the charge stripe period and magnitude of the charge modulations. Preliminary results do not give a clear picture, and more studies are needed.

An interesting aspect of feedback effects on the local pairing interaction could arise in some iron-based superconductors, where a near-degeneracy of several pairing channels can occur, because the spin susceptibility supports different ordering vectors. In a work by Graser *et al.* [79] it was shown how the leading superconducting instability can shift between different symmetry channels due to a small change in Coulomb repulsion. In principle, feedback effects from a momentum dependent gap could also lead to a change from one favored pairing symmetry to a different pairing symmetry, if these are close in energy. In addition, local modulations of the spin susceptibilities could also affect the balance. This requires a generalization of the one-band formalism to the multi-orbital case and constitutes an interesting further study.

In the spin symmetry broken phase, the local formulation of feedback effects is complicated by the importance of keeping the spin order of the matrix indices. But we are also challenged by a more profound problem in this case, since the spin-fluctuation mediated pairing mechanism has to be reformulated altogether in order to take into account the presence of magnetic order. In the next chapter we will treat this problem.

Chapter 5

Spin-fluctuation mediated pairing in the spin-density wave phase

Part of the material in this chapter has been presented in New Journal of Physics **17***, 023022 (2015) and has been submitted to Phys. Rev. B. The manuscript is available at arXiv:1505.03003. We study the phase diagram of the Hubbard model in the weak-coupling limit for coexisting spin-density wave order and spin-fluctuation mediated superconductivity. Both longitudinal and transverse spin fluctuations contribute significantly to the effective interaction potential which creates Cooper pairs of the quasi-particles of the antiferromagnetic metallic state. We find a dominant* $d_{x^2-y^2}$*-wave solution in both electron- and hole-doped cases. In the triplet channel, the longitudinal fluctuations give rise to an effective attraction, supporting a p-wave gap, but strong repulsive contributions from the transverse fluctuations disfavors the p-wave pairing compared to* $d_{x^2-y^2}$*. The sub-leading pair instability is found to be in the g-wave channel, but complex admixtures of d and g are not energetically favored since their nodal structures coincide. Thus, in conclusion, the* $d_{x^2-y^2}$ *gap dominates for both hole and electron doping inside the spin-density wave phase as well as in the paramagnetic phase in the vicinity of the magnetic region.*

5.1 Introduction

In this chapter we address the coexistence phase of antiferromagnetic metallic order and spin-fluctuation mediated superconductivity. The Hubbard model was discussed in chapter 2 in the context of spin-fluctuation mediated pairing in the limit of no magnetic ordering. As seen in the previous chapter, the Hubbard model also contains the essential ingredients for a description of spin-density wave (SDW) order, i.e. magnetic order in a metallic system. In this chapter we restrict the discussion to homogeneous systems, where the SDW order is described by commensurate antiferromagnetism. We take into account four parameters in the one-band model: onsite Coulomb repulsion U, nearest (t) and next-nearest (t') neighbor hoppings together with doping away from half filling parametrized by the chemical potential μ. Superconductivity is induced by spin fluctuations derived from higher order interactions in U, similar to the treatment of the paramagnetic phase, but the electrons that interact are dressed by the magnetic order.

The competition between the hopping energies and the onsite Coulomb repulsion, which favors localization of the electrons on separate sites, gives rise to a rich phase diagram. For sizeable values of the Coulomb repulsion there exists a large doping regime for which a mean field decoupling in spin-up and spin-down densities will show a SDW ordered phase. The sea of electrons is organized into an itinerant antiferromagnet as a direct result of the onsite Coulomb repulsion. But the Coulomb interaction plays

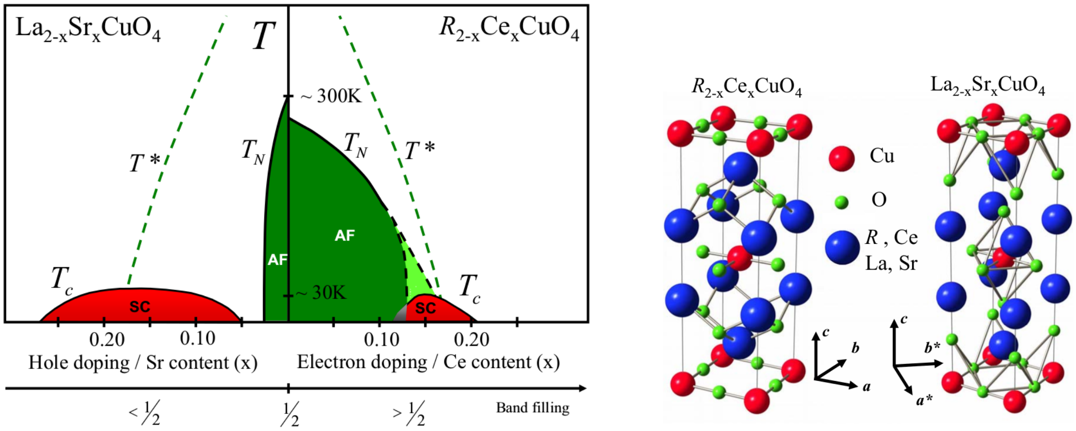

Figure 5.1: (**left:**) Cuprate phase diagram as a function of electron and hole doping. (**right:**) Crystal structure of electron and hole doped cuprates. In electron doped cuprates the apical oxygen is absent and the coordinate number for Cu is 4. Adapted from Armitage *et al.* , Ref. [1].

another crucial role; higher order interactions in U gives rise to an effective electron-electron interaction through spin and charge fluctuations. Now, the fluctuations bear the fingerprint of the antiferromagnetic order; the Goldstone mode of the ordered phase is manifested the transverse fluctuations, and the longitudinal fluctuations display a gapped spectrum. Both types of fluctuations will participate in the formation of Cooper pairs. The pairing strength in each channel is quantified by an evaluation of the real part of the spin susceptibilities at zero energy. In this chapter we investigate the presence of itinerant antiferromagnetism and superconductivity simultaneously; we assume that the SDW phase is well-developed and solve the superconducting gap equation in this phase. Since the magnetic order is homogeneous, it is natural to formulate the model in reciprocal space.

In chapter 2 we saw how pairing due to spin fluctuations in the paramagnetic system supports the development of a superconducting $d_{x^2-y^2}$ gap in the proximity to a SDW instability, i.e. close to half filling and for $|t'/t| < 0.5$. Now we focus on the case where the magnetic order is well-established, and have brought about a reconstruction of the Fermi surface as well as a Goldstone mode. The question is, how these two drastic changes to the metallic system affect the predicted symmetry of the superconducting gap and how the different types of spin fluctuations, i.e. longitudinal and transverse, contribute at different doping levels.

In two earlier works, Refs. [80] and [81], the coexistence of antiferromagnetism and superconductivity was studied, but limited to very weak hole dopings. We address the question of how the pairing interactions and resulting gap symmetry in the one-band Hubbard model, treated within the full spin fluctuation approach with self-consistently determined SDW order, evolve as a function of doping throughout the phase diagram, including the coexistence dome of SDW order and superconductivity.

5.2 The cuprate phase diagram

The cuprate phase diagram is depicted in Fig. 5.1(left), which shows the overall features of the hole-doped $La_{2-x}Sr_xCuO_4$ system and the electron-doped $Nd_{2-x}Ce_xCuO_{4\pm\delta}$ system. The two compounds differ in the crystal structures in that hole-doped crystals contain apical oxygens whereas electron-doped crystals do not. This is shown in Fig. 5.1(right). Another clear difference between the two systems is the extent to which antiferromagnetic order persists as a function of doping. For the hole-doped system, commensurate antiferromagnet order dies off extremely fast as a function of doping, although another incommensurate magnetic order occurs for dopings $x \leq 0.13$. We shall return to this in the subsequent

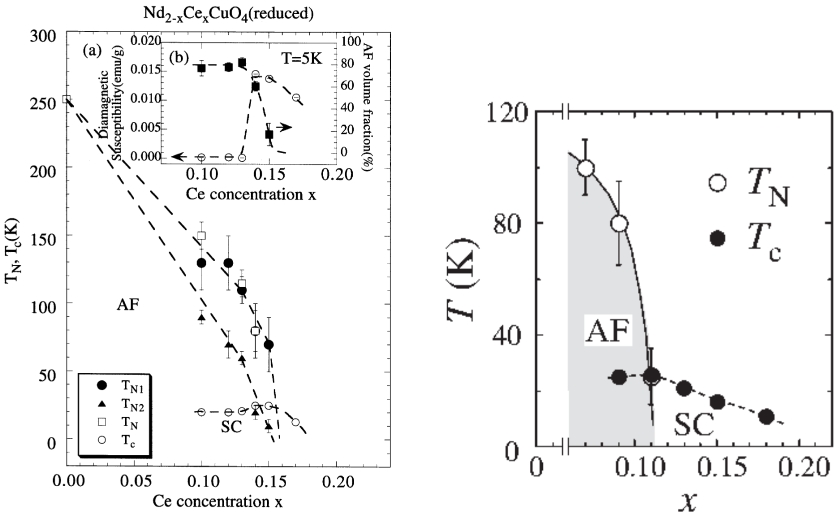

Figure 5.2: (**left**:) Phase diagram measured by muon spin relaxation and magnetic susceptibility measurements in $Nd_{2-x}Ce_xCuO_{4\pm\delta}$. T_{N2} denotes the onset of long range magnetic order. From the inset it is seen that the diamagnetic response is very small (almost zero) at dopings $x = 0.1, 0.12, 0.13$, and this is very sensitive to heat treatment. On the other hand, the onset T_c of the diamagnetic response is insensitive to the heat treatment. Adapted from Uefuji *et al.*, Ref. [83]. (**right:**) Phase diagram of $Pr_{1-x}LaCe_xCuO_{4-\delta}$ measured by neutron scattering and SQUID. Adapted from Fujita *et al.*, Ref. [84].

chapters. In the case of electron-doped cuprates, the commensurate antiferromagnetism persists for a large doping range. A lot of effort has been put into investigations of whether superconductivity and antiferromagnetism coexist in these systems, and it is still a issue of debate [2, 15].

Several reports show a coexistence region of both phases, but it remains unclear if there is a spatial competition between the two. In Fig. 5.2, two phase diagrams are depicted. These phase diagrams do indeed show coexistence of both phases at least close to the critical doping of the magnetic order. In $Nd_{2-x}Ce_xCuO_{4\pm\delta}$ the diamagnetic response is weak at the dopings $x = 0.1, 0.12, 0.13$, where the magnetic volume fraction is large. The diamagnetic response is very sensitive to the annealing conditions, but the response occurs at roughly the same critical temperature, as seen from Fig. 5.2(right).

5.2.1 Band structure in electron-doped cuprates

The band structure of cuprates have been extensively studied by Angle Resolved Photoemission Spectroscopy (ARPES) [1, 8]. This technique provides a way of mapping the electronic band structure, and is therefore also sensitive to possible band reconstruction occuring as a result of ordering phenomena in the system. The ARPES technique can not tell the origin of the reconstruction, i.e. whether the ordering is of magnetic, superconducting or a third origin. This information must be provided by complementary techniques. A vast number of ARPES experiments have been performed to map out the Fermi surface and gap structure of the cuprates as a function of both electron and hole doping. In either case, the simple paramagnetic bands arising from the Hubbard model are insufficient to describe the observations in the underdoped regime, i.e. for dopings smaller than optimal. A reconstruction of the bands take place and for hole doping, the lowest energy states are located at $(\frac{\pi}{2}, \frac{\pi}{2})$, while they appear at $(\pi, 0)$ in the electron-doped cuprates [8]. The band evolution measured by ARPES [85] for the electron-doped compound $Nd_{2-x}Ce_xCuO_{4\pm\delta}$ is shown in Fig. 5.3. The Fermi surface is consistent with a band reconstruction of the paramagnetic bands of a one-band Hubbard model folded around the antiferromagnetic zone boundary. This signifies that the reconstruction arises from an ordering phenomena characterized by a wave vector $\mathbf{Q} = (\pi, \pi)$. The proximity to the antiferromagnetic phase makes it

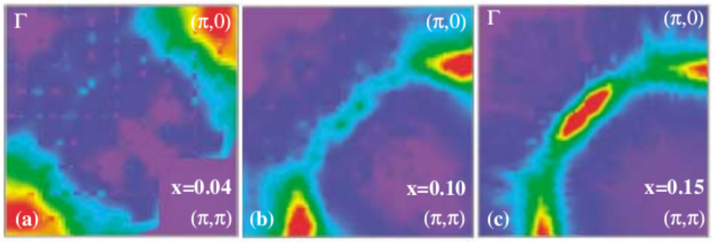

Figure 5.3: Fermi surface plots of $Nd_{2-x}Ce_xCuO_{4\pm\delta}$ measured by ARPES (energy integrated in a window from -40 meV to 20 meV around the Fermi energy). (a) $x = 0.04$, (b) $x = 0.10$, and (c) $x = 0.15$. Adapted from Ref. [85].

natural to interprete the ARPES result as an indication that electron-doped cuprates are well-described by itinerant antiferromagnetism. However, one should bear in mind that it is possible that different ordering phenomena could also explain the observed ARPES spectra. The evolution of the Fermi surface upon electron doping is as follows; in the limit of small electron doping only Fermi pockets around the $(\pi, 0)$ and $(0, \pi)$ points are present, but as the electron doping is increased, pockets at $(\frac{\pi}{2}, \pm\frac{\pi}{2})$ become visible. Transport data of the electron-doped compounds show an abrupt sign change of the Hall coefficient between $x = 0.16$ and $x = 0.17$, which was interpreted as a signature of a (possibly magnetic) quantum critical point [91]. This doping evolution of the Fermi surface, shown in Fig. 5.3, is captured by a mean-field treatment of antiferromagnetic order within the one-band Hubbard model, as shown in Fig. 5.4 (middle and right-most figure). In the case of hole doping, the antiferromagnetic bands give the lowest energy states around $(\frac{\pi}{2}, \frac{\pi}{2})$, but the simple form of a hole pocket centered at $(\frac{\pi}{2}, \frac{\pi}{2})$ is not consistent with ARPES measurements in hole-doped compounds. It is believed that different ordering phenomena such as the pseudogap and the charge-density wave order play a crucial role in this doping regime.

5.2.2 Annealing

One major complication regarding the electron-doped system is the fact that annealing processes are very crucial for the development of superconductivity. Unannealed crystals are never superconducting [1]. Since the evaporation and reorganization of the oxygens in the crystal structure depends on the heating temperature as well as the amount of time the crystal is being annealed, different procedures might cause differences in the final crystal structure. For instance, in the case of $Pr_{2-x}Ce_xCuO_{4-\delta}$, Brinkmann and coworkers [86] developed an improved reduction technique for which the superconducting dome expands

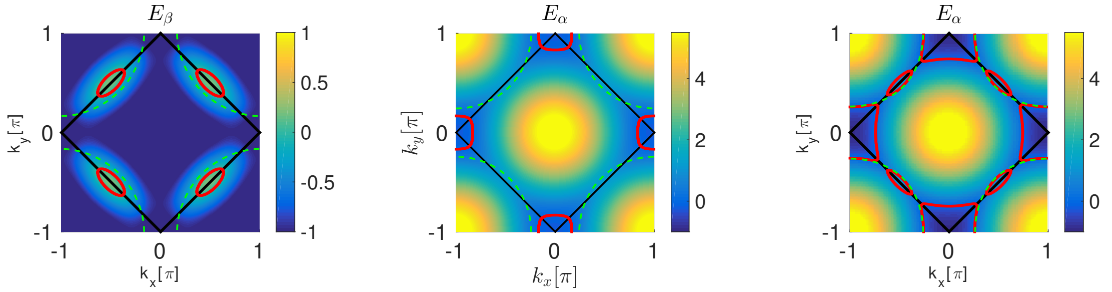

Figure 5.4: Band and Fermi surface evolution as a function of hole ($p = 0.04$) and electron ($n = 0.05, 0.12$) doping of the Hubbard model with $t' = -0.35$. The paramagnetic Fermi surface is shown by the green dashed line and the reconstructed Fermi surface of the antiferromagnetic SDW is shown by red full lines.

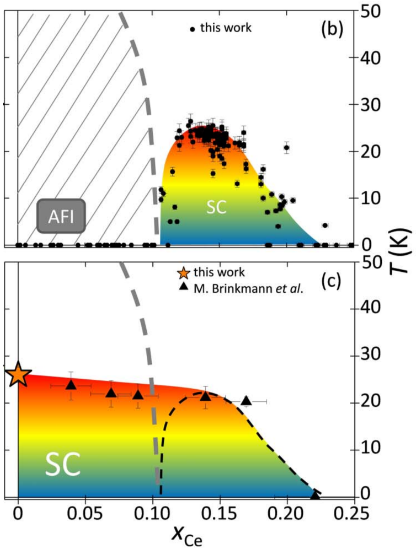

Figure 5.5: Phase diagrams of electron-doped $Pr_{2-x}Ce_xCuO_{4-\delta}$ for two different annealing procedures. The top figure shows the result of standard annealing. The bottom figure shows the result of a more complete annealing procedure, in which all apical oxygen are removed from the crystal structure. With this procedure even undoped $Pr_{2-x}Ce_xCuO_{4-\delta}$ ($x = 0$) becomes superconducting. Adapted from Ref. [2].

for a much larger doping regime all the way down to $x = 0.04$, as opposed to earlier reports where superconductivity was observed only in a very narrow region around a Ce doping of $x = 0.15$ after annealing. Recently, Krockenberger and coworkers [2] re-addressed the question of the importance of annealing in electron-doped cuprates, asking how it could be that five different groups all investigating $Pr_{2-x}Ce_xCuO_{4-\delta}$ reported different critical Ce dopings x_c for which superconductivity sets in. The authors came to the conclusion that the oxygen reduction procedure severely affects the competition between the antiferromagnetic insulating and superconducting states. Ideally, electron-doped crystals are arranged in the T′ structure as depicted in Fig. 5.1(right); the coordination number of the Cu atoms is 4 since no apical oxygens are present. However, as-grown electron-doped crystals might have some oxygens residing at the apical positions which can be removed by annealing. Krockenberger *et al.* showed that even undoped $Pr_{2-x}Ce_xCuO_{4-\delta}$ ($x = 0$) becomes superconducting if annealed carefully by a two-step procedure, see Fig. 5.5. The claim is that if all apical oxygens are removed from the crystal structure by very careful annealing, then the CuO_2 planes are metallic and superconducting even at half filling. In Ref. [2] it is argued that the presence of apical oxygens in the standard annealed crystals causes a charge transfer gap and thereby gives rise to a antiferromagnetic insulating phase. Whether SDW order is present in this regime for the well-annealed crystals is not yet completely settled. Whereas most ARPES data on $Pr_{2-x}Ce_xCuO_{4-\delta}$, which was obtained from less annealed crystals, show clear folding around the antiferromagnetic zone boundary, this does not seem to be the case for the well-annealed crystals [2]. Therefore, microscopic coexistence of antiferromagnetism and superconductivity in electron-doped crystals continues to be an issue of debate.

5.2.3 Gap symmetry in the cuprates

ARPES experiments provided compelling evidence for $d_{x^2-y^2}$-wave gap symmetry in the hole-doped cuprate $Bi_2Sr_2CaCu_2O_8$ in experiments by Shen *et al.* in 1993, Ref. [7]. A similar experiment was not doable in the electron-doped compounds until 2001 due to the limited energy resolution of ARPES and the smallness of the superconducting gap in electron-doped compounds. Three independent reports found evidence for a vanishing gap along the zone diagonals in $Nd_{2-x}Ce_xCuO_{4\pm\delta}$([89, 90]) and in $Pr_{1-x}LaCe_xCuO_{4-\delta}$([18]), see Fig. 5.6. The latter experiment provided a detailed map of the angle dependence of the gap, which was found to have a non-monotonic behavior, with significant deviations from the $\cos(k_x) - \cos(k_y)$ functional form. The superconducting gap exhibits the largest value at positions where the Fermi surface intersects the magnetic zone boundary. At these positions another energy

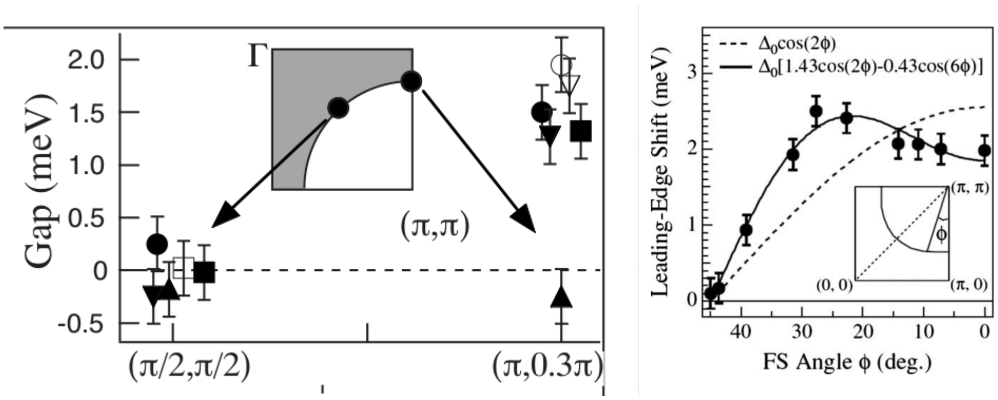

Figure 5.6: Superconducting gap extracted from ARPES measurements consistent with a $d_{x^2-y^2}$-wave gap. (**left:**) Gap in $\mathrm{Nd}_{2-x}\mathrm{Ce}_x\mathrm{CuO}_{4\pm\delta}$ $x = 0.15$. The underlying Fermi surface is shown in Fig. 5.3 (right), with strong indications of bandfolding around the antiferromagnetic zone boundary. Adapted from Armitage *et al.*, Ref. [89]. (**right:**) Gap in $\mathrm{Pr}_{1-x}\mathrm{LaCe}_x\mathrm{CuO}_{4-\delta}$ $x = 0.11$. As in the case of $\mathrm{Nd}_{2-x}\mathrm{Ce}_x\mathrm{CuO}_{4\pm\delta}$ $x = 0.15$ the underlying Fermi surface is a hole pocket around (π, π), with a substantial suppression at the positions where the hole pocket and the antiferromagnet zone boundary intersect, i.e. at the hotspot. This additional gap has been dubbed the pseudogap of electron-doped cuprates. Note that the maximum value of the superconducting gap is found at the position of the pseudogap. Adapted from Matsui *et al.*, Ref. [18].

gap, a so-called pseudogap of the electron-doped cuprates that persists for $T > T_c$, is also present. The non-monotonicity of the superconducting gap structure was also reported by Raman spectroscopy [19].

Further support for $d_{x^2-y^2}$-wave symmetry is found from neutron scattering where a resonance has been observed at (π, π) in $\mathrm{Pr}_{1-x}\mathrm{LaCe}_x\mathrm{CuO}_{4-\delta}$ [92] and $\mathrm{Nd}_{2-x}\mathrm{Ce}_x\mathrm{CuO}_{4\pm\delta}$ [93]. Tunneling experiments reveal a V-shaped density of states consistent with the existence of nodes of the superconducting gap. This rules out s-wave, and is consistent with d-wave, but in principle other gap symmetries with nodes could give rise to a V-shaped density of states. In fact, the V-shaped density of states requires that the normal state displays Fermi weigth at the $\mathbf{k}$ positions where the gap nodes appear. For instance, if the normal state Fermi surface consisted of well-separated electron pockets at positions $(\pi, 0)$ and $(0, \pi)$, the opening of a $d_{x^2-y^2}$ superconducting gap would give rise to a density of states similar to the one commonly observed in an s-wave superconductor, i.e. a full gap. This has not been observed. One possible explanation is that the gap symmetry displays line nodes through the electron pockets, e.g. d_{xy} or extended s-wave. This is however not consistent with the ARPES results, see Fig. 5.6. Another possibility is that superconductivity sets in only when hole pockets are present at (or very close to) the Fermi level.

In conclusion, the observations from tunneling and ARPES experiments suggest that superconductivity only arises for systems where both hole- and electron pockets are present at the Fermi level. In the existing reports on ARPES measurements, lighty doped samples for which only electron pockets are present are non-superconducting. But as discussed by Krockenberger [2], improved annealing can give superconducting samples at lighty doped (even undoped) samples. It remains to be observed whether there exists weakly electron-doped compounds that are superconducting and at the same time displays the characteristic band structure of the commensurate SDW phase, i.e. electron pockets around $(\pi, 0)$, $(0, \pi)$. If such a coexistence phase exists we can expect a $d_{x^2-y^2}$ superconducting gap to be manifested in a very different way.

5.2.4 "The nodal gap" for weakly hole-doped systems

For the hole-doped cuprates there is solid evidence for a $d_{x^2-y^2}$ gap at all doping values [8]. However, in the very weakly hole-doped cuprate superconductors a full gap has been observed by ARPES experiments [101, 102]; In the **k**-space positions which are gapless in a $d_{x^2-y^2}$ superconductor, the so-called nodal positions, a gap is opened. This observation has been given the slightly confusing name "nodal gap". In the studies reported in Refs. [101, 102], of which one was on $\mathrm{La}_{2-x}\mathrm{Sr}_x\mathrm{CuO}_4$ $x = 0.08$ $T_c = 20$ K and $x = 0.145$ $T_c = 33$ K [101] and the other was on $\mathrm{Bi_2Sr_2CaCu_2O_8}$ for $x = 0.04, 0.055, 0.07, 0.08, 0.10$ [102] (only the last sample is superconducting), it was observed that the gap is nodeless in the very weakly doped system, and becomes a usual nodal $d_{x^2-y^2}$ gap as doping or temperature is increased. In the $\mathrm{Bi_2Sr_2CaCu_2O_8}$ crystal studied by Peng and coworkers [102] the nodal gap disappeared at $x = 0.10$ at which superconductivity sets in, and was therefore reported a competitor to the superconducting phase. In contrast, the nodal gap observed in $\mathrm{La}_{2-x}\mathrm{Sr}_x\mathrm{CuO}_4$ by Razzoli and coworkers was interpreted as arising from superconductivity alone, and that the angle dependence of the gap was consistent with the chiral form $\Delta_{d_{x^2-y^2}} + i\Delta_{d_{xy}}$.

On the theoretical approach, one explanation of the nodal gap was given in terms of impurity scattering inherent of the dirty systems [103]. In this interpretation, the nodal gap observed in the very underdoped regime is not a superconducting gap, but arises due to locally induced magnetic order which competes with superconductivity. As opposed to this approach, a recent paper by Y.-M. Lu and coworkers [104] put forward a scenario in which a fully gapped superconducting state appears in the very underdoped regime arising from a homogeneous coexistence of antiferromagnetism and superconductivity. We will discuss the model of Ref. [104] in detail below, and relate it to our weak-coupling approach of the coexistence phase. First, we introduce our model in sections 5.3-5.7 and discuss our results in sections 5.8-5.11.

5.3 The theoretical approach to the coexistence phase

For the doped one-band Hubbard model with standard commensurate (π, π) ordering, the existence of pairing and its consequences for the symmetry of the superconducting order parameter was initially investigated by Schrieffer, Wen and Zhang [80]. The authors calculated the effective pairing interaction within the random phase approximation (RPA) arising from longitudinal spin fluctuations in the magnetically ordered phase, and neglected the contribution to pairing from the transverse spin fluctuations, arguing that even though such modes lead to a divergent contribution to the spin susceptibility at the ordering vector **Q**, the coherence factors of the SDW phase screen the bare electron-electron interaction vertex which therefore vanishes at **Q**. The important point to realize is that it is not the bare electrons which pair up, but the quasi-particles of the SDW metal. The argument given in Ref. [80] was that doped holes live at the top of the valence bands and in this region the coherence factors for the transverse channel are zero. The intuitive picture put forward by Schrieffer, Wen and Zhang was the idea that each hole leads to a local suppression of the antiferromagnetic order, and by this forms a quasiparticle that can be visualized as a "spin-bag". Only the magnitude, but not the direction of the magnetic order was affected by the hole. The idea is, that by sharing the same spin bag two holes can effectively attract each other.

Frenkel and Hanke [81] put forward a complementary picture where they argued that transverse spin fluctuations do provide contributions to the effective pairing. Their motivation was due to observations by Shraiman and Siggia [82], who showed that within the $t-J$ model single holes couple to transverse spin fluctuations. In the limit of large U/t, the Hubbard model should behave similar, at least qualitatively. Therefore it seemed unlikely that the transverse fluctuations should completely decouple from the holes. Based on this idea one should expect an effective hole-hole interaction to arise due to tranverse fluctuations as well. Indeed, Frenkel and Hanke [81] showed that within the Hubbard model, transverse fluctuations mediate pairing and contribute to the pairing interaction by the same order of magnitude as the longitudinal fluctuations. The reason is that although the coherence factors screen the divergence and thereby remove any unphysically large pairing contribution, the transverse contribution is not complete cancelled as proposed by Schrieffer *et al.* Rather, the multiplication of the divergent term from the transverse fluctuations and a vanishing term from the magnetic coherence factor amounts to a finite pairing contribution. So one can think of the "bag" as a distortion not only of the magnitude of the magnetic order, but also the orientation. Schrieffer *et al.* showed that the RPA approach reproduced the spin-wave velocity and dispersion relation of a $S = \frac{1}{2}$ Heisenberg model in the limit of large U/t. With the additional insights of Frenkel and Hanke, we are somewhat justified in our approach using a large-U/t Hubbard model to describe physics taking place close to the Mott insulator region.

For electron-doped cuprates, the one-band Hubbard model seems to provide a reasonable minimal model since the doped electrons reside primarily on the copper sites. Furthermore, calculations of band parameters for the electron-doped cuprates point to the fact that the Coulomb interaction is smaller than the bandwidth [1], in contrast to their hole-doped counterparts. In consequence, the mean field treatment of the SDW order works quite well for the normal state properties of the electron-doped systems. In particular, ARPES reports show a Fermi surface evolution upon increased electron doping which agrees well with the band reconstruction of the one-band Hubbard model due to commensurate (π, π) order, as shown in Figs. 5.3 and 5.4. Therefore an investigation of the coexistence region is particularly interesting in this case. In the case of hole doping, commensurate antiferromagnetic order does not appear to be stable neither experimentally or theoretically. Experimentally, (quasi)-static magnetic order is observed in the hole-doped compounds in the underdoped regime, but is incommensurate with the underlying lattice and better reconciled in a picture of antiferromagnetic stripes intersected by charge rivers. Theoretically, calculations of the spin wave spectrum suggest that the commensurate (π, π) order in this case is not the ground state solution [96, 94], but stable in the case of electron doping [94].

5.4 The spin-density wave metal

There exist in principle two different ways of describing magnetism; either a localized picture, where the electrons are confined to certain lattice sites and the magnetic phase develops as a result of superexchange interactions, or the itinerant picture where the electronic wave functions are spread out, and the system remains metallic. In the latter case, the magnetic order is described as a wave of spin densities; the spin-density wave (SDW). The Hubbard model is a weak-coupling approach, where the magnetic order is itinerant. Electrons can hop from one site to the nearest and next-nearest neighbors by an energy t and t', respectively, and repel each other by the Coulomb energy U if they reside at same position. The number of electrons in the system is controlled by a change of the onsite energy at all sites in the lattice, i.e. by a change in the chemical potential μ. This is described in the one-band Hubbard Hamiltonian:

$$H = -\sum_{i,j,\sigma} t_{i,j} c^\dagger_{i\sigma} c_{j\sigma} + U \sum_i n_{i\uparrow} n_{i\downarrow} - \mu \sum_{i,\sigma} n_{i\sigma}. \tag{5.1}$$

In the present model we work with a translationally invariant system where the antiferromagnetic order is global. Therefore it is natural to formulate the model in reciprocal space. Fourier transformation of the Hubbard Hamilonian gives:

$$H = \sum_{k\sigma} \epsilon_k c^\dagger_{k\sigma} c_{k\sigma} + \frac{U}{2N} \sum_{k,k',q} \sum_{\sigma} c^\dagger_{k'\sigma} c^\dagger_{-k'+q\overline{\sigma}} c_{-k+q\overline{\sigma}} c_{k\sigma} \tag{5.2}$$

where

$$\epsilon_k = -2t[\cos(k_x) + \cos(k_y)] - 4t' \cos(k_x)\cos(k_y) - \mu.$$

The presence of SDW order in the ground state of the system can be captured by a mean field, W, defined by:

$$W = -\frac{U}{N} \sum_{\mathbf{k}} [\langle c^\dagger_{\mathbf{k}+\mathbf{Q}\uparrow} c_{\mathbf{k}\uparrow} \rangle - \langle c^\dagger_{\mathbf{k}+\mathbf{Q}\downarrow} c_{\mathbf{k}\downarrow} \rangle]. \tag{5.3}$$

Notice that the N in the normalization of Eq. (5.3) refers to the total number of states in the full structural Brillouin zone. By Fourier transformation we can relate the order parameter W to the magnetization of each lattice site, $m_i = \langle n_{r_i\uparrow}\rangle - \langle n_{r_i\downarrow}\rangle$:

$$\begin{aligned} W &= \frac{U}{N}[\sum_{\mathbf{k}}\sum_{i,j} e^{i(\mathbf{k}+\mathbf{Q})\mathbf{r}_i - \mathbf{k}\mathbf{r}_j}\langle c^{\dagger}_{\mathbf{r}_i\uparrow} c_{\mathbf{r}_j\uparrow}\rangle - \sum_{\mathbf{k}}\sum_{i,j} e^{i(\mathbf{k}+\mathbf{Q})\mathbf{r}_i - \mathbf{k}\mathbf{r}_j}\langle c^{\dagger}_{\mathbf{r}_i\downarrow} c_{\mathbf{r}_j\downarrow}\rangle \\ &= \frac{U}{N}\sum_{i} e^{i\mathbf{Q}\mathbf{r}_i}[\langle n_{\mathbf{r}_i\uparrow}\rangle - \langle n_{\mathbf{r}_i\downarrow}\rangle] \\ &= \frac{U}{N}\sum_{i} e^{i\mathbf{Q}\mathbf{r}_i} m_i. \end{aligned} \tag{5.4}$$

In the antiferromagnetically ordered state, the electron spin of one sublattice is primarily "spin up", whereas it will be primarily "spin down" on the other sublattice. Having $m_i = m$ for i on one sublattice and $m_i = -m$ for i on the other sublattice, and $\mathbf{Q} = (\pi, \pi)$ we get $W = Um$. We formulate the SDW mean field Hamiltonian:

$$H_{\text{SDW}} = {\sum_{\mathbf{k}}}' \sum_{\sigma} (c^{\dagger}_{\mathbf{k}\sigma} \quad c^{\dagger}_{\mathbf{k}+\mathbf{Q}\sigma}) \begin{pmatrix} \epsilon_{\mathbf{k}} & \sigma W \\ \sigma W & \epsilon_{\mathbf{k}+\mathbf{Q}} \end{pmatrix} \begin{pmatrix} c_{\mathbf{k}\sigma} \\ c_{\mathbf{k}+\mathbf{Q}\sigma} \end{pmatrix}. \tag{5.5}$$

The primed **k**-sum indicates that we only sum over **k**-values of the magnetic Brillouin zone, which is half the structural Brillouin zone. Diagonalization is obtained through the transformation:

$$c_{\mathbf{k}\sigma} = u_{\mathbf{k}}\alpha_{\mathbf{k}\sigma} + v_{\mathbf{k}}\beta_{\mathbf{k}\sigma}, \tag{5.6}$$

$$c_{\mathbf{k}+\mathbf{Q}\sigma} = \sigma[v_{\mathbf{k}}\alpha_{\mathbf{k}\sigma} - u_{\mathbf{k}}\beta_{\mathbf{k}\sigma}], \tag{5.7}$$

where $\sigma = \pm 1$ for spin up/ spin down. The reverse transformation is given by:

$$\alpha_{\mathbf{k}\sigma} = u_{\mathbf{k}}c_{\mathbf{k}\sigma} + \sigma v_{\mathbf{k}}c_{\mathbf{k}+\mathbf{Q}\sigma}, \tag{5.8}$$

$$\beta_{\mathbf{k}\sigma} = v_{\mathbf{k}}c_{\mathbf{k}\sigma} - \sigma u_{\mathbf{k}}c_{\mathbf{k}+\mathbf{Q}\sigma}. \tag{5.9}$$

The diagonalization gives:

$$H_{\text{SDW}} = {\sum_{\mathbf{k}}}' \sum_{\sigma} [E^{\alpha}_{\mathbf{k}}\alpha^{\dagger}_{\mathbf{k}\sigma}\alpha_{\mathbf{k}\sigma} + E^{\beta}_{\mathbf{k}}\beta^{\dagger}_{\mathbf{k}\sigma}\beta_{\mathbf{k}\sigma}], \tag{5.10}$$

where the eigenenergies are given by:

$$E^{\alpha,\beta}_{\mathbf{k}} = \frac{\epsilon_{\mathbf{k}} + \epsilon_{\mathbf{k}+\mathbf{Q}}}{2} \pm \sqrt{\left(\frac{\epsilon_{\mathbf{k}} - \epsilon_{\mathbf{k}+\mathbf{Q}}}{2}\right)^2 + W^2} \tag{5.11}$$

$$= [-4t'\cos(k_x)\cos(k_y) - \mu] \pm \sqrt{[-2t\left(\cos(k_x) + \cos(k_y)\right)]^2 + W^2}. \tag{5.12}$$

From this expression it is seen that electron-hole symmetry is broken in the presence of next-nearest neighbour interactions, t', and doping away from half filling, i.e. $\mu \neq 0$. We express the magnetic gap equation, Eq. (5.3), in terms of the eigenenergies $E^{\alpha,\beta}_{\mathbf{k}}$. The mean values are given by:

$$\langle c^{\dagger}_{\mathbf{k}\uparrow}c_{\mathbf{k}+\mathbf{Q}\uparrow}\rangle = u_{\mathbf{k}}v_{\mathbf{k}}[f(E^{\alpha}_{\mathbf{k}}) - f(E^{\beta}_{\mathbf{k}})], \tag{5.13}$$

$$\langle c^{\dagger}_{\mathbf{k}\downarrow}c_{\mathbf{k}+\mathbf{Q}\downarrow}\rangle = -u_{\mathbf{k}}v_{\mathbf{k}}[f(E^{\alpha}_{\mathbf{k}}) - f(E^{\beta}_{\mathbf{k}})] = -\langle c^{\dagger}_{\mathbf{k}\uparrow}c_{\mathbf{k}+\mathbf{Q}\uparrow}\rangle. \tag{5.14}$$

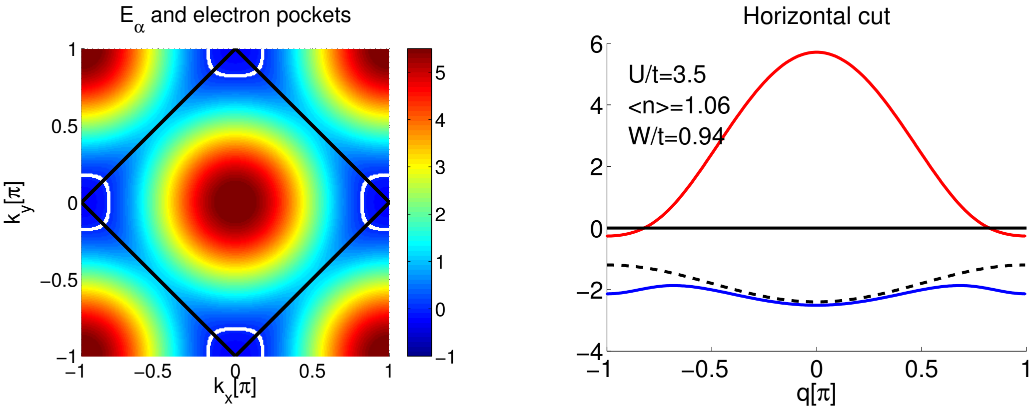

Figure 5.7: Plot of the dispersion $E^{\alpha}_{\mathbf{k}}$ for electron doping of 6 %. Electron pockets appear in the region around $(\pi, 0)$.

Since $u_{\mathbf{k}} v_{\mathbf{k}} = \frac{1}{2}\frac{W}{E^{-}_{\mathbf{k}}} = \frac{1}{2}\frac{W}{\sqrt{\left(\frac{\epsilon_{\mathbf{k}}-\epsilon_{\mathbf{k}+\mathbf{Q}}}{2}\right)^2+W^2}}$ we have:

$$
\begin{aligned}
W &= -\frac{U}{N}\sum_{\mathbf{k}}{}' \, 2u_{\mathbf{k}} v_{\mathbf{k}} [f(E^{\alpha}_{\mathbf{k}}) - f(E^{\beta}_{\mathbf{k}})] \\
&\Updownarrow \\
W &= -\frac{U}{N}\sum_{\mathbf{k}}{}' \frac{W}{\sqrt{\left(\frac{\epsilon_{\mathbf{k}}-\epsilon_{\mathbf{k}+\mathbf{Q}}}{2}\right)^2 + W^2}} [f(E^{\alpha}_{\mathbf{k}}) - f(E^{\beta}_{\mathbf{k}})] \\
&\Updownarrow \\
\frac{1}{U} &= -\frac{1}{N}\sum_{\mathbf{k}}{}' \frac{1}{\sqrt{\left(\frac{\epsilon_{\mathbf{k}}-\epsilon_{\mathbf{k}+\mathbf{Q}}}{2}\right)^2 + W^2}} [f(E^{\alpha}_{\mathbf{k}}) - f(E^{\beta}_{\mathbf{k}})].
\end{aligned}
\tag{5.15}
$$

This equation is solved self-consistently in order to obtain the mean field parameter W corresponding to a given set of parameters t, t', U and μ. Note that U is the value of the Coulomb repulsion in the real space Hubbard model and N is the number of states in the structural Brillouin zone. We always set $t = 1$ and express all other energies in units of t. In the cuprates the value of t is estimated to $350 - 400$ meV and $t' \simeq 80 - 200$ meV [1].

After having evaluated the magnetic gap equation self-consistently we consider the dispersions $E^{\alpha}_{\mathbf{k}}$ and $E^{\beta}_{\mathbf{k}}$ given in Eq. (5.12). The band given by $E^{\alpha}_{\mathbf{k}}$ gives rise to Fermi pockets that are electron-like, and appear in the antinodal regions around $(\pm\pi, 0)$ and $(0, \pm\pi)$. The band given by $E^{\beta}_{\mathbf{k}}$ gives rise to hole pockets in the nodal regions around $(\pm\frac{\pi}{2}, \pm\frac{\pi}{2})$ and $(\pm\frac{\pi}{2}, \mp\frac{\pi}{2})$. In Figs. 5.7 and 5.8 the energy bands for electron doping and hole doping are shown. In the electron-doped case we get electron pockets in the $(\pi, 0)$ region, while in the hole-doped case we get hole pockets in the $(\frac{\pi}{2}, \frac{\pi}{2})$ region. At small values of U and finite electron doping, when the magnetic gap becomes small enough, also hole pockets might shown up (not shown) and in this case both electron and hole pockets are present simultaneously. Note the structure of the bands revealed from the diagonal cut shown in Figs. 5.8(right); here we clearly see the reminiscent feature of the band crossing at $(\frac{\pi}{2}, \frac{\pi}{2})$ and $(-\frac{\pi}{2}, -\frac{\pi}{2})$ where electron and hole bands are gapped by $2W$. This is the structure giving rise to the (π, π) peak in the susceptibilities.

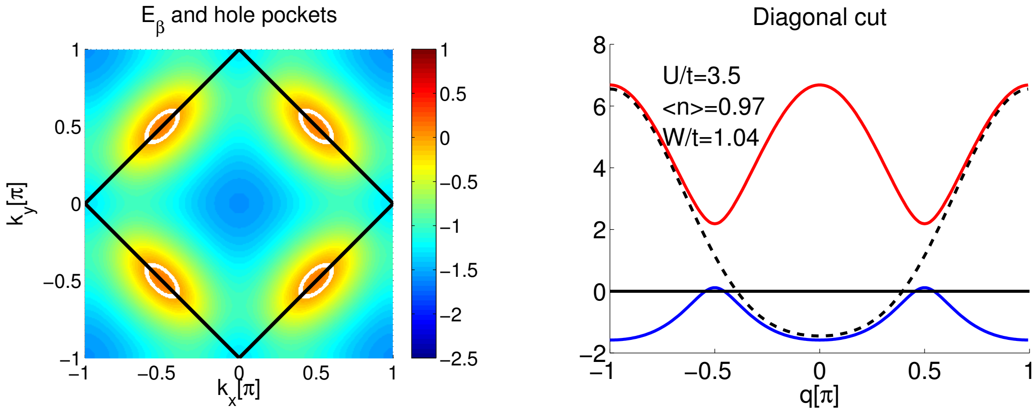

Figure 5.8: Plot of the dispersion $E^{\beta}_{\mathbf{k}}$ for hole doping of 3 %. Hole pockets appear in the $(\frac{\pi}{2}, \frac{\pi}{2})$ region.

5.5 Spin susceptibilities in the SDW state

We calculate the spin susceptibilities due to the ordered phase of electronic moments. The spin quantization axis is chosen along the z-axis, and the longitudinal (spin amplitude) susceptibility is given by:

$$\chi^z_0(\mathbf{q},\omega) = \frac{i}{2N}\int dt e^{i(\omega+i\eta)t}\langle T S^z_{\mathbf{q}}(t) S^z_{-\mathbf{q}}\rangle, \tag{5.16}$$

$$\tag{5.17}$$

whereas the transverse (spin orientational) susceptibility is given by:

$$\chi^{+-}_0(\mathbf{q},\omega) = \frac{i}{2N}\int dt e^{i(\omega+i\eta)t}\langle T S^+_{\mathbf{q}}(t) S^-_{-\mathbf{q}}\rangle. \tag{5.18}$$

In order to calculate the correlation functions, we must relate the spin operators to the electronic c-operators:

$$S^z_{\mathbf{q}} = \sum_{\mathbf{k}}[c^{\dagger}_{\mathbf{k}+\mathbf{q}\uparrow}c_{\mathbf{k}\uparrow} - c^{\dagger}_{\mathbf{k}+\mathbf{q}\downarrow}c_{\mathbf{k}\downarrow}], \tag{5.19}$$

$$S^+_{\mathbf{q}} = \sum_{\mathbf{k}} c^{\dagger}_{\mathbf{k}+\mathbf{q}\uparrow}c_{\mathbf{k}\downarrow}, \tag{5.20}$$

$$S^-_{\mathbf{q}} = \sum_{\mathbf{k}} c^{\dagger}_{\mathbf{k}+\mathbf{q}\downarrow}c_{\mathbf{k}\uparrow}. \tag{5.21}$$

$$\tag{5.22}$$

In the paramagnetic phase where spin rotation symmetry is preserved, the relation between the longitudinal and transverse susceptibility is simply $\chi^z_0 = 2\chi^{+-}_0$, since all spin directions are equivalent, $\chi^z_0 = \chi^x_0 = \chi^y_0$ and $\chi^{+-}_0 = \frac{1}{4}(\chi^x_0 + \chi^y_0)$.

In the SDW phase, a continuous global symmetry is broken when the spins align in a preferred direction. Therefore a Goldstone mode appears in the spin-orientational channel. This is the transverse spin fluctuations. In the SDW phase the longitudinal spin fluctuations become gapped. Expressing the susceptibilities in terms of the energy bands of the SDW phase gives:

$$\begin{aligned}\chi_0^{zz}(\mathbf{q},\omega) &= \frac{1}{2}\sideset{}{'}\sum_{\mathbf{k}}\sum_{\gamma}\underbrace{\left(1+\frac{\epsilon^+_{\mathbf{k}}\epsilon^-_{\mathbf{k}+\mathbf{q}}+W^2}{\sqrt{(\epsilon^-_{\mathbf{k}})^2+W^2}\sqrt{(\epsilon^-_{\mathbf{k}+\mathbf{q}})^2+W^2}}\right)}_{c^{zz,\mathrm{intra}}_{\mathbf{k},\mathbf{q}}}\frac{f(E^{\gamma}_{\mathbf{k}+\mathbf{q}})-f(E^{\gamma}_{\mathbf{k}})}{\omega+i0^+-E^{\gamma}_{\mathbf{k}+\mathbf{q}}+E^{\gamma}_{\mathbf{k}}}\\ &+\frac{1}{2}\sideset{}{'}\sum_{\mathbf{k}}\sum_{\gamma\neq\gamma'}\underbrace{\left(1-\frac{\epsilon^-_{\mathbf{k}}\epsilon^-_{\mathbf{k}+\mathbf{q}}+W^2}{\sqrt{(\epsilon^-_{\mathbf{k}})^2+W^2}\sqrt{(\epsilon^-_{\mathbf{k}+\mathbf{q}})^2+W^2}}\right)}_{c^{zz,\mathrm{inter}}_{\mathbf{k},\mathbf{q}}}\frac{f(E^{\gamma'}_{\mathbf{k}+\mathbf{q}})-f(E^{\gamma}_{\mathbf{k}})}{\omega+i0^+-E^{\gamma'}_{\mathbf{k}+\mathbf{q}}+E^{\gamma}_{\mathbf{k}}},\end{aligned}\tag{5.23}$$

and

$$\begin{aligned}\chi_0^{+-}(\mathbf{q},\omega) &= \frac{1}{2}\sideset{}{'}\sum_{\mathbf{k}}\sum_{\gamma}\underbrace{\left(1+\frac{\epsilon^-_{\mathbf{k}}\epsilon^-_{\mathbf{k}+\mathbf{q}}-W^2}{\sqrt{(\epsilon^-_{\mathbf{k}})^2+W^2}\sqrt{(\epsilon^-_{\mathbf{k}+\mathbf{q}})^2+W^2}}\right)}_{c^{+-,\mathrm{intra}}_{\mathbf{k},\mathbf{q}}}\frac{f(E^{\gamma}_{\mathbf{k}+\mathbf{q}})-f(E^{\gamma}_{\mathbf{k}})}{\omega+i0^+-E^{\gamma}_{\mathbf{k}+\mathbf{q}}+E^{\gamma}_{\mathbf{k}}}\\ &+\frac{1}{2}\sideset{}{'}\sum_{\mathbf{k}}\sum_{\gamma\neq\gamma'}\underbrace{\left(1-\frac{\epsilon^-_{\mathbf{k}}\epsilon^-_{\mathbf{k}+\mathbf{q}}-W^2}{\sqrt{(\epsilon^-_{\mathbf{k}})^2+W^2}\sqrt{(\epsilon^-_{\mathbf{k}+\mathbf{q}})^2+W^2}}\right)}_{c^{+-,\mathrm{inter}}_{\mathbf{k},\mathbf{q}}}\frac{f(E^{\gamma'}_{\mathbf{k}+\mathbf{q}})-f(E^{\gamma}_{\mathbf{k}})}{\omega+i0^+-E^{\gamma'}_{\mathbf{k}+\mathbf{q}}+E^{\gamma}_{\mathbf{k}}}.\end{aligned}\tag{5.24}$$

In addition, there is an Umklapp contribution to the transverse susceptibility in the SDW phase, and the RPA susceptibility in the transverse channel becomes a 2 × 2 matrix. However, in calculating the effective pairing strength we are restricted to $\omega = 0$, and since the Umklapp susceptibility is zero when evaluated at zero energy, the spin susceptibilities takes the usual RPA form:

$$\chi_z(\mathbf{q},0) = \frac{\chi_0^z(\mathbf{q},0)}{1-U\chi_0^z(\mathbf{q},0)},\tag{5.25}$$

$$\chi_{+-}(\mathbf{q},0) = \frac{\chi_0^{+-}(\mathbf{q},0)}{1-U\chi_0^{+-}(\mathbf{q},0)}.\tag{5.26}$$

The Goldstone mode is manifested by a gapless pole in the transverse susceptibility, and within the RPA this is given by $1-U\chi_0^{+-}(\mathbf{q},\omega=0)=0$ where $\mathbf{q}=\mathbf{Q}$ is the ordering vector. Evaluating the bare transverse susceptibility at zero energy and at $\mathbf{Q}$ gives:

$$\begin{aligned}\chi_0^{+-}(\mathbf{Q},\omega=0) &= \frac{1}{2}\sideset{}{'}\sum_{\mathbf{k}\gamma}\underbrace{\left(1+\frac{-(\epsilon^-_{\mathbf{k}})^2-W^2}{(\epsilon^-_{\mathbf{k}})^2+W^2}\right)}_{=0}\left(\frac{f(E^{\gamma}_{\mathbf{k}+\mathbf{q}})-f(E^{\gamma}_{\mathbf{k}})}{E^{\gamma}_{\mathbf{k}}-E^{\gamma}_{\mathbf{k}+\mathbf{q}}}\right)\\ &+\frac{1}{2}\sideset{}{'}\sum_{\mathbf{k},\gamma\neq\gamma'}\underbrace{\left(1-\frac{-(\epsilon^-_{\mathbf{k}})^2-W^2}{(\epsilon^-_{\mathbf{k}})^2+W^2}\right)}_{=2}\left(\frac{f(E^{\gamma'}_{\mathbf{k}+\mathbf{q}})-f(E^{\gamma}_{\mathbf{k}})}{E^{\gamma}_{\mathbf{k}}-E^{\gamma'}_{\mathbf{k}+\mathbf{q}}}\right)\\ &= \frac{2}{2}\sideset{}{'}\sum_{\mathbf{k}}\left[\frac{f(E^{\alpha}_{\mathbf{k}})-f(E^{\beta}_{\mathbf{k}})}{-E^{\alpha}_{\mathbf{k}}+E^{\beta}_{\mathbf{k}}}+\frac{f(E^{\beta}_{\mathbf{k}})-f(E^{\alpha}_{\mathbf{k}})}{-E^{\beta}_{\mathbf{k}}+E^{\alpha}_{\mathbf{k}}}\right]\\ &= -\sideset{}{'}\sum_{\mathbf{k}}\frac{2}{E^{\alpha}_{\mathbf{k}}-E^{\beta}_{\mathbf{k}}}\left[f(E^{\alpha}_{\mathbf{k}})-f(E^{\beta}_{\mathbf{k}})\right]\\ &= -\sideset{}{'}\sum_{\mathbf{k}}\frac{1}{E^{-}_{\mathbf{k}}}\left[f(E^{\alpha}_{\mathbf{k}})-f(E^{\beta}_{\mathbf{k}})\right].\end{aligned}\tag{5.27}$$

At the instability the denominator of the transverse RPA susceptibility equals zero. Thereby we obtain the equation:

$$1 - U\chi_0(\mathbf{Q}, \omega = 0) = 0 \Leftrightarrow \frac{1}{U} = -\sum_{\mathbf{k}}{}' \frac{1}{E^-_{\mathbf{k}}} \left[f(E^\alpha_{\mathbf{k}}) - f(E^\beta_{\mathbf{k}}) \right] \tag{5.28}$$

This equation is exactly the same at the gap equation for the magnetic mean field stated in Eq. (5.15). This means that when the magnetic gap equation is solved self-consistently, it is automatically ensured that the transverse spin susceptibility as calculated within RPA has a pole at the ordering vector $\mathbf{Q} = (\pi, \pi)$.

The spectrum for the transverse and longitudinal spin fluctuations are plotted in Fig. 5.9 for different bands. For the longitudinal spin waves it is seen that the spectrum is gapped at the ordering vector $\mathbf{Q}$ by $2W$. Notice that in the case of a band with hole pockets, see last row of Fig. 5.9, there are indications that the AFM order is not a stable solution as discussed in Ref. [94]. The value of the Coulomb interaction stated in the plots is the original real space Hubbard value as it appears in the Hamiltonian Eq. (5.1). Note that the U that is referred to in Ref. [94] is half of this value.

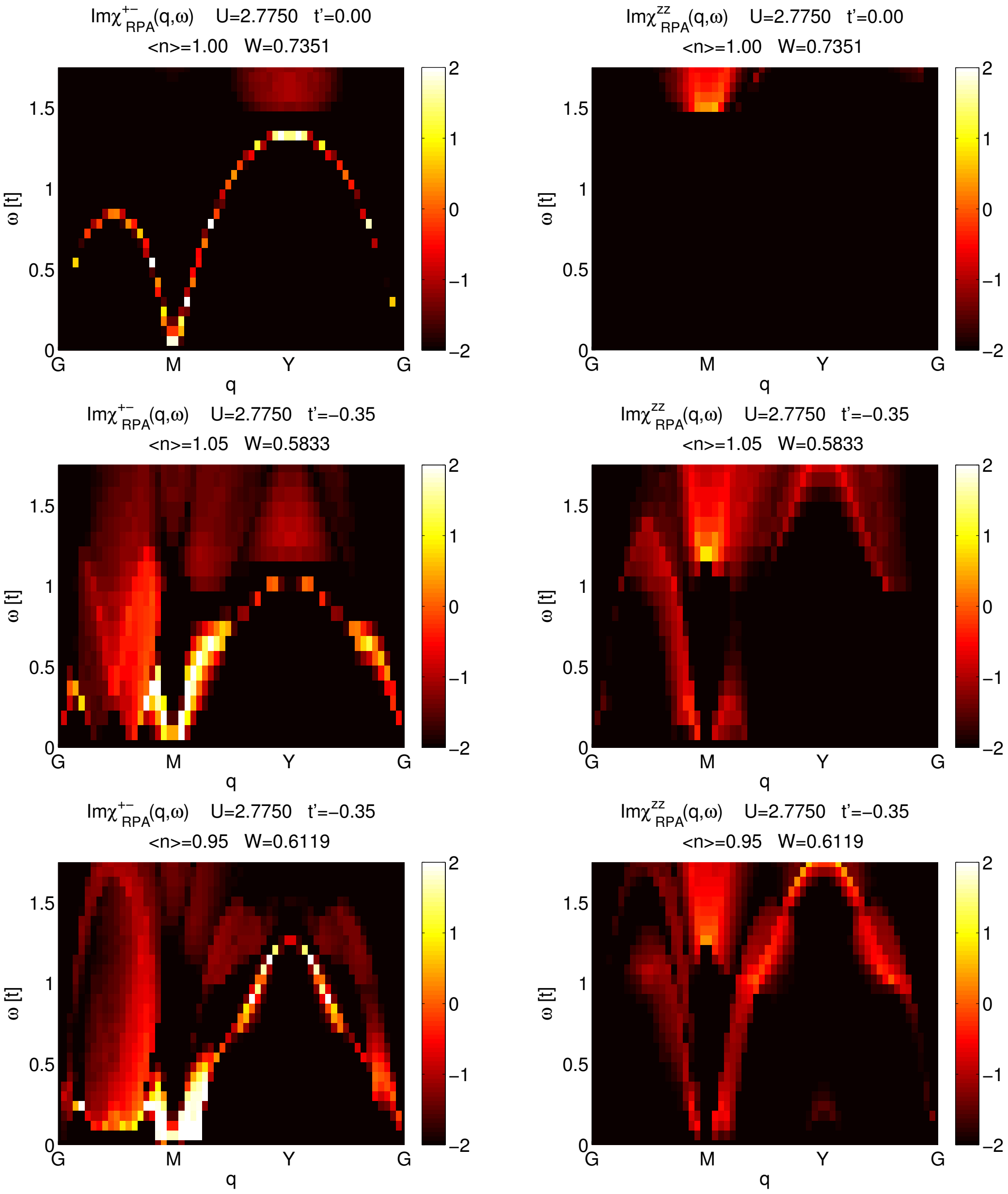

Figure 5.9: Transverse and longitudinal spin waves for the undoped case (**upper row**), 5% electron doped (**middle row**) and 5% hole doped (**lower row**) plotted on a logarithmic scale for a path in the reduced magnetic Brillouin zone from $G = (0, 0)$ to $M = (\pi, \pi)$ to $Y = (0, \pi)$ back to $G = (0, 0)$. In the undoped case there is a spin gap of size $2W$ for the longitudinal spin waves at the M position (In this simple band the energy minimum of the conduction band is W at (π, π) whereas the valence band has its maximum , $-W$, at this position). This reminiscent signature of the gap is still apparent in the case of weak hole- and electron doping, but spectral weight is shifted down in energy in these cases as a result of the appearance of Fermi pockets, i.e. amplitude spin fluctuations are possible for energies below $2W$. In the transverse RPA susceptibility of the undoped case the gapless mode at M is the Goldstone mode related to the broken spin rotation symmetry, see upper left corner. This mode is robust in the electron-doped case. However, in the hole-doped case the gapless feature is spread out in a region close to the (π, π) point. This indicates that the SDW phase with ordering vector $\mathbf{Q}$ is not a stable solution [94].

5.6 Superconducting pairing interactions in the SDW phase

The effective pairing interaction is derived diagrammatically by the same procedure as described in chapter 2. The reason is that the Coulomb interaction U connects the bare electrons, and not the quasi-particles of the SDW phase. As usual, we therefore start by:

$$H = U \sum_i n_{i\uparrow} n_{i\downarrow}. \tag{5.29}$$

We choose to represent the tranverse part of the interaction Hamiltonian as a spin flip interaction. In real space the two interaction Hamilonians are therefore expressed as:

$$\begin{aligned} H^{lo/ch} &= \sum_{i,j} V_{\text{bub}}(i,j) c^\dagger_{i\uparrow} c^\dagger_{j\downarrow} c_{j\downarrow} c_{i\uparrow} && \text{(non-spin flip)} \\ H^{tr} &= -\frac{1}{2} \sum_{i,j} \sum_\sigma V_{+-}(i,j) c^\dagger_{i\sigma} c^\dagger_{j\overline{\sigma}} c_{j\sigma} c_{i\overline{\sigma}} && \text{(spin flip)} \end{aligned} \tag{5.30}$$

Note that both interactions Hamiltonian turn into the original Hubbard Hamiltonian in the limit $V = U\delta_{i,j}$. The spin flip feature of the transverse fluctuations are seen from the fact, that an electron of spin $\overline{\sigma}$ is annihilated at site i, whereas an electron of spin σ is created at site i. The opposite is true for site j.

In reciprocal space the representation is:

$$H^{lo/ch} = \frac{1}{2N} \sum_{\mathbf{k},\mathbf{k}',\mathbf{q}} [V_{lo}(\mathbf{k}-\mathbf{k}') c^\dagger_{\mathbf{k}'\uparrow} c^\dagger_{-\mathbf{k}'\downarrow} c_{-\mathbf{k}\downarrow} c_{\mathbf{k}\uparrow} + h.c.] \tag{5.31}$$

$$H_{tr} = -\frac{1}{2N} \sum_{\mathbf{k},\mathbf{k}',\mathbf{q}} \left[V_{+-}(\mathbf{k}-\mathbf{k}') c^\dagger_{\mathbf{k}'\uparrow} c^\dagger_{-\mathbf{k}'\downarrow} c_{-\mathbf{k}\uparrow} c_{\mathbf{k}\downarrow} + h.c.\right] \tag{5.32}$$

The derivation of the Eq. (5.31) is given in chapter 2 and the derivation of Eq. (5.32) in appendix C. The bare interaction vertices are given by:

$$V_{lo}(\mathbf{q}) = U + V_z(\mathbf{q}) - V_c(\mathbf{q}), \tag{5.33}$$

with

$$V_z(\mathbf{q}) = \frac{U^2 \chi_0^z(\mathbf{q},0)}{1 - U\chi_0^z(\mathbf{q},0)}, \tag{5.34}$$

$$V_c(\mathbf{q}) = \frac{U^2 \chi_0^z(\mathbf{q},0)}{1 + U\chi_0^z(\mathbf{q},0)}, \tag{5.35}$$

and

$$V_{+-}(\mathbf{q}) = \frac{U^2 \chi_0^{+-}(\mathbf{q},0)}{1 - U\chi_0^{+-}(\mathbf{q},0)}. \tag{5.36}$$

Having established the interaction Hamiltonians in both channels in terms of bare electronic operators, we now turn to the formulation of the interaction Hamiltonians in terms of the SDW quasi-particles, α and β. We use the transformations given in Eqs. (5.6-5.7) and get the interaction Hamiltonians:

$$\begin{aligned} H_{c/z} = \frac{1}{4N} \sum_{\mathbf{k}\mathbf{k}'\sigma}{}^{'} \Big[& \Gamma^z_{\mathbf{k},\mathbf{k}'} (\alpha^\dagger_{\mathbf{k}'\sigma} \alpha^\dagger_{-\mathbf{k}'\overline{\sigma}} \alpha_{-\mathbf{k}\overline{\sigma}} \alpha_{\mathbf{k}\sigma} + \beta^\dagger_{\mathbf{k}'\sigma} \beta^\dagger_{-\mathbf{k}'\overline{\sigma}} \beta_{-\mathbf{k}\overline{\sigma}} \beta_{\mathbf{k}\sigma}) \\ & + \tilde{\Gamma}^z_{\mathbf{k},\mathbf{k}'} (\alpha^\dagger_{\mathbf{k}'\sigma} \alpha^\dagger_{-\mathbf{k}'\overline{\sigma}} \beta_{-\mathbf{k}\overline{\sigma}} \beta_{\mathbf{k}\sigma} + \beta^\dagger_{\mathbf{k}'\sigma} \beta^\dagger_{-\mathbf{k}'\overline{\sigma}} \alpha_{-\mathbf{k}\overline{\sigma}} \alpha_{\mathbf{k}\sigma}) \Big], \end{aligned} \tag{5.37}$$

$$
\begin{aligned}
H_{\pm} &= -\frac{1}{2N} \sum_{\mathbf{k}\mathbf{k}'\sigma}{}' \Big[\Gamma^{+-}_{\mathbf{k},\mathbf{k}'} (\alpha^{\dagger}_{\mathbf{k}'\sigma} \alpha^{\dagger}_{-\mathbf{k}'\overline{\sigma}} \alpha_{-\mathbf{k}\sigma} \alpha_{\mathbf{k}\overline{\sigma}} + \beta^{\dagger}_{\mathbf{k}'\sigma} \beta^{\dagger}_{-\mathbf{k}'\overline{\sigma}} \beta_{-\mathbf{k}\sigma} \beta_{\mathbf{k}\overline{\sigma}}) \\
&\qquad + \tilde{\Gamma}^{+-}_{\mathbf{k},\mathbf{k}'} (\alpha^{\dagger}_{\mathbf{k}'\sigma} \alpha^{\dagger}_{-\mathbf{k}'\overline{\sigma}} \beta_{-\mathbf{k}\sigma} \beta_{\mathbf{k}\overline{\sigma}} + \beta^{\dagger}_{\mathbf{k}'\sigma} \beta^{\dagger}_{-\mathbf{k}'\overline{\sigma}} \alpha_{-\mathbf{k}\sigma} \alpha_{\mathbf{k}\overline{\sigma}}) \Big], \qquad (5.38)
\end{aligned}
$$

and

$$
\begin{aligned}
H^{\mathrm{ss}}_{c/z} &= \frac{1}{2N} \sum_{\mathbf{k}\mathbf{k}'\sigma}{}' \Big[\Gamma^{\mathrm{ss}}_{\mathbf{k},\mathbf{k}'} (\alpha^{\dagger}_{\mathbf{k}'\sigma} \alpha^{\dagger}_{-\mathbf{k}'\sigma} \alpha_{-\mathbf{k}\sigma} \alpha_{\mathbf{k}\sigma} + \beta^{\dagger}_{\mathbf{k}'\sigma} \beta^{\dagger}_{-\mathbf{k}'\sigma} \beta_{-\mathbf{k}\sigma} \beta_{\mathbf{k}\sigma}) \\
&\qquad + \tilde{\Gamma}^{\mathrm{ss}}_{\mathbf{k},\mathbf{k}'} (\alpha^{\dagger}_{\mathbf{k}'\sigma} \alpha^{\dagger}_{-\mathbf{k}'\sigma} \beta_{-\mathbf{k}\sigma} \beta_{\mathbf{k}\sigma} + \beta^{\dagger}_{\mathbf{k}'\sigma} \beta^{\dagger}_{-\mathbf{k}'\sigma} \alpha_{-\mathbf{k}\sigma} \alpha_{\mathbf{k}\sigma}) \Big]. \qquad (5.39)
\end{aligned}
$$

The dressed pairing vertices are given by:

$$
\begin{aligned}
\Gamma^{z}_{\mathbf{k},\mathbf{k}'} &= [2U - V_c(\mathbf{k}-\mathbf{k}')] l^2(\mathbf{k},\mathbf{k}') - [2U - V_c(\mathbf{k}-\mathbf{k}'+\mathbf{Q})] m^2(\mathbf{k},\mathbf{k}') \\
&\quad + V_z(\mathbf{k}-\mathbf{k}') l^2(\mathbf{k},\mathbf{k}') - V_z(\mathbf{k}-\mathbf{k}'+\mathbf{Q}) m^2(\mathbf{k},\mathbf{k}'), \qquad (5.40)
\end{aligned}
$$

$$
\Gamma^{+-}_{\mathbf{k},\mathbf{k}'} = V_{+-}(\mathbf{k}-\mathbf{k}') n^2(\mathbf{k},\mathbf{k}') - V_{+-}(\mathbf{k}-\mathbf{k}'+\mathbf{Q}) p^2(\mathbf{k},\mathbf{k}'), \qquad (5.41)
$$

$$
\begin{aligned}
\Gamma^{\mathrm{ss}}_{\mathbf{k},\mathbf{k}'} &= -V_c(\mathbf{k}-\mathbf{k}') l^2(\mathbf{k},\mathbf{k}') - V_c(\mathbf{k}-\mathbf{k}'+\mathbf{Q}) m^2(\mathbf{k},\mathbf{k}') \\
&\quad - V_z(\mathbf{k}-\mathbf{k}') l^2(\mathbf{k},\mathbf{k}') - V_z(\mathbf{k}-\mathbf{k}'+\mathbf{Q}) m^2(\mathbf{k},\mathbf{k}'). \qquad (5.42)
\end{aligned}
$$

in agreement with the result of Schrieffer, Wen and Zhang, Ref. [80]. Details of the derivation is given in appendix C. The first two pairing contributions act between electrons of opposite spin and corresponds to interactions through longitudinal and transverse fluctuations, respectively. The last pairing contribution acts between electrons of same spin and is due to longitudinal fluctuations only, since in this case no spin flip processes can occur. The expression for the *inter*band pairings $\tilde{\Gamma}^{z}_{\mathbf{k},\mathbf{k}'}$, $\tilde{\Gamma}^{+-}_{\mathbf{k},\mathbf{k}'}$ and $\tilde{\Gamma}^{ss}_{\mathbf{k},\mathbf{k}'}$, are obtained by interchanging the coherence factors $p^2(\mathbf{k},\mathbf{k}') \leftrightarrow l^2(\mathbf{k},\mathbf{k}')$ and $m^2(\mathbf{k},\mathbf{k}') \leftrightarrow n^2(\mathbf{k},\mathbf{k}')$ in the Eqs. (5.40) and (5.41).
The bare interactions, V_c, V_z and V_{+-} are dressed by coherence factors of the SDW phase, which are given by

$$
\begin{aligned}
m^2(\mathbf{k},\mathbf{k}') &= (u_{\mathbf{k}} v_{\mathbf{k}'} + v_{\mathbf{k}} u_{\mathbf{k}'})^2 = \frac{1}{2}\Big(1 - \frac{\epsilon^{-}_{\mathbf{k}} \epsilon^{-}_{\mathbf{k}'} - W^2}{E^{-}_{\mathbf{k}} E^{-}_{\mathbf{k}'}}\Big) \qquad (5.43) \\
l^2(\mathbf{k},\mathbf{k}') &= (u_{\mathbf{k}} u_{\mathbf{k}'} + v_{\mathbf{k}} v_{\mathbf{k}'})^2 = \frac{1}{2}\Big(1 + \frac{\epsilon^{-}_{\mathbf{k}} \epsilon^{-}_{\mathbf{k}'} + W^2}{E^{-}_{\mathbf{k}} E^{-}_{\mathbf{k}'}}\Big) \qquad (5.44) \\
p^2(\mathbf{k},\mathbf{k}') &= (u_{\mathbf{k}} v_{\mathbf{k}'} - v_{\mathbf{k}} u_{\mathbf{k}'})^2 = \frac{1}{2}\Big(1 - \frac{\epsilon^{-}_{\mathbf{k}} \epsilon^{-}_{\mathbf{k}'} + W^2}{E^{-}_{\mathbf{k}} E^{-}_{\mathbf{k}'}}\Big) \qquad (5.45) \\
n^2(\mathbf{k},\mathbf{k}') &= (u_{\mathbf{k}} u_{\mathbf{k}'} - v_{\mathbf{k}} v_{\mathbf{k}'})^2 = \frac{1}{2}\Big(1 + \frac{\epsilon^{+}_{\mathbf{k}} \epsilon^{-}_{\mathbf{k}'} - W^2}{E^{-}_{\mathbf{k}} E^{-}_{\mathbf{k}'}}\Big) \qquad (5.46)
\end{aligned}
$$

Derivation of the expressions above make use of the eigenvector relations:

$$
\begin{aligned}
u^2_{\mathbf{k}}, v^2_{\mathbf{k}} &= \frac{1}{2}\Big(1 \pm \frac{\epsilon^{-}_{\mathbf{k}}}{E^{-}_{\mathbf{k}}}\Big), \qquad (5.47) \\
u_{\mathbf{k}} v_{\mathbf{k}} &= \frac{W}{2E^{-}_{\mathbf{k}}}, \qquad (5.48)
\end{aligned}
$$

where

$$\begin{aligned}\epsilon^{\pm}_{\mathbf{k}} &= \frac{\epsilon_{\mathbf{k}} \pm \epsilon_{\mathbf{k+Q}}}{2}, &(5.49)\\ E^{-}_{\mathbf{k}} &= \frac{E^{\alpha}_{\mathbf{k}} - E^{\beta}_{\mathbf{k}}}{2} = \sqrt{(\epsilon^{-}_{\mathbf{k}})^2 + W^2}. &(5.50)\end{aligned}$$

In principle, the gap structure can be inferred directly from knowledge about the **k**-space structure of the pairing potential. A naïve inspection of the sign of $\Gamma_{\mathbf{k},\mathbf{k}'}$ for a certain pair of $\mathbf{k}$ and $\mathbf{k}'$ tells us the favored relative sign of $\Delta_{\mathbf{k}}$ and $\Delta_{\mathbf{k}'}$: if $\Gamma_{\mathbf{k},\mathbf{k}'} < 0$ then it is favored to have $\text{sign}[\Delta_{\mathbf{k}}] = \text{sign}[\Delta_{\mathbf{k}'}]$, whereas if $\Gamma_{\mathbf{k},\mathbf{k}'} > 0$ then it is favorable to have $\text{sign}[\Delta_{\mathbf{k}}] = -\text{sign}[\Delta_{\mathbf{k}'}]$. The simplest example of this is the repulsive interaction for $\mathbf{k} - \mathbf{k}' = (\pi, \pi)$ supporting a $d_{x^2-y^2}$ gap in the paramagnetic phase close to half filling. In addition, transformation properties of the effective dressed pairing vertices have implications for the possible gap symmetries. We note that since $\epsilon^{-}_{\mathbf{k+Q}} = -\epsilon^{-}_{\mathbf{k}}$, the coherence factors satisfy:

$$\begin{aligned}m^2(\mathbf{k+Q},\mathbf{k}') &= m^2(\mathbf{k},\mathbf{k}'+\mathbf{Q}) = l^2(\mathbf{k},\mathbf{k}'), &(5.51)\\ l^2(\mathbf{k+Q},\mathbf{k}') &= l^2(\mathbf{k},\mathbf{k}'+\mathbf{Q}) = m^2(\mathbf{k},\mathbf{k}'), &(5.52)\\ p^2(\mathbf{k+Q},\mathbf{k}') &= p^2(\mathbf{k},\mathbf{k}'+\mathbf{Q}) = n^2(\mathbf{k},\mathbf{k}'), &(5.53)\\ n^2(\mathbf{k+Q},\mathbf{k}') &= n^2(\mathbf{k},\mathbf{k}'+\mathbf{Q}) = p^2(\mathbf{k},\mathbf{k}'). &(5.54)\end{aligned}$$

By inspection of Eqs. (5.40-5.42) it is seen that the transformation properties given above leads to the following transformation property of the pairing potentials:

$$\begin{aligned}\Gamma^{z}_{\mathbf{k+Q},\mathbf{k}'} &= \Gamma^{z}_{\mathbf{k},\mathbf{k}'+\mathbf{Q}} = -\Gamma^{z}_{\mathbf{k},\mathbf{k}'},\\ \Gamma^{+-}_{\mathbf{k+Q},\mathbf{k}'} &= \Gamma^{+-}_{\mathbf{k},\mathbf{k}'+\mathbf{Q}} = -\Gamma^{+-}_{\mathbf{k},\mathbf{k}'},\\ \Gamma^{ss}_{\mathbf{k+Q},\mathbf{k}'} &= \Gamma^{ss}_{\mathbf{k},\mathbf{k}'+\mathbf{Q}} = -\Gamma^{ss}_{\mathbf{k},\mathbf{k}'}.\end{aligned} \tag{5.55}$$

This symmetry carries over to the superconducting state, and thus in the SDW phase the only allowed gap symmetries are the ones complying with:

$$\Delta_{\mathbf{k+Q},\mathbf{k}'} = \Delta_{\mathbf{k},\mathbf{k}'+\mathbf{Q}} = -\Delta_{\mathbf{k},\mathbf{k}'} \tag{5.56}$$

As mentioned in chapter 2, the gap solutions of the two dimensional square lattice can be classified according to the five irreducible representations of the D_{4h} group that are even under reflection in the horizontal plane, i.e. ext. s-wave, $d_{x^2-y^2}$, d_{xy}, g_{xy} and the triplet solution, p_x/p_y, which is doubly degenerate. In the SDW phase we are faced with an additional symmetry constraint, Eq. (5.56), which disqualifies the d_{xy} solution. As a result we expect the leading gap symmetries among the possibilities:

$$\begin{aligned}\text{ext. } s &= \cos(k_x) + \cos(k_y), &(5.57)\\ d_{x^2-y^2} &= \cos(k_x) - \cos(k_y), &(5.58)\\ g_{xy} &= [\cos(k_x) - \cos(k_y)]\sin(k_x)\sin(k_y), &(5.59)\\ p_x &= \sin(k_x). &(5.60)\end{aligned}$$

In addition we state a higher order triplet solution, which we have dubbed p'-wave.

$$p'_x = [\cos(k_x) - \cos(k_y)][\cos(k_x) + \cos(k_y)]\sin(k_x). \tag{5.61}$$

We shall see that this will be the leading solution among all triplet solutions for any doping. However, as we shall see below, it never dominates over the singlet solutions.

5.7 Superconducting gap equation in the coexistence phase

When we calculate the superconducting gap, we restrict ourselves to Cooper pairing within each band. The reason is that Cooper pairs of zero total momentum or Umklapp Cooper pairs, which carry momentum $\mathbf{Q}$ cannot be constructed by having one dressed electron in the α band and the other dressed electron in the β-band. This simplifies the interaction Hamilonian considerably. Pair scattering interactions can take place between two Cooper pairs of the same band, or between the bands through the mean fields of the superconducting order. This gives rise to two coupled self-consistent equations for $\Delta^{\alpha}_{\mathbf{k}}$ and $\Delta^{\beta}_{\mathbf{k}}$.

The presence of magnetic order breaks time reversal symmetry. Superconducting gaps defined in terms of the original c-operators, the bare electrons, can not be classified into a singlet and triplet part since these channels will not be well-separated. The reason is that SDW order leads to different spatial wave functions of the spin up and spin down electrons and the wave function of a pair of electrons can not be split into a spin-part and a momentum part. However, even though time reversal symmetry is broken, inversion symmetry is still preserved. Therefore, it is possible to classify the gap solutions in terms of singlet and triplet gap solutions, which are even and odd under $\mathbf{k} \to -\mathbf{k}$, respectively. The important point to note is, that singlet and triplet gaps must be defined in terms of the new quasi-particle operators, which we call α-particles for those living on the electron pockets and β-particles for the ones at the hole pockets.

Now we ask the following question: What does it mean to have a gap, which is singlet in terms of e.g. β-operators? This gap will be even under $\mathbf{k} \to -\mathbf{k}$. In order to see how it relates to the original bare electron operators, we rewrite the β-singlet and triplet gaps in terms of c-operators:

$$\begin{aligned}
\Delta^{\beta}_{\text{sing/trip}} = \Delta^{\beta}_{\uparrow\downarrow} \mp \Delta^{\beta}_{\downarrow\uparrow} &= \langle \beta_{-\mathbf{k}\downarrow}\beta_{\mathbf{k}\uparrow}\rangle \mp \langle \beta_{-\mathbf{k}\uparrow}\beta_{\mathbf{k}\downarrow}\rangle \\
\\
\langle \beta_{-\mathbf{k}\downarrow}\beta_{\mathbf{k}\uparrow}\rangle &= \langle (v_{\mathbf{k}}c_{-\mathbf{k}\downarrow} + u_{\mathbf{k}}c_{-\mathbf{k}+\mathbf{Q}\downarrow})(v_{\mathbf{k}}c_{\mathbf{k}\uparrow} - u_{\mathbf{k}}c_{\mathbf{k}+\mathbf{Q}\uparrow})\rangle \\
&= \langle v^2_{\mathbf{k}}c_{-\mathbf{k}\downarrow}c_{\mathbf{k}\uparrow} - u^2_{\mathbf{k}}c_{-\mathbf{k}+\mathbf{Q}\downarrow}c_{\mathbf{k}+\mathbf{Q}\uparrow} - u_{\mathbf{k}}v_{\mathbf{k}}c_{-\mathbf{k}\downarrow}c_{\mathbf{k}+\mathbf{Q}\uparrow} + u_{\mathbf{k}}v_{\mathbf{k}}c_{-\mathbf{k}+\mathbf{Q}\downarrow}c_{\mathbf{k}\uparrow}\rangle \\
\langle \beta_{-\mathbf{k}\uparrow}\beta_{\mathbf{k}\downarrow}\rangle &= \langle (v_{\mathbf{k}}c_{-\mathbf{k}\uparrow} - u_{\mathbf{k}}c_{-\mathbf{k}+\mathbf{Q}\uparrow})(v_{\mathbf{k}}c_{\mathbf{k}\downarrow} + u_{\mathbf{k}}c_{\mathbf{k}+\mathbf{Q}\downarrow})\rangle \\
&= \langle v^2_{\mathbf{k}}c_{-\mathbf{k}\uparrow}c_{\mathbf{k}\downarrow} - u^2_{\mathbf{k}}c_{-\mathbf{k}+\mathbf{Q}\uparrow}c_{\mathbf{k}+\mathbf{Q}\downarrow} + u_{\mathbf{k}}v_{\mathbf{k}}c_{-\mathbf{k}\uparrow}c_{\mathbf{k}+\mathbf{Q}\downarrow} - u_{\mathbf{k}}v_{\mathbf{k}}c_{-\mathbf{k}+\mathbf{Q}\uparrow}c_{\mathbf{k}\downarrow}\rangle
\end{aligned}$$

$$\begin{aligned}
\Delta^{\beta}_{\text{sing}} &= v^2_{\mathbf{k}}[\langle c_{-\mathbf{k}\downarrow}c_{\mathbf{k}\uparrow}\rangle - \langle c_{-\mathbf{k}\uparrow}c_{\mathbf{k}\downarrow}\rangle] \\
&\quad -u^2_{\mathbf{k}}[\langle c_{-\mathbf{k}+\mathbf{Q}\downarrow}c_{\mathbf{k}+\mathbf{Q}\uparrow}\rangle - \langle c_{-\mathbf{k}+\mathbf{Q}\uparrow}c_{\mathbf{k}+\mathbf{Q}\downarrow}\rangle] \\
&\quad -u_{\mathbf{k}}v_{\mathbf{k}}[\langle c_{-\mathbf{k}\downarrow}c_{\mathbf{k}+\mathbf{Q}\uparrow}\rangle + \langle c_{-\mathbf{k}\uparrow}c_{\mathbf{k}+\mathbf{Q}\downarrow}\rangle] \\
&\quad +u_{\mathbf{k}}v_{\mathbf{k}}[\langle c_{-\mathbf{k}+\mathbf{Q}\downarrow}c_{\mathbf{k}\uparrow}\rangle + \langle c_{-\mathbf{k}+\mathbf{Q}\uparrow}c_{\mathbf{k}\downarrow}\rangle]
\end{aligned} \tag{5.62}$$

We see that the Umklapp Cooper pair terms (last two lines) are triplet-like, while the normal Cooper pairs (two first lines) appear in the singlet form. For the triplet gap the results reads:

$$\begin{aligned}
\Delta^{\beta}_{\text{trip}} &= v^2_{\mathbf{k}}[\langle c_{-\mathbf{k}\downarrow}c_{\mathbf{k}\uparrow}\rangle + \langle c_{-\mathbf{k}\uparrow}c_{\mathbf{k}\downarrow}\rangle] \\
&\quad -u^2_{\mathbf{k}}[\langle c_{-\mathbf{k}+\mathbf{Q}\downarrow}c_{\mathbf{k}+\mathbf{Q}\uparrow}\rangle + \langle c_{-\mathbf{k}+\mathbf{Q}\uparrow}c_{\mathbf{k}+\mathbf{Q}\downarrow}\rangle] \\
&\quad -u_{\mathbf{k}}v_{\mathbf{k}}[\langle c_{-\mathbf{k}\downarrow}c_{\mathbf{k}+\mathbf{Q}\uparrow}\rangle - \langle c_{-\mathbf{k}\uparrow}c_{\mathbf{k}+\mathbf{Q}\downarrow}\rangle \\
&\quad +u_{\mathbf{k}}v_{\mathbf{k}}[\langle c_{-\mathbf{k}+\mathbf{Q}\downarrow}c_{\mathbf{k}\uparrow}\rangle - \langle c_{-\mathbf{k}+\mathbf{Q}\uparrow}c_{\mathbf{k}\downarrow}\rangle)
\end{aligned} \tag{5.63}$$

In this case the normal Cooper pairs appear in the triplet form, while the Umklapp pairs appear in the singlet combination. This shows that if we define the gaps in terms of the bare c-operators, there is a mixing of singlet and triplet gaps, with one component being a usual zero-momentum gap and the other component being an "Umklapp" gap which is present only in the SDW phase. In the following we will express everything in terms of the new quasiparticle operators, $\alpha_{\mathbf{k}}$ and $\beta_{\mathbf{k}}$, in which case the singlet and triplet part remain well-separated.

We derive the gap equations in the SDW phase. For simplicity we show the detailed derivation for the case of only one type of pockets. Here we have chosen the hole pockets. The derivation of the gap equation in the case of electron pockets or in the presence of both types of pockets is similar. We express the superconducting mean field Hamiltonian in terms of β-operators with $\Gamma_z(\mathbf{k},\mathbf{k}')$ and $\Gamma_{+-}(\mathbf{k},\mathbf{k}')$ defined in Eqs. (5.40) and (5.41):

$$\begin{aligned} H &= {\sum_{\mathbf{k}}}' E^{\beta}_{\mathbf{k}}[\beta^{\dagger}_{\mathbf{k}\uparrow}\beta_{\mathbf{k}\uparrow} + \beta^{\dagger}_{\mathbf{k}\downarrow}\beta_{\mathbf{k}\downarrow}] \\ &\quad + \frac{1}{8N}{\sum_{\mathbf{k},\mathbf{k}'}}' \{[\Gamma_z(\mathbf{k},\mathbf{k}') + 2\Gamma_{+-}(\mathbf{k},\mathbf{k}')]\Big(\langle\beta^{\dagger}_{\mathbf{k}'\uparrow}\beta^{\dagger}_{-\mathbf{k}'\downarrow}\rangle - \langle\beta^{\dagger}_{\mathbf{k}'\downarrow}\beta^{\dagger}_{-\mathbf{k}'\uparrow}\rangle\Big)[\beta_{-\mathbf{k}\downarrow}\beta_{\mathbf{k}\uparrow} - \beta_{-\mathbf{k}\uparrow}\beta_{\mathbf{k}\downarrow}] + h.c.\} \\ &\quad + \frac{1}{8N}{\sum_{\mathbf{k},\mathbf{k}'}}' \{[\Gamma_z(\mathbf{k},\mathbf{k}') - 2\Gamma_{+-}(\mathbf{k},\mathbf{k}')]\Big(\langle\beta^{\dagger}_{\mathbf{k}'\uparrow}\beta^{\dagger}_{-\mathbf{k}'\downarrow}\rangle + \langle\beta^{\dagger}_{\mathbf{k}'\downarrow}\beta^{\dagger}_{-\mathbf{k}'\uparrow}\rangle\Big)[\beta_{-\mathbf{k}\downarrow}\beta_{\mathbf{k}\uparrow} + \beta_{-\mathbf{k}\uparrow}\beta_{\mathbf{k}\downarrow}] + h.c.\}. \end{aligned} \tag{5.64}$$

The second line we refer to as the singlet channel since the operator $S_{\mathbf{k}} = [\beta_{-\mathbf{k}\downarrow}\beta_{\mathbf{k}\uparrow} - \beta_{-\mathbf{k}\uparrow}\beta_{\mathbf{k}\downarrow}]$ is odd under spin exchange and even under $\mathbf{k} \to -\mathbf{k}$. The third line is named the triplet channel; the operator $T_{\mathbf{k}} = [\beta_{-\mathbf{k}\downarrow}\beta_{\mathbf{k}\uparrow} + \beta_{-\mathbf{k}\uparrow}\beta_{\mathbf{k}\downarrow}]$ is even under exchange of the spins and odd under $\mathbf{k} \to -\mathbf{k}$.

5.7.1 Singlet channel

Now we derive the gap equation for the singlet channel. Defining

$$\Delta^{\beta}_{\mathbf{k}} = -\frac{1}{8N}{\sum_{\mathbf{k}'}}'[\Gamma_z(\mathbf{k},\mathbf{k}') + 2\Gamma_{+-}(\mathbf{k},\mathbf{k}')]\Big(\langle\beta^{\dagger}_{\mathbf{k}'\uparrow}\beta^{\dagger}_{-\mathbf{k}'\downarrow}\rangle - \langle\beta^{\dagger}_{\mathbf{k}'\downarrow}\beta^{\dagger}_{-\mathbf{k}'\uparrow}\rangle\Big), \tag{5.65}$$

we write the mean field Hamiltonian for the singlet channel in the following way:

$$\begin{aligned} H^{\text{sing}}_{\beta} &= {\sum_{\mathbf{k}}}'[\beta^{\dagger}_{\mathbf{k}\uparrow}\ \beta_{-\mathbf{k}\downarrow}]\begin{bmatrix} E^{\beta}_{\mathbf{k}} & -\Delta^{\beta*}_{\mathbf{k}} \\ -\Delta^{\beta}_{\mathbf{k}} & -E^{\beta}_{\mathbf{k}} \end{bmatrix}\begin{bmatrix} \beta_{\mathbf{k}\uparrow} \\ \beta^{\dagger}_{-\mathbf{k}\downarrow} \end{bmatrix} + [\beta^{\dagger}_{-\mathbf{k}\uparrow}\ \beta_{\mathbf{k}\downarrow}]\begin{bmatrix} 0 & -\Delta^{\beta*}_{\mathbf{k}} \\ -\Delta^{\beta}_{\mathbf{k}} & 0 \end{bmatrix}\begin{bmatrix} \beta_{-\mathbf{k}\uparrow} \\ \beta^{\dagger}_{\mathbf{k}\downarrow} \end{bmatrix} \\ &= \sum_{\mathbf{k}}[\beta^{\dagger}_{\mathbf{k}\uparrow}\ \beta_{-\mathbf{k}\downarrow}]\begin{bmatrix} E^{\beta}_{\mathbf{k}} & -(\Delta^{\beta*}_{\mathbf{k}} + \Delta^{\beta*}_{-\mathbf{k}}) \\ -(\Delta^{\beta}_{\mathbf{k}} + \Delta^{\beta}_{-\mathbf{k}}) & -E^{\beta}_{\mathbf{k}} \end{bmatrix}\begin{bmatrix} \beta_{\mathbf{k}\uparrow} \\ \beta^{\dagger}_{-\mathbf{k}\downarrow} \end{bmatrix} \\ &= \sum_{\mathbf{k}}[\beta^{\dagger}_{\mathbf{k}\uparrow}\ \beta_{-\mathbf{k}\downarrow}]\begin{bmatrix} E^{\beta}_{\mathbf{k}} & -\Delta^{\beta,s*}_{\mathbf{k}} \\ -\Delta^{\beta,s}_{\mathbf{k}} & -E^{\beta}_{\mathbf{k}} \end{bmatrix}\begin{bmatrix} \beta_{\mathbf{k}\uparrow} \\ \beta^{\dagger}_{-\mathbf{k}\downarrow} \end{bmatrix}. \end{aligned} \tag{5.66}$$

This Hamiltonian is diagonalized with the two eigenvalues

$$\pm\Omega^{\beta}_{\mathbf{k}} = \pm\sqrt{(E^{\beta}_{\mathbf{k}})^2 + |\Delta^{s}_{\mathbf{k}}|^2}. \tag{5.67}$$

The eigenvectors satisfy:

$$u^2_{\mathbf{k}} + v^2_{\mathbf{k}} = 1, \tag{5.68}$$

$$u^2_{\mathbf{k}} = \frac{1}{2}\Big(1 + \frac{E^{\beta}_{\mathbf{k}}}{\Omega^{\beta}_{\mathbf{k}}}\Big), \tag{5.69}$$

$$v^2_{\mathbf{k}} = \frac{1}{2}\Big(1 - \frac{E^{\beta}_{\mathbf{k}}}{\Omega^{\beta}_{\mathbf{k}}}\Big), \tag{5.70}$$

$$u_{\mathbf{k}}v_{\mathbf{k}} = \frac{\Delta^{\beta,s}_{\mathbf{k}}}{2\Omega^{\beta}_{\mathbf{k}}}. \tag{5.71}$$

The transformation gives:

$$\langle \beta^\dagger_{\mathbf{k}\uparrow}\beta^\dagger_{-\mathbf{k}\downarrow}\rangle \;=\; -\langle \beta^\dagger_{\mathbf{k}\downarrow}\beta^\dagger_{-\mathbf{k}\uparrow}\rangle = u_\mathbf{k} v_\mathbf{k}(1-2f(\Omega^\beta_\mathbf{k})). \tag{5.72}$$

Therefore we have:

$$\langle \beta^\dagger_{\mathbf{k}\uparrow}\beta^\dagger_{-\mathbf{k}\downarrow}\rangle - \langle \beta^\dagger_{\mathbf{k}\downarrow}\beta^\dagger_{-\mathbf{k}\uparrow}\rangle = 2u_\mathbf{k} v_\mathbf{k}\tanh\Big(\frac{\Omega^\beta_\mathbf{k}}{2k_BT}\Big) = \frac{\Delta^\beta_\mathbf{k}}{\Omega^\beta_\mathbf{k}}\tanh\Big(\frac{\Omega^\beta_\mathbf{k}}{2k_BT}\Big). \tag{5.73}$$

Finally the singlet gap equation therefore becomes:

$$\begin{aligned}
\Delta^{\beta,s}_\mathbf{k} &= \Delta^\beta_\mathbf{k} + \Delta^\beta_{-\mathbf{k}} \\
&= -\frac{1}{8N}\sideset{}{'}\sum_{\mathbf{k}'}[\Gamma_z(\mathbf{k},\mathbf{k}') + 2\Gamma_{+-}(\mathbf{k},\mathbf{k}') + \Gamma_z(-\mathbf{k},\mathbf{k}') + 2\Gamma_{+-}(-\mathbf{k},\mathbf{k}')]\Big(\langle \beta^\dagger_{\mathbf{k}'\uparrow}\beta^\dagger_{-\mathbf{k}'\downarrow}\rangle - \langle \beta^\dagger_{\mathbf{k}'\downarrow}\beta^\dagger_{-\mathbf{k}'\uparrow}\rangle\Big) \\
&= -\frac{1}{8N}\sideset{}{'}\sum_{\mathbf{k}'}[\Gamma_z(\mathbf{k},\mathbf{k}') + 2\Gamma_{+-}(\mathbf{k},\mathbf{k}') + \Gamma_z(-\mathbf{k},\mathbf{k}') + 2\Gamma_{+-}(-\mathbf{k},\mathbf{k}')]\frac{\Delta^{\beta,s}_\mathbf{k}}{\Omega^\beta_\mathbf{k}}\tanh\Big(\frac{\Omega^\beta_\mathbf{k}}{2k_BT}\Big). \qquad (5.74)
\end{aligned}$$

5.7.2 Triplet channel

In the triplet channel the gap is defined by:

$$\Delta^\beta_\mathbf{k} = -\frac{1}{8N}\sideset{}{'}\sum_{\mathbf{k}'}[\Gamma_z(\mathbf{k},\mathbf{k}') - 2\Gamma_{+-}(\mathbf{k},\mathbf{k}')]\Big(\langle \beta^\dagger_{\mathbf{k}'\uparrow}\beta^\dagger_{-\mathbf{k}'\downarrow}\rangle + \langle \beta^\dagger_{\mathbf{k}'\downarrow}\beta^\dagger_{-\mathbf{k}'\uparrow}\rangle\Big). \tag{5.75}$$

Now the mean field Hamiltonian takes the form:

$$\begin{aligned}
H^{\text{trip}}_\beta &= \sideset{}{'}\sum_{\mathbf{k}}[\beta^\dagger_{\mathbf{k}\uparrow}\;\beta_{-\mathbf{k}\downarrow}]\begin{bmatrix} E^\beta_\mathbf{k} & -\Delta^{\beta*}_\mathbf{k} \\ -\Delta^\beta_\mathbf{k} & -E^\beta_\mathbf{k}\end{bmatrix}\begin{bmatrix}\beta_{\mathbf{k}\uparrow} \\ \beta^\dagger_{-\mathbf{k}\downarrow}\end{bmatrix} - [\beta^\dagger_{-\mathbf{k}\uparrow}\;\beta_{\mathbf{k}\downarrow}]\begin{bmatrix} 0 & -\Delta^{\beta*}_\mathbf{k} \\ -\Delta^\beta_\mathbf{k} & 0\end{bmatrix}\begin{bmatrix}\beta_{-\mathbf{k}\uparrow} \\ \beta^\dagger_{\mathbf{k}\downarrow}\end{bmatrix} \\
&= \sum_{\mathbf{k}}[\beta^\dagger_{\mathbf{k}\uparrow}\;\beta_{-\mathbf{k}\downarrow}]\begin{bmatrix} E^\beta_\mathbf{k} & -(\Delta^{\beta*}_\mathbf{k} - \Delta^{\beta*}_{-\mathbf{k}}) \\ -(\Delta^\beta_\mathbf{k} - \Delta^\beta_{-\mathbf{k}}) & -E^\beta_\mathbf{k}\end{bmatrix}\begin{bmatrix}\beta_{\mathbf{k}\uparrow} \\ \beta^\dagger_{-\mathbf{k}\downarrow}\end{bmatrix} \\
&= \sum_{\mathbf{k}}[\beta^\dagger_{\mathbf{k}\uparrow}\;\beta_{-\mathbf{k}\downarrow}]\begin{bmatrix} E^\beta_\mathbf{k} & -\Delta^{\beta,t*}_\mathbf{k} \\ -\Delta^{\beta,t}_\mathbf{k} & -E^\beta_\mathbf{k}\end{bmatrix}\begin{bmatrix}\beta_{\mathbf{k}\uparrow} \\ \beta^\dagger_{-\mathbf{k}\downarrow}\end{bmatrix}. \qquad (5.76)
\end{aligned}$$

The eigenvectors satisfy $u_\mathbf{k} v_\mathbf{k} = \frac{\Delta^{\beta,t}_\mathbf{k}}{2\Omega^\beta_\mathbf{k}}$, and we have the final gap equation:

$$\begin{aligned}
\Delta^{\beta,t}_\mathbf{k} &= \Delta^\beta_\mathbf{k} - \Delta^\beta_{-\mathbf{k}} \\
&= -\frac{1}{8N}\sideset{}{'}\sum_{\mathbf{k}'}[\Gamma_z(\mathbf{k},\mathbf{k}') - 2\Gamma_{+-}(\mathbf{k},\mathbf{k}') - \Gamma_z(-\mathbf{k},\mathbf{k}') + 2\Gamma_{+-}(-\mathbf{k},\mathbf{k}')]\Big(\langle \beta^\dagger_{\mathbf{k}'\uparrow}\beta^\dagger_{-\mathbf{k}'\downarrow}\rangle - \langle \beta^\dagger_{\mathbf{k}'\downarrow}\beta^\dagger_{-\mathbf{k}'\uparrow}\rangle\Big) \\
&= -\frac{1}{8N}\sideset{}{'}\sum_{\mathbf{k}'}[\Gamma_z(\mathbf{k},\mathbf{k}') - 2\Gamma_{+-}(\mathbf{k},\mathbf{k}') - \Gamma_z(-\mathbf{k},\mathbf{k}') + 2\Gamma_{+-}(-\mathbf{k},\mathbf{k}')]\frac{\Delta^{\beta,t}_\mathbf{k}}{\Omega^\beta_\mathbf{k}}\tanh\Big(\frac{\Omega^\beta_\mathbf{k}}{2k_BT}\Big). \qquad (5.77)
\end{aligned}$$

5.7.3 Coupled gap equation

In the most general case, both electron and hole pockets are present at the Fermi surface, and we must include the interband potential contributions. By similar calculations as shown in the two preceeding sections we arrive to a final expression for the two coupled superconducting gap equations:

$$\Delta^{\alpha,(\mathrm{s/t})}_\mathbf{k} \;=\; -\frac{1}{8N}\sideset{}{'}\sum_{\mathbf{k}'}\Big[\Gamma^{(\mathrm{s/t})}_{\mathbf{k},\mathbf{k}'}\frac{\Delta^{\alpha,(\mathrm{s/t})}_{\mathbf{k}'}}{\Omega^{\alpha,(\mathrm{s/t})}_{\mathbf{k}'}}\tanh\Big(\frac{\Omega^{\alpha,(\mathrm{s/t})}_{\mathbf{k}'}}{2k_BT}\Big) + \tilde{\Gamma}^{(\mathrm{s/t})}_{\mathbf{k},\mathbf{k}'}\frac{\Delta^{\beta(\mathrm{s/t})}_{\mathbf{k}'}}{\Omega^{\beta(\mathrm{s/t})}_{\mathbf{k}'}}\tanh\Big(\frac{\Omega^{\beta(\mathrm{s/t})}_{\mathbf{k}'}}{2k_BT}\Big)\Big], \tag{5.78}$$

and similarly for $\Delta_{\mathbf{k}}^{\beta,(\mathrm{s/t})}$ by interchanging $\alpha \leftrightarrow \beta$. The *intra*band effective pairing interaction for the singlet and triplet channel are given by:

$$\begin{aligned}
\Gamma^{(\mathrm{s})}_{\mathbf{k},\mathbf{k}'} &= (\Gamma^{z}_{\mathbf{k},\mathbf{k}'} + 2\Gamma^{+-}_{\mathbf{k},\mathbf{k}'}) + (\Gamma^{z}_{-\mathbf{k},\mathbf{k}'} + 2\Gamma^{+-}_{-\mathbf{k},\mathbf{k}'}), && (5.79)\\
\Gamma^{(\mathrm{t})}_{\mathbf{k},\mathbf{k}'} &= (\Gamma^{z}_{\mathbf{k},\mathbf{k}'} - 2\Gamma^{+-}_{\mathbf{k},\mathbf{k}'}) - (\Gamma^{z}_{-\mathbf{k},\mathbf{k}'} - 2\Gamma^{+-}_{-\mathbf{k},\mathbf{k}'}). && (5.80)
\end{aligned}$$

We stress that the symmetrization of the pairing interactions in the singlet and triplet channels is a direct consequence of solving the mean field equation, and not something "put in by hand".

The equation stated in Eq. (5.78) is the full mean field BSC equation. We solve this equation self-consistently by invoking an energy cut-off around the Fermi surface. In addition, we also solve the simplified linearized version which provides information about sub-dominant solutions. In the linearized approach we use that close to the critical temperature the gap, $\Delta_{\mathbf{k}}$, is small and therefore we may use the approximation $\Omega^{\alpha,\beta}_{\mathbf{k}} = \sqrt{(E^{\alpha,\beta}_{\mathbf{k}})^2 + |\Delta^{\alpha,\beta}_{\mathbf{k}}|^2} \simeq |E^{\alpha,\beta}_{\mathbf{k}}|$. Using this approximation we have:

$$\Delta_{\mathbf{k}}^{\alpha,(\mathrm{s/t})} = -\frac{1}{4N}\sum_{\mathbf{k}'}{}' \Big[\Gamma^{(\mathrm{s/t})}_{\mathbf{k},\mathbf{k}'}\frac{\Delta^{\alpha,(\mathrm{s/t})}_{\mathbf{k}'}}{2|E^{\alpha}_{\mathbf{k}'}|}\tanh\Big(\frac{|E^{\alpha}_{\mathbf{k}'}|}{2k_BT}\Big) + \tilde{\Gamma}^{(\mathrm{s/t})}_{\mathbf{k},\mathbf{k}'}\frac{\Delta^{\beta(\mathrm{s/t})}_{\mathbf{k}'}}{2|E^{\beta}_{\mathbf{k}'}|}\tanh\Big(\frac{|E^{\beta}_{\mathbf{k}'}|}{2k_BT}\Big)\Big] \qquad (5.81)$$

As in the calculation done in the paramagnetic phase, we rewrite this equation by defining

$$\begin{aligned}
G^{\gamma(\mathrm{s/t})}(\mathbf{k}') &= -\frac{1}{4N}\Gamma^{(\mathrm{s/t})}_{\mathbf{k},\mathbf{k}'}\Delta^{\gamma(\mathrm{s/t})}_{\mathbf{k}'},\\
G^{\gamma(\mathrm{s/t})}(\mathbf{k}') &= -\frac{1}{4N}\tilde{\Gamma}^{(\mathrm{s/t})}_{\mathbf{k},\mathbf{k}'}\Delta^{\overline{\gamma}(\mathrm{s/t})}_{\mathbf{k}'},\\
F(E^{\gamma}_{\mathbf{k}'}) &= \frac{\tanh(\frac{|E^{\gamma}_{\mathbf{k}'}|}{2k_BT_c})}{2|E^{\gamma}_{\mathbf{k}'}|}.
\end{aligned}$$

where if $\gamma = \alpha$ the $\tilde{\gamma} = \beta$ and visa versa, and by this we obtain the following equation for the α band:

$$\begin{aligned}
\Delta_{\mathbf{k}}^{\alpha(\mathrm{s/t})} &= \sum_{\mathbf{k}'} F(E^{\alpha}_{\mathbf{k}'})G^{\alpha(\mathrm{s/t})}(\mathbf{k}') + \sum_{\mathbf{k}'} F(E^{\beta}_{\mathbf{k}'})G^{\beta(\mathrm{s/t})}(\mathbf{k}')\\
&= \frac{N}{(2\pi)^2}\int d\mathbf{k}' F(E^{\alpha}_{\mathbf{k}'})G^{\alpha(\mathrm{s/t})}(\mathbf{k}') + \frac{N}{(2\pi)^2}\int d\mathbf{k}' F(E^{\beta}_{\mathbf{k}'})G^{\beta(\mathrm{s/t})}(\mathbf{k}')\\
&= \frac{N}{(2\pi)^2}\int_{FS} d\mathbf{k}' \int dE\,\delta(E - E^{\alpha}_{\mathbf{k}'})F(E)G^{\alpha(\mathrm{s/t})}(\mathbf{k}') + \frac{N}{(2\pi)^2}\int_{FS} dk' \int dE\,\delta(E - E^{\beta}_{\mathbf{k}'})F(E)G^{\beta(\mathrm{s/t})}(\mathbf{k}')\\
&= \frac{N}{(2\pi)^2}\Big[\int_{FS,\alpha}\frac{d\mathbf{k}'}{|v_{\mathbf{k}'}|}G^{\alpha,(\mathrm{s/t})}(\mathbf{k}') + \int_{FS,\beta}\frac{d\mathbf{k}'}{|v_{\mathbf{k}'}|}G^{\beta,(\mathrm{s/t})}(\mathbf{k}')\Big]\int dE F(E) \qquad \text{(invoke energy cutoff, } E_c\text{)}\\
&= \frac{N}{(2\pi)^2}\Big[\int_{FS,\alpha}\frac{d\mathbf{k}'}{|v_{\mathbf{k}'}|}G^{\alpha,(\mathrm{s/t})}(\mathbf{k}') + \int_{FS,\beta}\frac{d\mathbf{k}'}{|v_{\mathbf{k}'}|}G^{\beta,(\mathrm{s/t})}(\mathbf{k}')\Big]\int_{-E_c}^{E_c} dE\frac{1}{2|E|}\tanh(\frac{|E|}{2k_BT_c}). && (5.82)
\end{aligned}$$

Now in the limit where $E_c << k_BT_c$ we have

$$\int_{-E_c}^{E_c} dE\frac{1}{2|E|}\tanh\Big(\frac{|E|}{2k_BT_c}\Big) = \int_{0}^{E_c} dE\frac{1}{|E|}\tanh\Big(\frac{|E|}{2k_BT}\Big) \sim \ln\Big[\frac{1.13E_c}{k_BT_c}\Big]. \qquad (5.83)$$

The remaining part of the linearized gap equation is expressed as an eigenvalue problem where we approximate the Fermi surface integral with a sum of $\mathbf{k}$ values on the Fermi surface. The matrix of the eigenvalue problem is defined by:

$$M_{\mathbf{k},\mathbf{k}'} = -\frac{1}{4(2\pi)^2}\frac{l_{\mathbf{k}'}}{|v_{\mathbf{k}'}|}\Big[\Gamma^{(\mathrm{s/t})}_{\mathbf{k},\mathbf{k}'} + \tilde{\Gamma}^{(\mathrm{s/t})}_{\mathbf{k},\mathbf{k}'}\Big]. \qquad (5.84)$$

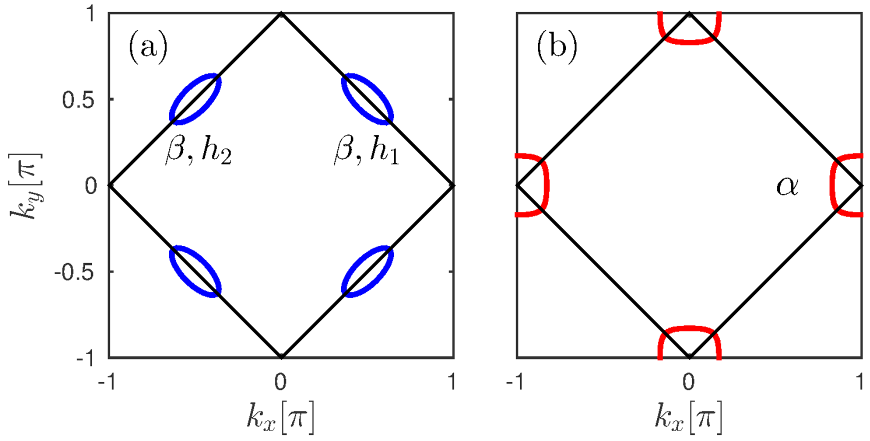

Figure 5.10: Fermi surfaces in the case of (a) small hole doping, $\langle n \rangle = 0.96$ and (b) small electron doping $\langle n \rangle = 1.05$ for $U = 3$ and $t' = -0.35$.

We denote $l_{\mathbf{k}'}$ the length of the Fermi surface path represented by the point $\mathbf{k}'$ which is due to the conversion of an integral to a sum. Thus we are left with the eigenvalue problem:

$$-\frac{1}{4(2\pi)^2} M_{\mathbf{k},\mathbf{k}'} \Delta_{\mathbf{k}'} = \lambda \Delta_{\mathbf{k}'} \tag{5.85}$$

where

$$M_{\mathbf{k},\mathbf{k}'} = \begin{bmatrix} \Gamma^{\alpha\alpha}_{\mathbf{k},\mathbf{k}'} l^{\alpha}_{\mathbf{k}'}/|v^{\alpha}_{\mathbf{k}'}| & \tilde{\Gamma}^{\alpha\beta_{h_1}}_{\mathbf{k},\mathbf{k}'} l^{\beta}_{\mathbf{k}'}/|v^{\beta}_{\mathbf{k}'}| & \tilde{\Gamma}^{\alpha\beta_{h_2}}_{\mathbf{k},\mathbf{k}'} l^{\beta}_{\mathbf{k}'}/|v^{\beta}_{\mathbf{k}'}| \\ \tilde{\Gamma}^{\beta_{h_1}\alpha}_{\mathbf{k},\mathbf{k}'} l^{\alpha}_{\mathbf{k}'}/|v^{\alpha}_{\mathbf{k}'}| & \Gamma^{\beta_{h_1}\beta_{h_1}}_{\mathbf{k},\mathbf{k}'} l^{\beta}_{\mathbf{k}'}/|v^{\beta}_{\mathbf{k}'}| & \Gamma^{\beta_{h_1}\beta_{h_2}}_{\mathbf{k},\mathbf{k}'} l^{\beta}_{\mathbf{k}'}/|v^{\beta}_{\mathbf{k}'}| \\ \tilde{\Gamma}^{\beta_{h_2}\alpha}_{\mathbf{k},\mathbf{k}'} l^{\alpha}_{\mathbf{k}'}/|v^{\alpha}_{\mathbf{k}'}| & \Gamma^{\beta_{h_2}\beta_{h_1}}_{\mathbf{k},\mathbf{k}'} l^{\beta}_{\mathbf{k}'}/|v^{\beta}_{\mathbf{k}'}| & \Gamma^{\beta_{h_2}\beta_{h_2}}_{\mathbf{k},\mathbf{k}'} l^{\beta}_{\mathbf{k}'}/|v^{\beta}_{\mathbf{k}'}| \end{bmatrix}.$$

The intraband ($\Gamma_{\mathbf{k}\mathbf{k}'}$) and interband ($\tilde{\Gamma}_{\mathbf{k}\mathbf{k}'}$) pairings must be expressed in the singlet and triplet symmetrized versions in accordance with Eqs. (5.79-5.80). The largest eigenvalue, λ, gives the leading instability since it corresponds to the largest superconducting critical temperature. The symmetry of the gap is stated in the corresponding eigenvector:

$$\Delta_{\mathbf{k}} = \begin{bmatrix} \Delta^{\alpha}_{\mathbf{k}} \\ \Delta^{\beta,\mathrm{h}_1}_{\mathbf{k}} \\ \Delta^{\beta,\mathrm{h}_2}_{\mathbf{k}} \end{bmatrix}, \tag{5.86}$$

which is a function of momentum $\mathbf{k}$. The momentum is located on the electron pocket around $(\pi, 0)$, which we denote by α, and on the two hole pockets, denoted by β_{h_1}/β_{h_2}, around $(\frac{\pi}{2}, \frac{\pi}{2})/(-\frac{\pi}{2}, \frac{\pi}{2})$, respectively, see Fig. 5.10. We solve the eigenvalue problem Eq. (5.84) for $\mathbf{k}$ and $\mathbf{k}'$ on these three closed pockets, which is equivalent to solving it in the whole magnetic Brillouin zone.

The leading eigenvalue identifies the dominating gap symmetry with the critical temperature given by:

$$\begin{aligned} \lambda &= \ln\left[\frac{1.13 E_c}{k_B T_c}\right] \Leftrightarrow \\ k_B T_c &= 1.13 E_c e^{-1/\lambda} \end{aligned} \tag{5.87}$$

Note however, that the energy cut-off is not clearly defined. In the conventional BCS superconductors where pairing is mediated by phonons, the natural energy scale is the Debye frequency. In the early work

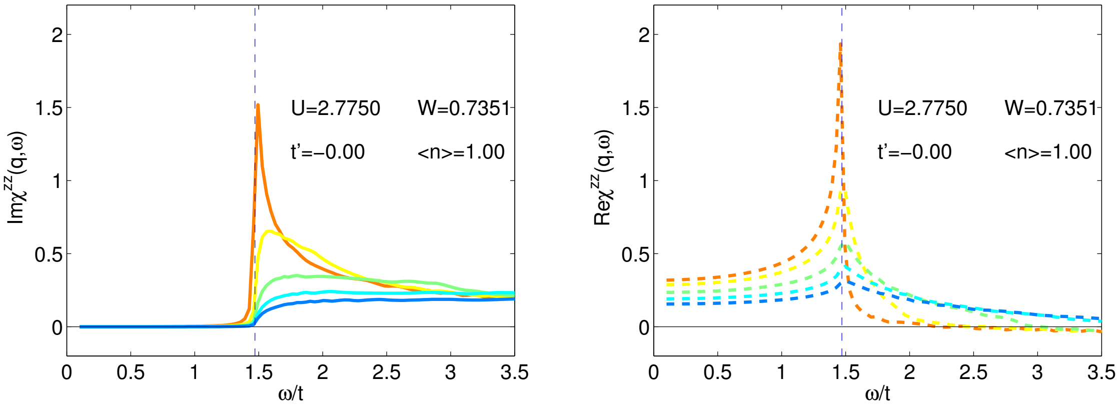

Figure 5.11: Imaginary and real part of the longitudinal RPA susceptibility $\chi^{zz}_{\mathrm{RPA}}(q,\omega)$ for the simple band $t' = \mu = 0$. Notice the spectral weight contribution at $\omega \sim 2W$. The 5 lines correspond to $|q - Q| = 0.1n|Q|$ for $n = 0, \ldots, 4$, where the red line is $n = 0$ and blue line is $n = 4$. Compare Ref. [80] Fig. 10.

by Schrieffer *et al.* [80] it was argued that the spectral function given by the longitudinal spin fluctuations, i.e. $\mathrm{Im}\chi^{z}_{\mathrm{RPA}}(Q,\omega)$, displays a behavior that bear resemblance to a physical mode at $\omega = 2W$. This is because the longitudinal mode is gapped by $2W$ at $\mathbf{Q} = (\pi,\pi)$. In Ref. [80] the pairing interaction of the superconducting state for very small doping values was approximated by the contribution from longitudinal spin fluctuations only and the energy dependence of the pairing was modelled with a peak at $2W$ due to the energy dependence of the longitudinal RPA susceptibility, see Fig. 5.11. In our case the transverse fluctuations are equally important for the pairing, and the transverse mode is not gapped. Quite contrary, it displays a Goldstone mode. So this channel has no clear analog to the Debye frequency. However, it is expected to be most active in a thin shell around the Fermi surface for momentum transfers of $\mathbf{Q} = (\pi,\pi)$.

5.8 Leading Angular Harmonics Approximation

In the analytic approach to the coexistence phase, small electron and hole dopings are studied. This is work done in collaboration with Wenya Rowe and has been published in Ref. [98]. Close to half filling the Fermi surface consists of small Fermi pockets, either small hole pockets in the weakly hole-doped system, or small electron pockets in weakly electron-doped systems. In both cases, expansions of the pairing interaction due to longitudinal and transverse fluctuations were performed.

The Leading Angular Harmonics Approximation (LAHA) [99] is a useful approach to predict gap symmetries from complicated pairing interactions in case of small Fermi pockets. With the basic assumption that these pockets are circular, the pairing potential is expanded as a function of angle around the pockets. In the case of spin-fluctuation pairing in the antiferromagnetically ordered state, the approach provides a useful test of how the multiplication of the divergent transverse susceptibility with the magnetic coherence factor in fact ensures a well-behaved finite pairing potential. The Goldstone mode causes a divergence of the transverse RPA susceptibility $\chi^{+-}_{\mathbf{k}-\mathbf{k}'+\mathbf{Q}}$ for $\mathbf{k} = \mathbf{k}'$. This divergence enters through the term $V_{+-}(\mathbf{q}) = U^2\chi^{+-}(\mathbf{q})$ in

$$\Gamma^{+-}_{\mathbf{k},\mathbf{k}'} = V_{+-}(\mathbf{k}-\mathbf{k}')n^2(\mathbf{k},\mathbf{k}') - V_{+-}(\mathbf{k}-\mathbf{k}'+\mathbf{Q})p^2(\mathbf{k},\mathbf{k}')$$

as stated in Eq. (5.41). Now, the coherence factor $p^2(\mathbf{k},\mathbf{k}') = 0$ for $\mathbf{k} = \mathbf{k}'$ and therefore there is a screening of the divergence. The LAHA procedure shows that the transverse potential does indeed contribute with a finite, but non-zero value to the pairing interaction. The details of the LAHA calculations were done mainly by Wenya Rowe and Ilya Eremin, and are discussed in Refs. [98, 100]. Here we provide only a short description and a discussion of the results. The idea is to express the momenta in a local coordinate system with the origin located at the center of the Fermi pocket. The Fermi vector k_F is given by the radius of the pocket. For the electron pocket at $(\pi, 0)$ we have:

$$\begin{aligned} k_x &= \pi + k_F^e \cos\phi \\ k_y &= k_F^e \sin\phi \end{aligned}$$

where k_F^e is the radius of the electron pocket.
For the hole pockets centered at $(\pm\frac{\pi}{2}, \frac{\pi}{2})$ we have

$$\begin{aligned} k_x &= \pm\frac{\pi}{2} + k_F^h \cos(\theta + \frac{\pi}{4}) \\ k_y &= \frac{\pi}{2} + k_F^h \sin(\theta + \frac{\pi}{4}) \end{aligned}$$

The angles ϕ and θ are defined in Fig. 5.12. By use of these expansions, we derive the angle dependence for the ext. s-wave, $d_{x^2-y^2}$ and p-wave gap. The results are shown in Table 5.1. The singlet solution $g = [\cos(k_x) - \cos(k_y)] \sin(k_x) \sin(k_y)$ has not been shown. In the case of hole pockets it has a structure similar to the $d_{x^2-y^2}$, whereas in the case of electron pockets the structure is similar to p_x on the pocket around $(\pi, 0)$ and p_y on the pocket around $(0, \pi)$.

	Electron pocket	Hole h_1 pocket	Hole h_2 pocket
ext. s	$\cos(2\phi)$	$\cos\theta$	$\sin\theta$
$d_{x^2-y^2}$	$1 + \alpha_e^d \cos(4\phi)$	$\sin\theta$	$\cos\theta$
p_x/p_y	$\sin\phi/\cos\phi$	1	1

Table 5.1: Angular dependence of the gap symmetries.

Expansion of the longitudinal potential gives rise to the following expansions [98, 100]:

$$\begin{aligned} V^l_{h1h1}(\theta, \theta') &\approx c_h + a_h \cos\theta\cos\theta' + b_h \sin\theta\sin\theta' + c_h(\cos 2\theta + \cos 2\theta') \\ V^l_{h2h2}(\theta, \theta') &\approx c_h + a_h \sin\theta\sin\theta' + b_h \cos\theta\cos\theta' + c_h(\cos 2\theta + \cos 2\theta') \\ V^l_{ee}(\phi, \phi') &\approx c_e + d_e(\cos\phi\cos\phi' + \sin\phi\sin\phi') \end{aligned} \tag{5.88}$$

where $c_h \equiv \bar{V} + \left[\widetilde{V} - \frac{2t^2\bar{V}}{W^2}\right]{k_F^h}^2$, $a_h \equiv \left[-\widetilde{V} + \frac{4t^2\bar{V}}{W^2}\right]{k_F^h}^2$, $b_h = \widetilde{V}{k_F^h}^2$, $c_e \equiv \bar{V} + \widetilde{V}{k_F^e}^2$, $d_e \equiv \widetilde{V}{k_F^e}^2$, with $Y(x) = 4U\frac{\chi_0^{z\prime\prime}(x)V_z(x)}{1+U\chi_0^z(x)}\left(1 + \frac{V_z(x)^2U^{-2}}{(1+U\chi_0^z(x))^2}\right)$, $\bar{V} \equiv [V_z(0) - V_c(0) + (V_c(\mathbf{Q}) - V_z(\mathbf{Q}))]$, and $\widetilde{V} \equiv Y(0) - Y(\mathbf{Q})$. Note that $\bar{V}$ is negative (attractive), since $V_z(\mathbf{Q})$ is the largest term and the same is true for $\widetilde{V}$.

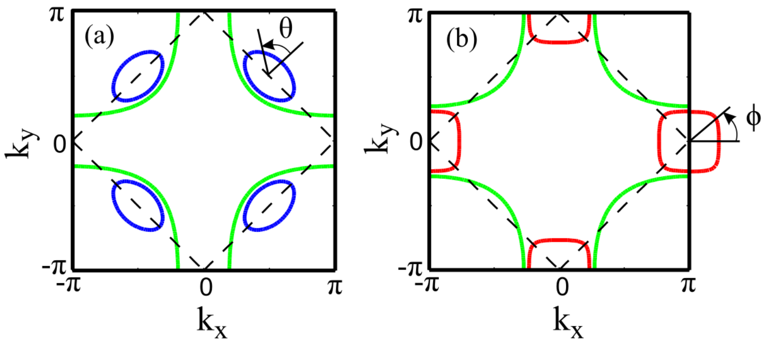

Figure 5.12: Fermi surface in the SDW phase for hole (a) and electron (b) doping. From Ref. [98].

It is important to note that the expressions for the expanded potentials is derived from the unsymmetrized pairing potentials. In the case of the longitudinal potential, the potential stated in Eq. (5.40) is expanded on small pockets to give Eq. (5.88). As shown in detail in section 5.7, the symmetrized / antisymmetrizated versions of the potentials enter the gap equations. Therefore it becomes important to state the transformation properties of the coefficients under the transformation $\mathbf{k} \to -\mathbf{k}$ (or $\mathbf{k}' \to -\mathbf{k}'$). The analysis shows that the coefficients c_h and d_e are *odd* under $\mathbf{k} \to -\mathbf{k}$, and therefore these contribute to triplet Cooper-pairing only. The other coefficients a_h, b_h, and c_e are *even* under $\mathbf{k} \to -\mathbf{k}$ and will therefore contribute to the singlet pairing.

To understand which pairing symmetries will be favored in each case we turn to a linearized gap equation expressed in terms of the parametrization angle ϕ;

$$\lambda\Delta(\phi) = -\int_{\phi'} d\phi' \frac{D(0)}{2\pi}\Gamma(\phi,\phi')\Delta(\phi'). \tag{5.89}$$

where $D(0)$ is the density of states at the Fermi level and the angular integral runs over the Fermi pocket. If the structure of $\Gamma(\phi,\phi')$ supports a certain pairing symmetry it will give rise to $\lambda > 0$ for that particular symmetry. In this case we call it "pair-building", otherwise it is "pair-breaking" for that symmetry. If it is pair-breaking for a given symmetry, the leading solution appears in a different symmetry class.

In the case of hole doping, the dominant contribution is given by the attractive constant term c_h. It does not give rise to a conventional s-wave state due to the symmetry stated in Eq. (5.56), but the p-wave which to first order is constant on the hole pocket is a valid solution;

$$\lambda\Delta = -\int_{\phi'} d\phi' \frac{D(0)}{2\pi} 2c_h\Delta \Leftrightarrow \lambda = -D(0)2c_h \qquad (c_h < 0) \tag{5.90}$$

Thus, the p-wave solution is favoured by longitudinal spin fluctuations in the hole-doped case.

In the electron-doped system, the constant term c_e is attractive. This term possesses even symmetry and will favor $d_{x^2-y^2}$, since this is constant on the electron pockets, as seen from Table 5.1. For the *triplet* solution on the electron-doped side we have:

$$\lambda\Delta_e\cos\phi = -\int_{\phi'} d\phi' \frac{D(0)}{2\pi} 2d_e\cos\phi\cos\phi'\Delta_e\cos\phi' \Leftrightarrow \lambda = -D(0)d_e \qquad (d_e < 0) \tag{5.91}$$

This shows that the longitudinal fluctuations provide a pair-building contribution for a p-wave gap in the case of electron doping. The magnitude of the solution depends on the size of the electron pockets, since $d_e \equiv \widetilde{V}{k_F^e}^2$, as opposed to the singlet $d_{x^2-y^2}$ solution, which is independent of the pocket size. In principle, it requires a detailed evaluation of the pairing potential to figure out which of the two candidates, $d_{x^2-y^2}$ and p-wave, will be leading for a given doping. However, more importantly, the presence of transverse spin fluctuations might alter the picture altogether, and we therefore need to do the same exercise in the transverse pairing channel to settle which pairing symmetries will be favored by both types of spin fluctuations at the same time.

Expansion of the transverse part of the pairing potential, i.e.

$$-2V_{+-}(\mathbf{k}-\mathbf{k}')n^2(\mathbf{k},\mathbf{k}') + 2V_{+-}(\mathbf{k}-\mathbf{k}'+\mathbf{Q})p^2(\mathbf{k},\mathbf{k}')$$

gives [98, 100]:

$$\begin{aligned}
V^{tr}_{h1h1}(\theta,\theta') &\approx A_h(\pm 1 - \cos\theta\cos\theta' + \sin\theta\sin\theta') + B_h(\pm 2 + 4\cos\theta\cos\theta' \pm \cos 2\theta \pm \cos 2\theta') \\
V^{tr}_{h2h2}(\theta,\theta') &\approx A_h(\pm 1 + \cos\theta\cos\theta' - \sin\theta\sin\theta') + B_h(\pm 2 + 4\sin\theta\sin\theta' \mp \cos 2\theta \mp \cos 2\theta') \\
V^{tr}_{ee}(\phi,\phi') &\approx A_e(1 \pm \cos\phi\cos\phi' \pm \sin\phi\sin\phi' \mp \frac{1}{2}(\cos 3\phi\cos\phi' - \sin 3\phi\sin\phi' + \cos\phi\cos 3\phi' - \sin\phi\sin 3\phi') \\
&\quad - \cos 2\phi\cos 2\phi' + \sin 2\phi\sin 2\phi')
\end{aligned} \tag{5.92}$$

where in terms of

$$y = \frac{16}{N}\sum_{\mathbf{k}} \frac{\sin^2 k_x \left(1 - 6\frac{(\varepsilon_k^-)^2}{(E^\alpha_{\mathbf{k}} - E^\beta_{\mathbf{k}})^2}\right) - \frac{1}{2}\cos^2 k_x - \frac{1}{2}\cos k_x \cos k_y}{(E^\alpha_{\mathbf{k}} - E^\beta_{\mathbf{k}})^3} - \frac{32(t')^2}{t^2 N}\sum_{\mathbf{k}} \frac{\sin^2 k_x \cos^2 k_y}{(E^\alpha_{\mathbf{k}} - E^\beta_{\mathbf{k}})^3}$$

we have $A_h \equiv \frac{2}{yW^2}$, $B_h \equiv V_\pm(0)\left(\frac{tk_F^h}{W}\right)^2$, and $A_e \equiv -\frac{k_F^{e\,2}}{2yW^2}$. Here, y is related to the spin wave stiffness and is positive once commensurate AF order is stable. The terms which are stated with ± or ∓ are odd under $\mathbf{k} \to -\mathbf{k}$. The other terms contribute to singlet pairing. As in the case of longitudinal pairing, we consider the simplified version of the gap equation. In the expansion given above, the over all sign is relevant for the triplet channel. In the singlet channel the sign is reversed (see Eq. (5.41)).

For hole doping, we find the leading term A_h is repulsive (positive) in the triplet channel. Therefore, it acts as a pair-breaker for the p-wave solution. In the singlet channel the sign of A_h is reversed and therefore we get a pair-building contribution for the $d_{x^2-y^2}$ channel;

$$\lambda\Delta_{h_1}\sin\phi = -\int_{\phi'} d\phi' \frac{D(0)}{2\pi}[-2A_h \sin\theta\sin\theta']\Delta_{h_1}\sin\theta' \Leftrightarrow \lambda = D(0)A_h \qquad (A_h > 0) \tag{5.93}$$

Also in the case of electron doping the transverse fluctuations turn out to be pair-breaking for p-wave and pair-building for $d_{x^2-y^2}$.

We state the results in a schematic overview in Table 5.2 and Table 5.3, for the triplet and singlet channel, respectively. In the triplet channel, Table 5.2, we observe that the longitudinal channel favors a p-wave solution, but this is destroyed by the transverse fluctuations, both in the case of electron and hole doping. We will return to this point later. In the singlet channel, Table 5.3, both types of spin fluctuations favor $d_{x^2-y^2}$.

In conclusion, the analytical approach to the pairing problem provides evidence for a leading $d_{x^2-y^2}$ solution both in the case of electron and hole doping, since longitudinal and transverse channel act in concert to support this pairing symmetry. This is not accomplished in the triplet channel, where the p-wave solution is only supported by the longitudinal fluctuations. Therefore, by the assumption that the strength of both types of pairing is comparable, we conclude that the favored symmetry of the superconducting order in the coexistence phase is $d_{x^2-y^2}$. Below we provide a more thorough investigation of this claim by numerically solving the gap equation as a function of filling. The numerical approach allows us to study the spin fluctuation mediated pairing at higher dopings, since we are not restricted to the approximation of having small circular pockets around $(\pi, 0)$ or $(\frac{\pi}{2}, \frac{\pi}{2})$ for electron and hole doping, respectively. This allows for the generalization where both electron and hole pockets are present at the Fermi surface, which seems particularly relevant from observations of the Fermi surface measured by ARPES experiments as discussed in section 5.2.1. In the numerical approach we also include the pairing contributions between pockets, which was omitted in the analytical approach.

Now we turn to a discussion the results obtained from the linearization procedure presented in Eq. (5.85) by which we can obtain a clear quantitative comparison between the dominant and subdominant superconducting gap symmetries. But first we provide a rather technical discussion of the break-down of the stability of commensurate antiferromagnetism, and how this is treated in our approach.

	Electron pocket		Hole pocket	
	long./ch.	transverse	long./ch.	transverse
Pair-building contribution	$d_e \sim \mathcal{O}((k_F^e)^2)$	–	$c_h \sim \mathcal{O}(1)$	–
Pair-breaking contribution	–	$A_e \sim \mathcal{O}((k_F^e)^2)$		$A_h \sim O(1)$

Table 5.2: Contributions of the spin-fluctuation mediated Cooper-pairing potential expanded up to $\mathcal{O}(k_F^2)$ in the p-wave spin triplet channel.

	Electron pocket		Hole pocket	
	long./ch.	transverse	long./ch.	transverse
Pair-building $d_{x^2-y^2}$	$c_e \sim \mathcal{O}(1)$	$A_e \sim \mathcal{O}((k_F^e)^2)$	$b_h \sim\sim \mathcal{O}((k_F^h)^2)$	$A_h \sim \mathcal{O}(1)$

Table 5.3: Contributions of the spin-fluctuation mediated Cooper-pairing potential expanded up to $\mathcal{O}(k_F^2)$ in the spin singlet $d_{x^2-y^2}$-wave channel. Note that all contributions in the extended s-wave symmetry channel are pair-breaking.

5.9 Fermi surface at large electron dopings

We discuss the structure of the Fermi surface, close to the critical electron doping value, where magnetic order disappears. As discussed in section 5.2.1, ARPES data suggests that upon sufficient doping, the Fermi surface consists of both electron and hole pockets. Numerically, this situation can be stabilized close to critical doping, i.e. for small magnetizations. It requires that the critical doping is relatively small, such that the non-reconstructed Fermi surface crosses the magnetic zone boundary. However, it poses a problem since the presence of hole pockets introduce additional nesting, which in principle destabilizes commensurate antiferromagnetism. A solution of the magnetic gap equation resulting in a Fermi surface that consists of both electron and hole pockets is numerically possible, but it requires very big system sizes to achieve convergence.

The intrapocket nesting due to the hole pockets gives rise to a problem for the pairing interaction. This is because the divergence of the RPA susceptibilities is only screened away at the ordering vector $\mathbf{Q} = (\pi, \pi)$, but not at the peaks arising from additional intrapocket nesting. The problem of intrapocket nesting is illustrated in Fig. 5.13; the presence of hole pockets, which occurs at a doping of 7.7 %, causes intrapocket contributions to the susceptibilities. This leads to a break-down of the RPA formalism, since the real part of the bare susceptibilities becomes larger than $1/U$ at some wave vectors. This is a signature of the commensurate antiferromagnetism not being the correct ground state of this model. However, we want to explore the solutions by forcing stability of the commensurate order. Therefore, in this model we simply turn off the additional intrapocket contribution. In the case of small hole doping the same problem arises. In this doping regime it was shown by Chubukov and Frenkel [96], that vacuum renormalization leads to a stability of the commensurate antiferromagnetic order. In our approach, we completely turn off all intraband susceptibility contributions. In this way, the RPA formalism becomes controlled, as shown in Fig. 5.14.

On the paramagnetic side close to critical doping the susceptibility also shows the signatures of this "intrapocket" nesting, i.e. peaks at positions away from the $\mathbf{Q}$ vector. But on this side the susceptibility is simply calculated from the paramagnetic band by the Lindhard function, and does not provide a quick fix as on the SDW side, where we could screen away the additional nesting. To deal with this situation, we speculate a small reduction in the Coulomb interaction in the paramagnetic phase compared to the SDW phase, which is justified by the fact that we are doping the system away from the more strongly coupled situation.

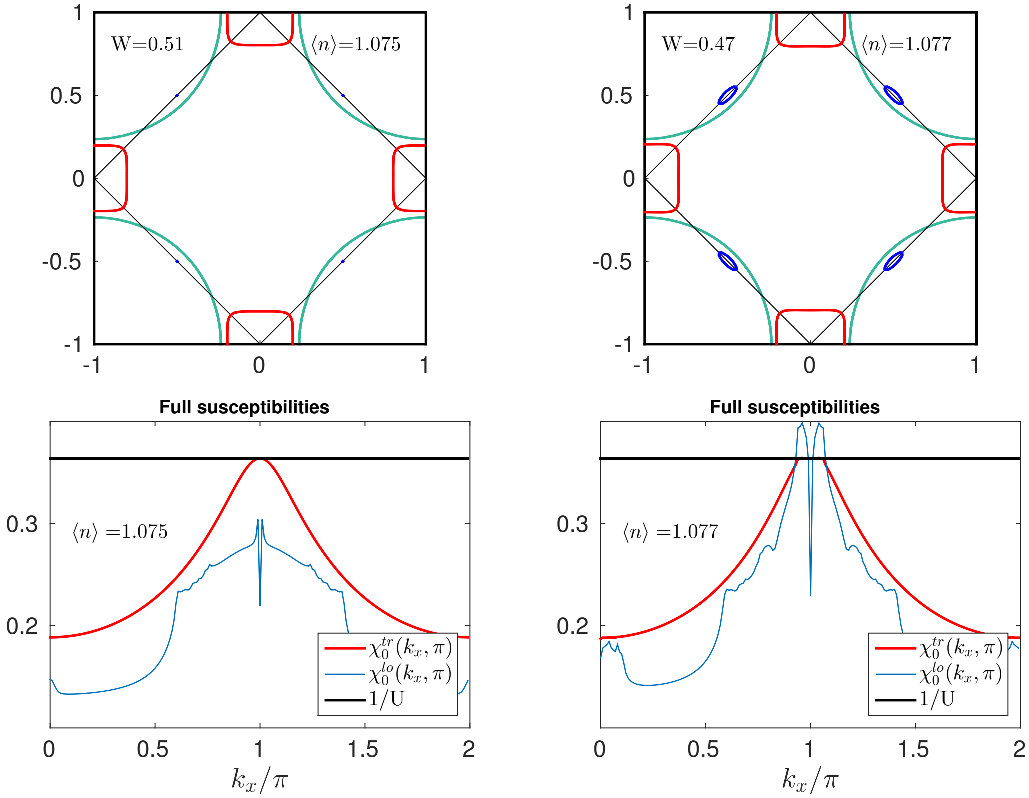

Figure 5.13: **First row:** Fermi surfaces at electron dopings of 7.5 % and 7.7 % with $t' = -0.35$ and $U = 2.75$. The Fermi surface due to the non-reconstructed paramagnetic band is shown in light blue. The reconstructed Fermi surface of the SDW phase is shown by electron pockets in red and hole pockets in blue. **Second row:** Longitudinal (blue line) and transverse (red line) spin susceptibility cuts through (k_x, π) in the two cases. The black line shows the value of $1/U$. Note how the presence of hole pockets at the Fermi surface causes a break-down of the RPA formalism, since $Re\chi_0(\mathbf{q}) > 1/U$ in a regime close to $\mathbf{q} = \mathbf{Q}$.

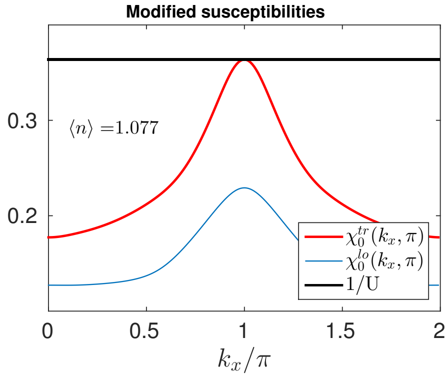

Figure 5.14: Intraband susceptibility contributions removed from the longitudinal and transverse susceptibility. We apply this modification for 7.7% and 8% electron doping in the calculation of the phase diagram shown in Fig. 5.21.

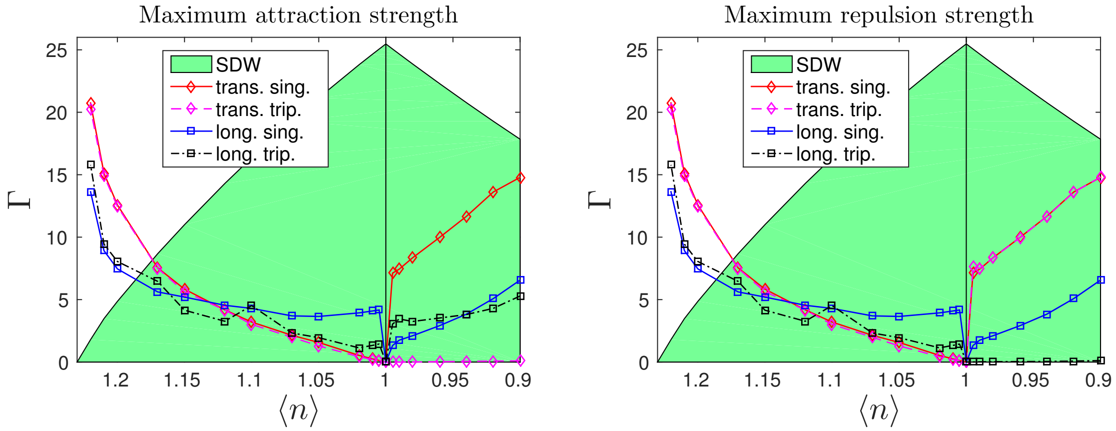

Figure 5.15: The doping evolution of the value of the pair scattering $\Gamma^{s/t}_{\mathbf{k},\mathbf{k}'}$ for which the *attractive /repulsive* pairing strength is maximal for any pair of momenta $(\mathbf{k},\mathbf{k}')$ on the Fermi surface. Attraction is manifested in negative pairing contributions. We plot the absolute value. Parameters are $U = 3.0$, $t' = -0.35$.

5.10 Pairing strength and structures from longitudinal and transverse fluctuations

The strength and structure of the pairing potentials between opposite spin electrons arising from longitudinal and transverse spin fluctuations depend on the details of the reconstructed bands of the SDW phase, and are manifested quite differently in distinct regions of the phase diagram. In Fig. 5.15 we plot the value of the pair scattering $\Gamma^{s/t}_{\mathbf{k},\mathbf{k}'}$ for which the pairing attraction/repulsion is maximal for any pair of momenta $(\mathbf{k},\mathbf{k}')$ on the Fermi surface. In the low doping limit, we observe that the interaction through transverse fluctuations is much stronger for hole doping than for electron doping. For interactions in the longitudinal channel, the situation is circumvent since in this case the pairings are strongest for small electron doping compared to small hole doping. A close inspection of the longitudinal contribution in the triplet channel reveals that pure attraction is obtained on the hole-doped side, see Fig. 5.15 (black squares with dashed line). On the contrary, the transverse contribution in the triplet channel is purely repulsive on the hole-doped side, as observed by inspection of the pink diamonds in Fig. 5.15. These observations are in agreement with the analytical findings stated in Table 5.2. Generally for the hole-doped system, the contribution from transverse fluctuations is stronger than the contribution from longitudinal fluctuations. Therefore the sum of the two pairing contributions gives an overall intrapocket repulsion in the triplet channel for the hole-doped system. This disfavors the p-wave solution. For electron dopings, the longitudinal fluctuations dominate close to half filling, whereas both types of pairings contribute more equally at larger doping levels. In fact, the strength of the pairing interactions in both channels builds up towards the critical electron doping, where the AF order disappears. This naïvely suggests an increase in superconductivity close to critical electron doping. However, a closer inspection of the $(\mathbf{k},\mathbf{k}')$ dependence of the pairing reveals that it develops a sign change for a part of the intrapocket potential and becomes strongly repulsive for nearby points at the Fermi surface. This leads to a gap suppression despite the increased interaction strength.

In general, knowledge of the $(\mathbf{k},\mathbf{k}')$ structure of the pairing potential is crucial in order to decide what kind of superconducting instabilities are favored in the SDW phase. To address this question, in Figs. 5.16 and 5.17 we map out both the singlet and triplet pair scattering potentials due to longitudinal and transverse spin fluctuations for hole- and electron doping, respectively. In the case of small hole doping (Fig. 5.16), the singlet pairing interactions from longitudinal and transverse spin fluctuations are similar in structure; there is an effective attractive (negative) interaction for $\mathbf{k}$ and $\mathbf{k}'$ on the same side of the zone diagonal, whereas the interaction becomes repulsive (positive) when **k** and **k**′ are on opposite sides of the zone diagonal, as deduced from Fig. 5.16(a-b). This structure supports $d_{x^2-y^2}$ as well as g-wave states. In the triplet channel, the remarkable difference between longitudinal and transverse fluctuations becomes clearly visible, see Fig. 5.16(c-d). As before, we conclude that whereas the longitudinal fluctuation channel supports a p-wave triplet superconductor by an intrapocket attractive potential, the transverse fluctuations completely obstruct this solution. As a result, the triplet solution is higher order with additional nodes at the Fermi surface, and as we shall see, it becomes sub-dominant to the singlet solution.

For electron doping, the pairing interaction in the singlet channel is locally attractive for **k** and **k**′ residing on the same electron pocket, as shown in Fig. 5.17(a-b). Attractive pairing occurs due to both longitudinal and transverse spin fluctuations. As opposed to the hole-doped case, it is the longitudinal fluctuations that mediate the strongest effective pairing. In this regime, it is clearly the $d_{x^2-y^2}$ solution which will be favored due to the symmetry $\Gamma_{\mathbf{k},\mathbf{k}'+\mathbf{Q}} = -\Gamma_{\mathbf{k},\mathbf{k}'}$. Upon increasing the electron doping the purely attractive intrapocket interaction is replaced by partly repulsive regions and this will diminish the resulting superconducting gap value. In the triplet channel the pairings from both types of fluctuations will be quite weak, see Fig. 5.17(c-d). As in the case of hole doping, the longitudinal fluctuations support a p-wave gap since it is attractive for **k** and **k**′ located at the same side of the Fermi pocket and repulsive for **k** and **k**′ on opposite sides, as shown in Fig. 5.17(c). The transverse fluctuations display the reverse structure as evident from in Fig. 5.17(d), which is the reason why the p-wave solution becomes suppressed also on the electron-doped side.

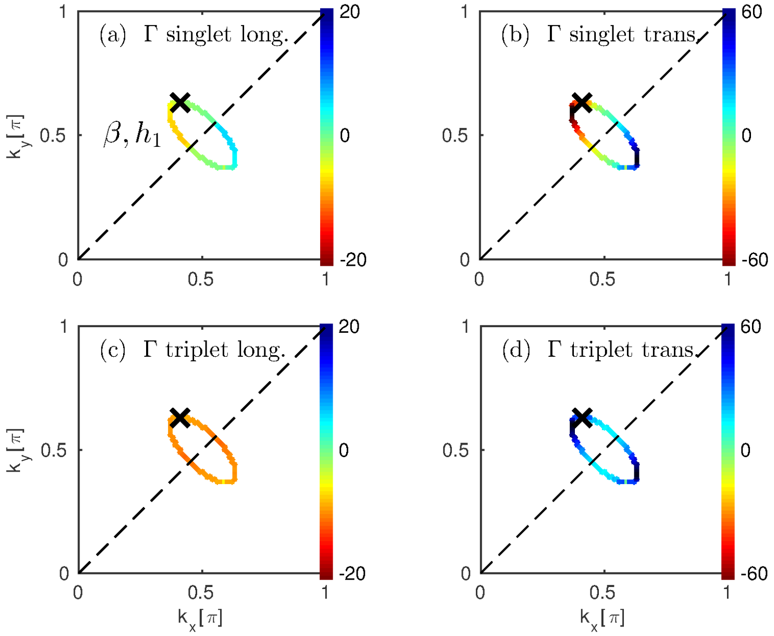

Figure 5.16: Effective pairing contributions from longitudinal (a,c) and transverse (b,d) spin fluctuations in the singlet and triplet channel on the hole pocket centered at $(\frac{\pi}{2}, \frac{\pi}{2})$. The black cross denotes the position of **k**′ and the value of $\Gamma^{s/t}_{\mathbf{k},\mathbf{k}'}$ is shown as a function of **k** around the hole pocket. Negative potential contributions correspond to effective attraction. The zone diagonal is indicated by a dashed line. The filling is $\langle n \rangle = 0.96$ and $U = 3.0$, $t' = -0.35$. Note the different color scale for pairing potentials in the longitudinal and transverse channels.

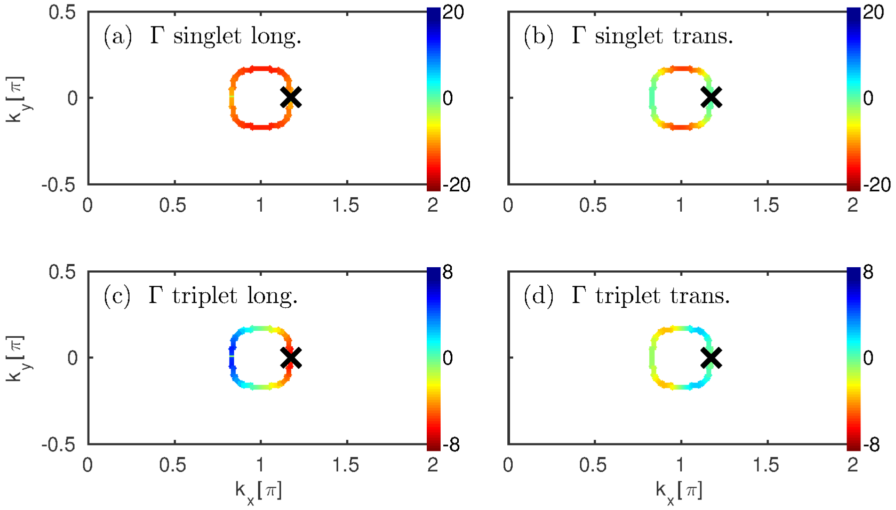

Figure 5.17: Effective pairing contributions from longitudinal (a,c) and transverse (b,d) spin fluctuations in the singlet and triplet channel on the electron pocket centered at $(\pi, 0)$ for a filling of $\langle n\rangle = 1.05$ and $U = 3.0$, $t' = -0.35$. The black cross denotes the position of $\mathbf{k}'$ and the value of $\Gamma^{s/t}_{\mathbf{k},\mathbf{k}'}$ is shown as a function of $\mathbf{k}$ around the hole pocket.

5.11 Solutions to the linearized gap equation

Keeping in mind the pairing structures described above, we now turn to the solutions to the linearized gap equation, Eq. (5.85). We consider three qualitatively different types of Fermi surfaces. First, we study a Fermi surface consisting of hole pockets at $(\pm\frac{\pi}{2}, \pm\frac{\pi}{2})$ which occurs at the hole-doped side, see Fig. 5.18(a,b). Second, we turn to electron pockets at $(\pm\pi, 0)$ and $(0, \pm\pi)$ which occur for small and intermediate electron doping levels, see Fig. 5.18(c,d), and third, we study the occurrence of both electron and hole pockets very close to critical doping as in Fig. 5.18(e,f), i.e. the doping level for which SDW order disappears. As discussed above, the presence of hole pockets destabilizes the commensurate AF by additional intrapocket contributions to the bare spin susceptibilities. In this case, we force stability of the commensurate AF order by turning off the intrapocket contributions by hand.

By inspection of the intrapocket potential structure on the hole pocket shown in Fig. 5.16(a-b) we expect either of the two solutions $d_{x^2-y^2}$ or g for the weakly hole-doped system. From the intrapocket potential structure it is not possible to distinguish between these two solutions. The only way that the system would choose one solution over the other would be from the structure of the pairing potential for $\mathbf{k}$ on one hole pocket and $\mathbf{k}'$ on the neighboring pocket. However, from the numerical potential evaluation it turns out that the interpocket pairing contribution is an order of magnitude smaller than the intrapocket pairing and its symmetry does not favor one of the solutions over the other. This is the reason why we see two degenerate singlet solutions, namely $d_{x^2-y^2}$ and the g solutions, in Fig. 5.18(a-b).

The existence of two degenerate solutions in principle allows for their mixture as a TRSB solution, or for orthorhombic distortions as a direct mixture. At the mean field level, the preference of a TRSB solution might be expected when it is possible to remove gap nodes at the Fermi surface, since removal of gaps from $|\Delta_{\mathbf{k}}|$ leads to an increase in the condensation energy. In the present case of the degenerate solutions $d_{x^2-y^2}$ and g, however, we note that these share the same nodes along the zone diagonal. Thus, there will be no clear gain of energy by constructing a TRSB solution of the form $d_{x^2-y^2} \pm ig$. In fact, solving the full gap equation as stated in Eq. (5.78) reveals that the $d_{x^2-y^2}$ solution is energetically favored.

Turning to the case of 5 % electron doping shown in Fig. 5.18(c-d), we see that the $d_{x^2-y^2}$ solution is clearly favored over the sub-leading solution g, which becomes strongly suppressed. This is a direct

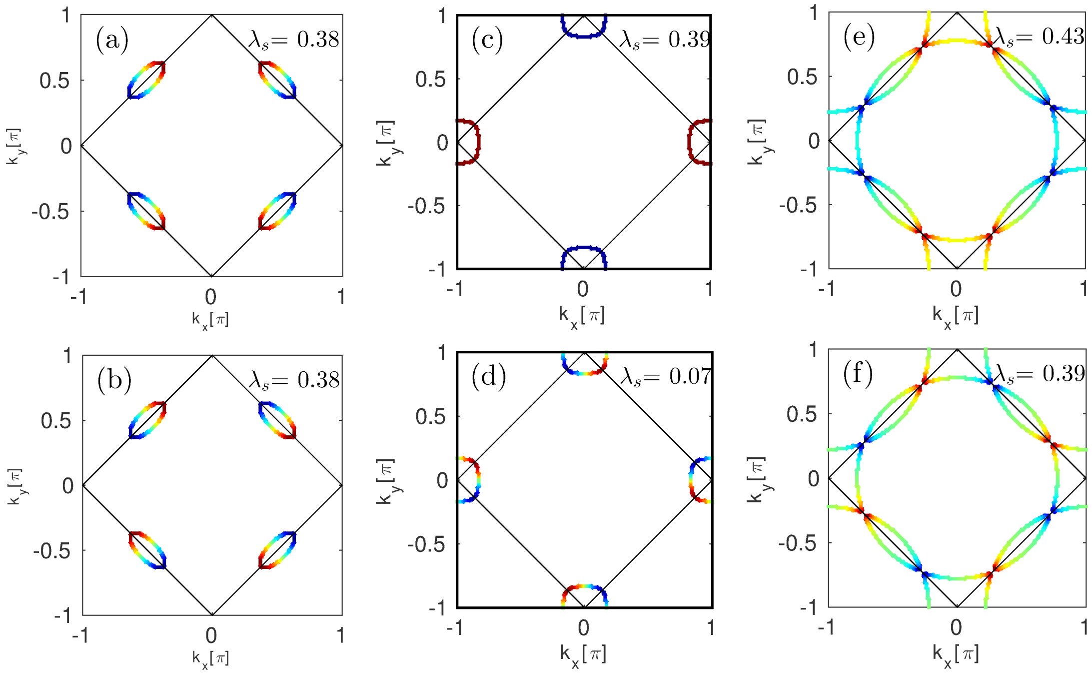

Figure 5.18: Solutions to the linearized gap equation in the presence of (a,b) only hole pockets (4 % hole doping and $U = 3$), (c,d) only electron pockets (5 % electron doping and $U = 3$) or (e,f) both types of pockets (5% electron doping and $U = 2.735$). Positive gap values are shown by red, while negative gap values are shown in blue. The last situation is obtained very close to the AF quantum critical point, i.e. for $W \to 0$. In all three cases the leading solution is $d_{x^2-y^2}$, and the sub-leading solution is g-wave. The latter differs from s-wave by being odd under $k_x \to -k_x$ and $k_y \to -k_y$. Note that in the case of hole doping the two solutions $d_{x^2-y^2}$ and g are nearly degenerate. In the case of small and intermediate electron doping, the $d_{x^2-y^2}$ solution becomes strongly dominant. Upon increased electron doping approaching the quantum critical point, the g-wave solution becomes increasingly important, although always subdominant.

consequence of the intrapocket attraction between $\mathbf{k}$ and $\mathbf{k}'$ residing on the same electron pocket. Upon increasing doping, the electron pockets grow in size, but throughout the SDW region, the $d_{x^2-y^2}$ solution continues to be the leading solution although the sub-leading g-wave gets closer. Also close to the crossover to the paramagnetic phase, where both electron and hole pockets are present at the Fermi surface the leading solution is $d_{x^2-y^2}$, see Fig. 5.18(e-f). Note that the triplet solution is never among the two leading solutions. As we shall show below, the p'-wave solution occurs as the second subleading solution at all doping values, below the g-wave.

5.11.1 Coexistence phase diagram

The complete doping evolution of the three leading superconducting order parameters, $d_{x^2-y^2}$, g and p'-wave, is shown in the phase diagram in Fig. 5.19. On the hole-doped side, we limit the study to the underdoped region. The near-degeneracy of the $d_{x^2-y^2}$ and g-wave solutions, which was observed very close to half filling, is split when hole doping is increased and the $d_{x^2-y^2}$ solution becomes clearly dominant in this regime. In the case of electron doping, the d-wave solution is strongest very close to half filling even though this is not where the longitudinal and transverse pairing potentials achieve their maximum strengths, see Fig. 5.15. The reason is that in the limit where electron pockets are small, the structure of the intrapocket pairing potentials is purely attractive, as shown in Fig. 5.17(a-b), and this

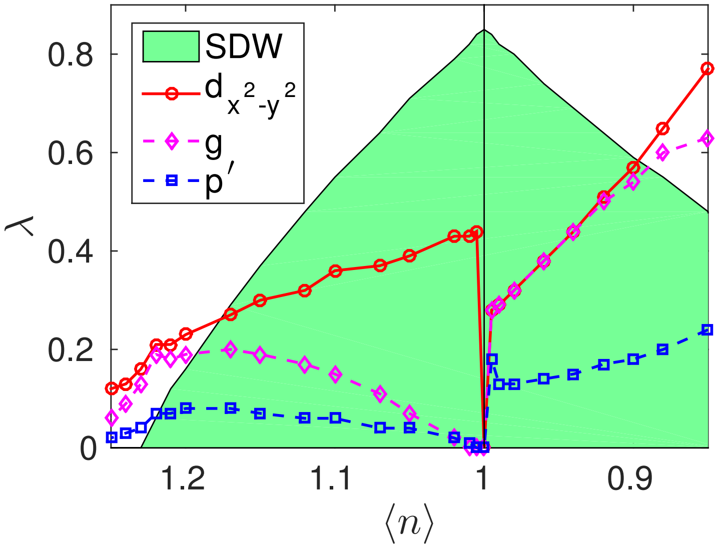

Figure 5.19: Three leading superconducting instabilities as a function of filling. The SDW region is shown by the green area. The three largest eigenvalues to the linearized gap equation, Eq. (5.85), are shown. The $d_{x^2-y^2}$ solution (red line) dominates at all fillings. The next-nearest neighbor hopping is $t' = -0.35$ and the bare Coulomb interaction is $U = 3$.

strongly supports a d-wave solution. We note that this feature of a well-developed gap in the limit of small electron dopings is an inherent result of the weak-coupling approach to the coexistence phase. At critical electron doping for which $W \to 0$, the Fermi arcs just touch the magnetic zone boundary and as a consequence, nesting by $\mathbf{Q}$ on the paramagnetic side is rapidly weakened upon increased electron doping. As seen from Fig. 5.19 solution of the linearized gap equation there is a small jump in the magnitudes of the eigenvalues for the three leading gap symmetries, but the continuation of the three solutions is smooth in the sense that $d_{x^2-y^2}$ continues to being the leading solution, g the sub-leading, and the third solution being the p'-wave, which in the PM phase takes the simpler form $[\cos(k_x) - \cos(k_y)]\sin(k_x)$. The small jump in the corresponding eigenvalues is due to the weak nesting properties of the Fermi surface on the paramagnetic side. In fact, the paramagnetic Fermi surface, which is a hole pocket centered at (π, π) is roughly circular thereby preventing nesting not only at $\mathbf{Q}$, but at any $\mathbf{q}$-vector. As a result spin-fluctuation mediated superconductivity rapidly dies off. The evolution of the $d_{x^2-y^2}$ solution was previously discussed in Ref. [22], where the possibility of a different pairing mechanism close to the crossover between SDW and paramagnetism was speculated. In Ref. [22] the pairing was treated at a phenomenological level. Here we note that also the full treatment of the spin-mediated pairing gives rise to a rapid decrease in the superconductivity upon entering the paramagnetic region.

In figure 5.20 we show estimations of the critical temperatures of the commensurate AF order, T_N, as well as the superconducting ordering temperature, T_c. The value of T_c is estimated from the eigenvalue λ obtained for the leading d-wave solution as a function of doping. Note that this is a very crude estimation that should be taken with a grain of salt, and not as a quantitative measure. It can, however, show what we expect qualitatively for the shape of the superconducting dome. Whereas T_c drops off upon increasing electron doping it shows the opposite evolution as a function of hole doping. At $\langle n \rangle = 1$ the superconducting instability is absent due to a full gapping of the Fermi surface by the magnetic order.

It is tempting to compare the phase diagram on the electron-doped side with the experimental observations reported in Refs. [86, 2], reproduced in Fig. 5.5. The experiments found the highest superconducting temperature at the smallest electron dopings with a monotonic decrease upon increased electron

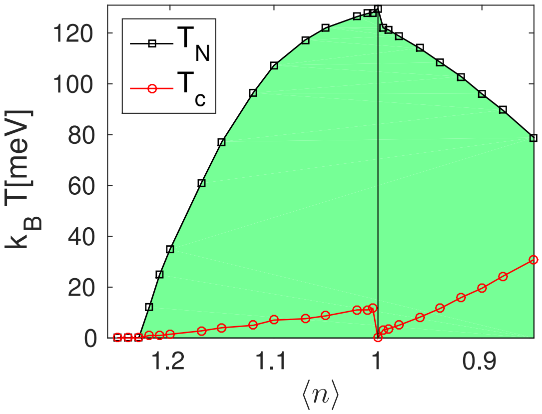

Figure 5.20: The critical temperature, $T_c = 1.13\epsilon_c e^{-1/\lambda}$, with the energy cut off set to $\epsilon_c = 0.25t$ and $t = 400$ meV. The superconducting instability is $d_{x^2-y^2}$ at all fillings. The SDW region is shown by the green area. The next-nearest neighbor hopping is $t'/t = -0.35$ and the bare Coulomb interaction is $U = 3t$. Note that within the weak-coupling approach the SDW ground state is always metallic away from $\langle n\rangle = 1$ and therefore, does not cover the Mott insulating behavior of in the underdoped region of hole-doped cuprates.

doping. This agrees qualitatively with our phase diagram shown in Fig. 5.20 . However, one should note that the underlying Fermi surface of the experiment is not known. Most important, it remains an open question whether SDW order is present in this case.

In the phase diagram shown in Figs. 5.19 and 5.20 we have set $U = 3$. With this Coulomb interaction strength, the critical doping of 23 % is defined by a Fermi surface, which only touches the magnetic zone boundary. This means that hole pockets are absent at all electron doping values. To address the situation, where hole pockets appear at the Fermi surface in the SDW phase close to critical doping, we lower the Coulomb interaction to $U = 2.75$. In addition, we turn off intraband contributions to the susceptibilities at dopings where hole pockets are present, and lower the value of U slightly to $U = 2.5$ in the paramagnetic phase, as discussed in section 5.9. By this procedure we obtain the phase diagram shown in Fig. 5.21. We observe that beside the fact that superconductivity survives for a larger doping regime on the paramagnetic side, the overall features of the phase diagram is similar to the previous

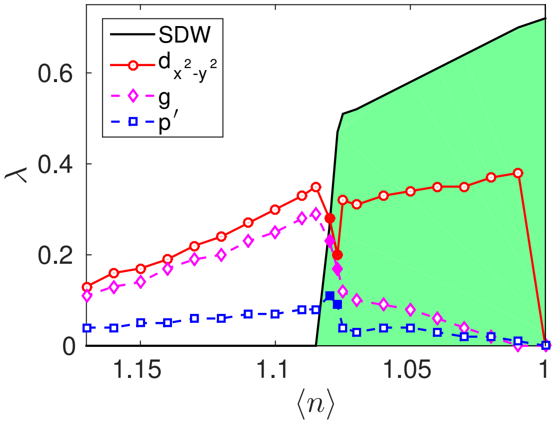

Figure 5.21: Phase diagram for electron dopings. Parameters are $t' = -0.35$ and $U = 2.75$ in the SDW phase and $U = 2.5$ in the paramagnetic phase. Critical doping is 8.5 %. The filled symbols show the eigenvalues at doping levels where the Fermi surface contains both electron and hole pockets. At these doping values, the intraband contributions to the spin susceptibilities is turned off, as discussed in the text. This leads to a small drop in interaction strength in the singlet channel and therefore also in the eigenvalues. The size of the eigenvalues on the paramagnetic side depends on the renormalization of U, which we note is put in by hand.

phase diagram for $U = 3$. The screening of intraband susceptibility contributions leads to a small drop in the eigenvalues of the singlet solutions for dopings of 7.7 % and 8 %, but the order of the three leading solutions remains unchanged; $d_{x^2-y^2}$ is dominant, g-wave subdominant, and p'-wave the third leading solution. In conclusion, there is no drastic consequences for the favored superconducting gap when both types of Fermi pockets are present concurrently.

5.12 Comparison to a $t - J$ model approach to the coexistence phase

The results on the hole-doped side contrast the recent findings of Lu and coworkers, Ref. [104], where a p-wave solution appears as the leading instability. In this paper, the coexistence of commensurate antiferromagnetism and superconductivity was investigated in a $t - J$ model, where the superconducting pairing interactions arise based on nearest-neighbor magnetic superexchange, i.e. $J = t^2/U$. In the coexistence phase, this study found the leading superconducting instability to be triplet p-wave in the case of hole doping, providing a potential explanation for recent photoemission measurements of the "nodal gap"[101, 102, 103], discussed in section 5.2.4. It is worth noting, however, that in the original strong-coupling study of unconventional superconductivity driven by the spin waves by Kuchiev, Flambaum and Sushkov [97], studied within the $t - J$ model, the $d_{x^2-y^2}$-wave symmetry of the superconducting gap was found to be the only stable solution. In the study of Kuchiev and Sushkov [105] the emergence of two-hole bound states in a Néel ordered system was reported; short-range two-hole bound states include $d_{x^2-y^2}$ and p-wave superconducting states, but these vanish at realistic values of $t/J \simeq= 2 - 3$. Thus, according to Ref. [105], the exchange interaction J is too weak to mediate hole-hole bound states. Instead, longer range interactions through spin-wave excitations are investigated and claimed to provide sufficient pairing strengths. With this pairing interaction, however, there is no longer support for a p-wave superconducting state.

In contrast to the strong coupling approaches of Refs. [104, 105, 106], our approach is usually denoted a weak-coupling approach. However, as we have discussed in section 5.3 the large-U/t Hubbard model actually correctly reproduce the spin-wave velocity and dispersion relation of the Heisenberg model. Therefore, there is reason to expect agreement between the strong-coupling approach and the Hubbard model in the limit of large U/t. Indeed, our model which includes longer range interactions through spin fluctuations finds that $d_{x^2-y^2}$ is the dominating instability for weak hole doping, similar to the work by Kuchiev and Sushkov [105]. However, their approach is very different than ours, complicating a direct comparison. On the contrary, the formalism of Ref. [104] is very closely related to our treatment of the SDW phase and this enables a very direct comparison in this case. Thus, it is interesting to investigate exactly in what aspect our approaches differ.

The model of Lu *et al.* [104] is the $t - J$ model:

$$H_{t-J} = -t \sum_{\langle ij \rangle \sigma} [c^\dagger_{i\sigma} c_{j\sigma} + h.c.] + J \sum_{\langle ij \rangle} \mathbf{S}_i \cdot \mathbf{S}_j \tag{5.94}$$

where $c^\dagger_{i\sigma}/c_{i\sigma}$ creates/annihilates a doped particle, which can be either an electron or hole. The spin operator is given by $\mathbf{S}_i = \frac{1}{2} c^\dagger_{i\alpha} \sigma_{\alpha\beta} c_{i\beta}$, where $\sigma_{\alpha\beta}$ are the Pauli matrices. In the case of half filling the $t - J$ model corresponds to the Heisenberg model described solely by the second term of Eq. (5.94). Away from half filling the doped electrons or holes can jump from one site to the neighboring sites. In this case double occupancy can in principle occur. The $t - J$ model only maps to the Heisenberg model if such double occupancies are projected out. This is not the case in Ref. [104], and this is therefore not strictly speaking a strong-coupling approach.

In Ref. [104], the effective interaction Hamiltonian is derived from a Hamiltonian of the form given in Eq. (5.94) in two steps; first the spin operators are expressed in terms of electronic c-operators. Thereafter the c-operators are transformed to the ψ-operators, which diagonalize the antiferromagnetic mean field Hamiltonian. This last step is very similar to our approach, with the important difference in origin and form of the superconducting pairing interaction Hamiltonian.

The interaction Hamiltonian takes the form (for simplicity we write the interaction Hamilonian in the presence of hole pockets only):

$$\begin{aligned} V_{\text{eff}} &= \frac{1}{N}\sideset{}{'}\sum_{k,k'}\sum_{\sigma}\underbrace{\Big[-2J(\mathbf{k}+\mathbf{k}')[n^2(\mathbf{k},\mathbf{k}')+p^2(\mathbf{k},\mathbf{k}')]-J(\mathbf{k}-\mathbf{k}')[m^2(\mathbf{k},\mathbf{k}')+l^2(\mathbf{k},\mathbf{k}')]\Big]}_{\Lambda_{\mathbf{k},\mathbf{k}'}} \\ &\qquad\times\beta^{\dagger}_{\mathbf{k}\sigma}\beta^{\dagger}_{-\mathbf{k}\bar{\sigma}}\beta_{-\mathbf{k}'\bar{\sigma}}\beta_{\mathbf{k}'\sigma}. \end{aligned} \tag{5.95}$$

Here $J(\mathbf{q}) = J[\cos(\mathbf{q}_x)+\cos(\mathbf{q}_y)]$ is given by the nearest neighbor interaction. Note that since $J(\mathbf{q}+\mathbf{Q}) = -J(\mathbf{q})$ and the coherence factors transform by: $n^2(\mathbf{k},\mathbf{k}'+\mathbf{Q}) = p^2(\mathbf{k},\mathbf{k}')$ and $m^2(\mathbf{k},\mathbf{k}'+\mathbf{Q}) = l^2(\mathbf{k},\mathbf{k}')$, the effective pairing potential will satisfy: $\Lambda_{\mathbf{k},\mathbf{k}'+\mathbf{Q}} = -\Lambda_{\mathbf{k},\mathbf{k}'}$. This symmetry constraint of the pairing potential is also obtained in the weak-coupling pairing approach. In both cases it carries over to the superconducting gap which must therefore satisfy:

$$\Delta_{\mathbf{k}+\mathbf{Q}} = -\Delta_{\mathbf{k}}. \tag{5.96}$$

The Hamiltonian as given in Eq. (5.95) is stated in the supplementary information of Ref. [104] Eqs. (13)-(14). Here I have related the coherence factors to the form used in our formalism, i.e. in terms of $n^2(\mathbf{k},\mathbf{k}')$, $p^2(\mathbf{k},\mathbf{k}')$, etc. For a closer inspection of the features of the effective pairing interaction as stated in Eq. (5.95) in the specific case of only hole pockets at the Fermi surface, we plot the evaluated $J(\mathbf{k}+\mathbf{k}')$, $J(\mathbf{k}-\mathbf{k}')$ and the coherence factors seperately in Fig. 5.22.

For $\mathbf{k}$ and $\mathbf{k}'$ around the hole pocket, the momentum $\mathbf{k}-\mathbf{k}'$ is small. Since the pairing is very local in real space involving only nearest-neighbor sites, it is broad in reciprocal space. Therefore, for $\mathbf{k}$ and $\mathbf{k}'$ on the same hole pocket we achieve an almost constant attraction of the order $-J(\mathbf{k}-\mathbf{k}') \sim -2J$, see Fig. 5.22(b), and likewise a constant repulsion of twice the magnitude from the term $2J(\mathbf{k}+\mathbf{k}')$, since $\mathbf{k}+\mathbf{k}' \sim (\pi,\pi)$, see Fig. 5.22(a). As seen in Fig. 5.22(c,d) the coherence factors $m^2(\mathbf{k},\mathbf{k}')+l^2(\mathbf{k},\mathbf{k}')$ are larger than $p^2(\mathbf{k},\mathbf{k}')+n^2(\mathbf{k},\mathbf{k}')$. Due to this, the attractive part of the interaction is enhanced with respect to the repulsion, which is why an overall attraction is achieved.

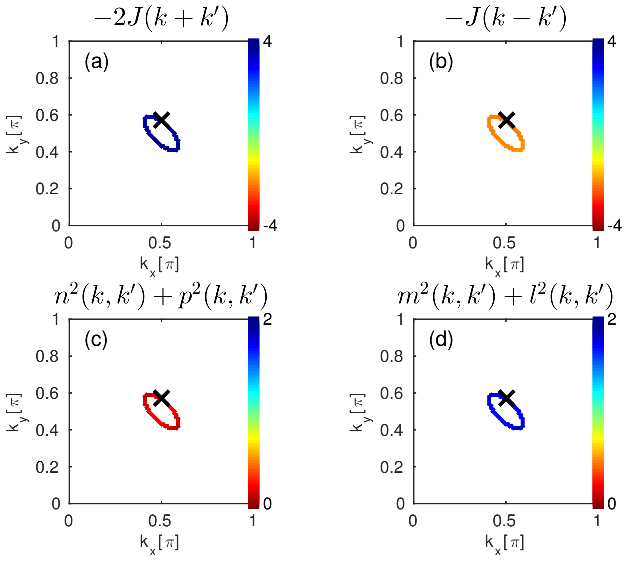

Figure 5.22: Potential components on hole pocket h_1 for a filling of $\langle n\rangle = 0.98$ in the strong-coupling approach as derived in Ref. [104]. Here we have taken a value of $J = 1$ in units of t.

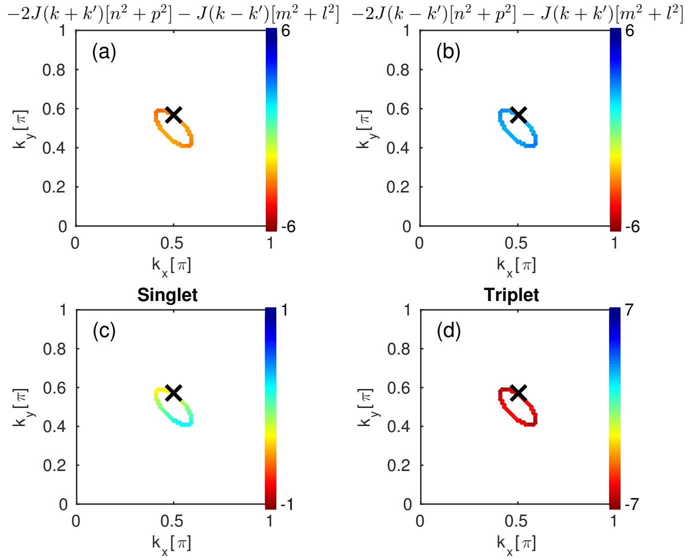

Figure 5.23: Potential on hole pocket h_1 for a filling of $\langle n \rangle = 0.98$ within the $t - J$ model approach as derived in Ref. [104], $t = J = 1$ and $t' = -0.35$. The singlet potential supports a $d_{x^2-y^2}$ solution. The triplet potential supports a p-wave solution.

The full potential is shown below in Fig. 5.23. When solving the gap equation, it is the properly symmetrized versions of the potential which is of interest. In the triplet channel we must perform an antisymmetrization of the potential, and due to the specific form of the coherence factors as discussed above, the interaction is attractive in the triplet channel. Thus, the approach of Ref. [104] supports a p-wave solution, which is favored over the singlet $d_{x^2-y^2}$ solution. The reason why this is not achieved in the weak-coupling approach is because the pairing interaction structure is different. To compare directly, we state the interaction Hamiltonian in our weak-coupling approach in case of hole pockets only, to be compared with the interaction Hamiltonian of the strong-coupling approach as stated in Eq. (5.95):

$$H_{\text{int}} = \frac{1}{4N} \sum_{k,k'}{}' \sum_{\sigma} \Big[\Gamma_c(\mathbf{k}-\mathbf{k}') + \Gamma_z(\mathbf{k}-\mathbf{k}') + 2\Gamma_{\pm}(\mathbf{k}+\mathbf{k}') \Big] \beta^{\dagger}_{\mathbf{k}\sigma} \beta^{\dagger}_{-\mathbf{k}\overline{\sigma}} \beta_{-\mathbf{k}'\overline{\sigma}} \beta_{\mathbf{k}'\sigma} \tag{5.97}$$

with the three pairing channel contributions being

$$\Gamma_c(\mathbf{k}-\mathbf{k}') = [2U - V_c(\mathbf{k}-\mathbf{k}')] l^2(\mathbf{k},\mathbf{k}') - [2U - V_c(\mathbf{k}-\mathbf{k}'+\mathbf{Q})] m^2(\mathbf{k},\mathbf{k}') \tag{5.98}$$

$$\Gamma_z(\mathbf{k}-\mathbf{k}') = V_z(\mathbf{k}-\mathbf{k}') l^2(\mathbf{k},\mathbf{k}') - V_z(\mathbf{k}-\mathbf{k}'+\mathbf{Q})] m^2(\mathbf{k},\mathbf{k}') \tag{5.99}$$

$$\Gamma_{\pm}(\mathbf{k}+\mathbf{k}') = V_{\pm}(\mathbf{k}+\mathbf{k}') n^2(\mathbf{k},\mathbf{k}') - V_{\pm}(\mathbf{k}+\mathbf{k}'+\mathbf{Q})] p^2(\mathbf{k},\mathbf{k}') \tag{5.100}$$

(5.101)

To perform a direct comparison between the two approaches, we compare the evaluated potentials of the strong-coupling approach, Fig. 5.23, with our weak-coupling model, see Fig. 5.24. In the singlet channel we see an effective potential which supports a $d_{x^2-y^2}$ solution. The same structure is found in the singlet channel of the strong coupling approach, see Fig. 5.23 (right). The strong- and weak-coupling approaches differ significantly in the triplet channel. Here the strong-coupling approach find support for a p-wave solution, which is not the case in the weak-coupling approach. In the strong-coupling approach the strength of the pairing interaction is directly related to the strength of the exchange interaction,

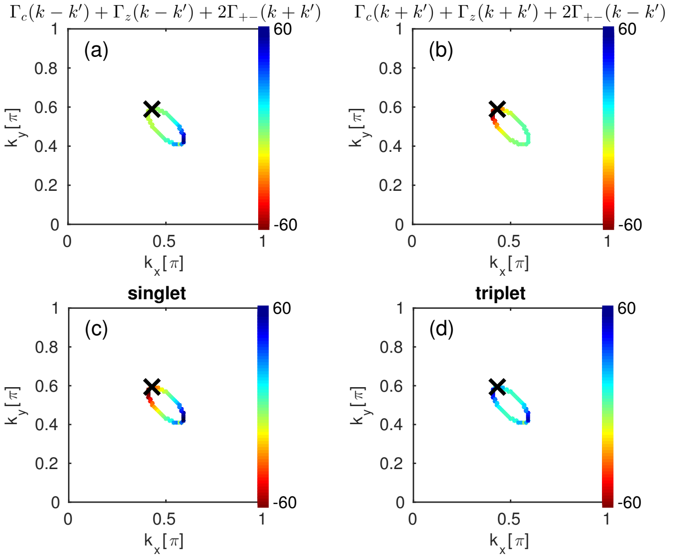

Figure 5.24: Potential on hole pocket h_1 for filling of $\langle n\rangle = 0.98$, $t- = -0.35$ and $U = 3$ within our weak-coupling approach. In the singlet channel there is support for $d_{x^2-y^2}$ superconductivity, while the triplet channel does not support a p-wave solution.

which in the cuprates is of the order of 100 meV, i.e. the same order of magnitude as the nearest-neighbor hopping integral [162]. In the weak-coupling approach the strength is related to the Coulomb interaction and the spin susceptibilities in the SDW phase. In Fig. 5.24 the potential values are given in units of $t \sim 300$ meV, and we see that the pairing strength in the weak-coupling approach is larger than the exchange coupling.

Finally, for completeness we show in Figs. 5.25 and 5.26 the leading triplet solution and the subleading singlet solutions calculated from the linearized gap equation with the strong-coupling version of the pairing interaction, i.e. with the superconducting interaction Hamilonian given in Eq. (5.95.

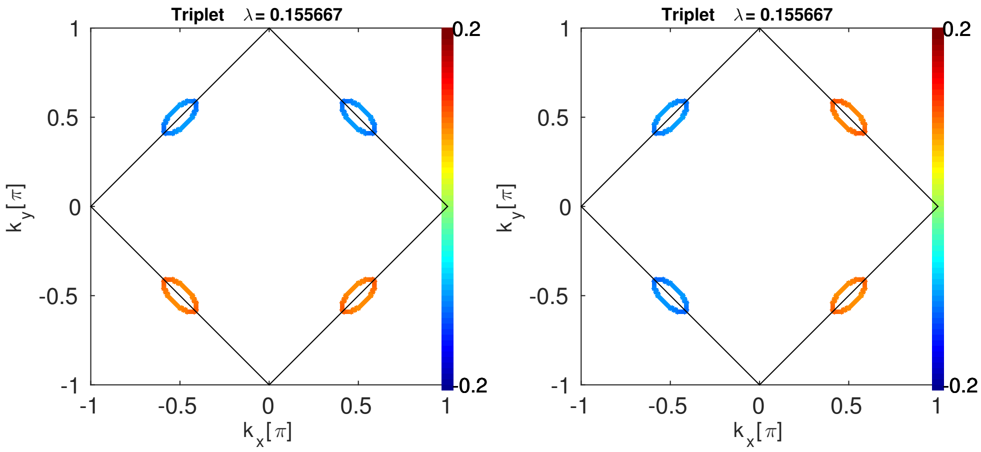

Figure 5.25: Triplet solution to the gap equation in the strong-coupling approach with $\langle n\rangle = 0.98$, $t' = -0.35$ and $J = 1$. The twofold degenerate triplet p-wave solution dominates over the singlet solutions shown in Fig. 5.26.

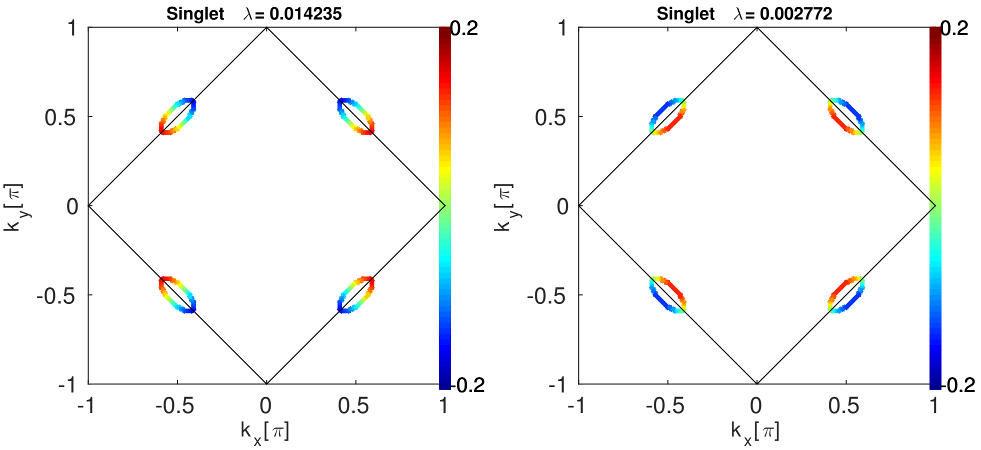

Figure 5.26: Singlet solutions to the gap equation in the strong-coupling approach with $\langle n \rangle = 0.98$, $t' = -0.35$ and $J = 1$. The solutions are given by $d_{x^2-y^2}$ and ext. s-wave, which are strongly suppressed compared to the triplet solution shown in Fig. 5.25.

5.13 Conclusions

We have shown that the $d_{x^2-y^2}$ solution is the leading superconducting instability for all electron doping levels. In the hole-doped case, we limit ourselves to small hole doping only and force the (π, π) order to be stable by a suppression of additional intrapocket nesting contributions to the transverse spin susceptibility. This approach also yields a coexistence phase with $d_{x^2-y^2}$ order. We find that the subleading instability is a singlet g-wave solution, which shares common nodes with the $d_{x^2-y^2}$ solution along the zone diagonals, and has additional nodes along the momenta axes. In the hole-doped case where the Fermi pockets are located far away from the zone axis, g and $d_{x^2-y^2}$ become accidentally degenerate. However, since the two solutions share common nodes, there is no gain in condensation energy for e.g. a time reversal symmetry broken solution of the form $d + ig$, and the solution of the full gap equation in fact favors $d_{x^2-y^2}$ over g. Both transverse and longitudinal spin fluctuations contribute significantly to the pairing interaction. In the singlet channel both types of fluctuations support the same gap symmetry. In the triplet channel the longitudinal fluctuations in fact support a p-wave solution both in the case of small hole and electron doping due to an effective intraband attraction on hole or electron pockets, respectively. However, the strong contribution from transverse fluctuations destroys this effective attraction and destabilizes the p-wave solution. In case of hole-doping, the van Hove effect discussed in chapter 2 supports a triplet gap in a small doping range close to the van Hove critical density in the paramagnetic regime. Since the electron-doped system does not have a similar critical density for which the van Hove singularity crosses the Fermi level, such an effect is restricted to the hole-doped side. In the paramagnetic regime, above the critical doping for which long-range magnetic order vanishes, the spin-fluctuation pairing mechanism becomes strongly suppressed, since the nesting conditions are rapidly weakening as the Fermi surface segments of the paramagnetic phase move apart.

Chapter 6

Neutron Scattering studies of magnetic order and magnetic field effect

In this chapter we will give a brief review of the basics of neutron scattering and discuss some results of magnetic order and field effects reported in the literature with particular focus on the cuprates.

6.1 The technique of Neutron Scattering

Neutrons provide a tool for measuring atomic structures of single crystals, and furthermore, since neutrons are spin-1/2 particles, they also scatter from magnetic structures. The fact that they are chargeless make them interact only weakly with matter, and this enables a penetration into the bulk of the crystal structure. The neutron wavelength is similar to the typical lattice spacings of a crystal and the energy scale of approximately 25 meV makes them appropriate for low energy dynamic measurements, phonons as well as magnons. Depending on the neutron energy, ranging from "ultra cold" to "epithermal" different wave vectors and energies of the crystal structures and excitations are reached. Neutron scattering is a non-local probe and averages over the (magnetic) structure of the entire crystal.

In the next two chapters we will discuss detailed measurements of the magnetic order and low energy excitations of the cuprate $\mathrm{La}_{2-x}\mathrm{Sr}_x\mathrm{CuO}_4$ of 12 % Strontium doping by use of a Triple-Axis-Spectrometer. Cold neutrons of energy ~ 5 meV are used, and we probe magnetic order at a typical wavevector length scale of $\sim 1\text{Å}^{-1}$ as well as magnetic excitations in an energy range of $\hbar\omega = 0.3-7$ meV. In this section, we briefly review the technique of neutron scattering on single crystals with emphasis on neutron scattering from a magnetic structure using unpolarized neutrons. Thereafter, in sections 6.2- 6.8 we review some of the important features of the magnetic order in $\mathrm{La}_{2-x}\mathrm{Sr}_x\mathrm{CuO}_4$ and related system discussed in the literature. Since there has been a lot of activity in the field in more that 25 years, the literature is extensive and only a very small part of it is covered.

6.1.1 Scattering from the atomic and magnetic structures

Electrons act with matter primarily by two means; 1) the neutron is scattered from the nuclei in the crystal structure via the strong nuclear force, and 2) magnetic moments of unpaired electrons of the atomic shells interact with the neutrons through the electromagnetic force. The scattering of the neutrons is quantified by the differential cross section, $\frac{d^2\sigma}{d\Omega dE}$. The differential cross section is a measure of how many neutrons pr. second are scattered in a solid angle $\Omega \pm d\Omega$ with an outcoming energy $E \pm dE$, divided by the incoming flux. The general expression for the differential cross section is[1]:

$$\frac{d^2\sigma}{d\Omega dE} = \frac{k_f}{k_i}\left(\frac{m}{2\pi\hbar^2}\right)^2 |\langle \mathbf{k}_f\lambda_f|V(\mathbf{r})|\mathbf{k}_i\lambda_i\rangle|^2\delta(E_{\lambda_i} - E_{\lambda_f} + E_i - E_f) \tag{6.1}$$

The initial/final wavevector of the neutron is denoted by $\mathbf{k}_i/\mathbf{k}_f$ with energies E_i/E_f and the initial/final state of the crystal is denoted by λ_i/λ_f. In the case of *structural* scattering, the interaction potential is the Fermi's pseudopotential, $V(\mathbf{r}) = \frac{2\pi\hbar^2}{m}b\delta(\mathbf{r})$, since the interaction by the strong nuclear force is very short-ranged. The scattering length, b, is determined empirically.

Scattering from the atomic structure gives rise to two different types of scattering; coherent and incoherent scattering. Coherent scattering is the scattering one would obtain if all atoms had the same scattering length, and this type of scattering is wavevector dependent and reveals presence of structures in the system. Incoherent scattering is due to the fact that not all atoms in the structure have the same scattering length. This can be due to disorder, presence of isotopes or spin of the nucleus and will not contain any information about structures in the lattice, since the variations are non-periodic. In neutron scattering experiments, we are therefore only interested in the scattering arising from the coherent scattering, whereas the incoherent scattering will be regarded as background.

As mentioned above, neutrons provide an ideal tool for magnetic scattering. This is due to the fact that neutrons are spin-1/2 particles with a magnetic moment, and therefore a magnetic dipole interaction occurs between the spin of the neutron and the spin of the electrons from unfilled atomic shells of the crystal. It is possible to map out the magnetic structure of the crystal and probe for magnetic excitations by use of elastic and inelastic scattering, respectively. In principle, spin polarized neutrons are needed to ultimately determine if structures are of magnetic or structural character. In the case of the cuprates, it is already well-established that the order which is measured close to the position of the commensurate antiferromagnetic ordering vector is of magnetic origin and therefore in our case it suffices to use unpolarized neutrons, probing the sample below the magnetic ordering temperature. To obtain the differential cross section for *magnetic* scattering, the interaction potential in the general cross section expression, Eq. (6.1), is given by the Zeeman potential for the interaction between the neutron spin and the dipole moment of the magnetic atoms, with the dipole moment arising from unpaired electrons in the atomic shells. The thermal average in Eq. (6.1) must now also account for the spin state of the neutron. If the crystal has only one type of magnetic atoms, then the magnetic differential cross section becomes[2]:

$$\begin{aligned}\frac{d^2\sigma}{d\Omega dE} &= \frac{N}{\hbar}\frac{k_f}{k_i}\left(\frac{\gamma r_0}{2}\right)^2 g^2 F(\mathbf{q})^2 e^{-2W} \\ &\quad \underbrace{\sum_{\alpha,\beta}(\delta_{\alpha,\beta} - q_\alpha q_\beta)\underbrace{\frac{1}{2\pi}\int_{-\infty}^{\infty} dt e^{-i\omega t}\sum_l e^{i\mathbf{q}\cdot\mathbf{r}_l}\langle S_0^\alpha(0)S_l^\beta(t)\rangle}_{S^{\alpha\beta}(\mathbf{q},\omega)}}_{S(\mathbf{q},\omega)}\end{aligned} \tag{6.2}$$

The fraction $\frac{k_f}{k_i}$ in the cross section refers to the experimental setup, while the remaining quantities depend on properties of the sample only. The prefactor N is the number of unit cells, $\gamma = 1.913$ is the gyromagnetic ratio, r_0 is the electron radius $r_0 = \frac{e^2}{m_e c^2}$ and g is the Landé splitting factor. The magnetic form factor, $F(\mathbf{q})$, is the Fourier transform of the spin density of one atom:

$$F(\mathbf{q}) = \int d^3 r s(\mathbf{r}) e^{i\mathbf{q}\cdot\mathbf{r}} \tag{6.3}$$

In the cuprate system, the spatial distribution of the spin is $d_{x^2-y^2}$-wave, since the Cu-atom spin arises from an unpaired electron in the d-shell. For large scattering vectors (beyond the first Brillouin zone)

---

[1] Ref. [107] Eq. (2.15)

[2] Eq. (2.65) and (2.66) in [108].

the magnetic form factor falls off to zero. The factor e^{-2W} is the Debye-Waller factor which arises because of atomic thermal vibrations away from the equilibrium positions. This suppresses the signal with increasing temperature.

The function $\langle S_0^\alpha(0)S_l^\beta(t)\rangle$ gives the correlation between the components of two spins separated by the distance l and by a time t with α, β being Cartesian coordinates, $\alpha, \beta \in \{x, y, z\}$. The angle brackets denotes a thermal average over configurations. The correlation function is Fourier transformed in space and time and the factor $(\delta_{\alpha,\beta} - q_\alpha q_\beta)$ reflects the fact that only spin components perpendicular to the scattering vector $\mathbf{q}$ contribute to the scattering signal. If for instance $\hat{\mathbf{q}} = (0, 0, 1)$ then we will only see contributions from the correlation functions $S^{xx}(\mathbf{q}, \omega)$ and $S^{yy}(\mathbf{q}, \omega)$, whereas there will be no contribution from $S^{zz}(\mathbf{q}, \omega)$ or the "mixed" terms $S^{xy}(\mathbf{q}, \omega)$ etc. The sum over the Cartesian coordinates $\alpha, \beta \in \{x, y, z\}$ gives the function $S(\mathbf{q}, \omega)$, which is the denoted the scattering function. The monitor efficiency is proportional to $1/k_i$ [108]. By counting at constant monitor and doing the measurements at fixed k_f the fraction $\frac{k_f}{k_i}$ will be constant during a measurement and thereby we get a signal which is proportional to the scattering function modified by the magnetic form factor and the Debye-Waller factor.

The intensity recorded by the neutron detector is the convolution of the instrumental resolution function with the scattering function, $S(\mathbf{q}, \omega)$ of Eq. (6.2), which in turn is related to the imaginary part of the generalized magnetic susceptibility $\chi''(\mathbf{Q}, \omega, T)$ via the fluctuation dissipation theorem [108]:

$$S(\mathbf{q}, \omega, T) = \frac{\chi''(\mathbf{q}, \omega, T)}{1 - e^{-\hbar\omega/k_B T}} \tag{6.4}$$

In addition to the magnetic scattering $S(\mathbf{q}, \omega, T)$, the raw experimental data also contain contributions which do not arise from electronic magnetism, but are due to scattering from atomic nuclei as well as incoherent background contributions. To obtain $\chi''(\mathbf{q}, \omega, T)$ it is important to cleanly separate these contributions, as well as to account for resolution effects of the experimental setup. When such a separation is performed, i.e. the scattering function of the magnetic signal $S(\mathbf{q}, \omega)$ is extracted from the measured intensity, the fluctuation-dissipation theorem provides the connection between theory and experiment.

6.1.2 Elastic and inelastic scattering

In *elastic* neutron scattering, the neutrons diffract from the crystal according to Bragg's law

$$q = 2k \sin\theta$$

where the scattering vector, $\mathbf{q} = \mathbf{k}_i - \mathbf{k}_f$, is a reciprocal lattice vector of the crystal and $|\mathbf{k}_i| = |\mathbf{k}_f|$. No energy transfer takes place between the neutron and the nucleus. This technique is used for probing the atomic structure as well as the static magnetic structure of the sample.

The equation of *elastic nuclear* scattering from an ordered structure is given by[3]:

$$\begin{aligned} \frac{d\sigma}{d\Omega} &= e^{-2W} |\sum_j b_j e^{i\mathbf{q}\cdot\mathbf{r}_j}|^2 \\ &= N\frac{(2\pi)^3}{V_0} e^{-2W} |F_N(\mathbf{q})|^2 \sum_{\mathbf{Q}} \delta(\mathbf{q} - \mathbf{Q}) \end{aligned} \tag{6.5}$$

where the sum in the first line is over all lattice vectors $\mathbf{r}_j$. The nuclear structure factor is given by:

$$F_N(\mathbf{q}) = \sum_i b_i e^{i\mathbf{q}\cdot\mathbf{d}_i}$$

---

[3] Eqn. (7.3) and (7.21) in [109]

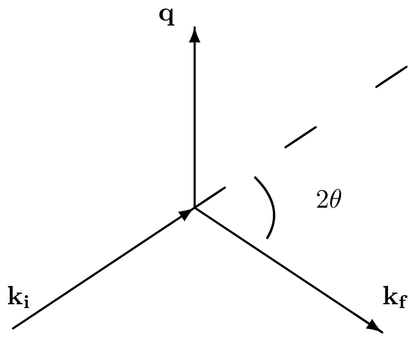

Figure 6.1: The scattering triangle giving the incoming and outgoing neutron wavevector $\mathbf{k_i}$ and $\mathbf{k_f}$, the scattering vector $\mathbf{q} = \mathbf{k_i} - \mathbf{k_f}$ and the scattering angle 2θ.

where the sum is over all lattice vectors in a unit cell, N is the number of lattice sites, V_0 is the volume of one unit cell and $\mathbf{Q}$ is a reciprocal lattice vector satisfying $e^{i\mathbf{r}\cdot\mathbf{Q}} = 1$ for $\mathbf{r}$ being any lattice vector.

Elastic scattering from a magnetic structure gives rise to magnetic Bragg peaks at the reciprocal lattice vectors of the magnetic structure. The equation for elastic magnetic scattering from an ordered structure is given by[4]:

$$\frac{d\sigma}{d\Omega} = (\gamma r_0)^2 \frac{N(2\pi)^3}{V_0} \left(\frac{g}{2}\right)^2 |F(\mathbf{q})|^2 |F_M(\mathbf{q})|^2 e^{-2W} \sum_{\mathbf{Q}_M} \delta(\mathbf{q} - \mathbf{Q}_M) \tag{6.6}$$

where $\mathbf{Q}_M$ is a magnetic ordering vector. The magnetic structure factor is:

$$F_M(\mathbf{q}) = \sum_{\mathbf{d}} e^{-i\mathbf{q}\cdot\mathbf{d}} \langle \mathbf{s}_\perp(\mathbf{d}) \rangle \tag{6.7}$$

The sum runs over the lattice vectors $\mathbf{d}$ in a magnetic unit cell and $\langle \mathbf{s}_\perp(\mathbf{d}) \rangle$ denotes the thermal average of the spin components perpendicular to the scattering vector. Magnetic scattering can be distinguished from nuclear scattering by measuring at temperatures below the magnetic ordering temperature or by use of polarized neutron scattering [109].

The magnetic unit cell is in general larger than the structural unit cell. In Fig. 6.2 we give the simple example of scattering from a square lattice with commensurate antiferromagnetic structure. The structural peaks occur at the reciprocal lattice vectors $(q_x, q_y) = (\frac{2\pi}{a}h, \frac{2\pi}{a}k)$ with h and k being integers. Due to the magnetic structure there will be additional scattering at positions $(q'_x, q'_y) = (\frac{2\pi}{\sqrt{2}a}h, \frac{2\pi}{\sqrt{2}a}k)$ with the new (orthorhombic) coordinate system tilted 45^o with respect to the old (tetragonal) coordinate system. This is illustrated in Fig. 6.2 to the right.

---

[4] Eqn. (9.39) and (9.40) in [109]

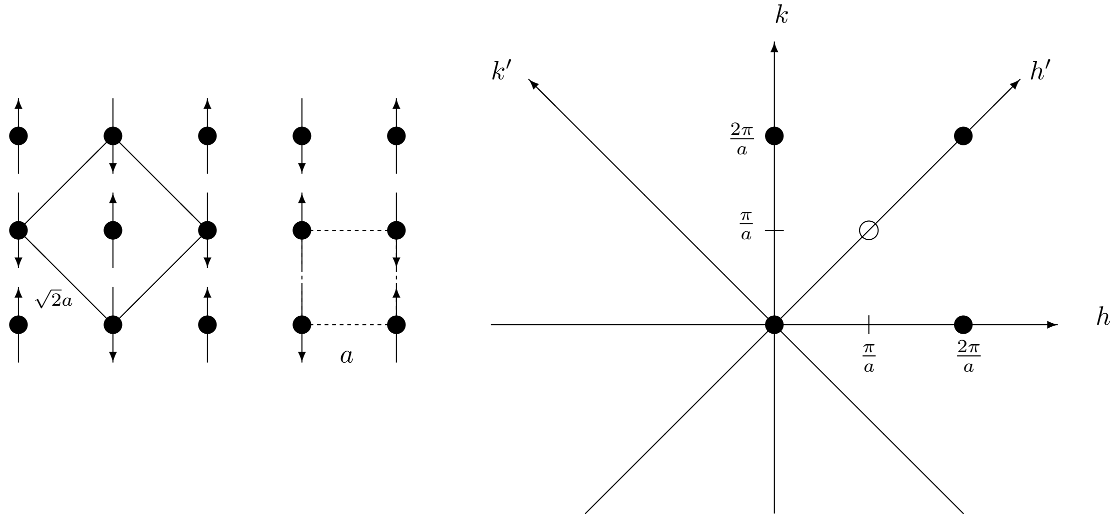

Figure 6.2: A two-dimensional square lattice with commensurate antiferromagnetic order. The dashed box marks a structural unit cell of lattice constant a. The antiferromagnetic unit cell is twice the size of the structural unit cell and contains two atoms of opposite spin. The lattice constant of the AFM unit cell is $\sqrt{2}a$. The AFM order gives rise to additional scattering. In the right figure, scattering from the atomic ordering has been indicated by filled dots whereas magnetic scattering from the antiferromagnetic structure is depicted by the unfilled dot.

One should be aware of the fact that the notion of "static" is a relative statement, which is limited to the time scale of a neutron scattering experiment. An energy resolution of ΔE is related to the time scale of the scattering process through the uncertainty relation $t \sim \frac{\hbar}{\Delta E}$. In a typical experiment the energy resolution is of the order of tenths of meV. This means that the typical time scale for a neutron scattering experiment is of the order $t \simeq \frac{6.6 \cdot 10^{-16} eV s}{10^{-4} eV} \simeq 10^{-11} s$. In principle, if fluctuations occur on a time scale which is larger than $\sim 10^{-11} s$, the neutrons will measure *static* order, even though the moments are slowly fluctuating. What is probed in this case is strictly speaking low-energy fluctuations, with a characteristic energy smaller than the resolution of the experimental setup.

Additional information about the nature of the measured neutron signal – whether the order is static or fluctuating – can be obtained by e.g. a local probe like muon spin rotation (μSR). In this technique, one muon is implanted at a specific position in the unit cell, where it will precess around the local magnetic field. The mean life time of a muon is $2.2 \cdot 10^{-6}$ s, and moments which are measured as static by a μSR experiment fluctuates on a time scale longer than microseconds.

As we shall see, the different time scales associated with a neutron and a muon experiment is manifested in different estimations for the ordering temperature. The ordering temperature as deduced from a neutron experiment, simply state that the magnetic fluctuations are slower than picoseconds. Thus we can not tell from a neutron experiment if static order is really present, the only information we obtain is that the magnetic fluctuations are slow compared to 10-100 picoseconds. In principle, the same constraint goes for the ordering temperature obtained by a muon experiment, only that in this case fluctuations must be slower than microseconds.

When the neutrons scatter *inelastically* from the sample, energy is either lost or gained when the neutron interacts with a nucleus in the sample. The scattering function therefore depends both on the momentum deposited in the sample $\mathbf{q} = \mathbf{k}_i - \mathbf{k}_f$ as well as the energy transfer $\hbar\omega = E_i - E_f = \frac{\hbar^2}{2m_n}(k_i^2 - k_f^2)$. Inelastic scattering is used to probe fluctuations in the sample, e.g. phonons or magnons. Usually we probe the samples at very low temperatures, and measure the cross section from neutrons that have deposited energy in the sample. In chapter 7, we present neutron scattering studies of the low-energy magnetic fluctuations of $La_{2-x}Sr_xCuO_4$.

6.1.3 Triple Axis Spectrometer

A triple axis spectrometer is an instrument for investigating order and fluctuations in a single crystal. A very schematic drawing is shown in Fig. 6.3. By the monochromator angle, θ_M we select the wavevector of the incoming neutrons by Bragg's law; $Q_M = 2k_i \sin\theta_M$, where $\mathbf{Q}_M$ is a reciprocal lattice vector of the monochromator. If $\mathbf{Q}_M$ is a reciprocal lattice vector so is $2\mathbf{Q}_M$ and therefore so-called higher order neutrons are also present, i.e. neutrons of wavelength $\frac{\lambda}{2}$, $\frac{\lambda}{3}$ etc. The higher order neutrons can be avoided by use of Be-filters, which let only through neutrons of wavelengths $\lambda > 3.9$ Å.

At the analyzer, we select which neutrons are detected, i.e. the traveling direction and wavelength of the detected neutrons. By this arrangement we are able to search through reciprocal space and thereby map out the order and excitations possible in the investigated sample.

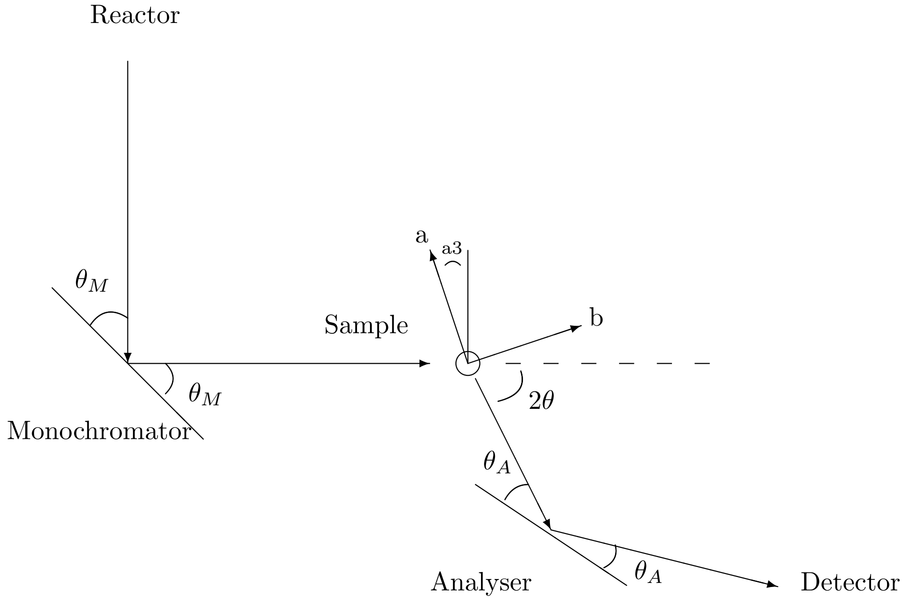

Figure 6.3: Schematic drawing of a Triple Axis Spectrometer. The three axes are the arm between the monochromator and sample, the sample and analyzer and the analyzer and detector. It is the arrangement of the two arms after the sample position that allow for detection of outcoming neutrons of varying energies thereby making it possible to measure excitations. In contrast, a Two Axis Spectrometer has only one arm after the sample and can only detect static order.

Sample rotation scan /a3 scan:
The angle a3 is the angle between the incoming beam and one orientation of the sample as depicted in Fig. 6.3. When performing an a3-scan, the sample is turned around without changing the position of the monochromator or the analyzer. Hereby the angle 2θ, which is the angle between $\mathbf{k}_i$ and $\mathbf{k}_f$, is kept constant. In this way the length of the scattering vector $\mathbf{q}$ is also constant throughout the scan, which corresponds to scanning along the circumference of a circle of radius q in reciprocal space. An a3-scan of

a structural peak reveals the peak broadening due to mosaicity of the crystal as well as the broadening due to the instrumental resolution. The latter depends on the configuration of the instrument and changes significantly when changing the orientation of the monochromator and analyzer. In an a3-scan one expects a flat or slowly varying background.

Possible powder lines arising from Aluminium and Copper in the vicinity of the sample can reach the detector when the angle 2θ corresponds to the Bragg angle of the elastic scattering from one of these two compounds. Such powder lines can be quite disturbing. A good way to avoid the problem of powder lines is to do a3-scans. Then one can position the monochromator and analyser such that 2θ does not correspond to a scattering vector of Al or Cu. Even if 2θ happens to coincide with a Bragg angle this will only raise background to a higher, but constant level.

Scan through a line in reciprocal space
Another possibility is to scan through a line in reciprocal space. This will cause both a3 and 2θ to change during a scan. The background level can change during such scans due to powder lines or change in the resolution function. The advantage is that one gets to probe any line in reciprocal space and can choose the steps in units of h, k and l.

6.1.4 Resolution

In general, there is a finite spread in the directions and energies of the neutrons. This divergence of the beam causes a finite resolution in a neutron scattering experiment. The divergence can be made smaller by inserting collimators. Collimators consist of parallel absorbing plates of a certain length and height, which are separated by a fixed distance. This distance determines the collimation of the beam; the smaller the distance the more collimated beam. Insertion of collimators improve the resolution, but flux is lost and we must always weigh out the gains in resolution with the loss in flux.

The finite resolution is described by distributions about the average wave vectors, $\overline{\mathbf{k}}_i$ and $\overline{\mathbf{k}}_f$. The distribution $P_i(\mathbf{k}_i - \overline{\mathbf{k}}_i)$ is determined by the mosaicity[5] of the monochromator and the collimations of the neutron beam before it hits the sample. The incoming resolution volume $V_i = \int d\mathbf{k}_i P_i(\mathbf{k}_i)$ is a measure of the spread in incoming $\mathbf{k}_i$-values. Likewise $P_f(\mathbf{k}_f - \overline{\mathbf{k}}_f)$ is determined by the collimators after the sample position and the mosaicity of the analyzer.

The signal we measure is the convolution of the spectrometer resolution function and the scattering function and deconvolution is needed to separate the scattering function and the resolution function. The measured intensity at some wavevector $\mathbf{q}_0$ and energy transfer $\hbar\omega_0$ is given by[6]:

$$I(\omega_0, \mathbf{q}_0) = \int d\omega d\mathbf{q} R(\omega - \omega_0, \mathbf{q} - \mathbf{q}_0) S(\mathbf{q}, \omega) \tag{6.8}$$

where the resolution function is defined by

$$R(\omega - \omega_0, \mathbf{q} - \mathbf{q}_0) = \frac{\hbar^2}{V_i m_n} \int d\mathbf{k}_i d\mathbf{k}_f P_i(\mathbf{k}_i - \overline{\mathbf{k}}_i) P_f(\mathbf{k}_f - \overline{\mathbf{k}}_f) \delta(\mathbf{q} - \mathbf{k}_f + \mathbf{k}_i) \delta(\omega - \frac{\hbar^2}{2m_n}(k_i^2 - k_f^2)) \tag{6.9}$$

A reasonable approximation is to assume that the beam profiles, which emerge from the different components of the spectrometer, e.g. monochromator and collimators, are Gaussian distributions. An analytic calculation of the resolution function gives in this approximation a four dimensional ellipsoid, the four dimensions being the 3 components of the scattering vector, q_x, q_y, q_z, and the energy, $\hbar\omega$. The cross section between the resolution ellipsoid and e.g. the scattering plane (q_x, q_y) as well as the projection of the resolution ellipsoid onto the scattering plane give ellipses. In an elastic scattering experiment, the momentum resolution can be determined by the width of a structural Bragg peak. It is important to be aware of the fact that the resolution is a function of the scattering vector. The trick of using the Bragg

---

[5] The monochromator consists of many perfect crystallites with small relative misorientations. The small misorientations cause a divergence of the neutron beam, but they are necessary in order to get an acceptable neutron flux.

[6] Eq. (4.13) in [108].

peak width as a measure of the resolution therefore only works if we are measuring at an ordering vector very close to the position of the structural peak. Otherwise simulations of the experimental setup by e.g. *Reslib* [110] for *Matlab* or *McStas* [111] are useful tools.

6.1.5 Correlation length

The signal obtained from a neutron scattering experiment is a peak of finite width. The broadening of the signal is partially due to the resolution of the experimental setup as discussed above, and partially due to an intrinsic width of the scattering from the structural or magnetic order in the crystal. For a spin-spin correlation function between two spins at the sites i and j of a crystal lattice that decays exponentially for increasing separation of site i and j, $\langle S_i^\alpha S_j^\alpha \rangle \propto e^{-\kappa(|R_i - R_j|)}$, the Fourier transform is given by a Lorentzian function with Half Width Half Max (HWHM) given by κ [112]. Considering a ideal experiment where there is no broadening due to resolution effects, the width of the peak is then directly related to the correlation length by $1/\kappa = 1/\mathrm{HWHM}$. Thus, the intrinsic width gives information about the how long- or short-range the order is. For very long range order, the intrinsic peak is extremely narrow and in this case, the measured peak width will be limited by the resolution function. The detection of a resolution limited peak allows us to give only a lower bound of the correlation length. If the order is short-range, the width of the peak might exceed the resolution limited width and in that case we need to deconvolute the contributions from the resolution and the intrinsic width. Taking both the scattering signal and the resolution to be Gaussian distributions of widths σ_s and σ_R respectively, the measured signal will itself be a Gaussian of width

$$\sigma_m = \sqrt{\sigma_R^2 + \sigma_s^2}$$

If the scattering signal width is of the order of the resolution limited width one must deconvolute the different contributions to the measured signal. In this case a program (e.g. *Reslib* or *McStas*) which takes into account all geometries of the experimental setup is used to calculate the resolution function at any position in reciprocal space. For very broad signals, i.e. much broader than the resolution limited width, a deconvolution is not so crucial since the resolution plays a very subdominant role to the broadening of the signal. In this case, the data should be fitted to a Lorentzian function and the (short) correlation length is estimated directly from the raw signal. In chapter 8 we shall see that the incommensurate magnetic order observed in $La_{1.88}Sr_{0.12}CuO_4$ is long ranged and resolution limited within the CuO_2 planes, but extremely short ranged between the CuO_2 planes.

6.2 Competition of superconductivity and SDW order

In many superconducting systems, magnetic order and fluctuations show up in very close proximity to the superconducting phase. In case of the cuprates, heavy fermions and iron-based superconductors, some regions are characterized by the presence of magnetic order and superconductivity at the same time. The important question of how these two orders compete or cooperate is still being debated. In addition, a number of other distinct phases appear throughout the phase diagrams, with the pseudogap and the possibly related charge order in cuprates being a focus for much activities in the cuprates, and the nematicity a highly debated subject in the case of iron-based superconductivity.

In some systems the coexistence of SDW and superconductivity has proven to be microscopic. One example[113] is the iron-based superconductor $Ba(Fe_{1-x}Co_x)_2As_2$, in which evidence for competition between static order with superconductivity is obtained; upon application of an external magnetic the magnetic order parameter is enhanced, but the effect is only observed for temperatures below the superconducting transition temperature, see Fig. 6.4. This can be understood from a microscopic model in which the presence of vortices induce additional magnetic order, and at the same time suppresses superconductivity. Recently, observations has been reported for the iron-based superconductor $Ca_{1-x}Na_xFe_2As_2$ [115], where the presence of superconducting order leads to a suppression of the magnetic order. In both cases the observations tell us, that there is a strong interplay between the two

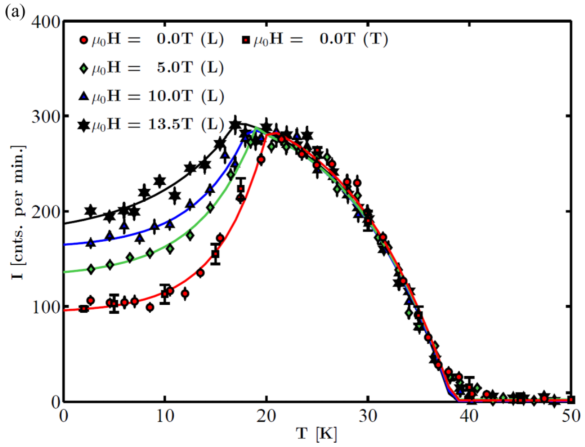

Figure 6.4: Magnetic field effect on the elastic neutron response of the magnetic order in $Ba(Fe_{1-x}Co_x)_2As_2$with superconducting transition temperature $T_c \simeq 20$ K and magnetic transition temperature (measured by μSR) of $T_N \simeq 40$ K. Adapted from J. Larsen *et al.*, Ref. [113].

ordering phenomena. This is after all not so surprising, since the electrons are the main ingredient for both the magnetic ordering as well as the superconductivity. If the two orders coexist on a microscopic level, it will be the same electrons participating in both the magnetic ordering as well as superconductivity. It seems plausible that the emergence of static order will act as a competitor of superconductivity. A similar picture of competition between static magnetism and superconductivity is obtained in case of the cuprates, as we see below.

6.3 Stripy SDW order of the cuprates

Undoped cuprates are charge transfer insulators (Mott insulators) that upon charge-carrier doping of the CuO_2 layers become superconducting. For carrier concentrations lower than optimal for superconductivity, *i.e.* in the underdoped regime, several competing or coexisting order parameters have been identified among which incommensurate spin ordering has been extensively studied. It was first observed as a spin and charge stripe order in $La_{1.6-x}Nd_{0.4}Sr_xCuO_4$ (Nd-LSCO) [116] when the hole-doping level p was tuned to $p = x = 1/8$. A similar type of stripe order has also been observed in $La_{2-x}Ba_xCuO_4$ (LBCO) [117, 118] and $La_{1.8-x}Eu_{0.2}Sr_xCuO_4$ (Eu-LSCO) [119, 120], at $p = 1/8$. In all three cases, competition between incommensurate spin-charge order and superconductivity causes a dramatic drop of T_c, which reaches very low values at $x = 1/8$, where the stripe ordering tendencies are most pronounced. The cuprate which is investigated in this thesis, $La_{2-x}Sr_xCuO_4$, also displays incommensurate spin order that survives within the superconducting dome. As opposed to the genuinely stripy compounds, Nd-LSCO, LBCO and Eu-LSCO, it shows only a weak anomaly around $p = 1/8$, where SDW order is particularly pronounced, and the superconducting transition temperature is somewhat suppressed compared to systems of slightly higher or smaller doping. However, the suppression is about 10 %, i.e. only a few Kelvin, and much smaller than in the other stripe compounds. In addition to the almost ubiquitous presence of SDW order, charge density wave order has now been established in almost all members of the cuprate family. Most recently, charge order has been reported in $YBa_2Cu_3O_7$ [121, 122] and $La_{2-x}Sr_xCuO_4$ [123, 124, 125]. Two different charge orders have been observed. First, long range order characterized by the ordering vector $\mathbf{q}_{CDW} = 2\mathbf{q}_{SDW}$, is commonly observed in the 214 cuprates and was the type of charge order originally reported by Tranquada in $La_{1.6-x}Nd_{0.4}Sr_xCuO_4$ [116]. The same type of order has been observed in $La_{2-x}Ba_xCuO_4$ and, most recently, in $La_{2-x}Sr_xCuO_4$. Second, short range correlations with modulations along the Cu-O-Cu axes with $\mathbf{q} = (\delta_1, 0, 0.5)$ and $\mathbf{q} = (\delta_2, 0, 0.5)$,

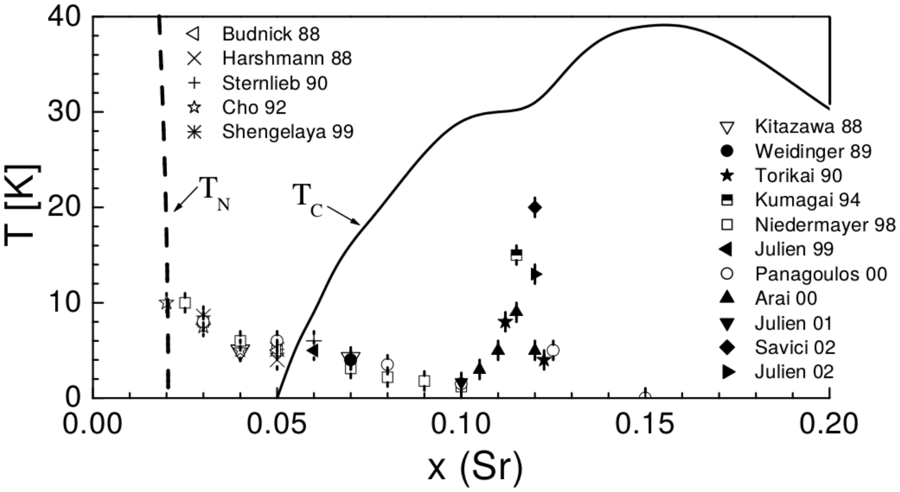

Figure 6.5: Magnetic ordering temperature in $La_{2-x}Sr_xCuO_4$ as a function of Sr doping, x. Data has been obtained by the local probes μSR, NQR and NMR measurements. At $x = 0.12$ the magnetic ordering temperature displays a strong enhancement. Adapted from M.-H. Julien, Ref. [126].

where $\delta_1 \simeq \delta_2 \simeq 0.3$ is reported in for example $Bi_2Sr_2CaCu_2O_8$ and $YBa_2Cu_3O_7$. In the recent review by Fradkin, Kivelson and Tranquada [114], it is proposed that both types of charge order are manifestations of the same underlying electronic texture.

6.4 Magnetic order and field effects in $La_{2-x}Sr_xCuO_4$

Now we turn to the system of this thesis, namely the cuprate superconductor $La_{2-x}Sr_xCuO_4$. In this single-layer cuprate, quasi two-dimensional magnetic order and fluctuations coexist with superconductivity. We have studied a sample of doping $x = 0.12$, close to the 1/8 anomaly. A sharp increase in the magnetic order has been measured by local probes, muon spin resonance μSR, nuclear magnetic resonance (NMR) and nuclear quadropole resonance (NQR) [126], as shown in Fig. 6.5. This also indicates a small suppression in the superconducting transition temperature right around the doping level of $x = 0.12$. Recently, a number of X-ray experiments have found evidence for charge order in this compound [123, 124, 125], and the system thus show quite strong resemblance with the genuinely stripy compounds $La_{2-x}Ba_xCuO_4$and $La_{1.6-x}Nd_{0.4}Sr_xCuO_4$ where stripes are observed as joint order of modulated antiferromagnetism and charge stripes[116, 127, 128, 129].

The magnetic ordering in $La_{2-x}Sr_xCuO_4$ have been observed at a quartet of IC positions around the magnetic ordering vector in the parent compound La_2CuO_4 (LCO), i.e. $\mathbf{Q}_{\mathrm{IC}} = (1 \pm \delta_H, \ \pm \delta_K \ , 0)$ in orthorhombic notation[130, 131, 133, 134, 135]. In the doping range $0.06 \leq x \leq 0.13$ the incommensurability δ scales linearly with the doping, $\delta \approx x$ [136]. Application of an external magnetic field is expected to influence the magnetic order, since it couples directly to the spins. Several neutron scattering experiments for dopings $0.10 \leq x \leq 0.135$ have investigated the field effect and found an enhancement of the magnetic order [137, 138, 139, 140]. As an example, we show in Fig. 6.6 how the application of a magnetic field leads to an enhancement of the magnetic scattering signal in $La_{2-x}Sr_xCuO_4$ of doping $x = 0.105$ and $x = 0.12$ [139]. The temperature dependence resembles the temperature dependence of the magnetic signal in $La_{1.6-x}Nd_{0.4}Sr_xCuO_4$, in which the magnetic signal is unaffected by a magnetic field, and ordering is thus considered fully developed already in zero field. Modeling of a doped system, where a magnetic field is applied and impurities are present, gives a similar temperature dependence of the magnetic moments [141], see Fig. 6.6(right).

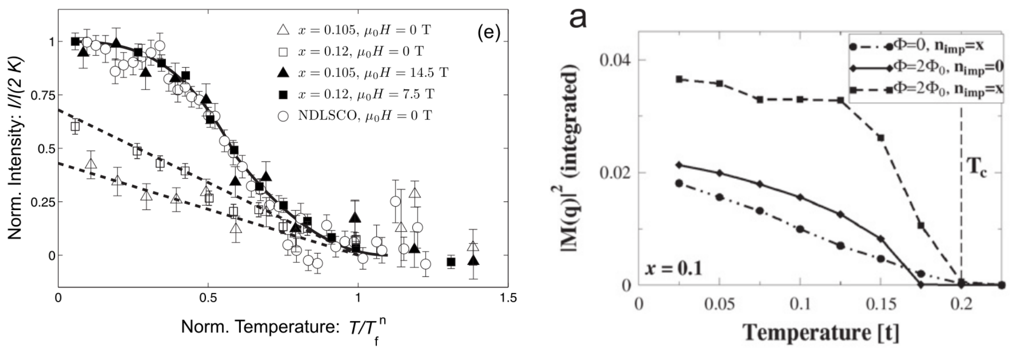

Figure 6.6: (**left**:) Temperature dependence of the peak intensity of the magnetic order in $La_{2-x}Sr_xCuO_4$and $La_{1.6-x}Nd_{0.4}Sr_xCuO_4$ of $x = 0.12$ in zero field and applied field of 14.5 T/7.5 T. Upon field application, the magnetic signal of $La_{2-x}Sr_xCuO_4$ is increased and the temperature dependence is similar to zero field $La_{1.6-x}Nd_{0.4}Sr_xCuO_4$data. Adapted from J. Chang *et al.*, Ref. [139]. (**right**:) Model for temperature dependence of the peak intensity of the magnetic order in zero field and finite field with and without an impurity density of $x = 10$ % for a system of 10 % doping. Adapted from B. M. Andersen *et al.*, Ref. [141].

In addition to the field enhancement magnetic order shown in Fig. 6.6, Katano *et al.* [137] reported a resistivity measurement, that shows severe suppression of the superconducting transition temperature occurs upon the application of a magnetic field perpendicular to the CuO_2 planes in for $La_{1.88}Sr_{0.12}CuO_4$. This indicates a strong competition between static magnetic order and superconductivity.

In $La_{2-x}Sr_xCuO_4$ of higher doping ($x > 0.135$), no static order is present, but it has been shown that magnetic order can be induced by application of a magnetic field [139, 142, 143]. For instance, in Fig. 6.7 $La_{2-x}Sr_xCuO_4$ $x = 0.145$ shows no static magnetic order in zero applied field, but a magnetic signal develops for applied fields $H \geq 7.5$ T. It is important to note, that only the field component *perpendicular* to the CuO_2 planes affects the magnetic order. This was shown explicitly by Lake *et al.* in Ref. [144] by applying the field with an angle to the CuO_2 planes and comparing to the experiment done with the field perpendicular to the planes. This emphasize the role the induced vortices might play

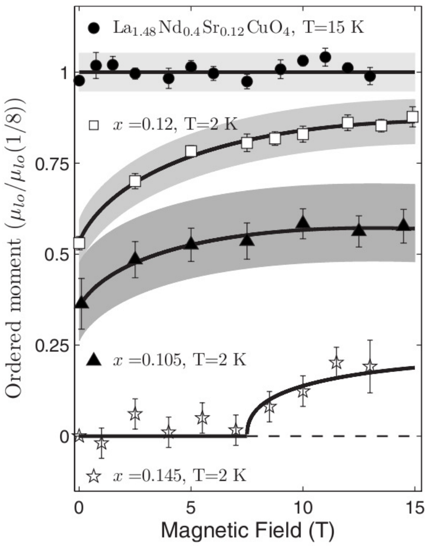

Figure 6.7: Magnetic field effect for three different dopings of $La_{2-x}Sr_xCuO_4$and $La_{1.6-x}Nd_{0.4}Sr_xCuO_4$ of $x = 0.12$. In $La_{2-x}Sr_xCuO_4$ for dopings $x = 0.105$ and $x = 0.12$, static order is present and becomes increasingly strong upon a magnetic field application. For the $x = 0.145$ static order is not present at zero applied field, but is induced upon field application. Adapted from J. Chang *et al.*, Ref. [139].

in the competition between static magnetism and superconductivity.

This increase of magnetic signal could arise from different reasons;

- An increase in the magnetic volume fraction
- A rotation of the magnetic moments
- An increase of the average magnetic moments
- An increase in the interplanar magnetic correlations, i.e. correlations between the $\mathrm{CuO_2}$ planes

The first option of increasing the magnetic volume fraction is only relevant in samples where the magnetic volume fraction is less than 100 % before applying a magnetic field. From muon spin rotation measurements the magnetic volume fraction can be estimated with a resolution of 20 Å given by the effective range over which a muon is sensitive to the presence of static electronic moments.

The second possibility is a rotation of the magnetic moments and it is not so easy to establish if such an effect occurs. If the moments were rotated out of the $\mathrm{CuO_2}$ plane then a measurement of the magnetic order by neutron scattering with the $\mathrm{CuO_2}$ plane probed in the scattering plane would cause a decrease in the signal, which is not observed. If the spins rotated in the plane due to some indirect interaction, then an enhancement of the signal would occur at some ordering vectors, but a decrease of the signal would unavoidably happen at some other ordering vectors, since the order visible to the neutron is the component of the spin perpendicular to the scattering vector. A decrease in the order has not yet been observed at any of the incommensurate positions, neither in the literature, nor in an experiment where we were explicitly looking for it by probing several different incommensurate positions in zero field and $H = 13.5$ T applied field.[7] In addition, intraplanar components of the field does not affect the magnetic signal either [144], whichi is tied to the fact that the exchange couplings in $\mathrm{La_{2-x}Sr_xCuO_4}$ are far stronger than the energy scale of a 10 T magnetic field; $\mu_B B \simeq 1$ meV to be compared with the exchange couplings of the order of 100 meV (In the parent compound $\mathrm{La_2CuO_4}$ $J = 110 - 130$ meV, but it is expected to decrease in the doped system). In conclusion, the scenario of rotation of spins seems unlikely.

Therefore we are left with the two last options, and this define the aim of our investigations reported in chapter 8. We will determine if the field-induced enhancement of the magnetic order is due to an increase of the magnetic moments, as suggested by J. Chang and coworkers in the interpretation put forward in Ref. [139], see Fig. 6.6, or if there is an increase in interplanar magnetic correlations due to the applied field. The slowing down and subsequent pinning of static magnetic order by vortices and disorder in the one-band Hubbard model was shown by B. M. Andersen *et al.* [141], see Fig. 6.6(right). The effect of both magnetic field application and disorder in the lattice is to move spectral weight of the transverse susceptibility from high energies to small energies, i.e. the spin dynamics is slowed down and eventually static order develops.

Within the scenario of vortex-induced magnetic order, it seems likely that interplanar correlations becomes enhanced. This supports the fourth scenario given above; that that interplanar correlations between the $\mathrm{CuO_2}$ planes becomes enhanced upon application of a field. In fact, the possibility of such an effect raises a concern with the purely two-dimensional models of the cuprate systems. One could speculate that parts of, or in principle all of, the field-induced signal observed in measurements using the more common (a, b) plane crystal orientation may be due to the induced correlations, and not to an increase of magnetic volume fraction or ordered magnetic moments in the superconductor, as commonly believed. This is the motivation for the experimental study to be presented in chapter 8, where we perform a comprehensive study of the field-induced signal of a $\mathrm{La_{1.88}Sr_{0.12}CuO_4}$ crystal. As a matter of fact, we will see that both effects play a role; much of the observed IC signal in our experiments arises from an actual increase of the magnetic moments in the system, and in addition, short range c-axis correlations develop. Before turning to the details of our neutron scattering experiments in the next chapter, we briefly review the previous work on c-axis correlations in the cuprates. This is a quite

---

[7] A. T. Rømer, Master thesis, University of Copenhagen (2009).

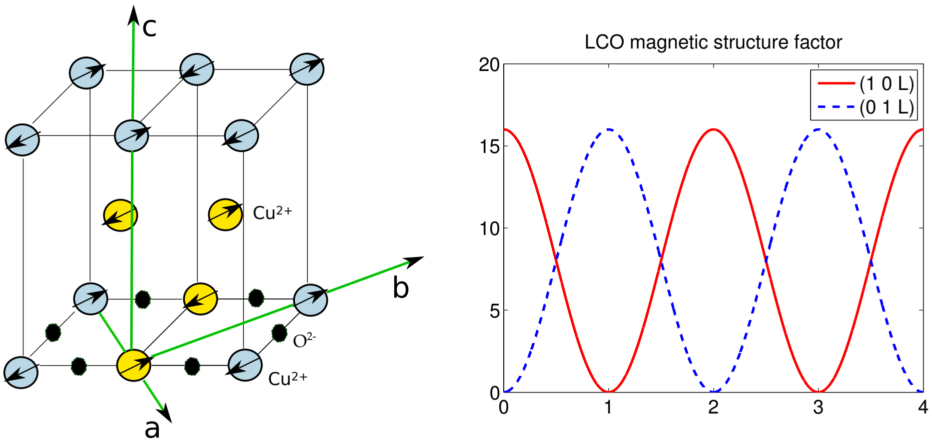

Figure 6.8: (**left:**) Magnetic structure of the undoped compound La_2CuO_4. For simplicity, only the copper atoms as well as the oxygen atoms of the bottom layer are shown. The magnetic unit cell is indicated by the four yellow copper atoms. The green lines show the orthorhombic axes. Note that the spins point in the direction of the b-axis. (**right:**) Magnetic structure factor for La_2CuO_4 as a function of L. Note the peaks at $Q = (10L)$ (L even) and $Q = (01L)$ (L uneven).

limited exercise, since not much attention has been drawn to this field in the literature. This is of course due to the fact that the cuprates are quasi-two dimensional systems, with magnetic ordering and superconductivity confined primarily to the CuO_2 planes.

We start out by describing the well-established magnetic order of the parent compound, and thereafter we turn to two important studies of the interplanar magnetic correlations, one in the purely oxygen-doped La_2CuO_{4+y} and the predecessor of our experiment, namely a study of the three-dimensionality of magnetic order in $La_{2-x}Sr_xCuO_4$ of $x = 0.11$.

6.5 Three-dimensional order in the parent compound La_2CuO_4

The parent compound La_2CuO_4 has an orthorhombic structure below $T_{HTT \to LTO} \sim 500$ K and orders antiferromagnetically below $T_N \sim 300$ K with a unique 3D antiferromagnetic pattern first proposed by Vaknin *et al.* [145]. The 3D magnetic structure was confirmed in a single crystal study of twinned samples [146, 147]. In Ref. [146] it was specifically shown that magnetic peaks occur at positions $\mathbf{q} = (1\ 0\ L)$ of even L and $\mathbf{q} = (0\ 1\ L)$ for odd L, where the $\mathbf{q}$-vectors are stated in orthorhombic notation and the orthorhombic axes shown by the green arrows in Fig. 6.8. The finding of Ref. [146] is consistent with the spins lying along the orthorhombic b-axis and forming ferromagnetic planes spanned by the b and c axes, see the spin structure depicted in Fig. 6.8. Thus the magnetic unit cell relevant for La_2CuO_4 contains 4 spins, i.e. 2 spins for each layer, which is indicated by the yellow Cu atoms in Fig. 6.8. This unit cell is characterized by two "spin up" electrons at the positions $\mathbf{r} = (0, 0, 0)$ and $(0, \frac{b}{2}, \frac{c}{2})$ and two "spin down" electrons at $\mathbf{r} = (-\frac{a}{2}, \frac{b}{2}, 0)$ and $(-\frac{a}{2}, 0, \frac{c}{2})$. The magnetic structure factor becomes:

$$M(H, K, L) = 1 - e^{-i\pi(H+K)} + (e^{i\pi K} - e^{-i\pi H})e^{i\pi L} \tag{6.10}$$

Therefore, when probing the magnetic order by neutron scattering, we expect the signal to comply with the following selection rules:

$$\begin{aligned} |M(1\ 0\ L)|^2 &= 2 + 2e^{i\pi L} \text{ , i.e. zero for odd values of } L \text{ and maximal for even values of } L \\ |M(0\ 1\ L)|^2 &= 2 - 2e^{i\pi L} \text{ , i.e. zero for even values of } L \text{ and maximal for odd values of } L \end{aligned}$$

Thus, from the magnetic structure factor of La_2CuO_4 we expect to have signals of maximum intensity at even values of L and zero intensity at odd values of L for scattering vectors $\mathbf{q} = (2\pi/a, 0, 2\pi L/c)$, while

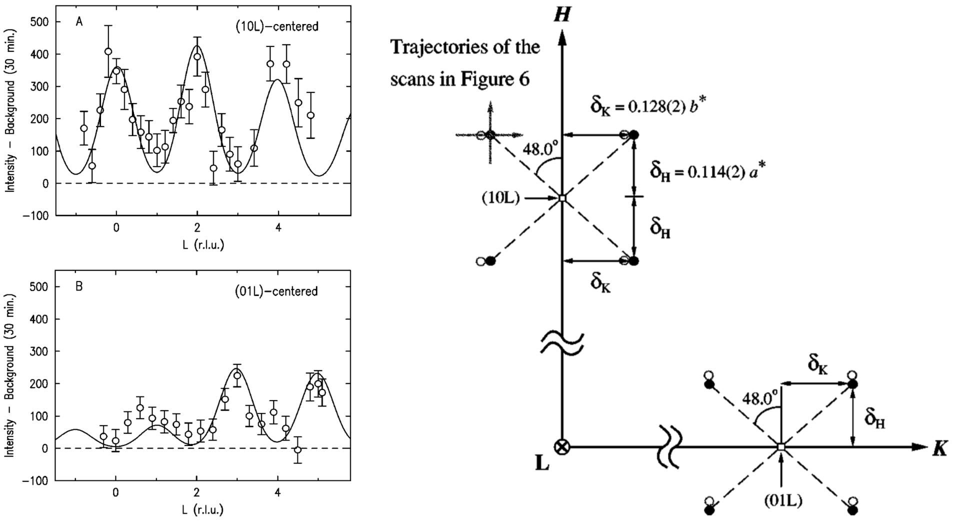

Figure 6.9: (**left:**) L dependence of the incommensurate magnetic signal in excess-oxygen-doped $LaCuO_{4+y}$. Notice that the signal is peaked at *even* L for an incommensurate signal centered at $(1\ 0\ L)$ whereas it is peaked at *odd* L for a signal centered at $(0\ 1\ L)$. (**right:**) Sketch of the position of the magnetic incommensurate signal from the two twins. Both signals can be probed by the same scan as shown by the trajetory arrows. Adapted from Y. S. Lee *et al.*, Ref [148].

we expect the opposite pattern for scattering vectors $\mathbf{q} = (0, 2\pi/b, 2\pi L/c)$.

6.6 Zero-field interplanar order in oxygen-doped $LaCuO_{4+y}$

Weak interplanar order was found in zero applied field in La_2CuO_{4+y} by Y. S. Lee and coworkers [148]. In this work, a splitting of the incommensurate magnetic signal is directly related to the splitting of the structural Bragg peak, and therefore originates from the twinning of the sample in the orthorhombic phase. The position of the Bragg peaks of each twins are related by a rotation of 0.7°, which is more than three times the rotation observed in our $La_{1.88}Sr_{0.12}CuO_4$ crystal. This large splitting enables a clear distinction between the two twin signals, and in particular the L dependence of the magnetic signal for each IC twin could be mapped out. The authors found that the interplanar spin arrangement bears strong resemblances to the three dimensional magnetic order of the parent compound discussed in the previous section, i.e. a maximum intensity at *even* L values for peaks around $(1\ 0\ L)$ and maximum intensity at *odd* L values for peaks around $(0\ 1\ L)$. It was therefore concluded, that the magnetic structure in excess-oxygen-doped La_2CuO_4 is similar to the order in the parent compound; in the CuO_2 plane the commensurate antiferromagnetic order is replaced by a new IC type of order, but the results of Ref. [148] suggest, that the spins of neighboring CuO_2 planes are aligned in a fashion which is similar to La_2CuO_4. A cartoon picture of the magnetic unit cell is shown in Fig. 6.10. We calculate the magnetic structure factors for a unit cell consisting of 8×2 Cu atoms of one plane and 8×2 Cu atoms of the plane above. The size of the unit cell in the interplanar direction depends on how the charge stripes are displaced when going from one plane to the next. Here we consider the simplest case, with the smallest unit cell that has a period 8 antiferromagnetic stripe within one CuO_2 plane. The result is given in Fig. 6.11. Note that the L dependence is roughly the same as for the simple calculation of La_2CuO_4.

Returning now to the experiment on La_2CuO_{4+y} by Lee *et al.* [148], the interplanar interactions are much weaker compared to the magnetic order in La_2CuO_4. From the peak width, see Fig. 6.9, the interplanar correlation length in La_2CuO_{4+y} is estimated to 13 Å. This means that that spins are

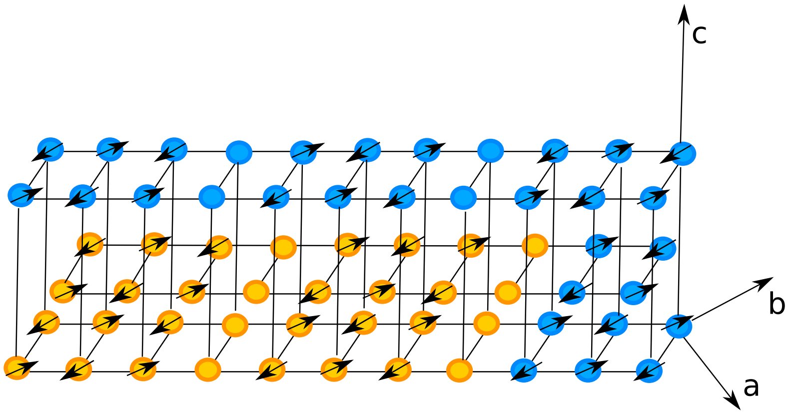

Figure 6.10: Cartoon magnetic structure of a stripe with period 8 along one direction and period 2 along the other direction within one CuO_2 plane. In this picture, the stripe ordering occurs along the (1 1 0) direction. The unit cell is given by two 8×2 magnetic cells on top of each other with the given charge modulation shown, i.e. it consists of 32 Cu atoms depicted by orange atoms in the drawing.

correlated only between one or two neighboring CuO_2 planes. The findings in this work provides an outset for the interpretation of the incommensurate signal in $La_{1.88}Sr_{0.12}CuO_4$, which we will return to below.

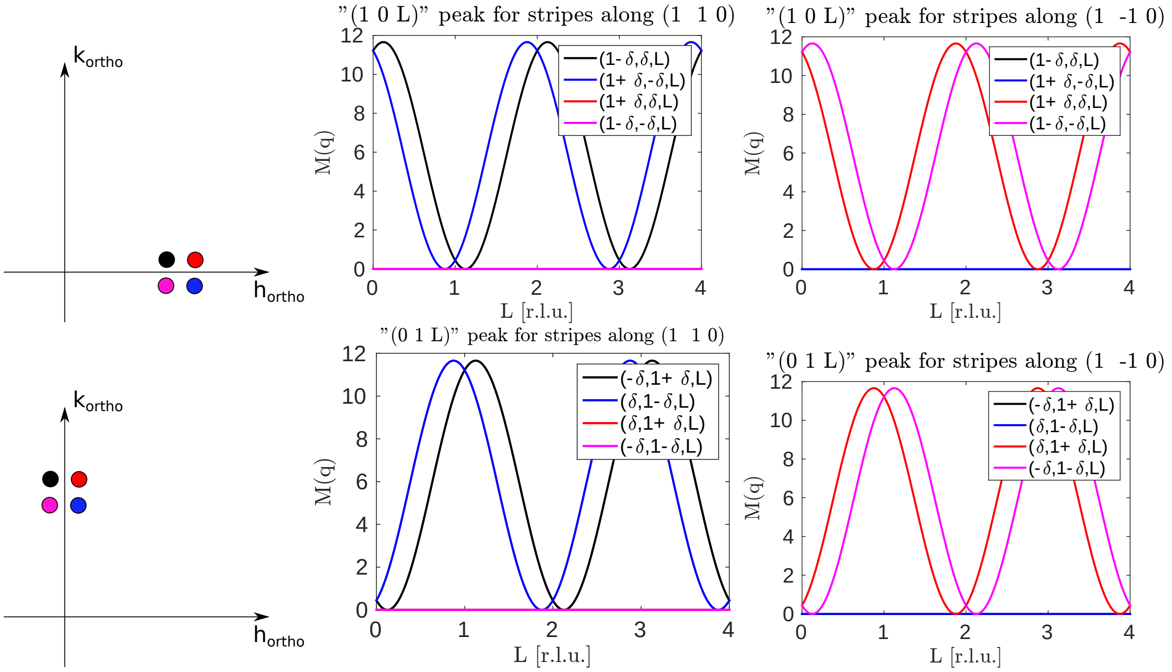

Figure 6.11: (**Upper row:**) Magnetic structure factor as a function of L for the incommensurate quartet $(1 \pm \delta, \pm\delta, L)$ with $\delta = 1/8$. The period eight modulation is either along the (1 1 0) direction (middle figure) or the (1 $\bar{1}$ 0) direction (right figure). The signal is peaked around even values of L. (**Lower row:**) Magnetic structure factor as a function of L for the incommensurate quartet $(\pm\delta, 1 \pm \delta, L)$ with $\delta = 1/8$. The signal is peaked around odd L.

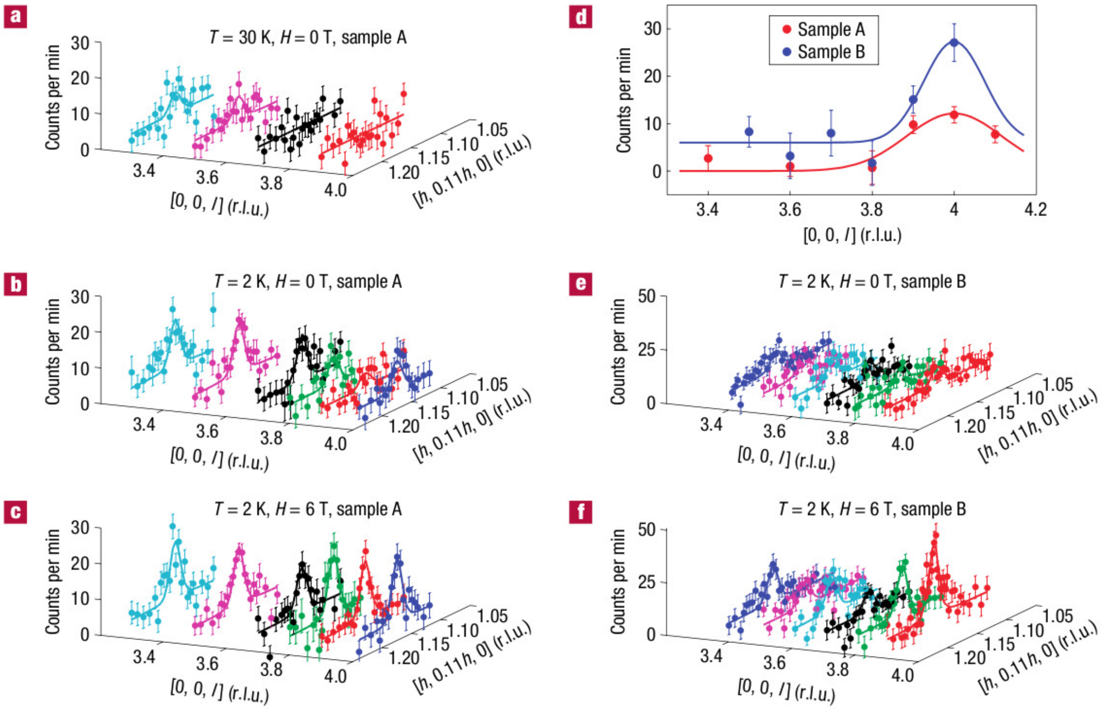

Figure 6.12: L dependence In (d) the zero-field signal has been subtracted from the 6 T signal and it is concluded that the field-enhanced IC signal is more three-dimensional, i.e. exhibits stronger interplanar correlations. Adapted from B. Lake *et al.* Ref. [144].

6.7 Field-induced interplanar order in $La_{1.89}Sr_{0.11}CuO_4$

In $La_{2-x}Sr_xCuO_4$ of doping $x \sim 0.11$, one experiment by Lake *et al.* [144] has shown indications of enhanced interplanar correlations between the CuO_2 planes when a magnetic field is applied perpendicular to the planes. Scans where performed through the peaks at different values of L in the range 3.4-4.1, where crystallographically $L = 4$ corresponds to L= 0. The limited scan range was dictated by severe limitations in the scattering vector due to the experimental setup with a horizontal magnet. Note that the range is much narrower than for the zero field measurements in La_2CuO_{4+y} discussed above, and the L range does not include an odd value of L.

As seen in Fig. 6.12, there is a finite IC signal at every value of L in zero field, and the effect of an applied field ($H = 6$ T) is to enhance the scattering signal at the IC position at $L = 4$, while the signal away from that position is unchanged. Lake et al. concludes that while the zero field signal is purely two-dimensional the field-induced signal is more three-dimensional, i.e. interplanar correlations between the CuO_2 build up in a field. This additional correlation was discussed in relation to vortex-induced magnetism, for which the magnetically ordered puddles will naturally line up along the c-axis if the vortex lines go straight through the sample, perpendicular to the CuO_2 planes. In Fig. 6.12(d) the intensity difference between zero field and field data is shown as a function of L. The fact that the scattering signal at $L = 4$ is enhanced while the offposition scattering signals are unchanged indicates that the integrated moment is increased. Thus either the magnetic volume fraction or the magnetic moments increase when applying a magnetic field.

6.8 Low-energy spin fluctuations and the "spin gap"

The intensity of the magnetic fluctuations in $La_{2-x}Sr_xCuO_4$ has been extensively studied by inelastic neutron scattering in the literature. As mentioned previously, there is static order in the low doping regime of $x \leq 0.13$ whereas a gap opens at higher doping values. The clear energy gap observed for $x > 0.13$ has been dubbed the "spin gap", and the fact that the magnitude of this gap scales with the superconducting transition temperature has led to speculations about the relation between the spin gap and the emergence of superconductivity [149].

Systems that do not display a spin gap are still superconducting, which means that the gapping of the spin fluctuation spectrum is not a necessary condition for development of superconductivity. However, it might well be that the lowest energy spin fluctuations compete more with superconductivity than the fluctuations above the "spin gap", and that the higher energy fluctuations above the spin gap play a more important role as the Cooper pairing glue. A study of Chang *et al.* [149] showed how fluctuations below $\hbar\omega = 1$ meV are suppressed in the superconducting state, but not in the normal state, see Fig. 6.13(left). In this work, it was also shown how the application of a 10 T magnetic field would boost the lowest energy magnetic fluctuations. This indicates a competition of superconductivity and static (or very slowly fluctuating) order.

Kofu *et al.* [140] presented measurements of the low-energy fluctuations at three doping levels in the regime where the spin gap occurs, see Fig. 6.13(right). The data was interpreted in terms of a two-component picture in which a phase separation of two distinct magnetic phases in real space occurs in samples without a spin gap, i.e. for $x \leq 0.13$. This suggests that parts of the sample are superconducting, and show a spin gapped spectrum, whereas other parts of the sample are non-superconducting and display static magnetic order as well as very low energy fluctuations related to spin stripe-ordered or stripe-frozen domains. This two component interpretation is visualized by the pink and blue color in the spectrums of Fig. 6.13(right). Clearly, the interpretation put forward by Kofu *et al.* is incompatible with a magnetic volume fraction of 100 %. In our $La_{1.88}Sr_{0.12}CuO_4$ crystal, muon spin rotation measurements show that magnetic moments are ordered in the entire crystal volume, and cannot be viewed in terms of a two-component model.

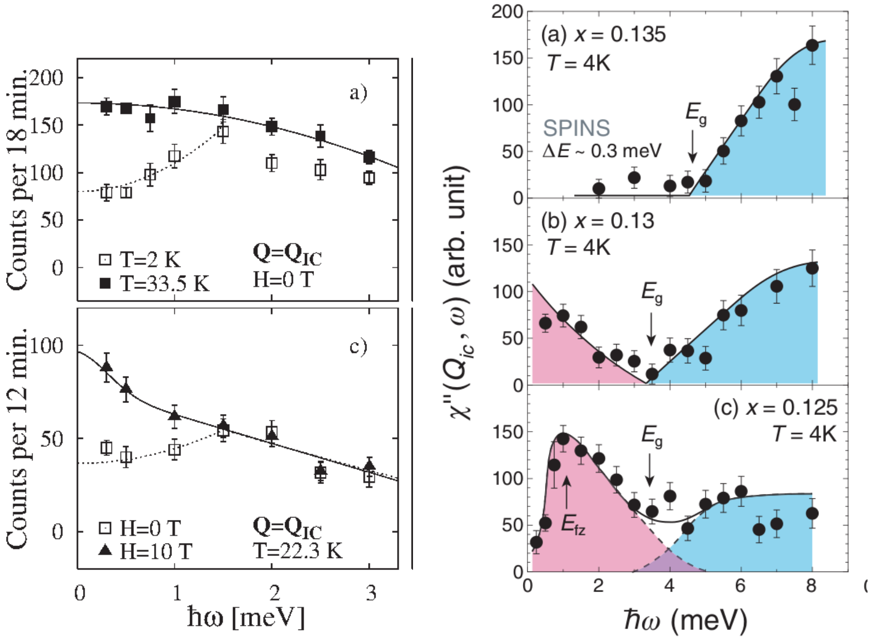

Figure 6.13: (**left:**) Low energy spectrum of magnetic fluctuations in $La_{2-x}Sr_xCuO_4$ of $x = 0.105$ with $T_c = 30$ K. At zero field, the magnetic order is suppressed below T_c for $\hbar\omega < 1.5$ meV, indicating a competition between low-energy fluctuations and superconducting. Application of a field enhances the signal from the low-energy fluctuations at temperatures below T_c. Adapted from J. Chang *et al.* Ref. [149]. (**right:**) Low energy spectrum of magnetic fluctuations in $La_{2-x}Sr_xCuO_4$ of three dopings $x = 0.135, 0.13, 0.125$. Excitations above $E_g = 4$ meV are characterized by a short correlation length of ~ 50 Å, whereas excitations below E_g are longer range. The energy $E_{fz} = 1$ meV is associated to the freezing of spins into a magnetically ordered state. Adapted from Kofu *et al.* Ref. [140].

Chapter 7

Glassy low-energy spin fluctuations and anisotropy gap in $La_{1.88}Sr_{0.12}CuO_4$

This work presented in this chapter was initiated in Ref. [150], where the details of the data analysis are described. Here we will focus on the discussion of the data and interpretation of the results, which has also been published in Phys. Rev. B **87**, *144513 (2013). We present high-resolution triple-axis neutron scattering studies of the low-energy fluctuations of* $La_{1.88}Sr_{0.12}CuO_4$. *The temperature dependence of the low-energy incommensurate magnetic fluctuations reveals distinctly glassy features. The glassiness is confirmed by the difference between the ordering temperature* $T_N \simeq T_c$ *inferred from elastic neutron scattering and the freezing temperature* $T_f \simeq 11$ *K obtained from muon spin rotation studies. The magnetic field independence of the observed excitation spectrum as well as the observation of a partial suppression of magnetic spectral weight below* 0.75 *meV for temperatures smaller than* T_f, *indicate that the stripe frozen state is capable of supporting a spin anisotropy gap, of a magnitude similar to that observed in the spin and charge stripe ordered ground state of* $La_{1.875}Ba_{0.125}CuO_4$. *The difference between* T_N *and* T_f *implies that the significant enhancement in a magnetic field of nominally elastic incommensurate scattering is caused by strictly inelastic scattering – at least in the temperature range between* T_f *and* T_c *– which is not resolved in the present experiment. Combining the results obtained from our study with neutron scattering work on samples with chemical composition close to* 0.12 *% doping, where local probes indicate a sharp maximum in* T_f, *we arrive at the view that the low-energy fluctuations are strongly dependent on composition in this regime. At dopings sufficiently close to* $x = 0.12$ *anisotropy gaps dominate the low-energy spectrum, whereas superconducting spin gaps dominate elsewhere.*

7.1 Introduction

When we investigate systems that reside in the coexistence region of SDW and superconductivity it is always a very interesting and fundamental question whether the same electrons are responsible for both ordering phenomena at the same time, i.e. if the coexistence is microscopic. In chapter 5 we presented a theoretical approach to the scenario where two orders are really microscopically coexisting; Cooper pairs are build from the *dressed* electrons living in an antiferromagnetic environment, and furthermore, it is the electrons themselves which are responsible for the SDW order. In the electron-doped cuprates the coexistence region seems to be quite well-described by commensurate antiferromagnetism; ARPES results show a Fermi surface which is consistent with this simple picture, namely a reconstructed Fermi surface due to (π, π) order. For hole-doped cuprates, the situation is more subtle and more competing orders are at play with charge-density-wave order and the pseudogap being very important players in the game. Note, however, that very recently, electron-doped cuprates have also shown charge-density-wave order [151]. In the cuprates, the nature of the coexistence phases it is still being debated. The important question is, which of the two scenarios is more adequate: do all electrons participate in all types of ordering phenomena at the same time, or does the system display a phase separation with different ordering phenomena taking place in different parts of the crystal? From neutron scattering results this can not be established; it requires investigations by local probes such as μSR which provide very valuable complementary information to the results obtained by neutrons.

A general feature in most systems is the fact that there seems to be a competition between superconductivity and static (or very slowly fluctuating) order. However, such a competition could occur both in case of a phase separated system and in the case of orders that coexist microscopically; either there is a competition between volume fractions or there is a more intrinsic competition taking place for every electron.

In relation to $La_{2-x}Sr_xCuO_4$, it has been discussed which of the two scenarios is most likely. In the doping-dependent study of the low-energy dynamics by M. Kofu *et al.* [140], the data was interpreted in terms of a phase separation into two components: superconducting regions which give a spin-gapped response similar to what is observed at optimal doping,as in the report of Mason *et al.* [152], and non-superconducting regions with spin stripe-ordered or stripe-frozen domains. In contrast to this view, J. Chang *et al.* [149] proposed that for $x = 0.105$ magnetic order renormalizes the value of the superconductivity-related spin gap. In higher doped $La_{2-x}Sr_xCuO_4$ of $x = 0.145$, where no static order is present in zero field, the spin gap is found to decrease continuously upon application of a magnetic field, thus behaving like a soft-mode that slows down close to a quantum critical transition [142, 153]. Had the field instead introduced other domains in the crystal, which were non-superconducting regions with spin stripe-ordered, this would have introduced spectral weight all the way down to $\hbar\omega = 0$ immediately. Therefore we conjecture that the two-component view also is in contrast to what is observed in $La_{2-x}Sr_xCuO_4$ $x = 0.145$. We conclude that both the experiment at $x = 0.105$ and $x = 0.145$ favors a more unified description in which all electrons participate in both phenomena. Doping or external field can drive the ordering tendencies in one direction or another. Common in both cases is the sensivity to an external magnetic field, which either acts to enhance a pre-existing SDW order ($x = 0.105$) or causes a slowing down of a soft mode ($x = 0.145$).

Here we present results of experiments designed to improve our understanding of the low-energy dynamic magnetic fluctuations in $La_{1.88}Sr_{0.12}CuO_4$, which is in between the dopings described above, $x = 0.105$ and $x = 0.145$. To do so, we have studied the temperature and magnetic field-dependence of the spindynamics. In contrast to the clear effects of magnetic field on low-energy excitations reported both for the underdoped regime for $x < 1/8$ [149] and for the optimally doped regime for $x > 1/8$, [155, 165, 172, 142] we observe no field-effect in $La_{1.88}Sr_{0.12}CuO_4$. The temperature-dependence of the spin fluctuations reveal glassy dynamics and, at the lowest energy transfers, a partial suppression of magnetic spectral weight below 0.75 meV. The latter observation in combination with the absence of a magnetic field effect on the low-energy excitations, suggests that LSCO near 1/8 can support a spin anisotropy gap despite the glassy nature of the ordering and despite superconductivity. We discuss the implications of our results and their relation to previously published work on $La_{2-x}Sr_xCuO_4$, $La_{2-x}Ba_xCuO_4$ and spin-charge ordered nickelates $La_{2-x}Sr_xNiO_4$.

7.2 Experimental method

The $La_{1.88}Sr_{0.12}CuO_4$ ($T_c \approx 27$ K) sample studied consisted of two single crystals that were cut from the same rod grown by the traveling solvent floating method. [174] In earlier work, [139] the Sr content $x = 0.120 \pm 0.005$ (and hence the hole concentration $p = x$) was determined from the structural transition temperature separating the high-temperature tetragonal (HTT) from the low-temperature orthorhombic

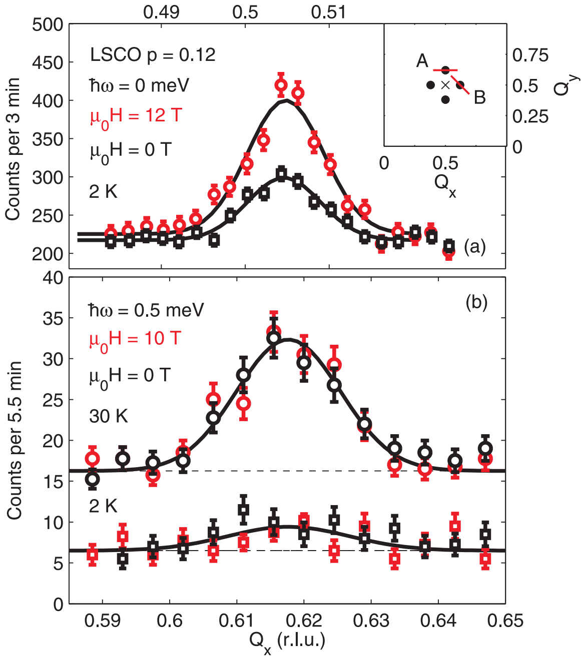

Figure 7.1: (a) Elastic scattering intensity at an incommensurate position Q_{IC} as indicated in the inset where circles mark the locii of incommensurate magnetic order and low-energy fluctuations. Black and red data points were taken at 0 T and 12 T field, respectively. Solid lines are Gaussian fits to data. These data are reproduced from Ref. [139]. The inset shows the two different scan directions for the elastic scattering data (A) and the inelastic scattering data (B). (b) Background-subtracted intensity for a constant energy scan with $\hbar\omega = 0.5$ meV. Notice that for visibility, the data have an arbitrary offset. Solid lines are Gaussian fits to data. Neither at 2 K $\ll T_{\mathrm{c}}$ nor in the normal state at 30 K $> T_{\mathrm{c}}$ does the application of a magnetic field of 10 T have any effect on the low-energy spin excitations at $\hbar\omega = 0.5$ meV. The nominally elastic and the inelastic peaks are all resolution limited; $\xi_{\mathrm{elastic}} \geq 110$ Å and $\xi_{0.5\ \mathrm{meV}} \geq 70$ Å. This figure was produced by J. Chang.

(LTO) phase. Muon spin rotation studies on one of the two single crystals revealed electronic moments that are static on the muon time scale below a freezing temperature $T_f \approx 11$ K [139, 175]. High-resolution inelastic neutron scattering experiments were carried out on the PANDA cold neutron triple axis spectrometer at the FRM-II research neutron source in Munich, Germany by J. Chang and K. Lefmann and coworkers, and the author "inherited" the raw data from the two experiments and did the analysis. In a first experiment, the two crystal rods were co-aligned to within less than one degree and the sample was inserted in a 15 T vertical field cryomagnet and the instrument configured with vertically focusing pyrolytic graphite (PG) monochromator and collimation sequence open-60′-open-open from source to detector. In a second, zero-field, experiment only one crystal was used in a setup with a double-focusing monochromator and no collimation. In both experiments, a cooled Be-filter was placed in front of the double-focusing PG analyzer to minimize contamination from higher-order neutrons. The sample was oriented with the crystallographic c axis vertical, allowing access to wave vectors of the form $Q = (H, K, 0)$. We use a notation of the reciprocal space corresponding to the high-temperature tetragonal crystal structure ($a \simeq b = 3.78$ Å, $c \simeq 13.18$ Å). In this notation, the propagation vector of the undoped antiferromagnetic parent compound $\mathrm{La_2CuO_4}$ [145] is $(1/2, 1/2, 0)$ while stripe magnetic ordering [116] is manifested in a quartet of peaks, incommensurate with the lattice at $Q_{\mathrm{IC}} = (1/2 \pm \delta, 1/2, L)$ and $(1/2, 1/2 \pm \delta, L)$ [see the inset in Fig. 7.1(a)]. For our sample, $\delta = 0.125(3)$ as reported earlier [139]. Note however, that a single incommensurability parameter δ is not sufficient to describe the exact position of the magnetic signal, as we shall discuss in chapter 8 below. For the strongly peaked response observed at low energies in LSCO, an effective background subtraction procedure is to estimate the non-magnetic contributions from the scattering observed at wave vectors sufficiently far away from the magnetic peaks. We studied the magnetic fluctuations over the temperature range 2-80 K and for energy transfers in the range 0.3-7 meV. Most of the results we report were obtained with fixed final neutron energy $E_{\mathrm{f}} = 5.0$ meV. For measurements of spin excitations at energy transfers, $\hbar\omega$ =0.3-0.5 meV we chose a lower final energy $E_{\mathrm{f}} = 4.1$ meV to avoid contamination from strictly elastic scattering through the finite energy resolution. In this case the energy resolution was 0.13 meV FWHM as compared to 0.18 meV at $E_f = 5.0$ meV.

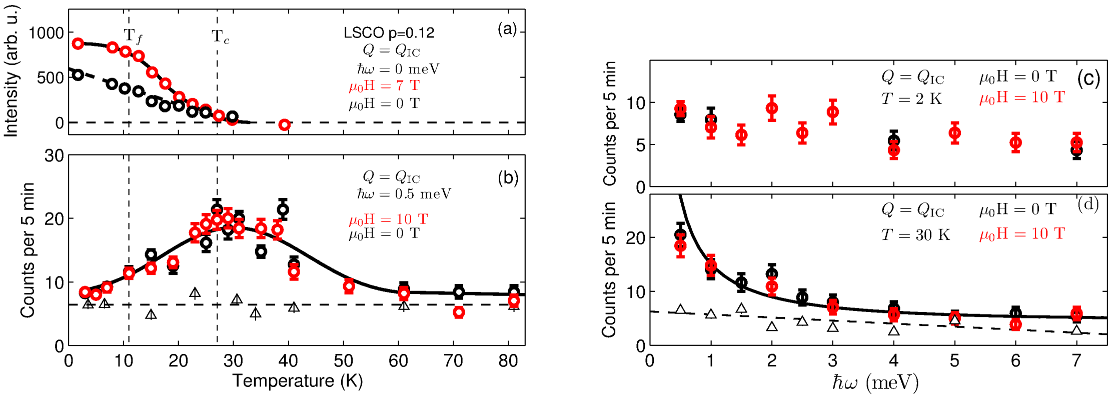

Figure 7.2: (a) Temperature dependence of the background-subtracted elastic response at $Q_{\rm IC}$ for $H = 0$ (black) and 7 T (red). The vertical dashed lines indicate the superconducting transition temperature, $T_{\rm c} \approx 27$ K and the freezing temperature for magnetic ordering, $T_f \approx 11$ K, obtained from muon spin rotation [175]. (b) Temperature dependence of the inelastic response (0.5 meV) at $Q_{\rm IC}$ in zero field (black) and 10 T (red). Open triangles are background data. (c) and (d) Inelastic response at $Q_{\rm IC}$ as a function of energy in the superconducting state at $T = 2$ K and normal phase at $T = 30$ K both with (red points) and without (black points) an applied field of 10 T. Open triangles are background data. The dashed line is a fit to a linear function. The solid black line in (d) is a fit to the Bose occupation factor, $(1 - e^{-\hbar\omega/k_BT})^{-1}$.

7.3 Results

The temperature and magnetic field dependencies of static magnetism in LSCO $x \sim 0.12$, as well as its momentum space characteristics, has previously been studied in great detail [132, 133, 137, 138, 139, 140]. In Fig. 7.1(a) we show a constant energy scan obtained with the spectrometer set to energy transfer $\hbar\omega = 0$ meV. A momentum-resolution limited peak is observed close to $(1/2, 1/2+\delta, 0)$ when performing a scan in the direction indicated by A in the inset of Fig. 7.1(a). The slight offset is consistent with the observation of Kimura *et al.* [133] that the incommensurate, nominally elastic peaks do not lie along the high-symmetry directions of the underlying CuO$_2$ lattice, but are slightly displaced. In our sample, the magnetic intensity increases significantly when a magnetic field is applied along the crystallographic c-axis, see Fig. 7.1(a) and Ref. [139]. The onset temperature for the magnetic order is essentially field-independent, as can be seen in Fig. 7.2(a).

Figure 7.1(b) displays the inelastic response at $Q_{\rm IC}$ with energy transfer $\hbar\omega = 0.5$ meV, probed at base temperature and just above T_c. The scan was performed along the direction indicated by B in the inset of Fig. 7.1(a). Data taken in zero field and at $H = 10$ T are shown. In strong contrast to the elastic response shown in Fig. 7.1(a), no detectable field effect was observed at any temperature, as seen in Fig. 7.2(b). The lack of field-effect persists throughout the energy range 0.3-7.0 meV at both $T = 2$ and $T = 30$ K as shown in Figs. 7.2(c) and 7.2(d), respectively. The peak position was determined by full Q-scans as in Fig. 7.1(b) and was observed to be independent of temperature and energy transfer within the temperature and energy range of this experiment. From the Q scans we found that the inelastic correlation length is resolution limited by $\xi(T, \omega) \geq 70$ Å for $\hbar\omega < 3$ meV and $T < 50$ K. Further data were therefore taken by three-point scans; counting at the peak position and two background positions on each side of the peak. The background estimates are subtracted from the peak intensities in Figs. 7.3(a)-7.3(c) and 7.4(a). The solid line in Fig. 7.2(d) is the Bose occupation factor, $(1 - e^{-\hbar\omega/k_BT})^{-1}$, scaled to the data. This lead us to the conclusion, that the energy dependence of $S(\mathbf{Q}_{\rm IC}, \omega, T)$ at 30 K

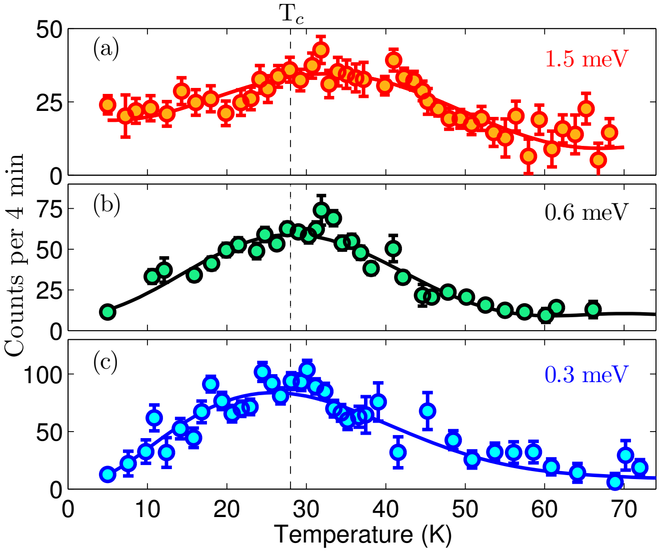

Figure 7.3: Background-subtracted inelastic response at $Q = Q_{\text{IC}}$ in zero field and plotted as intensity versus temperature for excitation energies: (a) 1.5, (b) 0.6, and (c) 0.3 meV. Vertical dashed line indicates the T_{c} of this compound and solid lines are guides to the eye. Since these measurements were obtained without a magnet there is a significant increase in intensity compared to the data shown in Figs. 7.1 and 7.2.

is dominantly given by the Bose occupation factor for energies in the range $1 - 7$ meV, and hence that $\chi''(\mathbf{Q}_{\text{IC}}, \omega, T)$ is roughly frequency independent.

To elucidate the details of the temperature dependence, we show in Fig. 7.3 the temperature dependence of the inelastic response for three different energies from 0.3 to 1.5 meV. As in Fig. 7.2(b), we observe a broad maximum around T_{c}. The position of the maximum shifts down in temperature as $\hbar\omega$ is decreased, and approaches T_c in the limit $\hbar\omega \to 0$ meV. For all energy transfers probed, the intensity decreases as the sample is cooled from T_c to base temperature. This tendency is much less pronounced for 1.5 meV than for 0.3 meV. At the former, the intensity remains finite in the low-temperature limit, whereas it approaches zero for the latter.

To investigate how the suppression of intensity at very low energies ($\hbar\omega < 1$ meV) manifests itself in the observed spectra, we show in Fig. 7.4 the energy dependence of the incommensurate signal for several temperatures above and below T_c. Figure 7.4(a) shows how the intensity is drastically reduced for energy tranfers lower than 0.75 meV at $T = 5$ K and, to a lesser extent, for $T = 13$ K. This shows that $\chi''(\mathbf{Q}_{\text{IC}}, \omega, T)$ becomes frequency-dependent for temperatures lower than and comparable to the freezing temperature $T_f \approx 11$ K deduced from μSR. The guide to the eye for the 5 K data suggests an interpretation in terms of two energy gaps. We return to this point in the discussion.

To illustrate the effects of the Bose occupation factor, see Eq. (6.4), we plot the corresponding dynamic susceptibilities in Figs. 7.4(b) and 7.4(c) for three temperatures; 5, 32, and 42 K. By contrast to the smooth energy dependence of the susceptibility at high temperatures, the 5 K data display an abrupt reduction by a factor of roughly four below $\hbar\omega \sim 0.75$ meV, see Fig. 7.4(b). This observation is consistent with measurements at a similar doping level, $x = 0.125$, by M. Kofu *et al.* [140]. We stress that the intensity suppression is only partial even at the lowest frequency, as seen in Figs. 7.3(c) and 7.4(b), but signatures of gapping of the spectrum are clear from Figs. 7.4, 7.3(b), 7.3(b)(c), and 7.2(b). Moreover, from Fig. 7.2(b), it is apparent that these gap signatures do not exhibit any magnetic field dependence. From Fig. 7.2(b), the signature of a gap is not visible. Note however, that the data in Fig. 7.2(b) are raw data, and more importantly these were obtained with the experimental setup of $E_f = 5.0$ meV. Thus, due to a poorer energy resolution of 0.18 meV compared to the lowest energy data shown in Fig. 7.4 (where $\Delta E = 0.13$ meV), we do not resolve the energy gaps in Fig. 7.2(b).

7.4 Discussion

In this section we first discuss the temperature dependence of the inelastic data and indications of glassy dynamics. Thereafter, we turn to the energy dependence and the intensity suppression observed at low energy transfers and relate this to exchange anisotropies of the magnetic order. Finally, we discuss the field dependence of the nominally elastic data and the field independence of the inelastic data.

7.4.1 Freezing and glassiness

First we comment of the importance of the time scale of the probe (in our case neutron or muon) for the deduced ordering temperatures. In the neutron scattering measurements, we observe a nominally elastic signal for $T < T_c$, see Fig. 7.2. For an energy resolution of $\Delta E \sim 0.18$ meV, the time resolution $\Delta t \sim \frac{\hbar}{\Delta E}$ is of the order tens of picoseconds. Fluctuations with a characteristic time scale slower than picoseconds will therefore appear as static. For our crystal the freezing temperature obtained by zero field μSR, for which the time resolution is of the order of microseconds, is $T_f \approx 11$ K [175]. Due to the insight in freezing temperature obtained by muons, we can deduce that the nominally elastic neutron scattering signal observed in the temperature range between T_f and T_c is actually caused by strictly inelastic, low-energy magnetic fluctuations picked up by the experimental resolution function of the spectrometer, *i.e.* fluctuations with characteristic energy scale 0.18 meV or lower. Note also that T_f obtained by μSR only sets an upper limit of the actual freezing temperature: an experimental technique probing the spin dynamics on a longer characteristic timescale than microseconds could give an even lower value. One should note that the magnetic ordering temperature as observed by neutron scattering is comparable to

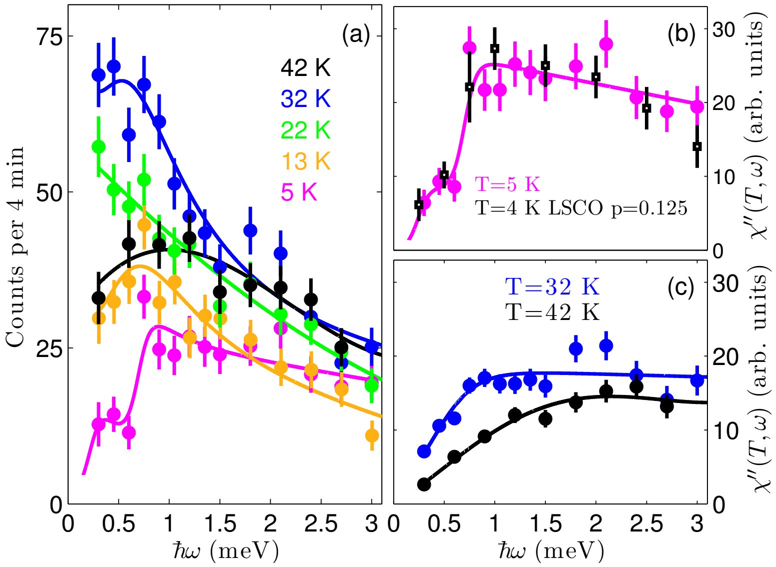

Figure 7.4: (a) Background-subtracted inelastic response as a function of excitation energy at different temperatures T. (b) Dynamical susceptibility $\chi''(\mathbf{Q}_{\text{IC}}, \omega, T)$ at $T = 5$ K obtained for our $x = 0.12$ sample and compared to low-temperature data reproduced from M. Kofu *et al.* [140] for their $x = 0.125$ sample at $T = 4$ K (c) Dynamical susceptibility $\chi''(\mathbf{Q}_{\text{IC}}, \omega, T)$ for fixed $T = 32$ K and 42 K. All lines are guides to the eye.

T_c only by a coincidence. The fact that $T_c \sim T_N$ complicates the interpretation of the data. For the (quasi-)static order, we can not compare magnetic intensities for temperatures above and below T_c, as was done in the case of $\mathrm{Ba(Fe_{1-x}Co_x)_2As_2}$ shown in Fig. 6.4. In the latter case, this comparison served to show how magnetic order and superconductivity compete. In our case, se simply do not have any magnetic order above T_c.

Now we present two different viewpoints for our data; On one hand, we can speculate that the fact that $T_c \sim T_N$ is not entirely accidental, but arises due to a cooperation between the two orders. Maybe, the onset of superconductivity drives a slowing down of spin fluctuations to very low energies, $\hbar\omega < 0.3$ meV, or – perhaps more likely – the slowing down of fluctuations drives superconductivity.

On the other hand, note that in Fig. 7.4(a,c) we observe a boost in the spin fluctuations at energies $\hbar\omega = 0.3 - 1.5$ meV for temperatures $T \sim T_c$. At higher and lower temperatures, the fluctuations loose intensity. This is seen from Fig. 7.4(a) in that the blue curve ($T = 32$ K) lies above all other curves. Further support for this observation is found from the fact that the low-energy fluctuations shown in Figs. 7.2(b) and 7.3 all display a general trend of suppression of the magnetic intensity for temperatures below T_c; we observe a peak in $S(\mathbf{Q}_{\mathrm{IC}}, \omega, T)$ at temperatures close to T_c. One could imagine that upon decreasing temperatures, the spin fluctuations gain intensity and slow down, but this evolution is interrupted by the onset of superconductivity. The fact that the intensity of the magnetic signal decreases below T_c, most pronounced in the case of small energy transfers, can be interpreted as a competition between the slowly fluctuating magnetic order ($\hbar\omega = 0.3 - 1.5$ meV) and superconductivity. In favour of the last scenario is the fact that the peaked response of the low-energy fluctuations is a common feature observed throughout the doping range in LSCO [149, 154, 155].

As opposed to slightly lower doping $x = 0.105$ (as shown in Fig. 6.13), and also contrary to the behavior in $\mathrm{Ba(Fe_{1-x}Co_x)_2As_2}$(Fig. 6.4), a magnetic field application does not enhance the magnetic signal at any temperature, in particular not for temperatures below T_c. This is quite a surprise; the low-energy fluctuations are insensitive to a magnetic field application, even though the static (on the muon time scale) order does get enhanced by a field, (Fig. 7.2(a)).

The peak shifts towards higher temperatures as the energy transfer, $\hbar\omega$, increases. A similar shift was also observed in very underdoped, non-superconducting LSCO $x = 0.04$ (see Keimer *et al.* Ref. [156]). In that case, the integrated spin intensity peaked at a temperature that increased for increasing energy; the peak temperature was given by $T \sim 2\hbar\omega$, which is consistent with glassy behavior. In our case, we probe only low-energy transfers, but the tendency is the same, *i.e.* the threshold temperature above which the intensity drops off increases with frequency, see Fig. 7.3. We stress that since the observed peak widths are roughly constant for the range of temperatures and energy transfers probed in our experiments, the peak amplitude at Q_{IC} is to a good approximation proportional to the integrated intensity discussed in Ref. [156]. We therefore conclude that our $\mathrm{La_{1.88}Sr_{0.12}CuO_4}$ crystal displays low-energy dynamics that are similar to what was found in the glassy ground state of very underdoped LSCO $x = 0.04$ [156, 157, 158].

7.4.2 Anisotropy gap

Figure 7.4 shows that for temperatures lower than T_f, we observe a partial suppression of low-energy fluctuations. There is an intensity drop at energy transfers lower than $\hbar\omega \sim 0.75$ meV. Below this scale, we do not see a spectral region of zero intensity, which means that the gap is not fully developed. We now turn to discuss the possible origin of these observations within a simple spin wave formalism. The energy gaps in the parent compound $\mathrm{La_2CuO_4}$ are due to exchange anisotropy and the Dzyaloshinskii-Moriya (DM) interaction. These gaps were reported by C. J. Peters *et al.* [159] to be 1.0 and 2.5 meV for the in-plane and out-of-plane gaps, respectively. Within the standard Heisenberg spin-only approach, an anisotropy gap is expected to scale with the ordered magnetic moment of the Cu atoms. This is a generic result also expected to hold for stripe ordered systems for which the static moments are known to be strongly diminished compared to $\mathrm{La_2CuO_4}$ [160], although it is of course an approximation to describe the system a with a spin-only approach in the doping regime where superconductivity is present. In the spin-only approach we include the exchange interactions in all three directions, as well as the DM interaction and the Zeeman energy due to the applied magnetic field. Let the $\mathrm{CuO_2}$ plane be given by (a, b) plane and let b be the easy axis, i.e. the axis along which the antiferromagnetic moments align. The magnetic field is applied along the c axis. The DM anisotropy and magnetic field both acts to cant the spins out of the $\mathrm{CuO_2}$ planes. The exchange Hamiltonian is given by:

$$H = \sum_{\langle i,j\rangle} S_i \cdot \hat{J} \cdot S_j \tag{7.1}$$

with

$$\hat{J} = \begin{pmatrix} J_{aa} & 0 & 0 \\ 0 & J_{bb} & J_{bc} \\ 0 & -J_{bc} & J_{cc} \end{pmatrix} \tag{7.2}$$

where the exchange energy J_{bc} is due to the DM anisotropy. We write out the Hamiltonian containing anisotropies and external field in a common global coordinate systems. Let S_i denote spins on one sublattice and S_j denote spins on the other sublattice.

$$\begin{aligned} H &= \sum_{\langle i,j\rangle} J_{aa} S_i^x S_j^x + (J_{bb} S_j^y + J_{bc} S_j^z) S_i^y + (-J_{bc} S_j^y + J_{cc} S_j^z) S_i^z - g\mu_B H[\sum_i S_i^z + \sum_j S_j^z] \\ &= \sum_{\langle i,j\rangle} J_{aa} S_i^x S_j^x + J_{bb} S_i^y S_j^y + J_{cc} S_i^z S_j^z + J_{bc}(S_i^y S_j^z - S_i^z S_j^y) - g\mu_B H[\sum_i S_i^z + \sum_j S_j^z] \end{aligned} \tag{7.3}$$

For this Hamiltonian, the dispersion relation is derived. The details are given in appendix D. First, we obtain an equation for the tilting angle θ, as a function of exchange couplings and field:

$$\sin\theta = \frac{-J_{bc}}{J_{bb} + J_{cc}} \frac{\cos 2\theta}{\cos\theta} + \frac{1}{J_{bb} + J_{cc}} (g\mu_B H)/(Sz) \tag{7.4}$$

Dependent on the sign of J_{bc}, the DM-term and the external field draw the spins in the same or opposite directions. In undoped $\mathrm{La_2CuO_4}$ the spins cant in opposite directions in alternate layers [162]. An example of either case is shown in Fig. 7.5. Note that in the case of $J_{bb} = J_{cc} = J = 1$ and $J_{bc} = -D \cdot J = -D$ the canting angle given in Eqn. (D.9) is identical to the expression derived in Ref. [161], Eqn. (5).

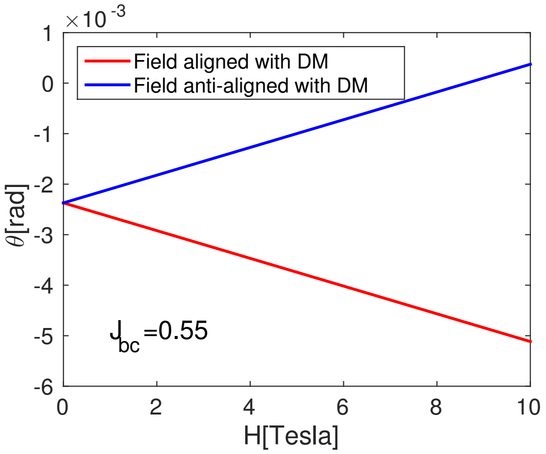

Figure 7.5: Canting angle out of the (a, b) plane due to a DM exchange $J_{bc} = 0.55$ meV for $J_{bb} = 116$ meV and small spin anisotropies along a and c of 0.0023 % and 0.015 %, respectively.

For small tilt angles, we get the dispersion relation:

$$\begin{aligned}(E_q^{f,g})^2 &= h_1^2 + z^2\gamma_q^2[h_3^2 - h_2^2] \pm 2z\gamma_q h_1 h_3 \\ &= S^2z^2[J_{bb}^2 - \gamma_q^2 J_{aa}J_{cc} \pm \gamma_q(J_{aa} - J_{cc})J_{bb}] \\ &\quad -S^2z^2[4J_{bb}J_{bc} + 2\gamma_q^2 J_{aa}J_{bc} \pm 2\gamma_q(J_{aa} + J_{bb} - J_{cc})J_{bc})]\theta \\ &\quad -S^2z^2[2J_{bb} \pm \gamma_q(J_{aa} - J_{cc})]\theta(g\mu_B H)/(Sz) \end{aligned} \tag{7.5}$$

where $|J_{bb}| > |J_{aa}| > |J_{cc}|$, $\gamma_q = \frac{1}{z}\sum_\delta e^{iq\cdot\delta}$ and $\theta \simeq \frac{-J_{bc}+(g\mu_B H)/(Sz)}{J_{bb}+J_{cc}}$.

The general expression, also valid for large tilting angles, is given by:

$$E^2 = h_1^2 + z^2\gamma_q^2[h_3^2 - h_2^2] \pm 2z\gamma_q h_1 h_3 \tag{7.6}$$

where h_1, h_2 and h_3 are given by:

$$\begin{aligned} h_1 &= Sz(J_{bb}\cos^2\theta - J_{cc}\sin^2\theta - 2J_{bc}\cos\theta\sin\theta) - g\mu_B H\sin\theta \\ h_2 &= \frac{S}{2}(J_{aa} - J_{bb}\sin^2\theta + J_{cc}\cos^2\theta - 2J_{bc}\cos\theta\sin\theta) \\ h_3 &= \frac{S}{2}(J_{aa} + J_{bb}\sin^2\theta - J_{cc}\cos^2\theta + 2J_{bc}\cos\theta\sin\theta) \end{aligned} \tag{7.7}$$

Limiting case: $J_{bc} = 0$ and $H = 0$

If we consider the case of no DM interaction as well as no external field, the expression in Eqn. (7.5) reduces to:

$$(E_q^{f,g})^2 = S^2z^2[(J_{bb} \pm J_{aa}\gamma_q)(J_{bb} \mp J_{cc}\gamma_q)] \tag{7.8}$$

If furthermore we set $J_{aa} = J_{bb} = J_{cc} = J$, we get the usual Heisenberg dispersion for an antiferromagnet:

$$E_q = SzJ\sqrt{1-\gamma_q^2} \tag{7.9}$$

Limiting case: $J_{bc} = 0$ and $J_{aa} = J_{bb} = J_{cc} = J$

In this case the expression in Eq. (7.5) reduces to:

$$\begin{aligned}(E_q^{f,g})^2 &= S^2z^2\Big[J^2(1-2\theta^2)^2 - 2J(1-2\theta^2)\frac{g\mu_B H}{zS}\theta + \Big(\frac{g\mu_B H}{zS}\Big)^2\theta^2 \\ &\quad +\gamma_q^2 J^2(2\theta^2 - 1) + \gamma_q\Big(2J^2\theta^2 - 2J\theta^2\frac{g\mu_B H}{zS}\Big)\Big] \end{aligned} \tag{7.10}$$

with $\theta = \sin^{-1}(\frac{g\mu_B H}{2JzS})$.

We plot the dispersion relation found in Eq. (7.6). We choose the DM-term $J_{bc} \sim 0.55$ meV [159] much larger than the differences between exchange couplings J_{bb} and J_{aa}/J_{cc}. We tune the exchange coupling differences to match the gaps found by Peters *et al.* [159] in case of zero field. This gives us the small exchange anisotropies of 0.0023 % along the a direction and 0.015 % along the b direction with the easy axis b having the exchange $J_{bb} = 116$ meV. Thus $|J_{bb} - J_{aa}| \sim 0.003$ meV and $|J_{bb} - J_{cc}| \sim 0.02$ meV, similar to the out-of-plane anisotropy derived by Peters *et al.* of 0.016 meV [159]. We have renormalized the spin quantum number $S = 1/2$ by a quantum renormalization factor of 0.63 [162]. This gives the dispersions for La_2CuO_4 in zero field and $H = 10$ T field as shown in Fig. 7.6. Note that the field effect is to change the two energy gaps by $\Delta E \sim 0.3 - 0.5$ meV in 10 Tesla, or a percentwise change of ~ 20 % in both cases.

In the case of doping with 12 % Sr the renormalization of S is stronger, and we use the estimation given by Chang *et al.*, Ref.[139]. The local ordered magnetic moment is estimated to $\mu_{\text{local}} \sim 0.18(2)\ \mu_B$. Using a renormalized value of $S = 0.18$, we get in Fig. 7.7(left) an estimation of the two energy gaps in zero field of 0.3 meV and 0.7 meV. An interpretation of our data which is consistent with these qualitative arguments is the following; we observe the larger energy gap at $\hbar\omega \sim 0.75$ meV, while our experiment does not resolve the smallest gap of 0.3 meV. This could explain why we observe only a partial suppression of the scattering signal rather than a fully developed energy gap.

When the moment is diminished, the effect from the magnetic field on the canting becomes stronger. In the case where the field direction is aligned with the DM interaction, the gap sizes are increased, and should in principle be visible by an experimental resolution of ~ 0.2 meV as a full gap opening for $\hbar\omega < 0.6$ meV, see Fig. 7.7(middle). However, at the same time there is a closing of the gap for the layers for which the field direction is anti-aligned with the DM interaction, as seen in Fig. 7.7(right). Since every other layer has the opposite DM canting, both situations occur concurrently. Note however, that here we have not taken into the discussion the presence of a first order spin flop transition for a field of ~ 5 T [162], in which all cantings align with the external field and as a result of this, a small ferromagnetic moment develops. Therefore, the most probable scenario for the system subjected to a 10 T field applied, is that the DM interaction and the external field act in concert, which is the situation shown in Fig. 7.7(middle). The naïve suggestion is that we should be able to detect a full gapping of the spectrum for $\hbar\omega < 0.6$ meV as well as a strong intensity decrease below $\hbar\omega \sim 1.5$ meV when applying a 10 T field, and cooling below the freezing temperature $T_f \sim 11$ K. From the data in Fig. 7.4, clearly none of these features appear at the lowest temperatures. We point to the fact, that our estimations in Fig. 7.7 are probably too crude. For instance, it is very likely that the size of the DM exchange interaction is doping dependent. In addition, it is also quite likely that the exchange couplings change with doping possibly through changing lattice constants.

Nevertheless, we investigate the dispersion relation Eq. (7.6) further in order to map out the changes in the two anisotropy gaps as a function of DM energy and field. In Fig. 7.8(left), we show the dependence of the gaps on the DM exchange energy in the case of zero field as well as 10 T applied field. We observe that if J_{bc} is diminished, the change in the lowest gap upon application of 10 T compared to no applied field might lie within the resolution of 0.13 meV. This could explain why we do not see a full gap even when a field is applied. In case of the larger gap, the red curves of Fig. 7.8, the change in gap size should be resolvable also at smaller values of J_{bc}, contrary to the experimental finding of field-insensitivity of the low-energy spectrum. However, as mentioned above, we cannot rule out changes in the other anisotropies J_{aa}/J_{bb} or J_{cc}/J_{bb} as a function of doping. We are thus left with the vague statement that without detailed knowledge of the exchange couplings it is hard to say anything decisive about whether a field effect would be discernible or not.

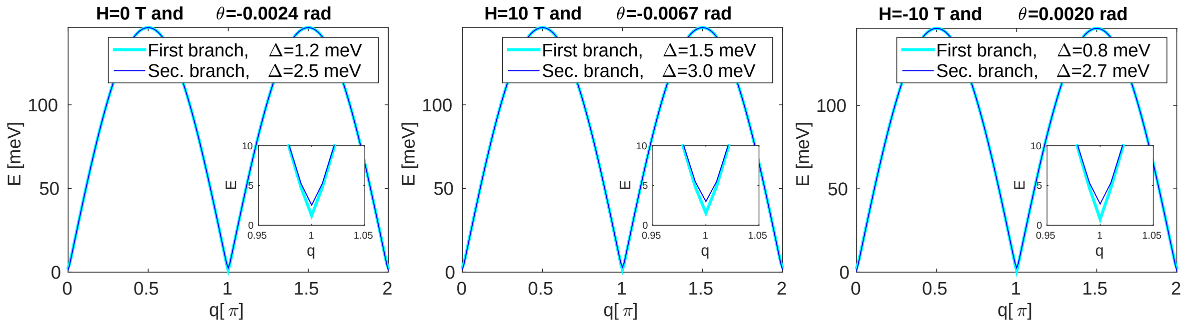

Figure 7.6: Dispersion relation Eq. (7.6) with spin renormalization factor 0.63 and $J_{bc} = 0.55$ meV. We show a diagonal cut, $\mathbf{q} = (q, q)$. Exchange couplings $J_{bb} = 116$ meV and small anisotropies of J_{aa} and J_{cc} of 0.0023 % along the a direction and 0.015 % along the c direction. The insets show a zoom of the dispersion at (π, π).

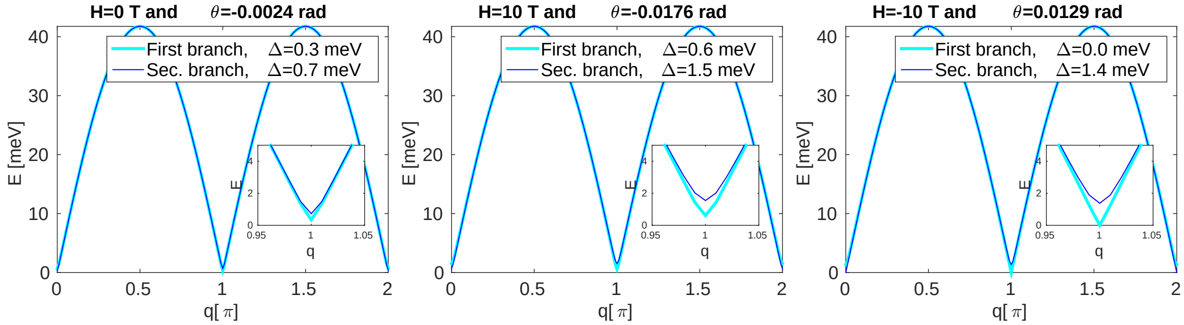

Figure 7.7: Dispersion relation Eq. (7.6) with spin renormalization factor 0.18 and $J_{bc} = 0.55$ meV. We show a diagonal cut, $\mathbf{q} = (q, q)$. Exchange couplings $J_{bb} = 116$ meV and small anisotropies of J_{aa} and J_{cc} of 0.0023 % along the a direction and 0.015 % along the c direction.

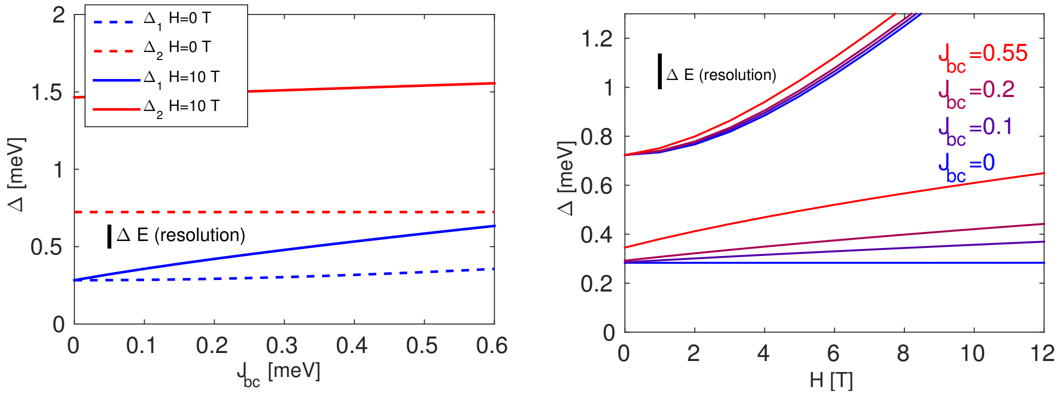

Figure 7.8: (**left:**) Energy gap size at (π, π) evaluated by Eq. (7.6)for zero field and H=10 T as a function of J_{bc}. (**right:**) Gap sizes at (π, π) as a function of field for four different values of $J_{bc} = 0, 0.1, 0.2, 0.55$. The spin is renormalized to $S = 0.18$, and exchange couplings are $J_{bb} = 116$ meV, and small anisotropies of J_{aa} and J_{cc} are 0.0023 % along the a direction and 0.015 % along the c-direction.

Now, we turn the discussion to evidence for anisotropy gaps observed in related systems. In LSCO of small doping ($x = 0.04$), evidence for a residual small spin anisotropy gap was discussed previously by Keimer *et al.* [156]. At this small doping, the crystal resides in the non-superconducting spin-glass regime. However, also superconducting systems have been reported to display anisotropy gaps. For instance, in the stripe-ordered $La_{1.875}Ba_{0.125}CuO_4$, a low-energy intensity suppression of the same magnitude below 0.7 meV, was recently observed [163, 164] and ascribed to spin anisotropy of the spin-ordered state. In that case, too, a magnetic field effect of the low-energy excitations was absent. Hence, we find striking similarities for the low-energy excitations between our sample and $La_{1.875}Ba_{0.125}CuO_4$, indicating that both samples have similar magnetic regions and anisotropy gaps.

The nickelates, $La_{2-x}Sr_xNiO_4$, also show a stripe-ordered phase upon doping with regions of antiferromagnetically ordered spins separated by lines of holes. Although nickelates do not become superconducting upon doping and also do not display the hourglass dispersion common to La-based cuprates [165, 166] and $La_{2-x}Sr_xCoO_4$, [167], the existence of stripe order in both justify a qualitative comparison. Studies of the low-energy magnetic dynamics in nickelates over a broad range of Sr content have shown evidence of an out-of-plane anisotropy gap which decreases with increasing doping [168, 169]. The decrease is about a factor of two comparing the parent compound La_2NiO_4 [170] to doping $x = 0.275 - 0.37$ (see Ref. [169]) and roughly a factor of three for doping values $x = 0.4 - 0.45$. [171] This trend is similar to the behavior we have identified in $La_{1.88}Sr_{0.12}CuO_4$. Summarizing the above, it appears that the low-energy spin dynamics in underdoped La-based cuprates and nickelates can display small residual anisotropy gaps, irrespective of whether they are stripe-ordered as $La_{1.875}Ba_{0.125}CuO_4$ [163, 164] and $La_{2-x}Sr_xNiO_4$ or undergoing glassy freezing as in $La_{2-x}Sr_xCuO_4$.

As we discussed in section 6.8, Kofu *et al.*[140] reported a study of the low-energy excitations in LSCO at doping values $x = 0.125 - 0.14$. The results were discussed in terms of a two-component scenario with a real space separation of two phases for $x \leq 0.13$. In the latter regime, spin fluctuations of short correlation length were proposed to exist at energies above an energy scale E_g comparable to the spin gap observed at optimal doping, and to coexist with low-energy fluctuations that have significantly longer correlation length. Our data do not allow us to confirm or dismiss a change in correlation length with energy transfer. We note, on the other hand, that a partial suppression of low-energy spectral weight below an energy scale ~ 1.0 meV was detected by M. Kofu *et al.* in their $x = 0.125$ sample (See Fig 7.4(b)). Moreover, no suppression was seen for $x = 0.13$, [140] which resides at the edge of magnetic order [126] and should therefore have a much smaller ordered moment and hence much smaller anisotropy gaps. Both observations are consistent with our interpretation of the low-energy intensity suppression as originating from an anisotropy gap.

In our $La_{1.88}Sr_{0.12}CuO_4$ crystal, we can not regard the stripe-ordered response as being due to only some parts of the crystal, since the muon reponse shows that ordered moments are present in the entire crystal volume. Therefore, a two-component interpretation can not be applied in our case. This should be kept in mind regarding the simplified presentation above, which discussed the anisotropy gap in terms of a spin-only model. If the magnetic order is microscopically coexisting with superconductivity, clearly the magnetism must be a SDW type of order. This does not change the overall idea of an anistropy gap, but the model becomes more involved, since also the charge degrees of freedom should be taken into account.

7.4.3 Magnetic field effect

An intriguing difference becomes apparent when comparing the magnetic field effect of the nominally elastic [see Figs. 7.1(a) and 7.2(a)] and inelastic [see Figs. 7.1(b) and 7.2(b)- 7.2(d) signals. Due to the finite energy resolution of a neutron experiment, we conclude from a comparison of Fig. 7.2(a) with μSR results that there is a significant field effect in the very low-energy fluctuations for temperatures below $T \sim 25$ K. These very low-energy fluctuations are picked up in the nominally elastic channel by the energy resolution of HWHM=0.09 meV and are therefore characterized by an energy of $\hbar\omega \leq 0.3$ meV (i.e. roughly $\sim 3\times$HWHM). This effect stands in contrast to the field-independent magnetic response in the energy range $0.5-7$ meV. The absence of a field effect in this range is distinctly different from the behavior observed for compositions with slightly smaller [149] as well as higher hole-doping, [155, 165, 172, 142] which exhibit a magnetic-field enhancement of the spectral weight in this energy range for temperatures below T_c. In the spin-only Heisenberg approach discussed above, we accounted for an easy axis and Dzyaloshinskii-Moriya anisotropies. As seen from Eq. (7.5) to first order in the canting angle, θ, the applied field enters the dispersion with a prefactor that includes the tilting angle, θ. If we let the canting angle be fixed to the value given in zero field, $\theta = -0.002$ rad. then the energy gaps would only depend weakly on the applied field, as shown in Fig. 7.9. If, however, the application of a magnetic field leads to a substantial increase in the tilting angle, then a field effect should be clearly discernible as seen from Fig. 7.8(right). Unfortunately, we do not have any experimental observation of the canting angle at finite doping and as a function of field, so the real value of the canting at $x = 0.12$ and 10 T applied field is not known. Therefore it remains an open question if the field effect on the anistropic gap values are best described by very weak dependence, as in Fig. 7.9, or a more significant field dependence as suggested in Fig. 7.8(right). As we have seen in the various plots of anisotropy gaps above, details of changes in the exchange interactions and canting angle as a function of doping, can play a major role in whether or not a field effect is observed. In this respect, we note that we do not necessarily expect to detect any significant effect of a magnetic field on the anisotropy gaps within the energy resolution.

Returning to the lowest energy ($\hbar\omega < 0.3$ meV) spin excitations in $La_{1.88}Sr_{0.12}CuO_4$ and their enhancement in a magnetic field, further experiments with improved energy resolution will be required to determine if they are of an origin distinct from the spin-wave-like excitations observed at higher energies, or whether – as the above arguments suggest – they are related to the anisotropy gap not resolved by the present experiment.

The observation of a magnetic field-effect for $x = 0.105$ and its interpretation as a renormalized superconducting spin-gap by Chang *et al.* in Ref. [149] may now be rationalized by the existence of a sharp peak around $x_{max} = 0.12$ in the freezing temperature T_f [126], see Fig. 6.5. This peak is associated with an increased competition between static magnetic order and superconductivity and a decrease of T_c [173]. We have argued that for $x = 0.12$, the spin-frozen low-temperature state permits an anisotropy gap akin to that observed in the parent insulator La_2CuO_4. Conversely, when the magnetic ordering/freezing tendencies are weakened by moving to away from x_{max}, the low-energy dynamics can be expected to become dominated by the physics of the superconductor with its superconducting spin gap opening at T_c, rather than that of the insulator with its anisotropy gaps. This physical picture goes a long way towards reconciling the disagreements of interpretations between Chang *et al.* [149] and Kofu *et al.* [140] .

7.5 Conclusions

We have studied the detailed temperature and energy dependence of low-energy magnetic fluctuations in $La_{1.88}Sr_{0.12}CuO_4$. A discrepancy between the magnetic ordering temperature derived by neutrons and muons shows that the spins undergo gradual freezing rather than a regular phase transition, i.e. for temperatures in the range $11 - 30$ K fluctuations are slowed down, but no static order develops. We find additional evidence for freezing in the temperature dependence of the low-energy fluctuations, which resembles the behavior observed in $La_{2-x}Sr_xCuO_4$ at much lower doping, in the non-superconducting, so-called spin-glass regime, and therefore conclude that even superconducting $La_{1.88}Sr_{0.12}CuO_4$ exhibits spin glass behavior.

Below the spin-freezing temperature $T_f \approx 11$ K of our sample, we have detected an incomplete suppression of magnetic spectral weight at energies larger than our energy resolution, ΔE, but smaller than 0.75 meV. We ascribe this effect to the development of a spin anisotropy gap in a spin frozen setting. Applying insights from spin wave theory, this interpretation is supported by the insensitivity, to within our experimental resolution, of the low-energy intensity suppression to an applied magnetic field of 10 T. It is notable, that the low-energy excitations in our $La_{1.88}Sr_{0.12}CuO_4$ sample are remarkably similar to those of $La_{1.875}Ba_{0.125}CuO_4$ which displays long-range spin and charge stripe order.

In contrast to the insensitivity of the anisotropy gap to applied magnetic field, a significant enhance-

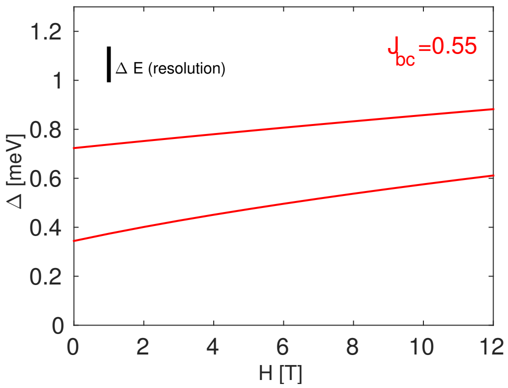

Figure 7.9: (Gap size at (π, π) as a function of field for fixed canting angle of $\theta = -0.002$ rad. and $J_{bc} = 0.55$ meV.) The spin is renormalized to $S = 0.18$, and exchange couplings are $J_{bb} = 116$ meV and small anisotropies of J_{aa} and J_{cc} are 0.0023 % along the a direction and 0.015 % along the c direction.

ment of nominally elastic, incommensurate magnetic signal was observed at temperatures lower than T_c. Given that muon spin rotation yields a freezing temperature T_f much smaller than T_c, the implication is that there must be a magnetic field effect on remnant spin excitations at energies inside our resolution window $\Delta E \simeq 0.18$ meV.

Our experimental data and a comparison with published data on LBCO and LSCO have illuminated that the sharp maximum in the spin freezing temperature T_f near $x = 0.12$ is reflected equally dramatically in the lowest energy magnetic excitations, as the spin gap – presumably intimately related to superconductivity – observed at optimal doping is replaced by a spin anisotropy gap sufficiently close to the maximum in T_f.

Chapter 8

Field-induced interplanar magnetic correlations in $La_{1.88}Sr_{0.12}CuO_4$

Some of the material in this chapter has been published in Phys. Rev. B, **91** *174507 (2015). Below we address the details of the three neutron scattering experiments reported in this publication. The experiments were designed to investigate the interplanar magnetic correlations in the cuprate superconductor* $La_{2-x}Sr_xCuO_4$*. In particular, we ask how a magnetic field applied perpendicular to the* CuO_2 *planes effect the magnetic correlations. We find that the effect of the magnetic field is to increase the magnetic scattering signal at all values of the out-of-plane wave vector L, indicating an overall increase of the magnetic moments. In addition, weak correlations between the copper oxide planes develop in the presence of a magnetic field. We discuss how the field-induced interplanar magnetic correlations provide indirect evidence for twinning of the incommensurate signal in* $La_{1.88}Sr_{0.12}CuO_4$*. Lastly, we report the interesting finding that fast cooling of the sample has similar effects on the SDW order as those obtained by applying a magnetic field.*

8.1 Motivation

It is well-known that application of a magnetic field perpendicular to the $\mathrm{CuO_2}$ planes in $\mathrm{La_{2-x}Sr_xCuO_4}$ leads to an enhancement of the magnetic signal intensity. The underlying origin of this enhancement effect is not clear, since several possibilities could be manifested in an increased magnetic signal. The motivation for studying the details of the magnetic field dependence of the incommensurate order in $\mathrm{La_{2-x}Sr_xCuO_4}$ was given in chapter 6, section 6.4. Our focus in this work, is to determine to what extend development of interplanar magnetic correlations plays a role. The main difficulty of the experiment is the smallness of the magnetic signal. This is further challenged by the unconventional experimental setup with the interplanar axis in the scattering plane. In addition, structural twinning provides a potential difficulty for the data analysis. But in fact, as we shall argue below, the current experimental setup actually provides indirect evidence for a twinning of the *magnetic* signal. This is to the best of our knowledge the first time that twinning of the incommensurate signal has been observed in Strontium doped samples. In excess-oxygen-doped samples a twinning of the incommensurate magnetic signal was observed a long time ago [148], since a larger difference between the in-plane lattice constants provides a larger splitting of the signals.

8.2 Sample properties of the $La_{1.88}Sr_{0.12}CuO_4$ crystal

We begin the discussion of the experimental details of the $La_{1.88}Sr_{0.12}CuO_4$ crystal under investigation with emphasis on the tendency towards twinning into structural subdomains. This tendency towards twinning is very crucial for the data interpretation presented below. Furthermore, the observation of twinning of the *magnetic* signal is a very interesting new finding of the present study, which brings some restrictions to the theoretical models. For instance, the simplest cartoon picture of magnetic stripes where one pair of peaks in an incommensurate quartet arises from one domain ($a < b$) the other from a domain ($a > b$) is clearly insufficient.

8.2.1 Three phase transitions and the critical temperatures

The $La_{1.88}Sr_{0.12}CuO_4$ sample studied in this work consists of a single crystal grown by the traveling solvent floating zone method. Upon cooling the crystal undergoes three second order phase transitions; a structural transition, a magnetic transition and a superconducting transition.

First, around $T = 255$ K [139] a structural phase transition takes place as the crystal goes from a High-Temperature-Tetragonal phase to Low-Temperature-Orthorhombic phase due to a tilt of the Copper-Oxygen octahedra. The tilt causes a small elongation of one of the Cu-Cu axis compared to the other. This might cause twinning of the crystal into structural domains, which is discussed further in section 8.2.2.

Magnetic ordering is revealed by an incommensurate signal, which appears below a critical temperature of $T_N \simeq 30$ K [139]. Muon spin rotation studies on the same crystal have shown electronic moments that are static on the muon time scale of microsconds below a freezing temperature $T_f \simeq 11$ K [139, 175]. Furthermore, these studies show that magnetic order persists throughout the entire volume of the sample with a resolution of 20 Å given by the effective range over which a muon is sensitive to the presence of electronic moments.

Finally, the crystal exhibits a superconducting transition temperature of $T_c = 27 \pm 1.5$ K, i.e. very close to the temperature T_N, for which neutron scattering observes magnetic ordering of the electronic moments. This indicates a strong interplay between the slowing down of the magnetic fluctuations and the development of superconductivity.

8.2.2 Twinning

A second-order structural phase transition from High-Temperature-Tetragonal (HTT) to Low-Temperature-Orthorhombic (LTO) occurs due to the tilting of the CuO_6 octahedra [177]. The octahedra can tilt around the axes (1 0 0) or (0 1 0) in orthorhombic notation, i.e. around the Cu-Cu axes. This tilt displaces the oxygen atoms away from the plane and within an orthorhombic unit cell, two oxygen atoms are moved upwards and two oxygen atoms are moved downwards with respect to the plane of the Cu atoms. The distortion causes an elongation of the Cu-Cu axis perpendicular to the rotation axis compared to the Cu-Cu axis parallel to the rotation axis. The two in-plane lattice vectors thereby become slightly different and this opens the possibility of forming different structural domains in the crystal. A pair of twins is developed for a part of the crystal sharing a common axis, which can be either of the two Cu-O-Cu axes (1 1 0) or ($1\ \bar{1}\ 0$). On each side of this common axis a twin of the "twin pair" is formed; in one of the twins the rotation takes place around the (1 0 0) axis, whereas for the other twin the rotation is about the (0 1 0) axis. One twin will satisfy $a > b$ for the two orthorhombic lattice constants a and b, whereas for the other twin $b > a$. This situation is sketched in Fig. 8.1 which is adapted from Braden *et al.*, Ref. [177]. In general, we can expect the development of four different structural domains upon entering the Low-Temperature-Orthorhombic phase, where the appearance of domains comes in pairs. For one twin pair, one of the twins will be of type $a > b$ and the other of type $a < b$. However, it is not necessary that both twins of a pair are equally represented in the crystal, since one twin of a pair might occupy a larger volume fraction than the other.

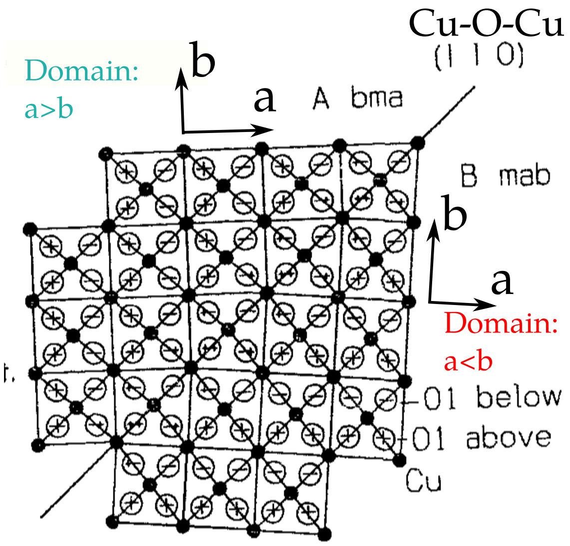

Figure 8.1: Illustration of a CuO_2 plane with two twins sharing the common axis (1 1 0) in orthorhombic notation. Adapted from Braden *et al.*, Ref. [177].

The crystal under investigation shows pronounced twinning into primarily two domains. We have verified that the domain pattern is reproducible for every slow cooling through the orthorhombic transition.[1] The twinning of the crystal is observed as a splitting of the structural Bragg peak, as shown in Fig. 8.2. The splitting is clear in the scans of the Bragg peaks (2 0 0) and (0 2 0). There is one dominant domain and two visible subdominant domains, as seen in Fig. 8.2. The dominating Bragg peak corresponds to the lattice constants of the orthorhombic unit cell at base temperature:

a [Å]	b [Å]
5.312	5.356

Note that the dominant domain has been dubbed an $a < b$ type in our choice of nomenclature. Calculation of the lattice constants of the subdominant domain gives $a = 5.354$ Å and $b = 5.314$ Å, which has $a > b$ as expected, if this domain share a twin boundary with the dominant domain. The lattice constant agrees with the calculated values of the dominant domain within 0.002 Å. The third visible domain is also of the type $a > b$. The last possible domain, which is expected to be of the type $a < b$, is not visible from the scans. Since all domain types come in pairs, with one domain being of type $a < b$ and the other being $a > b$, it is intriguing why we don't observe a fourth domain from the Bragg peak scans. The absence of a fourth Bragg peak is likely due to a smaller representation of this fourth domain in the bulk. In fact, there might be a very weak signal visible next the dominant peak in the Bragg peak scans of Fig. 8.2, which is also of type $a < b$. But it is quite weak and probably also masked by the tails of the dominant and sub-dominant peaks close by. In the discussion below we will focus on the two dominant domains. From scans through the second order peaks (1 0 0) and (0 1 0) we get the following peak positions:

Domain 1		Domain 2	
H [r.l.u.]	K [r.l.u.]	H [r.l.u.]	K [r.l.u.]
0.9998(2)	0.0013(2)	0.9920(3)	0.0051(1)
-0.0011(1)	0.9996(2)	-0.0061(1)	1.0075(1)

Relating the positions of these two domains, we find that the subdominant peak is shifted by 0.8 % from the dominant peak in both directions, i.e. $\frac{0.9998(2)-0.9920(3)}{0.9998(2)} = 0.0078(4)$ and likewise for the peaks

---

[1] Experiment at RITA-II in May 2012 by P.J. Ray, L. Udby and the author.

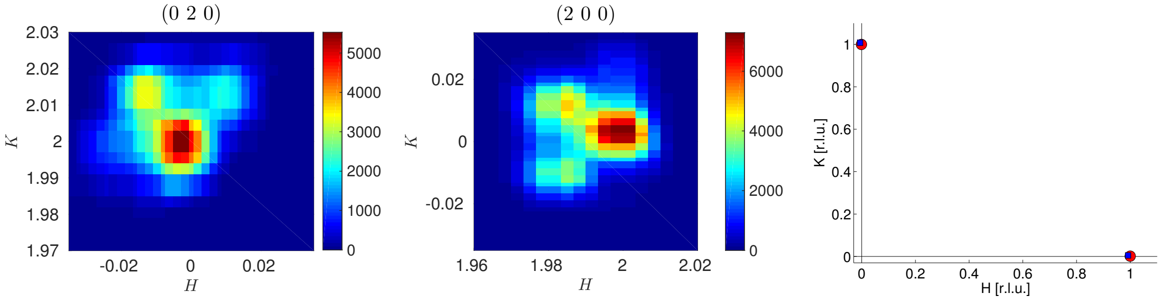

Figure 8.2: Scan through the structural Bragg peaks (0 2 0) and (2 0 0) and drawing of the two dominant domains.

close to (0 1 0). A calculation of the rotation angle between the two structural peaks gives an angle of 0.22°/0.28° for the peaks around (1 0 0) and (0 1 0), respectively. In a work of Kimura *et al.*, Ref. [133], the twin splitting in a similar sample, LSCO with 12 % doping, was reported to be ∼ 0.3°, and we conclude that our results are within reasonable agreement of the previous experiment.

Since we measure the incommensurate signal close to (1 0 0) we focus on the twin splitting at this position. The transformation which must be performed in order to bring the structural peak of the dominant twin to the same position as the structural peak of the sub-dominant twin is the following; First a rotation by 0.22° is performed and second, rescaling of the vector length accounts for the fact that whereas the dominant domain is of the type $a < b$ the subdominant domain is of the type $a > b$. If there is a twinning of the incommensurate signal, it is likely to imagine that IC twins are displaced from each other by the same transformation. We will return to this point below.

8.3 The three experiments

High-resolution elastic neutron scattering experiments were carried out on three different cold neutron triple axis spectrometers: 1) RITA-II at the SINQ neutron source at the Paul Scherrer Institute in Villigen, Switzerland, 2) FLEXX at the BER2 research reactor at HZB Berlin, Germany, as well as 3) PANDA at the FRM-II research reactor source in Munich, Germany. The PANDA experiment was carried out in zero field, whereas the two other experiments were performed in a horizontal field. Preliminary experiments at the thermal neutron triple axis spectrometer BT-7 at NIST, Washington were unsuccessful. However, during this experiment we gained valuable insight about the optimal setup for a LSCO c-axis experiment. In triple axis spectrometers, the resolution ellipsoid is strongly elongated out of the scattering plane. This means that in common experiments, where the (a, b) plane is in the scattering plane, the intensity is enhanced by resolution integration along the c-axis, along which the IC signal is broad. In the present crystal alignment with the c-axis in the scattering plane we do not gain intensity by these resolution effects, but obtain the same amount of incoherent background signal. Therefore the magnetic signal is very low and requires optimization of experimental setup as well as long counting times. In the NIST experiment we learned that sample rotation scans are optimal in this situation, since this limits distinct background contributions from e.g. powder lines arising from 2nd and 3rd order neutrons reflected by the monochromator and leaking through the Be-filter. On the contrary, incoherent scattering always gives a constant contribution that is less of a problem in data analysis. After the NIST experiment, all following experiments were therefore carried out by sample rotation scans only, with the exception of a few scans close to $L = 0$ in the zero field experiment at PANDA. In Figure 8.3 an illustration of the sample rotation scans though a signal rod is depicted. In particular, we show how the imaging mode of RITA-II enables measurements at distinct values of L for one sample rotation scan. This feature was very efficient in the current experiment. All experiments probed the *elastic* neutron response at an incommensurate position for magnetic order of $La_{1.88}Sr_{0.12}CuO_4$.

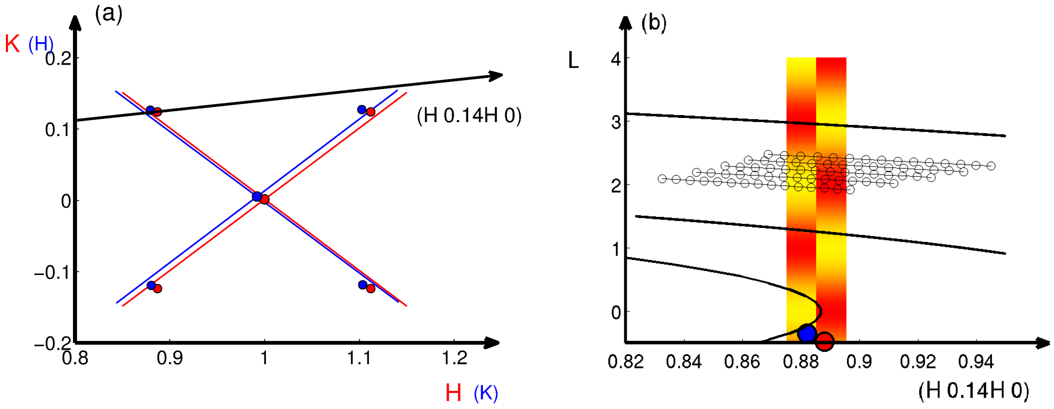

Figure 8.3: (a) Illustration of the quartet of IC peaks around (1 0 0) in orthorhombic notation. The scattering signal from the (1 0 0) structural second order peak belonging to the dominant domain is shown by the red circle. The crystal shows twinning into two sub-dominant domains of which we show the strongest by the blue circles. The red and blue lines show the Cu-O-Cu axes. Note that the IC peaks are shifted off these high symmetry axes in agreement with the earlier report of Kimura *et al* [133]. The black arrow shows the axis (H 0.14H 0), which we probe in the scattering plane. (b) Illustration of the scattering plane spanned by (H 0.14H 0) and (0 0 L). We show examples of a sample rotation scan through a signal rod with a proposed weak L dependence of the signal shown for the two twins of the IC signal, with maximum signal visualized by red color and minimum signal shown in yellow. The width of the signals along (H 0.14H 0) is exaggerated for clarity. Note that one twin (red circle) displays peaks at even L values and the twin shown by the blue circle exhibits peaks at odd L values. This scenario is discussed in detail in section 8.6.1. The white points visualize how the 9 analyzer blades of the monochromatic $\mathbf{q}$-dispersive mode (imaging mode) on RITA-II enable measurements at distinct values of L for one sample rotation scan. For clarity, only every second analyzer blade has been shown. The solid lines show the trajectory of the reciprocal lattice vectors in a sample rotation scan. From the scan line centered at $L = 0$, it is clear that a sample rotation scan is not applicable for small L-values. With increasing L, the change in L during one sample rotation scan through the signal rod becomes smaller.

8.3.1 Experimental setup at PANDA

The experiment at PANDA was done in June 2009 by Kim Lefmann and the author. It was done before a horizontal magnet was available, and therefore this experiment was performed in order to obtain a benchmark for the interplanar correlations in zero applied field. The crystal was mounted on a Aluminium holder shielded by Cadmium foil. A small Aluminium wire was tied around the crystal. A Cu adapter was used for the mounting, but was very far from the sample and hence not in the beam. The monochromator was set to horizontal flat mode and vertical focused mode with a resolution of roughly 4°. The analyser was in flat mode. We used 5.0 meV neutrons, i.e. $k_i = k_f = 1.55$ Å. The Be-filter was placed before the sample to remove the higher order neutrons thereby getting a very clean beam at the sample position. Collimators of $60'$ was used between the monochromator and sample and between the sample and analyser. When performing the experiment at PANDA we were not aware of possible sensitivity of the cooling rate on the magnetic signal. The sample was cooled very fast by 4 K/min. As we shall see below, there is evidence that the cooling rate in fact has influence on the interplanar magnetic order.

8.3.2 Experimental setup at RITA-II

This experiment was performed during two weeks in June 2012 by Pia J. Ray, Linda Udby and the author. The experimental setup at RITA-II was $E_i = E_f = 4.6$ meV ($k_i = k_f = 1.49$ Å), vertically focusing monochromator, and the 9-blade analyzer arranged in the monochromatic **q**-dispersive mode (in brief "imaging mode"). We used a $80'$ collimation before the sample and a Be filter with radial collimation after the sample. Due to the small size of each analyzer blade, the effective outgoing collimation was roughly $60'$. The sample was mounted in the horizontal field cryomagnet MA7 and data was taken in 6.8 T field applied along the *c*-axis as well as in zero field. In the RITA-II experiment cooling from 270 K to 190 K was very fast, while cooling from 190 K to 50 K was done slowly, (1 K/min) This experiment turned out to be very fruitful, which was due to the relatively long beam time and the optimal use of the imaging mode on RITA-II, in which 9 analyzer blades allow for a simultaneous measurement of 9 different **q**-values. In general we can use all 9 analyzer blades. However, for some of the scans we have too little background for the outermost blades to discern a peak. In this experimental setup we restricted all measurements to sample rotation scans, as discussed above. In that case the imaging mode amounts to 9 simultaneous sample rotation scans, i.e. each with a different value of $|\mathbf{q}|$, as illustrated in Fig. 8.3(b). We did no background scans (hereby we mean scans at temperatures above the magnetic ordering temperature).

8.3.3 Experimental setup at FLEXX

The experiment at FLEXX was performed in January and May 2013 by Henrik Jacobsen, Mads Bertelsen, Sonja L. Holm and Kim Lefmann. The sample was placed in the 6 T horizontal magnet HM1 with the same crystal alignment as in the RITA-II experiment. The experiment was performed with a vertically focusing monochromator and horizontally focusing, but vertically flat PG analyzer at energies $E_i = E_f = 5.0$ meV. To limit the dominating incoherent background from the sample, we used $60'$ collimation between monochromator and sample as well as between sample and analyzer. Second order contamination from the monochromator was eliminated by a velocity selector. Sample cooling from 300 K to 45 K was performed slowly by 1 K/min. In this experiment careful attention was drawn to the background in each scans with full scans at temperatures above as well as below the magnetic ordering temperature.

8.3.4 Alignment

In all experiments, the sample alignment was performed with the *c*-axis in the scattering plane. We probed the incommensurate signal near the position (0.89 0.12 0) by tilting the *a*-axis slightly out of the scattering plane with the *c*-axis being the axis of rotation. The tilting angle was given by: $\theta_{\text{tilt}} = \tan^{-1}(\frac{0.12}{0.89}) = 7.7°$. With this crystal orientation, the scattering plane is spanned by the two vectors $(0\ 0\ L)$ and $(H\ 0.14H\ 0)$. This allows us to probe different values of L, but we are restricted to an incommensurate signal very close to $(0.89\ 0.12\ L)$. As a surprise, this alignment in fact enabled an interesting feature of the incommensurate signal; it shows evidence for twinning. To the best of our knowledge, this is the first time that evidence for twinning of an incommensurate signal in $La_{2-x}Sr_xCuO_4$ has been observed.

8.4 Results from field experiments at RITA-II and FLEXX

8.4.1 Peak position

Figure 8.4 (a,b) shows the raw data taken on RITA-II through the IC position $\mathbf{Q}_{\text{IC}}$ at different magnetic fields for $L = 3$ and $L = 4$, respectively. For the zero field data, the peak intensity is roughly the same at $L = 3$ and $L = 4$, whereas the measurements in an applied field show a higher intensity at $L = 4$ than at $L = 3$. Due to the use of the imaging mode, the RITA-II experiment amounts to almost 80 individual scans. In figure 8.4 (a,b), the data of five blades have been combined for an integration range

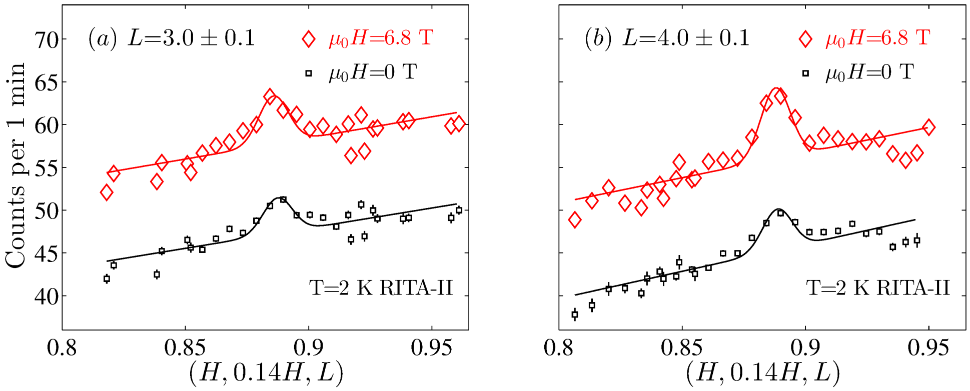

Figure 8.4: Raw data for sample rotation scans through the IC position $(H\ 0.14H\ L)$ for $L = 3.0$ and $L = 4.0$ in $H = 6.8$ T (red data) and zero (black data) applied field along the c-direction, taken at $T = 2$ K. This data was taken at RITA-II, PSI. For each scan the data of five blades have been combined leading to an uncertainty in L of 0.1 r.l.u.. Errorbars are smaller than the markersize. The field data are shifted upwards by a constant offset for clarity. The solid curves display fits to Gaussian functions on a sloping background.

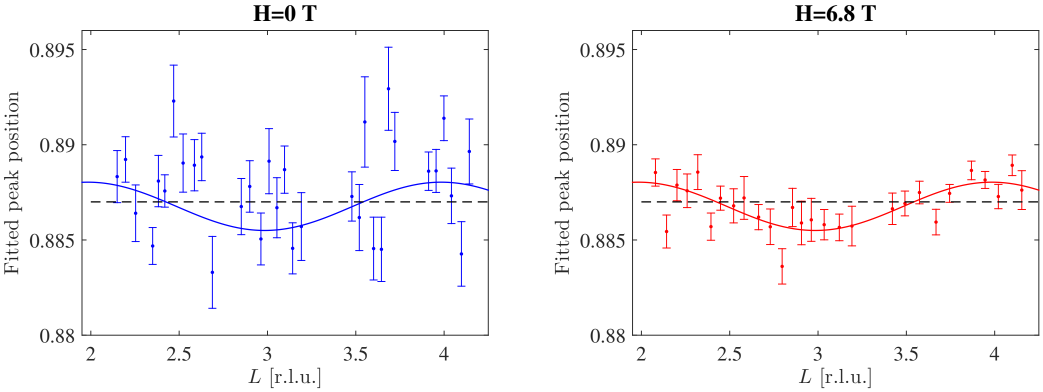

Figure 8.5: Fitted peak position H_{IC} as a function of L for zero field and H=6.8 T field data. The mean value of the peak position is in both cases $H_{\mathrm{IC}} = 0.887$ r.l.u.. The dashed black line shows a fit to a straight line and the full colored line displays a fit to a sine function. Due to the enhancement of the signal in field the peak position is more accurately determined in this case, and this reveals a small, but clear modulation of the magnetic signal as a function of L.

of $\Delta L = 0.1$ r.l.u.. We expect the signal to be resolution limited in the (a, b) plane, since long range order has previously been found in this crystal. Therefore, we choose to fit the signal with a fixed (resolution determined) width of $\sigma = 0.006$ r.l.u. which corresponds to a correlation length of $\xi_{\mathrm{in-plane}} \geq 120$ Å. This sets the lower bound for the magnetic correlation length in the CuO$_2$ planes, and is consistent with earlier measurements finding resolution limited correlations in the (a, b) plane [139, 178]. The raw data are fitted to a single Gaussian function on a sloping background like in the two examples shown in Fig. 8.4. All parameters except the width of the peak are free parameters of the fit.

For the individual scans the fitted center position of the peaks varies within ≈ 0.002 r.l.u. around the mean value of $H_{\mathrm{IC}} = 0.887$. Further inspection of the fitted peak center shows a clear modulation as a function of L as shown in Fig. 8.5 with $H_{\mathrm{IC}} = 0.888$ for even L and $H_{\mathrm{IC}} = 0.886$ for odd L. In section 8.2.2 the structural twinning of the LSCO crystal was discussed. Now we return to this point in a discussion of the incommensurate magnetic signal.

As mentioned above, we are interested in resolving if there is some internal structure of the incommensurate signal, since we speculate that the structural twinning of the crystal could lead to a twinned magnetic signal as well. The speculation is not completely taken out of the blue. In oxygen-doped compounds, which display a larger orthorhombicity, a clear twinning of the incommensurate signal was reported by Lee and coworkers in Ref. [148]. In our case, we tried to resolve a double peak feature of the incommensurate signal in each sample rotation scans, but this was not possible in any of the scans. The variation in the peak position is subtle; as seen from Fig. 8.5 the peak position varies with 0.002 r.l.u which is even smaller than the instrumental resolution of 0.006 r.l.u.. However, in general the center of a peak can be determined to much better than the instrument resolution and it is possible that the peak center variation is a real physical effect. We find the manifestation of some internal peak structure in a subtle way. The structure is only discernable when plotting the fitted center value as a function of L. When doing this, we find the following:

- The mean value of the peak is identical in the case of zero applied magnetic field as well as $H = 6.8$ T magnetic field; $H_{\mathrm{IC}} = 0.887$ r.l.u..
- In the zero field data, the errorbars are relatively large, which is due to the very weak signal.
- In a field the magnetic signal is enhanced, and the errorbars are reduced. In these data an important feature becomes evident; there is a clear modulation of the magnetic signal as a function of L. The reduced chi square of a fit to a sine function is $\chi^2 = 1.4$ (see full line in Fig. 8.5(right)), which should be compared to the reduced chi square of a fit to a linear function, $\chi^2 = 2.8$ (dashed line in Fig. 8.5(right)). This is statistically highly significant.

The sine-variation of the peak position that we observe is quite convincing. In the discussion in section 8.6.1 we relate this observation to the twinning of the crystal.

8.4.2 Peak intensity

In Fig. 8.6 we show scans at $L = 2$ from the independent experiment on FLEXX. In this experiment we carefully measured the background intensity by sample rotation scans above the magnetic ordering temperature at $T = 40$ K and performed a point-wise background subtraction of the incommensurate magnetic signal. For the zero-field data in Fig. 8.6, the signal is weak and when fitting the data with

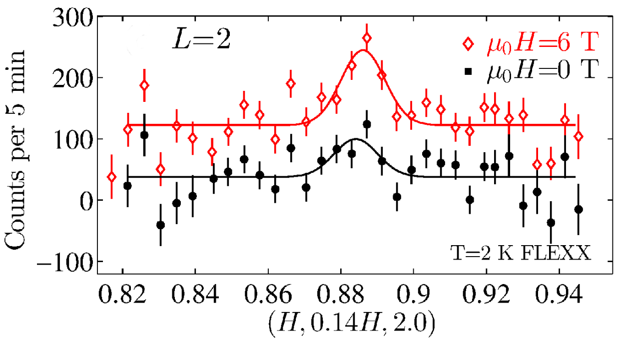

Figure 8.6: Measured peak intensity at $T = 2$ K for the IC position (H 0.14H 2.0) in 6 T field (red data) and zero field (black data). Point-wise background subtraction has been performed, using 40 K data as background. The solid curves are Gaussian fits to the data. This data was taken at FLEXX, HZB. The field data is shifted upwards by a constant offset for clarity.

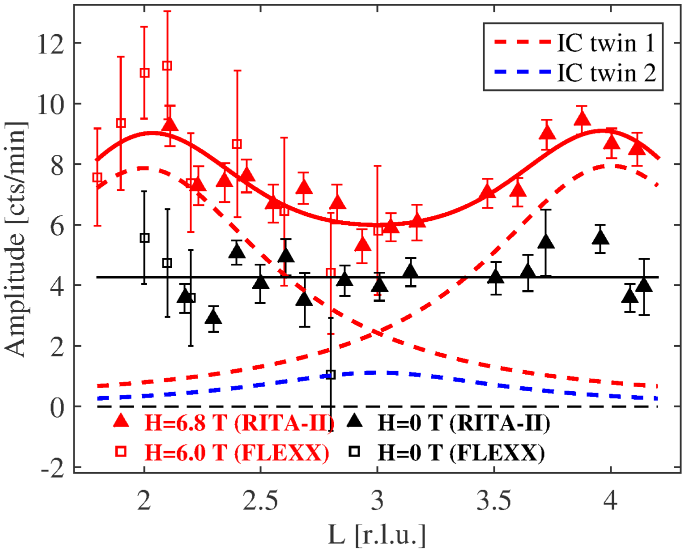

Figure 8.7: Background-subtracted elastic response at the IC position (0.887(2), 0.124(1), L) versus L in zero field, a 6.0 T field (FLEXX data), and a 6.8 T field (RITA-II data). The y-axis label corresponds to the counting rate at the RITA-II experiment. To compare the two data sets, the FLEXX data has been scaled by a constant factor determined by the fraction of the signal intensities at the common data point $L = 2.2$. The red solid line corresponds to a fit to three Lorentzian functions with the same width and fixed centers at $L = 2, 3$ and 4. The three Lorentzian functions are shown separately by the red and blue dashed lines, belonging to the first and second IC twin, respectively. The colorcode is the same as in the cartoon drawing Fig. 8.3(b).

a Gaussian we are guided by the clear presence of a magnetic signal in an applied field, as well as the presence of zero field static order measured in the same crystal in previous experiments with a more favorable alignment (the c-axis out of the scattering plane.) As for the RITA-II experiment, we fit both field and zero field data to a Gaussian function with a fixed Gaussian width, which is limited by resolution. For the zero field data, our procedure is supported by the values of the reduced chi squared which is 1.6 for the Gaussian fit versus 2.0 for a straight line fit, or a change in the unreduced chi square of more than 10. This is statistically significant. Hence, a small peak does appear to be present at $L = 2$, also at zero field. Having established the evidence for a zero field signal we conclude from Fig. 8.6, that the effect of a 6 T magnetic field is to roughly double the IC magnetic signal. This is in agreement with the previous finding at $L = 0$ in 7 T, as reported in chapter 7, figure 7.2.

8.4.3 Signal intensity along the interplanar direction

The main purpose of the experiments was to elucidate two possible mechanisms behind the observed field enhancement of the elastic neutron response; is there an overall increase of the magnetic moments, or a increased correlation of the moments along the interplanar direction? In order to do so, we now map out the full L-dependence of the IC signal in field and zero field. We did several scans similar to those shown in Fig. 8.4 (a,b) and Fig. 8.6 for L in the range 1.8 to 4.15. This span in L is significantly broader than in the previous field study by Lake *et al.*, Ref. [144]. The results are summarised in Fig. 8.7 for both the RITA-II and FLEXX experiments. Note that while cooling conditions and some parts of the experimental setups at RITA-II and FLEXX are similar, the detailed setups of the two instruments are not quite identical (The imaging mode at RITA-II uses 9 individual flat and narrow analyzer crystals, while at FLEXX we used a conventional triple axis spectrometer setup with vertically flat, but horizontally focusing analyzer crystals). For such reasons, one generally does not expect to achieve full quantitative agreement between data sets taken at two different instruments. Therefore, a normalization procedure is ultimately needed when comparing such data. The procedure we have chosen in Fig. 8.7 below is to scale the data taken at RITA-II and FLEX at $L = 2.2$.

In zero field, the measured IC signal is flat as a function of L, i.e. there is no observable interplanar correlations when the sample has been cooled down slowly. The effect of applying a magnetic field perpendicular to the copper oxide planes is twofold. First, weak correlations between the CuO_2 planes develop. In zero field there is no intensity modulation as a function of L, whereas a clear modulation builds up upon application of field. This is in agreement with the observations of Lake *et al.* in LSCO $x = 0.11$ [144]. Secondly, and more pronounced, an overall enhancement of the magnetic signal takes place for all values of L. A fit of the field data to three Lorentzian functions with same width and fixed centers at $L = 2, 3$ and 4 gives a broad modulation with HWHM= 0.7(1) r.l.u. In section 8.6.1 we will discuss the fitting procedure in detail. The very broad peaks signify that the spin order is characterized by a very short correlation length of 3 Å along the c-axis. The distance between neighboring CuO_2 planes is given by ~ 6.5 Å, and our result shows that the spins in neighboring planes are only *very weakly* correlated.

As a measure of the true enhanced intensity we integrate the signal measured in field along L and compare to the L-integrated zero-field signal. From Fig. 8.7 we get an L-integrated enhanced intensity of 77(8)%. For a comparison we calculate the enhancement effect at $L = 2$ from Fig. 8.7 and get 109(9)%. The latter corresponds to the effect which would be estimated from a measurement with the current crystal aligned in the (a, b) plane.

8.5 Results from the zero field experiment at PANDA

In Fig. 8.8 we show the results of the PANDA experiment[2], which was done at zero field, but under different experimental conditions since the crystal was fastly cooled by 4 K/min. We observe a small correlation between the CuO_2 planes even when no magnetic field is applied. As seen from Fig. 8.8, the signal intensity at $L = 2$ is roughly twice the signal intensity at $L = 1$. Since the peaks are very broad along L it is appropriate to fit to two Lorentzian functions centered at even L, which gives a width of HWHM= 0.58(8) r.l.u. similar to the broad modulation observed in field. This leaves us with the interesting observation that quench-cooling has the same qualitative effect of enhancing inter-planar correlations as the application of an external magnetic field in the c-direction.

8.6 Discussion

8.6.1 Peak position and incommensurate twins in $La_{2-x}Sr_xCuO_4$

We observe an IC signal at all values of L in field as well as in zero field. In field the position is at $H = 0.887(2)$ with a weak L dependence as shown in Fig. 8.4 (c). Under the assumption that this IC signal belongs to the dominating structural twin, the mean IC position corresponds to a displacement angle of $\theta = 2.7°$ away from the high symmetry axis of the underlying CuO_2 plane. This is consistent with the displacement angle of $\theta = 3°$ reported by Kimura *et al.*[133] on a crystal of similar doping. In zero field the mean peak position is the same as in field with a slightly larger uncertainty due to the very weak signal. In Fig. 8.5 we addressed the variation in peak position as a function of L. We established that there is a small, but clear sine modulation of the peak position along L measured in field, while in zero field there is no discernible variation. We speculate that the reason why we cannot see a sine modulation in the case of zero field is due to the large uncertainty in this case. In $La_{2-x}Sr_xCuO_4$ there exist no reports on twin components of the IC order and in particular, the signal structure along the L direction for different twin components of the IC order has not been adressed previously. Here we

---

[2] Further details of the experiment can be found in A. T. Rømer, Master thesis, University of Copenhagen (2009).

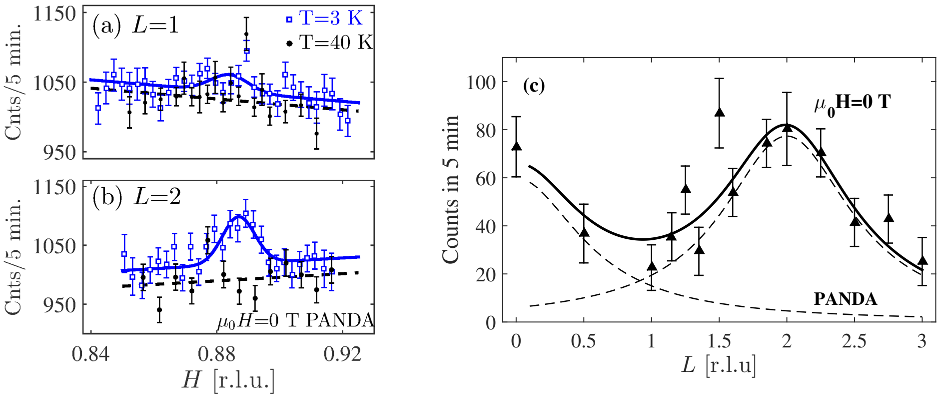

Figure 8.8: (a-b) Scans through (H $0.14H$ L) at T = 3 K (blue open squares) and T = 40 K (black points) in zero field for L = 1 (a) and L = 2 (b). In both figures, the solid blue line shows a fit to a Gaussian function on a sloping background. (c) L-dependence of the incommensurate magnetic signal above background in zero field measured at PANDA. The solid black line shows the fit to two Lorentzian functions with fixed centers at $L = 0$ and $L = 2$. The dashed lines show each of the Lorentzian functions seperately.

propose a model that relates the modulation of the peak position along L to a twinned incommensurate order. To do so, we will relate our observations to expectations stemming from the parent compound La_2CuO_4[145, 147] and super-oxygenated La_2CuO_{4+y} [148]. The parent compound La_2CuO_4 displays long-range three-dimensional antiferromagnetic order with spins aligned mainly along the orthorhombic b-axis [145, 147], as shown in Fig. 6.8. With this spin structure the magnetic signal is peaked at *even* L for scattering at (1 0 L) and at *odd* L for scattering at (0 1 L). In the work by Lee *et al.* [148] in super-oxygenated La_2CuO_{4+y}, a clear splitting of the incommensurate signal in the (a, b) plane due to large orthorhombicity, allowed measurements of IC signals centered at (1 0 L) and (0 1 L) simultaneously. In their work, Lee and coworkers report the presence of incommensurate peaks, which are broad along L; for the IC signal centered at (1 0 L) the peak is at even L while it occurs for odd L for the IC signal centered at (0 1 L). Thus, in La_2CuO_{4+y} the arrangement of the spins in the interplanar direction bear resemblance to the spin arrangement in the parent compound with the spins being correlated across two to three CuO_2 planes [148].

In our case, the orthorhombicity of the crystal is much smaller than in La_2CuO_{4+y}, which makes it harder to identify a possible twinning of the IC signal. As a consequence, splitting of the IC signal was never reported in $La_{1.88}Sr_{0.12}CuO_4$ or in fact in any $La_{2-x}Sr_xCuO_4$compounds. Twinning of the crystal can result in development of four different structural domains, as discussed in section 8.2.2. From scans through the structural peaks of the crystal, three structural domains are clearly visible, see Fig. 8.2, and from a scan of the (2 0 0) peak the subdominant domain has a relative signal amplitude of roughly 70 % compared to the strength of the dominant structural peak.[3]. The sub-dominant second order peak close to (1 0 0) is displaced from the dominant peak by 0.8 % in both directions. This corresponds to a rotation of 0.22° between the two twins. Now, we present a scenario suggesting where to expect a twin for the incommensurate signal. We take outset in the structural twinning presented in section 8.2.2 with focus on the dominant and the sub-dominant structural peak visualized in Fig. 8.2. The idea is to perform a transformation that brings the peak of the dominant domain on top of the peak of the sub-dominant domain. We apply the same transformation to the IC peak position at (0.888, 0.124, 0) in order to predict an expected position of the IC twin signal. By a rotation of 0.22° and a rescaling of the vector length, the structural peak of the dominant twin is brought to the same position as the structural peak of the sub-dominant twin. Performing the same transformation on the IC peak at (0.888, 0.124, 0)

---

[3] Details are given in Ref. [150]

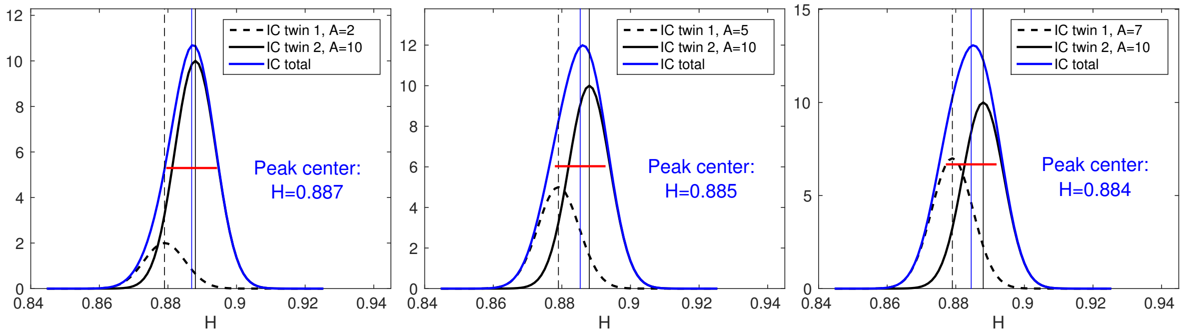

Figure 8.9: Two Gaussian functions of Gaussian width $\sigma = 0.006$ and center positions $H = 0.879$ (black dashed line) and $H = 0.888$ (black solid line). The amplitude of the individual signals are shown in the legend. The total signal (the sum of the two Gaussian contributions) are shown by the blue solid line. The center and width of the total signal varies as a function of amplitude ratio between the individual contributions. The solid red line shows the Full Width Half Max (FWHM$= 2\sqrt{2\ln 2}\sigma$) for $\sigma = 0.006$. For each case, the center of the total signal (fitted to a single Gaussian function) is given in blue text in the subfigures.

we obtain the expected position of an IC twin to be at (0.879, 0.126, 0). This predicts a larger deviation in peak center than expected from the lower value of the fitted peak center shown in Fig. 8.5 for $L = 3$ which is $H = 0.886$. Note, however, that the expected difference in peak position of the two IC twin signals is of the order of the resolution limitation of 0.006 r.l.u..

In order to clarify the suggested scenario, we now plot two resolution limited Gaussian functions of Gaussian width $\sigma = 0.006$ which centers of $H = 0.879$ and $H = 0.888$, respectively. Three different situations are shown in Fig. 8.9, where the only difference between the plots is the relative amplitude of the two Gaussian functions. From this figure it is clearly seen how the center of the total signal (the sum of the two Gaussian contributions) varies as a function of the relative weight of the individual contributions, i.e. for a relative weight of 20 % the peak is centered at $H = 0.887$, whereas for a larger contribution of the subdominant peak of 70 % the peak position is shifted to $H = 0.884$ and also slightly broader than the resolution limitation in this case.

Figure 8.9 shows the clear-cut case of how a variation in the center position of the IC signal reveals the presence of an internal structure, in this case the contribution of two individual IC twins. This suggests that the peak center variation shown in Fig. 8.5 is a manifestation of a larger fraction of the intensity originating from one IC twin at even values of L and another twin at odd values of L. Since we measure the IC signal centered at $(1\ 0\ L)$ defined with respect to the dominant structural domain, we expect interplanar correlations from the dominant twin to be peaked at even L. These expectations stems directly from the observations in La_2CuO_4 and La_2CuO_{4+y} discussed previously. The subdominant twin signal is centered at $(0\ 1\ L)$ and will therefore be peaked at odd L. Thus, the IC twin centered at (0.888, 0.124, 0) will dominate at even L and the other twin appears with weak intensity at odd L. In short, the dominant twin (centered at $H = 0.888$) has a relative stronger weigth at even values of L compared to odd values of L. This situation is illustrated by Fig. 8.9 (left). At odd values of L, the relative weight is shifted as illustrated in Fig. 8.9 (middle/right). We must expect both IC twin signals to contribute for all values of L, due to the resolution limitation along the $(H\ 0.14H\ 0)$ axis and broadness of the signals along the $(0\ 0\ L)$ axis.

In Fig. 8.7, we show the individual contributions to the field intensity by dashed lines. Since the twin showing correlations peaked at even L is more pronounced than the twin with correlations peaked at odd L, the total signal displays peaks at even $L = 2$ and 4, whereas the peak at $L = 3$ is masked by the tails of the other two. In principle we expect a larger amplitude of the IC twin 2 shown by the dashed blue line of Fig. 8.7, which ideally should be about 70 % of the amplitude of the IC twin 1, in order to fit with the structural domain representation. However, the broadness of the signal makes it difficult to obtain a very precise fit. However, note that the value obtained for the measured peak position at odd L in Fig. 8.5 (right), namely $H = 0.886$ r.l.u. is quite consistent with the concept of two IC twins at the predicted positions of a relative strength of roughly 50 %.

8.6.2 Field-induced c-axis correlations

From the two independent field experiments done at RITA-II and FLEXX, we find that the IC signal at (0.887(2) 0.124(1) L) is enhanced by a magnetic field at all values of L, but in particular for even L. The results of both experiments agree on the magnitude of the magnetic field enhancement at even L which is close to a factor of two in both cases.

Although the FLEXX experiment provided less data points, it is clear from Fig. 8.7 that both experiments agree on the development of weak interplanar correlations in a field as reflected in the L-dependence of the amplitude of the IC intensities. The peaks which are centered at even values of L are very broad and the correlation length is smaller than the interplanar distance of 6.5 Å. This deviates from the correlation length of more than 10 Å as found in Ref. [144] for LSCO $x = 0.11$. We note that the correlation length determined in Ref. [144] is likely uncertain due to the sparse data (as seen from Fig. 6.12(d) the peak is resolved with only two data points for one of the samples, and three datapoints in the other sample). However, we cannot rule out a real difference in the field-induced interplanar correlation length between these two crystals of different doping levels. Since our crystal displays enhanced magnetic order in zero field compared to smaller doping values [139], it might be harder to induce the interplanar correlations by a field.

The primary effect of an applied magnetic field is to enhance the magnetic signal either by enlarging the magnetic volume fraction or the ordered magnetic moments. Our neutron scattering experiment does not allow for a distinction between an enlarged magnetic volume fraction or increased ordered magnetic moments. However, muon spin rotation studies on the same crystal show that magnetic order is present throughout the entire volume of the sample (with a resolution of 20 Å) [139, 175] and we conclude that the main effect arises from enlargening of the ordered magnetic moments.

In addition, development of weak interplanar correlations occurs as a response to the applied magnetic field. As a consequence, the field effect reported in the literature on magnetism in the cuprates that has been measured in the usual configuration $L = 0$ must be re-quantified, since it is either overestimated or underestimated, depending on whether the dominant IC peak belongs to a "(1 0 0)" or "(0 1 0)" IC quartet. For our crystal, measuring at the IC peak at (0.887, 0.124, 0) with $L = 0$ would cause an overestimation of the field effect. At even L the amplitude enhancement is roughly 109% whereas the real increase of magnetic order measured from the L-averaged intensity is only 77%. Thus the field effect is overestimated by 40%.

8.6.3 Cooling-induced c-axis correlations

Another new finding in this work is the fact that interplanar correlations are also found in zero field under different experimental conditions where the crystal is quench cooled from room temperature down to base temperature below 4 K. In contrast to the experiments on RITA-II and FLEXX, where the temperature regime for ordering of possible excess oxygen was traversed slowly, this was passed extremely fast in the PANDA zero-field experiment. This is likely to have resulted in finite interplanar correlations as evident from Fig. 8.8, qualitatively similar to the result of an applied magnetic field.

To understand this behaviour, we first compare our sample to super-oxygenated crystals where the excess oxygens order in a three-dimensional structure upon slow cooling. Lee *et al.*[179] showed that fast cooling leads to an oxygen-disordered state displaying enhanced spin-density-wave (SDW) order compared to the oxygen-ordered state. In fact, in this work it was observed that disordering the excess oxygen by quench cooling has the same enhancement effect of the SDW signal as the application of a 7.5 T field. The study in Ref. [179] did not investigate interplanar magnetic correlations, but concentrated on in-plane momentum transfers $(H, K, L = 0)$, and it therefore remains unknown how disordered oxygen ions or applied magnetic field affect the magnetic correlations between the CuO_2 planes.

Our experiments support the viewpoint that the speed of cooling has a non-trivial effect on magnetic correlations. We show that the cooling history can be important for the interplanar correlations and thereby also affect the strength of the IC signal when measured in the $L = 0$ configuration. This result is consistent with, but complementary to the conclusions of Ref. [179]. Our results demonstrate for the first time that quench-cooling produces interplanar correlations similar to those produced by a magnetic field. A possible explanation for our observation is the following; the sample might have a small amount of excess oxygen since this is not easily avoided during crystal growth and subsequent annealing. Fast cooling through the temperature regime where ordering of possible excess oxygen takes place, which occurs down to $\sim$ 180 K [180], might cause random positions of the excess oxygen ions. Such impurities could act as pinning centers enhancing the magnetic correlations between the planes.

8.7 Conclusions

We have studied the field dependence of the interplanar magnetic correlations in $La_{1.88}Sr_{0.12}CuO_4$. The primary effect of an applied magnetic field is an enhancement of the magnetic moments. Further, there is an effect of increased interplanar correlations in the presence of an applied field. The interplanar correlation length is very short and implies correlations only between neighbouring planes. The weak coupling between the CuO_2 planes will lead to short-ranged vortex-induced magnetic order, but the extremely short c-axis correlations found here points to additional effects. Certainly, the full magnetic volume fraction already in zero field indicates that there is hardly any "room" for vortices to induce coherent spin correlations along the c-axis. Instead, the vortices lead to local enhancements of the magnetic moments and presumably adapt to the many pre-existing disorder-induced pinning centers and strongly meander along c. This would lead to only very weak c-axis field-induced correlations in qualitative agreement with our observations. Within this scenario, samples with less static magnetic order in zero field, should lead to longer-ranged and more pronounced c-axis correlations in the presence of a magnetic field, which might be the reason for the larger field-induced correlation length observed for $La_{2-x}Sr_xCuO_4$ $x = 0.11$ in Ref. [144].

We observe that a fast cooling procedure results in the same feature as application of a magnetic field, namely development of weak interplanar correlations. We speculate that disorder of possible excess oxygen could lead to pinning of the magnetic order between the CuO_2 planes thereby explaining why a quench-cooled system behaves similarly as a system subjected to an external field.

Appendix A

Mean field energy in the homogeneous and paramagnetic phase

We calculate the energy:

$$F = \langle H \rangle - TS \tag{A.1}$$

with

$$S = -k_B \sum_{\mathbf{k}} [f(E_{\mathbf{k}}) \ln f(E_{\mathbf{k}}) - f(-E_{\mathbf{k}}) \ln f(-E_{\mathbf{k}})] \tag{A.2}$$

and

$$H_{\text{int}} = \frac{1}{2N} \sum_{\mathbf{k},\mathbf{k}'} (V_{lo}(\mathbf{k}-\mathbf{k}') + V_{tr}(\mathbf{k}+\mathbf{k}'))[c^{\dagger}_{k'\uparrow} c^{\dagger}_{-\mathbf{k}'\downarrow} c_{-\mathbf{k}\downarrow} c_{\mathbf{k}\uparrow} + c^{\dagger}_{\mathbf{k}'\downarrow} c^{\dagger}_{-\mathbf{k}'\uparrow} c_{-\mathbf{k}\uparrow} c_{\mathbf{k}\downarrow}] \tag{A.3}$$

In the mean field approach the interaction Hamiltonian is decoupled in the BCS channel and splitted into the singlet and triplet part.

$$\begin{aligned} H^{sing/trip}_{mf} &= \frac{1}{8N} \sum_{\mathbf{k},\mathbf{k}'} \Big[\Big(2U - V_c(\mathbf{k}-\mathbf{k}') + V_z(\mathbf{k}-\mathbf{k}') + 2V_{+-}(\mathbf{k}+\mathbf{k}') \Big) \\ &\quad \times \Big[\langle c^{\dagger}_{\mathbf{k}'\uparrow} c^{\dagger}_{-\mathbf{k}'\downarrow} \rangle \mp \langle c^{\dagger}_{\mathbf{k}'\downarrow} c^{\dagger}_{-\mathbf{k}'\uparrow} \rangle \Big] \big(c_{-\mathbf{k}\downarrow} c_{\mathbf{k}\uparrow} \mp c_{-\mathbf{k}\uparrow} c_{\mathbf{k}\downarrow} \big) + h.c. \Big] \end{aligned} \tag{A.4}$$

As shown in the previous section this mean field Hamiltonian is diagonalized yielding a dispersion:

$$E^{s/t}_{\mathbf{k}} = \pm \sqrt{\xi^2_{\mathbf{k}} + |\Delta^{s/t}_{\mathbf{k}}|^2} \tag{A.5}$$

for the singlet and triplet channel, respectively. In the mean field procedure a constant energy shift E_0 was omitted from Eq. A.4. This must be taken into account when we are interested in calculating the energy associated with the superconducting state. The energy E_0 is referred to as the condensation energy and given by:

$$\begin{aligned} E_0 &= -\frac{1}{4N} \sum_{\mathbf{k},\mathbf{k}'} [2U - V_c(\mathbf{k}-\mathbf{k}') + V_z(\mathbf{k}-\mathbf{k}') + 2V_{+-}(\mathbf{k}+\mathbf{k}')] \\ &\quad \times \Big[\langle c^{\dagger}_{\mathbf{k}'\uparrow} c^{\dagger}_{-\mathbf{k}'\downarrow} \rangle \langle c_{-\mathbf{k}\downarrow} c_{\mathbf{k}\uparrow} \rangle + \langle c^{\dagger}_{\mathbf{k}'\downarrow} c^{\dagger}_{-\mathbf{k}'\uparrow} \rangle \langle c_{-\mathbf{k}\uparrow} c_{\mathbf{k}\downarrow} \rangle \Big] \end{aligned} \tag{A.6}$$

We will express the condensation energy is terms of the singlet and triplet gaps which requires a small rewriting which goes as follows:

$$\begin{aligned}
E_0 &= -\frac{1}{4N}\sum_{\mathbf{k},\mathbf{k}'}\underbrace{[2U - V_c(\mathbf{k}-\mathbf{k}') + V_z(\mathbf{k}-\mathbf{k}') + 2V_{+-}(\mathbf{k}+\mathbf{k}')]}_{V_{pm}(\mathbf{k},\mathbf{k}')} \\
&\qquad \times\Big[\langle c^\dagger_{\mathbf{k}'\uparrow}c^\dagger_{-\mathbf{k}'\downarrow}\rangle\langle c_{-\mathbf{k}\downarrow}c_{\mathbf{k}\uparrow}\rangle + \langle c^\dagger_{\mathbf{k}'\downarrow}c^\dagger_{-\mathbf{k}'\uparrow}\rangle\langle c_{-\mathbf{k}\uparrow}c_{\mathbf{k}\downarrow}\rangle\Big] \\
&= -\frac{1}{8N}\sum_{\mathbf{k},\mathbf{k}'}V_{pm}(\mathbf{k},\mathbf{k}')\Big[\langle c^\dagger_{\mathbf{k}'\uparrow}c^\dagger_{-\mathbf{k}'\downarrow}\rangle\langle c_{-\mathbf{k}\downarrow}c_{\mathbf{k}\uparrow}\rangle + \langle c^\dagger_{\mathbf{k}'\downarrow}c^\dagger_{-\mathbf{k}'\uparrow}\rangle\langle c_{-\mathbf{k}\uparrow}c_{\mathbf{k}\downarrow}\rangle\Big] \\
&\qquad +V_{pm}(-\mathbf{k},\mathbf{k}')\Big[\langle c^\dagger_{\mathbf{k}'\uparrow}c^\dagger_{-\mathbf{k}'\downarrow}\rangle\langle c_{\mathbf{k}\downarrow}c_{-\mathbf{k}\uparrow}\rangle + \langle c^\dagger_{\mathbf{k}'\downarrow}c^\dagger_{-\mathbf{k}'\uparrow}\rangle\langle c_{\mathbf{k}\uparrow}c_{-\mathbf{k}\downarrow}\rangle\Big] \\
&= -\frac{1}{8N}\sum_{\mathbf{k},\mathbf{k}'}V_{pm}(\mathbf{k},\mathbf{k}')\Big[\tilde\Delta^*_s(\mathbf{k}')\tilde\Delta_s(\mathbf{k}) + \tilde\Delta^*_t(\mathbf{k}')\tilde\Delta_t(\mathbf{k})\Big] \\
&\qquad +V_{pm}(-\mathbf{k},\mathbf{k}')\Big[\tilde\Delta^*_s(\mathbf{k}')\tilde\Delta_s(-\mathbf{k}) + \tilde\Delta^*_t(\mathbf{k}')\tilde\Delta_t(-\mathbf{k})\Big] \\
&= -\frac{1}{8N}\sum_{\mathbf{k},\mathbf{k}'}V_{pm}(\mathbf{k},\mathbf{k}')\Big[\tilde\Delta^*_s(\mathbf{k}')\tilde\Delta_s(\mathbf{k}) + \tilde\Delta^*_t(\mathbf{k}')\tilde\Delta_t(\mathbf{k})\Big] \\
&\qquad +V_{pm}(-\mathbf{k},\mathbf{k}')\Big[\tilde\Delta^*_s(\mathbf{k}')\tilde\Delta_s(\mathbf{k}) - \tilde\Delta^*_t(\mathbf{k}')\tilde\Delta_t(\mathbf{k})\Big] \\
&= -\frac{1}{8N}\sum_{\mathbf{k},\mathbf{k}'}[V_{pm}(\mathbf{k},\mathbf{k}') + V_{pm}(-\mathbf{k},\mathbf{k}')]\tilde\Delta^*_s(\mathbf{k}')\tilde\Delta_s(\mathbf{k}) \\
&\qquad +[V_{pm}(\mathbf{k},\mathbf{k}') - V_{pm}(-\mathbf{k},\mathbf{k}')]\tilde\Delta^*_t(\mathbf{k}')\tilde\Delta_t(\mathbf{k})
\end{aligned} \tag{A.7}$$

where we have defined

$$\tilde\Delta^*_{s/t}(\mathbf{k}) = \langle c^\dagger_{\mathbf{k}\uparrow}c^\dagger_{-\mathbf{k}\downarrow}\rangle \mp \langle c^\dagger_{\mathbf{k}\downarrow}c^\dagger_{-\mathbf{k}\uparrow}\rangle \tag{A.8}$$

In the gap equation we calculate the quantity:

$$\begin{aligned}
\Delta^{s/t*}_{\mathbf{k}} &= -\frac{1}{8N}\sum_{\mathbf{k}'}[V_{pm}(\mathbf{k},\mathbf{k}') \pm V_{pm}(-\mathbf{k},\mathbf{k}')]\Big[\langle c^\dagger_{\mathbf{k}'\uparrow}c^\dagger_{-\mathbf{k}'\downarrow}\rangle \mp \langle c^\dagger_{\mathbf{k}'\downarrow}c^\dagger_{-\mathbf{k}'\uparrow}\rangle\Big] \\
&= -\frac{1}{8N}\sum_{\mathbf{k}'}[V_{pm}(\mathbf{k},\mathbf{k}') \pm V_{pm}(-\mathbf{k},\mathbf{k}')]\tilde\Delta^*_{s/t}(\mathbf{k})
\end{aligned} \tag{A.9}$$

We therefore have:

$$E_0 = \sum_{\mathbf{k}}\Big[\Delta^{s*}_{\mathbf{k}}[\langle c_{-\mathbf{k}\downarrow}c_{\mathbf{k}\uparrow}\rangle - \langle c_{-\mathbf{k}\uparrow}c_{\mathbf{k}\downarrow}\rangle] + \Delta^{t*}_{\mathbf{k}}[\langle c_{-\mathbf{k}\downarrow}c_{\mathbf{k}\uparrow}\rangle + \langle c_{-\mathbf{k}\uparrow}c_{\mathbf{k}\downarrow}\rangle]\Big] \tag{A.10}$$

From the Bogoliubov transformation:

$$c_{\mathbf{k}\uparrow} = u_{\mathbf{k}}\gamma_{\mathbf{k}\uparrow} - v_{\mathbf{k}}\gamma^\dagger_{-\mathbf{k}\downarrow} \tag{A.11}$$

$$c^\dagger_{-\mathbf{k}\downarrow} = u_{\mathbf{k}}\gamma^\dagger_{-\mathbf{k}\downarrow} + v_{\mathbf{k}}\gamma^\dagger_{\mathbf{k}\uparrow} \tag{A.12}$$

$$\tag{A.13}$$

we have

$$\langle c_{-\mathbf{k}\downarrow}c_{\mathbf{k}\uparrow}\rangle = -u_{\mathbf{k}}v_{\mathbf{k}}(1-2f(E_{\mathbf{k}})) = -\frac{\Delta^*_{\mathbf{k}}}{2E_{\mathbf{k}}}\tanh(\frac{E_{\mathbf{k}}}{2k_BT}) \tag{A.14}$$

where $\Delta_{\mathbf{k}}$ and $E_{\mathbf{k}}$ are either for the singlet or the triplet channel. For the singlet channel we get:

$$\begin{aligned}\langle c_{-\mathbf{k}\downarrow}c_{\mathbf{k}\uparrow}\rangle - \langle c_{-\mathbf{k}\uparrow}c_{\mathbf{k}\downarrow}\rangle &= \frac{-\Delta^{s*}_{\mathbf{k}} - \Delta^{s*}_{-\mathbf{k}}}{2E^s_{\mathbf{k}}}\tanh(\frac{E^s_{\mathbf{k}}}{2k_BT}) \\ &= -\frac{\Delta^{s*}_{\mathbf{k}}}{E^s_{\mathbf{k}}}\tanh(\frac{E^s_{\mathbf{k}}}{2k_BT}) \qquad \text{(A.15)}\end{aligned}$$

For the triplet channel we have:

$$\begin{aligned}\langle c_{-\mathbf{k}\downarrow}c_{\mathbf{k}\uparrow}\rangle + \langle c_{-\mathbf{k}\uparrow}c_{\mathbf{k}\downarrow}\rangle &= \frac{-\Delta^{t*}_{\mathbf{k}} + \Delta^{t*}_{-\mathbf{k}}}{2E^t_{\mathbf{k}}}\tanh(\frac{E^t_{\mathbf{k}}}{2k_BT}) \\ &= -\frac{\Delta^{t*}_{\mathbf{k}}}{E^t_{\mathbf{k}}}\tanh(\frac{E^t_{\mathbf{k}}}{2k_BT}) \qquad \text{(A.16)}\end{aligned}$$

We therefore have the condensation energy for the singlet and triplet channel respectively:

$$E^s_0 = -\sum_{\mathbf{k}}\Delta^s_{\mathbf{k}}\frac{\Delta^{s*}_{\mathbf{k}}}{E^s_{\mathbf{k}}}\tanh\left(\frac{E^s_{\mathbf{k}}}{2k_BT}\right) \qquad \text{(A.17)}$$

$$E^t_0 = -\sum_{\mathbf{k}}\Delta^t_{\mathbf{k}}\frac{\Delta^{t*}_{\mathbf{k}}}{E^t_{\mathbf{k}}}\tanh\left(\frac{E^t_{\mathbf{k}}}{2k_BT}\right) \qquad \text{(A.18)}$$

The final expression for the energy of the superconducting system is therefore:

$$F = \sum_{\mathbf{k}} E^{s/t}_{\mathbf{k}} f(E^{s/t}_{\mathbf{k}}) - \frac{|\Delta^{s/t}_{\mathbf{k}}|}{E^{s/t}_{\mathbf{k}}}\tanh\left(\frac{E^{s/t}_{\mathbf{k}}}{2k_BT}\right) + k_BT\Big[f(E^{s/t}_{\mathbf{k}})\ln[f(E^{s/t}_{\mathbf{k}})] + f(-E^{s/t}_{\mathbf{k}})\ln[f(-E^{s/t}_{\mathbf{k}})]\Big] \qquad \text{(A.19)}$$

Appendix B

Feedback effects in a homogeneous and paramagnetic system

We derive the expression for spin-fluctuation mediated pairing with feedback effects from superconductivity

$$V_{\text{eff}}(\mathbf{k},\mathbf{k}') = U + \Big[\frac{3}{2}\frac{U^2\chi_0^s(\mathbf{k}-\mathbf{k}')}{1-U\chi_0^s(\mathbf{k}-\mathbf{k}')} - \frac{1}{2}\frac{U^2\chi_0^c(\mathbf{k}-\mathbf{k}')}{1+U\chi_0^c(\mathbf{k}-\mathbf{k}')}\Big], \tag{B.1}$$

with

$$\begin{aligned} \chi_0^{s,c}(\mathbf{q},i\omega_m) &= -T\sum_{\mathbf{k},n}[G(\mathbf{k}+\mathbf{q},i\omega_n+i\omega_m)G(\mathbf{k},\omega_n) \pm F^\dagger(\mathbf{k}+\mathbf{q},i\omega_n+i\omega_m)F(\mathbf{k},i\omega_n)] \\ &= -[G_{\mathbf{q}}G \pm F^\dagger_{\mathbf{q}}F] \end{aligned} \tag{B.2}$$

The susceptibilities are stated in short hand notation:

$$G_{\mathbf{q}}G = T\sum_{\mathbf{k},n}[G(\mathbf{k}+\mathbf{q},\omega_n+\omega_m)G(\mathbf{k},\omega_n) \quad \text{and} \quad F^\dagger_{\mathbf{q}}F = T\sum_{\mathbf{k},n}[F^\dagger(\mathbf{k}+\mathbf{q},\omega_n+\omega_m)F(\mathbf{k},\omega_n)] \tag{B.3}$$

In the figures below we draw the bubble diagrams and ladder diagrams. Three species are included; those that consists of only normal Green's functions propagators, those with only anomalous propagators or lastly, those containing both normal and anomalous propagators. For all diagrams we are restricted to an even number of normal bubbles, due to the fact that U only connects opposite spin propagators.

B.1 First and second order in U

To first order the expression Eq. (B.1) simply gives $V_{\text{eff}}^{(1)} = U$ which is the usual bare interaction vertex. The second order diagrams are drawn in Fig. B.1.
Note that concerning the bubble diagrams, it is not possible to have an uneven number of normal G_qG-loops due to spin, i.e. since U is an onsite interaction it must connect fermion lines of opposite spins only. There is no such restriction for the anomalous F_qF-loops, which are effectively spin neutral and carry no overall spin. As a consequence, for all *even* order diagrams the weight of purely anomalous diagrams is always the double of the purely normal diagrams. The term arising from the first diagram of Fig. B.1 is:

$$-V_{\text{bub}}^{(2)}/(-U)^2 = \sum_p F^\dagger(\mathbf{p}+(\mathbf{k}-\mathbf{k}'))F(\mathbf{p})]. \tag{B.4}$$

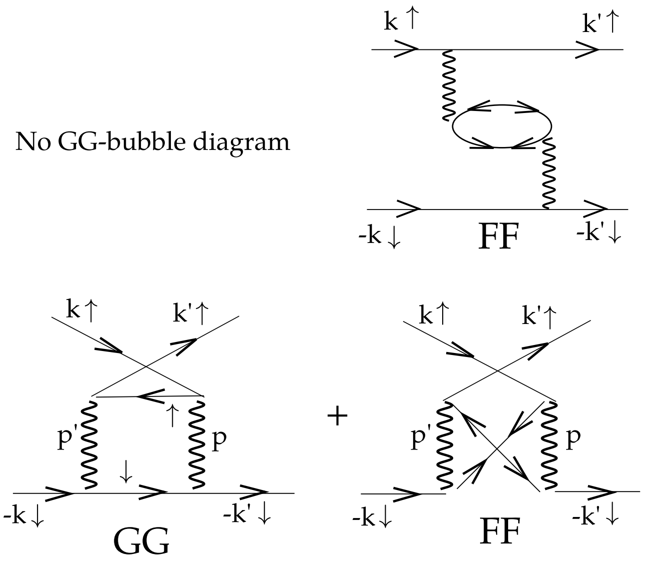

Figure B.1: Diagrams to second order. No GG bubble diagram is allowed since U only connects opposite spin propagators.

For the ladder diagram with normal propagators note that $-\mathbf{k}+\mathbf{p}'+\mathbf{p}=-\mathbf{k}'$. We get:

$$\begin{aligned}
-V^{(2)}_{\text{lad,norm}}/(-U)^2 &= \sum_{\mathbf{p}} G(\mathbf{k}-\mathbf{p})G(-\mathbf{k}+\mathbf{p}') \\
&= \sum_{\mathbf{p}} G(\mathbf{k}-\mathbf{p})G(-\mathbf{k}+\mathbf{k}-\mathbf{k}'-\mathbf{p}) \\
&= \sum_{\mathbf{p}} G(\mathbf{p})G(-\mathbf{k}-\mathbf{k}'+\mathbf{p}) \\
&= \sum_{\mathbf{p}} G(\mathbf{p}+(\mathbf{k}+\mathbf{k}'))G(\mathbf{p}). \qquad \text{(B.5)}
\end{aligned}$$

For the ladder diagram with anomalous propagators note that $\mathbf{p}=\mathbf{p}'$. We get:

$$\begin{aligned}
-V^{(2)}_{\text{lad,anom}}/(-U)^2 &= \sum_{\mathbf{p}} F^\dagger(\mathbf{k}-\mathbf{p})F(\mathbf{k}'+\mathbf{p}') \\
&= \sum_{\mathbf{p}} F^\dagger(\mathbf{k}-\mathbf{p})F(\mathbf{k}'+\mathbf{p}) \\
&= \sum_{\mathbf{p}} F^\dagger(\mathbf{k}+\mathbf{k}'-\mathbf{p})F(\mathbf{p}) \\
&= \sum_{\mathbf{p}} F^\dagger(\mathbf{p}+(\mathbf{k}+\mathbf{k}'))F(\mathbf{p}), \qquad \text{(B.6)}
\end{aligned}$$

where we have used that $F(-\mathbf{p})=F(\mathbf{p})$.
In total we get from the diagrammatic expansion above:

$$\begin{aligned}
-V^{(2)}_{\text{eff}}/(-U)^2 &= -V^{(2)}_{\text{bub}}/(-U)^2 - V^{(2)}_{\text{lad,norm}}/(-U)^2 - V^{(2)}_{\text{lad,anom}}/(-U)^2 \\
&= \sum_{p} F^\dagger(\mathbf{p}+(\mathbf{k}-\mathbf{k}'))F(\mathbf{p})] + \sum_{\mathbf{p}} G(\mathbf{p}+(\mathbf{k}+\mathbf{k}'))G(\mathbf{p}) + \sum_{\mathbf{p}} F^\dagger(\mathbf{p}+(\mathbf{k}+\mathbf{k}'))F(\mathbf{p}) \qquad \text{(B.7)}
\end{aligned}$$

Since we are only concerned with the singlet pairing expression, i.e. the Green's functions argument can be written as $\mathbf{k}-\mathbf{k}'$ instead of $\mathbf{k}+\mathbf{k}'$ and we have:

$$V_{\text{eff}}^{(2)}/U^2 \;=\; -\sum_{\mathbf{p}} G(\mathbf{p}+(\mathbf{k}-\mathbf{k}'))G(\mathbf{p}) - 2\sum_{\mathbf{p}} F^{\dagger}(\mathbf{p}+(\mathbf{k}-\mathbf{k}'))F(\mathbf{p}) \tag{B.8}$$

This agrees with the second order term derived from Eq. (B.1);

$$V_{\text{eff}}^{(2)}/U^2 = \frac{3}{2}\chi_0^s - \frac{1}{2}\chi_0^c = -[G_{\mathbf{q}}G + 2F_{\mathbf{q}}^{\dagger}F] \tag{B.9}$$

B.2 Third order in U

The third order diagrams are shown in Fig. B.2.

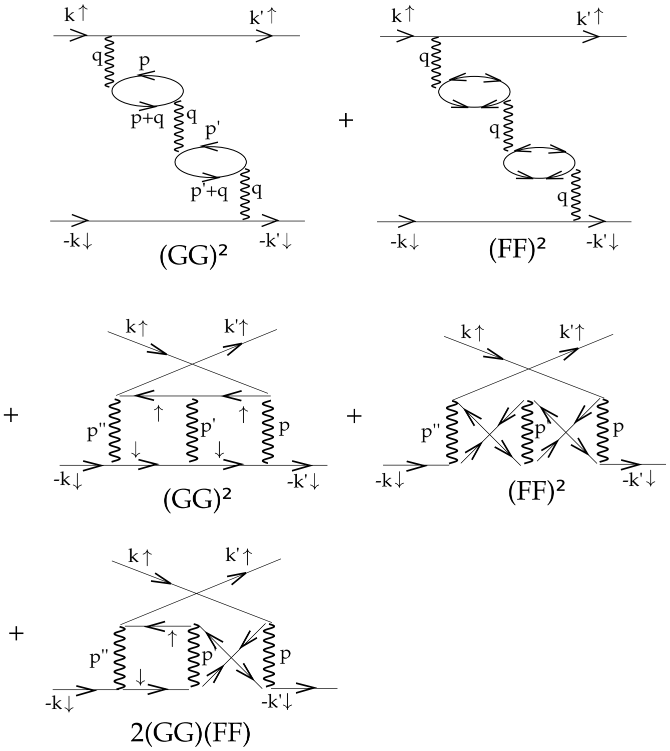

Figure B.2: Diagrams to third order in U. Due to the restriction of an even number of normal bubbles, no mixed bubble diagrams are allowed.

First, the bubble diagrams give:

$$\begin{aligned} -V_{\text{bub}}^{(3)}/(-U)^3 \;&=\; (-1)^2 \sum_{p} G(\mathbf{p}+(\mathbf{k}-\mathbf{k}'))G(\mathbf{p}) \sum_{\mathbf{p}'} G(\mathbf{p}'+(\mathbf{k}-\mathbf{k}'))G(\mathbf{p}') \\ &\quad + \sum_{\mathbf{p}} F^{\dagger}(\mathbf{p}+(\mathbf{k}-\mathbf{k}'))F(\mathbf{p}) \sum_{\mathbf{p}'} F^{\dagger}(\mathbf{p}'+(\mathbf{k}-\mathbf{k}'))F(\mathbf{p}'). \end{aligned} \tag{B.10}$$

For the normal ladder we get (note that $-\mathbf{k}' = -\mathbf{k} + \mathbf{p}'' + \mathbf{p}' + \mathbf{p}$):

$$\begin{aligned}
-V^{(3)}_{\text{lad,norm}}/(-U)^3 &= \sum_{\mathbf{p},\mathbf{p}'} G(\mathbf{k}-\mathbf{p})G(-\mathbf{k}+\mathbf{p}''+\mathbf{p}')G(\mathbf{k}-\mathbf{p}-\mathbf{p}')G(-\mathbf{k}+\mathbf{p}'') \\
&= \sum_{\mathbf{p},\mathbf{p}'} G(\mathbf{k}-\mathbf{p})G(-\mathbf{k}+\mathbf{k}-\mathbf{k}'-\mathbf{p}-\mathbf{p}'+\mathbf{p}')G(\mathbf{k}-\mathbf{p}-\mathbf{p}')G(-\mathbf{k}+\mathbf{k}-\mathbf{k}'-\mathbf{p}-\mathbf{p}') \\
&= \sum_{\mathbf{p},\mathbf{p}'} G(\mathbf{p})G(-\mathbf{k}-\mathbf{k}'+\mathbf{p})G(\mathbf{p}-\mathbf{p}')G(-\mathbf{k}-\mathbf{k}'+\mathbf{p}-\mathbf{p}') \\
&= \sum_{\mathbf{p},\mathbf{p}'} G(\mathbf{p})G(-\mathbf{k}-\mathbf{k}'+\mathbf{p})G(\mathbf{p}')G(-\mathbf{k}-\mathbf{k}'+\mathbf{p}') \\
&= \sum_{\mathbf{p}} G(\mathbf{p}+(\mathbf{k}+\mathbf{k}'))G(\mathbf{p})\sum_{\mathbf{p}'} G(\mathbf{p}'+(\mathbf{k}+\mathbf{k}'))G(\mathbf{p}'). \qquad \text{(B.11)}
\end{aligned}$$

For the anomalous ladder we get (note that now $-\mathbf{k}' - \mathbf{p}'' + \mathbf{p}' = -\mathbf{k} + \mathbf{p}$):

$$\begin{aligned}
-V^{(3)}_{\text{lad,anom}}/(-U)^3 &= \sum_{\mathbf{p},\mathbf{p}'} F^\dagger(\mathbf{k}-\mathbf{p})F(\mathbf{k}'+\mathbf{p})F^\dagger(\mathbf{k}-\mathbf{p}'')F(\mathbf{k}'+\mathbf{p}'') \\
&= \sum_{\mathbf{p},\mathbf{p}'} F^\dagger(\mathbf{k}-\mathbf{p})F(\mathbf{k}'+\mathbf{p})F^\dagger(\mathbf{k}-(\mathbf{p}'-\mathbf{p}+\mathbf{k}-\mathbf{k}'))F(\mathbf{k}'+\mathbf{p}'-\mathbf{p}+\mathbf{k}-\mathbf{k}') \\
&= \sum_{\mathbf{p},\mathbf{p}'} F^\dagger(\mathbf{k}-\mathbf{p})F(\mathbf{k}'+\mathbf{p})F^\dagger(\mathbf{p}-\mathbf{p}'+\mathbf{k}')F(\mathbf{p}'-\mathbf{p}+\mathbf{k}) \\
&= \sum_{\mathbf{p},\mathbf{p}'} F^\dagger(\mathbf{k}-\mathbf{p})F(\mathbf{k}'+\mathbf{p})F^\dagger(\mathbf{p}'+\mathbf{k}')F(-\mathbf{p}'+\mathbf{k}) \\
&= \sum_{\mathbf{p}} F^\dagger(\mathbf{p}+(\mathbf{k}+\mathbf{k}'))F(-\mathbf{p})\sum_{\mathbf{p}'} F^\dagger(\mathbf{p}'+(\mathbf{k}+\mathbf{k}'))F(-\mathbf{p}') \\
&= \sum_{\mathbf{p}} F^\dagger(\mathbf{p}+(\mathbf{k}+\mathbf{k}'))F(\mathbf{p})\sum_{\mathbf{p}'} F^\dagger(\mathbf{p}'+(\mathbf{k}+\mathbf{k}'))F(\mathbf{p}'). \qquad \text{(B.12)}
\end{aligned}$$

Lastly, the ladder diagram that contains both normal and anomalous propagators gives (note that $\mathbf{p}'' = \mathbf{p} - \mathbf{p}'$):

$$\begin{aligned}
-V^{(3)}_{\text{lad,mix}}/(-U)^3 &= \sum_{\mathbf{p},\mathbf{p}'} F^\dagger(\mathbf{k}-\mathbf{p})F(\mathbf{k}'+\mathbf{p})G(\mathbf{k}'+\mathbf{p}-\mathbf{p}')G(-\mathbf{k}+\mathbf{p}'') \\
&= \sum_{\mathbf{p},\mathbf{p}'} F^\dagger(\mathbf{k}-\mathbf{p})F(\mathbf{k}'+\mathbf{p})G(\mathbf{k}+\mathbf{p}-\mathbf{p}')G(-\mathbf{k}+\mathbf{p}-\mathbf{p}') \\
&= \sum_{\mathbf{p}} F^\dagger(\mathbf{k}-\mathbf{p})F(\mathbf{k}'+\mathbf{p})\sum_{\mathbf{p}'} G(\mathbf{k}'+\mathbf{p}')G(-\mathbf{k}+\mathbf{p}') \\
&= \sum_{\mathbf{p}} F^\dagger(\mathbf{p}+(\mathbf{k}+\mathbf{k}'))F(\mathbf{p})\sum_{\mathbf{p}'} G(\mathbf{p}'+(\mathbf{k}+\mathbf{k}'))G(\mathbf{p}'). \qquad \text{(B.13)}
\end{aligned}$$

The same expression as derived in Eq. (B.13) is obtained if we interchange the normal and anomalous propagators of the mixed ladder. In total we get from the diagrammatic expansion above:

$$\begin{aligned}
-V^{(3)}_{\text{eff}}/(-U)^3 &= -V^{(3)}_{\text{bub}}/(-U)^3 - V^{(3)}_{\text{lad,norm}}/(-U)^3 - V^{(3)}_{\text{lad,anom}} - 2V^{(3)}_{\text{lad,mix}}/(-U)^3 \\
&= (-1)^2 G_{(\mathbf{k}-\mathbf{k}')}G \cdot G_{(\mathbf{k}-\mathbf{k}')}G + F^\dagger_{(\mathbf{k}-\mathbf{k}')}F \cdot F^\dagger_{(\mathbf{k}-\mathbf{k}')}F \\
&\quad + G_{(\mathbf{k}+\mathbf{k}')}G_{(\mathbf{k}+\mathbf{k}')} \cdot G_{(\mathbf{k}+\mathbf{k}')}G_{(\mathbf{k}+\mathbf{k}')} + F^\dagger_{(\mathbf{k}+\mathbf{k}')}F \cdot F^\dagger_{(\mathbf{k}+\mathbf{k}')}F + 2F^\dagger_{(\mathbf{k}+\mathbf{k}')}F \cdot G_{(\mathbf{k}+\mathbf{k}')}G. \\
&\qquad \text{(B.14)}
\end{aligned}$$

Since we are only concerned with the singlet pairing expression, i.e. the Green's functions argument can be written as $\mathbf{k}-\mathbf{k}'$ instead of $\mathbf{k}+\mathbf{k}'$ and we have:

$$V_{\text{eff}}^{(3)}/U^3 \quad = \quad 2G_{(\mathbf{k}-\mathbf{k}')}GG_{(\mathbf{k}-\mathbf{k}')}G + 2F^{\dagger}_{(\mathbf{k}-\mathbf{k}')}FF^{\dagger}_{(\mathbf{k}-\mathbf{k}')}F + 2F^{\dagger}_{(\mathbf{k}+\mathbf{k}')}FG_{(\mathbf{k}+\mathbf{k}')}G. \tag{B.15}$$

This agrees with the third order term derived from Eq. (B.1);

$$V_{\text{eff}}^{(3)} = U^3[2(G_{\mathbf{q}}G)^2 + 2(F^{\dagger}_{\mathbf{q}}F)^2 + 2(G_{\mathbf{q}}G)(F^{\dagger}_{\mathbf{q}}F)] \tag{B.16}$$

Note that all terms have the same overall sign. This is because all fermion loops enter as a product of two, whereby the signs cancel.

B.3 Fourth order in U

All diagrams to fourth order are shown in Fig. B.3. Since these diagrams are an even order in U, the contribution from purely anomalous diagrams has double weigth than the contribution from the purely normal diagrams. Evaluation of the bubble diagrams is straightforward, since each bubble has its own internal index. We get no contribution for normal propagators only, since we cannot have an uneven

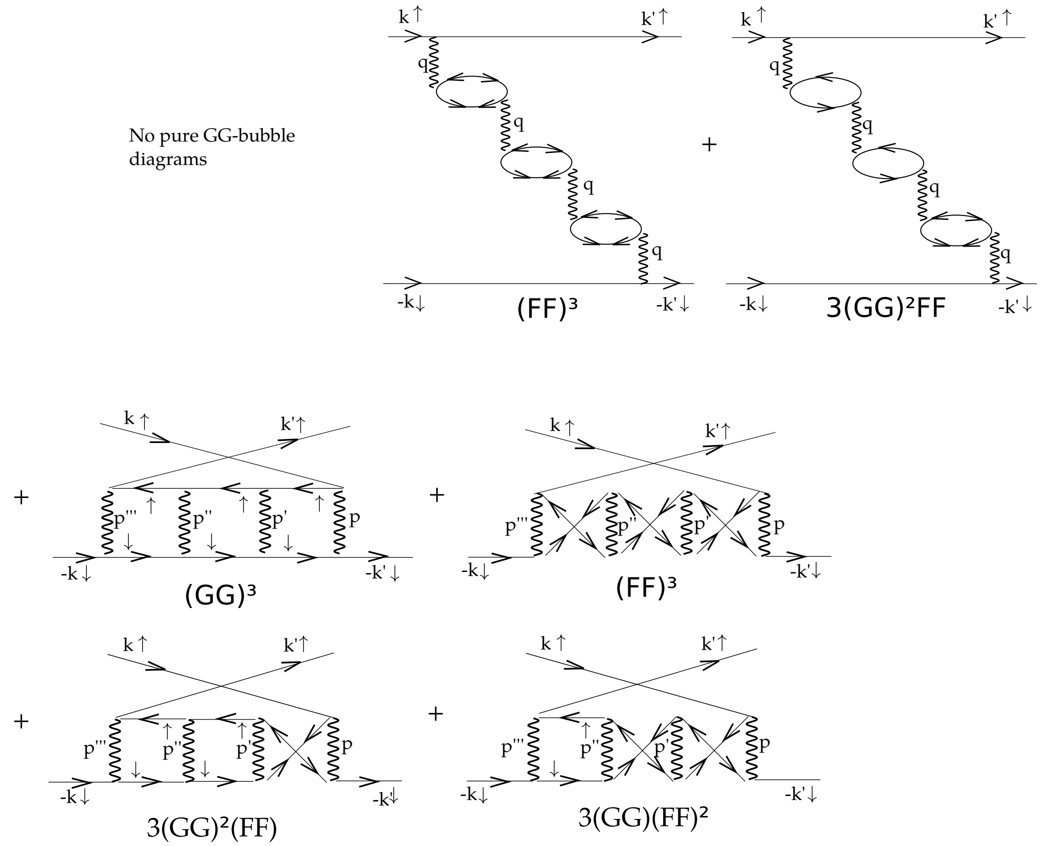

Figure B.3: Diagrams to fourth order. Note that due to spin conservation it is not possible to construct a bubble diagram consisting of normal propagators only. This causes the unequal weight of contributions from diagrams with normal propagators only compared to those with anomalous propagators only. This arises for all even order diagrams.

number of bubbles. For the anomalous bubbles we get:

$$-V^{(4)}_{\text{bub,anom}}/(-U)^4 = \sum_p F^\dagger(p+(k-k'))F(p)\sum_{p'} F^\dagger(p'+(k-k'))F(p')\sum_{p''} F^\dagger(p''+(k-k'))F(p''). \tag{B.17}$$

For mixed bubbles we get:

$$-V^{(4)}_{\text{bub,mix}}/(-U)^4 = \sum_p G(p+(k-k'))G(p)\sum_{p'} G(p'+(k-k'))G(p')\sum_{p''} F^\dagger(p''+(k-k'))F(p'') \tag{B.18}$$

For the ladder diagrams consisting of only normal propagators we have:

$$\begin{aligned} - \quad & V^{(4)}_{\text{lad,norm}}/(-U)^4 \\ &= \sum_{p,p',p''} G(k-p)G(-k'-p)G(k-p-p')G(-k'-p-p')G(k-p-p'-p'')G(-k'-p-p'-p'') \\ &= \sum_p G(p+(k+k'))G(p)\sum_{p'} G(p'+(k+k'))G(p')\sum_{p''} G(p''+(k+k'))G(p''). \end{aligned} \tag{B.19}$$

The last index p''' if Fig. B.3 is superfluous since $k' = k - p - p' - p'' - p'''$.
For the ladder consisting of only anomalous propagators we note that from the last upper vertex $k' + p - p' + p'' - p''' = k'$, i.e. $p''' = p - p' + p''$. We get:

$$\begin{aligned} - \quad & V^{(4)}_{\text{lad,anom}}/(-U)^4 \\ &= \sum_{p,p',p''} F^\dagger(k-p)F(k'+p)F^\dagger(k'+p-p')F(-k+p-p')F^\dagger(-k+p-p'-p'')F(k'+p-p'+p'') \\ &= \sum_p F^\dagger(p+(k+k'))F(p)\sum_{p'} F^\dagger(p'+(k+k'))F(p')\sum_{p''} F^\dagger(p''+(k+k'))F(p''). \end{aligned} \tag{B.20}$$

For the ladder diagram containing two crosses we get:

$$\begin{aligned} - \quad & V^{(4)}_{\text{lad,mix}}/(-U)^4 \\ &= \sum_{p,p',p''} G(k-p)G(-k'-p)F^\dagger(k-p-p')F(k'+p+p')F^\dagger(k'+p+p'-p'')F(k-p-p'+p'') \\ &= \sum_{p,p',p''} G(k+p)G(-k'+p)F^\dagger((k+k')-p-p')F(p+p')F^\dagger(p+p'-p''+(k+k))F(p''-p-p') \\ &= \sum_p G(p+(k+k'))G(p)\sum_{p'} F^\dagger(p'+(k+k'))F(p')\sum_{p''} F^\dagger(p''+(k+k))F(p''). \end{aligned} \tag{B.21}$$

For the ladder diagram containing one cross we get, using the labeling as in Fig. B.3:

$$\begin{aligned} - \quad & V^{(4)}_{\text{lad,mix}}/(-U)^4 \\ &= \sum_{p,p',p''} F^\dagger(k-p)F(k'+p)G(k'+p-p')G(-k+p-p')G(k'+p-p'-p'')G(-k+p-p'-p'') \\ &= \sum_p F^\dagger(p+(k+k'))F(p)\sum_{p'} G(p'+(k+k'))G(p')\sum_{p''} G(p''+(k+k'))G(p''). \end{aligned} \tag{B.22}$$

If the cross is placed in one of the other two positions, the same expression is obtained. In conclusion we have:

$$V_{\text{eff}}^{(4)} = -U^4[(G_qG)^3 + 2(F_q^\dagger F)^3 + 6(G_qG)^2(F_q^\dagger F) + 3(G_qG)(F_q^\dagger F)^2] \tag{B.23}$$

which is the same results as obtained from the full expression in Eq. (B.1) expanded to fourth order.

B.4 Fifth order in U

The expression to fifth order in U is given by:

$$V_{\text{eff}}^{(5)} = U^5[2(G_qG)^4 + 2(F_qF)^4 + 12(G_qG)^2(F_qF)^2 + 4(G_qG)^3(F_qF) + 4(G_qG)(F_qF)^3] \tag{B.24}$$

In Eq. (B.24), the first two terms are bubble and ladder diagrams which are un-mixed, i.e. either only normal or anomalous propagators. The third term corresponds to $6 = \binom{4}{2}$ bubble diagrams and 6 ladder diagrams where both types of propagators are present, and where there is an equal number of normal and anomalous propagators, i.e. two bubbles and two crosses. The two last terms correspond to ladder diagrams with one or three crosses, respectively.

To recapitulate, we get an effective pairing vertex from the diagrammatic expansion of the form:

$$\begin{aligned}
-V_{\text{eff}} &= (-U)^2[G_{\mathbf{q}}G + 2F_{\mathbf{q}}F] \\
&\quad +(-U)^3[2(G_{\mathbf{q}}G)^2 + 2(F_{\mathbf{q}}F)^2 + 2(G_{\mathbf{q}}G)(F_{\mathbf{q}}F)] \\
&\quad +(-U)^4[(G_{\mathbf{q}}G)^3 + 2(F_{\mathbf{q}}F)^3 + 3(G_{\mathbf{q}}G)(F_{\mathbf{q}}F)^2 + 6(G_{\mathbf{q}}G)^2(F_{\mathbf{q}}F)] \\
&\quad +\dots \\
&\quad \Updownarrow \\
V_{\text{eff}} &= -U^2[G_{\mathbf{q}}G + 2F_{\mathbf{q}}F] \\
&\quad +U^3[2(G_{\mathbf{q}}G)^2 + 2(F_{\mathbf{q}}F)^2 + 2(G_{\mathbf{q}}G)(F_{\mathbf{q}}F)] \\
&\quad -U^4[(G_{\mathbf{q}}G)^3 + 2(F_{\mathbf{q}}F)^3 + 3(G_{\mathbf{q}}G)(F_{\mathbf{q}}F)^2 + 6(G_{\mathbf{q}}G)^2(F_{\mathbf{q}}F)] \\
&\quad +\dots
\end{aligned} \tag{B.25}$$

This is compared to Eq. (B.1) expanded to fifth order in U:

$$\begin{aligned}
V_{\text{eff}} &= U + \frac{3U^2}{2}[\chi_0^s(1 + U\chi_0^s + (U\chi_0^s)^2 + (U\chi_0^s)^3 + \cdots] - \frac{U^2}{2}\chi_0^c(1 - U\chi_0^c + (U\chi_0^c)^2 - (U\chi_0^c)^3 + \cdots) \\
&= -U^2[G_{\mathbf{q}}G + 2F_{\mathbf{q}}F] \\
&\quad +U^3[2(G_{\mathbf{q}}G)^2 + 2(F_{\mathbf{q}}F)^2 + 2(G_{\mathbf{q}}G)(F_{\mathbf{q}}F)] \\
&\quad -U^4[(G_{\mathbf{q}}G)^3 + 2(F_{\mathbf{q}}F)^3 + 3(G_{\mathbf{q}}G)(F_{\mathbf{q}}F)^2 + 6(G_{\mathbf{q}}G)^2(F_{\mathbf{q}}F)] \\
&\quad +U^5[2(G_{\mathbf{q}}G)^4 + 2(F_{\mathbf{q}}F)^4 + 12(G_{\mathbf{q}}G)^2(F_{\mathbf{q}}F)^2 + 4(G_{\mathbf{q}}G)^3(F_{\mathbf{q}}F) + 4(G_{\mathbf{q}}G)(F_{\mathbf{q}}F)^3] \\
&\quad -\dots
\end{aligned} \tag{B.26}$$

We conclude that the diagrammatic expansion gives the same result as the expression by Pao and Bickers [77] as stated in Eq. (B.1). We have suppressed the internal structure of the momentum indices, since we are only concerned with the singlet channel. However, if triplet pairing is to be considered, the derivation should be kept general and the susceptibility dependence on either $\mathbf{k} - \mathbf{k}'$ (bubble diagrams) or $\mathbf{k} + \mathbf{k}'$ (ladder diagrams) must be stated explicitly.

Appendix C

Supplementary material for the coexistence phase

C.1 Derivation of the interaction Hamiltonian in the transverse channel

Below we discuss how the interaction Hamiltonian in the transverse channel can be expressed in terms of a spin-flip interaction Hamiltonian, and how this is equivalent to the usual representation of a non-spin flip form. First we show the arguments starting from a real space representation of the interaction.

For interactions through transverse spin fluctuations the Hamiltonian is written in the form:

$$H^{tr} = -\frac{1}{2}\sum_{i,j}\sum_{\sigma} V_{\mathrm{tr}}(i,j) c^{\dagger}_{i\sigma} c^{\dagger}_{j\overline{\sigma}} c_{j\sigma} c_{i\overline{\sigma}} \qquad \text{(spin flip)} \tag{C.1}$$

Note the spin-flip order of the c-operators. The interaction Hamiltonian is uniquely defined in such a way that it reduces to the original Hubbard Hamiltonian in the limit $V = U\delta_{i,j}$.

In the homogeneous system we want to express the interaction Hamiltonians is reciprocal space. This can be done either by Fourier transformation of the real space formulation given in Eq. (C.1) or by evaluation of the diagrams in reciprocal space. In the first approach we get:

$$\begin{aligned}
H^{tr} &= -\frac{1}{2}\sum_{i,j}\sum_{\sigma} V_{+-}(i,j) c^{\dagger}_{i\sigma} c^{\dagger}_{j\overline{\sigma}} c_{j\sigma} c_{i\overline{\sigma}} \\
&= -\frac{1}{2N^3}\sum_{i,j}\sum_{\mathbf{k},\mathbf{k}',\mathbf{p},\mathbf{p}',\mathbf{q}}\sum_{\sigma} V(\mathbf{q}) e^{i\mathbf{q}\cdot(\mathbf{r}_i-\mathbf{r}_j)} e^{i\mathbf{k}\cdot\mathbf{r}_i} e^{i\mathbf{k}'\cdot\mathbf{r}_j} e^{-i\mathbf{p}\cdot\mathbf{r}_j} e^{-i\mathbf{p}'\cdot\mathbf{r}_i} c^{\dagger}_{\mathbf{k}\sigma} c^{\dagger}_{\mathbf{k}'\overline{\sigma}} c_{\mathbf{p}\sigma} c_{\mathbf{p}'\overline{\sigma}} \qquad \text{(C.2)} \\
&= -\frac{1}{2N}\sum_{\mathbf{k},\mathbf{k}',\mathbf{q}}\sum_{\sigma} V_{+-}(\mathbf{k}-\mathbf{k}') c^{\dagger}_{\mathbf{k}'\sigma} c^{\dagger}_{-\mathbf{k}'+\mathbf{q}\overline{\sigma}} c_{-\mathbf{k}+\mathbf{q}\sigma} c_{\mathbf{k}\overline{\sigma}} \qquad \text{(C.3)} \\
&= \frac{1}{2N}\sum_{\mathbf{k},\mathbf{k}',\mathbf{q}}\sum_{\sigma} V_{+-}(\mathbf{k}-\mathbf{k}') c^{\dagger}_{\mathbf{k}'\sigma} c^{\dagger}_{-\mathbf{k}'+\mathbf{q}\overline{\sigma}} c_{\mathbf{k}\overline{\sigma}} c_{-\mathbf{k}+\mathbf{q}\sigma} \\
&= \frac{1}{2N}\sum_{\mathbf{k},\mathbf{k}',\mathbf{q}}\sum_{\sigma} V_{+-}(\mathbf{k}+\mathbf{k}') c^{\dagger}_{\mathbf{k}'\sigma} c^{\dagger}_{-\mathbf{k}'+\mathbf{q}\overline{\sigma}} c_{-\mathbf{k}\overline{\sigma}} c_{\mathbf{k}+\mathbf{q}\sigma} \qquad \text{(C.4)}
\end{aligned}$$

with $V_{+-}(\mathbf{q}) = \frac{U^2\chi_0^{+-}(\mathbf{q})}{1-U\chi_0^{+-}(\mathbf{q})}$. As shown above, basic manipulations allow us to express the transverse interaction either as a spin flip, Eq. (C.3), or as a non-spin flip interaction, Eq. (C.4). Both formulations of the interaction gives the same result of the superconducting gap. This is due to the explicit symmetrization into singlet and triplet superconducting gap, which appears directly in the derivation of the gap equation. Therefore the two representations are equivalent.

We can also derive the two Hamiltonian forms directly from the diagrammatics in reciprocal space. We have a general form of the interaction Hamiltonian:

$$H_{\text{int}} = \sum_{k_1,k_2,k_3,k_4} V(k_1,k_2,k_3,k_4) c^{\dagger}_{k_4\uparrow} c^{\dagger}_{k_3\downarrow} c_{k_2\downarrow} c_{k_1\uparrow} + h.c. \tag{C.5}$$

This we draw in the following way:

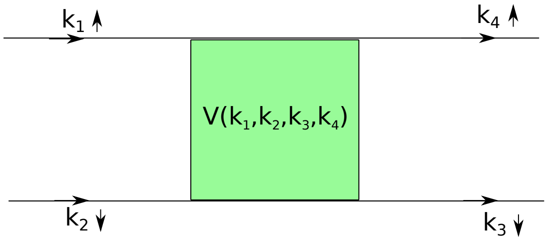

Figure C.1: We draw the vertex as a non-spin flipper, since the bare Coulomb interaction does not give rise to a spin flip.

Due to momentum conservation we have only three free momenta, which we will name $\mathbf{k}, \mathbf{k}'$ and $\mathbf{q}$ in the following. The specific relabeling of $\mathbf{k}_1$,$\mathbf{k}_2$,$\mathbf{k}_3$ and $\mathbf{k}_4$ will be shown explicitly below.

We start by the bare Coulomb interaction which can be written as:

$$H_{bare} = \frac{1}{2N} \sum_{\mathbf{k},\mathbf{k}',\mathbf{q}} U c^{\dagger}_{\mathbf{k}'\downarrow} c^{\dagger}_{-\mathbf{k}'+\mathbf{q}\downarrow} c_{-\mathbf{k}+\mathbf{q}\downarrow} c_{\mathbf{k}\uparrow} + h.c. \tag{C.6}$$

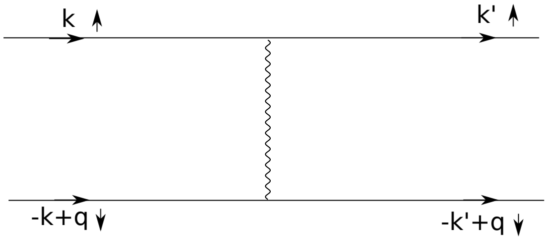

Figure C.2: Bare U interaction diagram.

C.1.1 Ladder diagrams

The interaction Hamiltonian can be written as:

$$H_{tr} = \frac{1}{2N} \sum_{\mathbf{k},\mathbf{k}',\mathbf{q}} V_{\text{tr}}(\mathbf{k},\mathbf{k}',\mathbf{q}) c^{\dagger}_{\mathbf{k}'\uparrow} c^{\dagger}_{-\mathbf{k}'+\mathbf{q}\downarrow} c_{\mathbf{k}\downarrow} c_{-\mathbf{k}+\mathbf{q}\uparrow} + h.c. \tag{C.7}$$

By interchanging the last two operators we obtain:

$$H_{tr} = -\frac{1}{2N} \sum_{\mathbf{k},\mathbf{k}',\mathbf{q}} V_{\text{tr}}(\mathbf{k},\mathbf{k}',\mathbf{q}) c^{\dagger}_{\mathbf{k}'\uparrow} c^{\dagger}_{-\mathbf{k}'+\mathbf{q}\downarrow} c_{-\mathbf{k}+\mathbf{q}\uparrow} c_{\mathbf{k}\downarrow} + h.c. \tag{C.8}$$

The latter way of writing is to show that the interaction can be considered a spin-flip process. In labeling of the vertex of the diagrammatics we must use the form given in Eqn. (C.7) to have the overall sign and spin-indices agreeing with the general form of the interaction Hamiltonian. This gives the diagram:

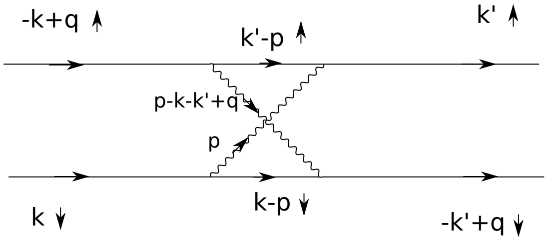

Figure C.3: Ladder interaction diagram second order. Labelling of interaction vertices corresponds to the form of the interaction Hamiltonian stated in Eqn. (C.7).

Evaluation of the interaction vertex gives:

$$\begin{aligned}
-V_{tr}(\mathbf{k},\mathbf{k}',\mathbf{q}) &= (-U)^2 \sum_{\mathbf{p}} G_\uparrow(\mathbf{k}'-\mathbf{p},\tau) G_\downarrow(\mathbf{k}-\mathbf{p},-\tau) \\
&= U^2 \sum_{\mathbf{p}} G_\uparrow(\mathbf{p}+\mathbf{k}',\tau) G_\downarrow(\mathbf{p}+\mathbf{k},-\tau) \\
&= U^2 \sum_{\mathbf{p}} G_\uparrow(\mathbf{p},\tau) G_\downarrow(\mathbf{p}+(\mathbf{k}-\mathbf{k}'),-\tau) \\
&= -U^2 [-\sum_{\mathbf{p}} G_\uparrow(\mathbf{p},\tau) G_\downarrow(\mathbf{p}+(\mathbf{k}-\mathbf{k}'),-\tau)] \\
&= -U^2 \chi^0_{+-}(\mathbf{k}-\mathbf{k}') \qquad \text{(C.9)}
\end{aligned}$$

The interaction Hamiltonian in the transverse channel to second order is therefore:

$$\begin{aligned}
H_{tr} &= \frac{1}{2N} \sum_{\mathbf{k},\mathbf{k}',\mathbf{q}} U^2 \chi_0^{+-}(\mathbf{k}-\mathbf{k}') c^\dagger_{\mathbf{k}'\uparrow} c^\dagger_{-\mathbf{k}'+\mathbf{q}\downarrow} c_{\mathbf{k}\downarrow} c_{-\mathbf{k}+\mathbf{q}\uparrow} + h.c. \\
&= -\frac{1}{2N} \sum_{\mathbf{k},\mathbf{k}',\mathbf{q}} U^2 \chi_0^{+-}(\mathbf{k}-\mathbf{k}') c^\dagger_{\mathbf{k}'\uparrow} c^\dagger_{-\mathbf{k}'+\mathbf{q}\downarrow} c_{-\mathbf{k}+\mathbf{q}\uparrow} c_{\mathbf{k}\downarrow} + h.c. \qquad \text{(C.10)}
\end{aligned}$$

We could also have taken a different representation of the interaction Hamiltonian (the non-spin flip version):

$$H_{tr} = \frac{1}{2N} \sum_{\mathbf{k},\mathbf{k}',\mathbf{q}} V_{\mathrm{tr}}(\mathbf{k},\mathbf{k}',\mathbf{q}) c^\dagger_{\mathbf{k}'\uparrow} c^\dagger_{-\mathbf{k}'+\mathbf{q}\downarrow} c_{-\mathbf{k}\downarrow} c_{\mathbf{k}+\mathbf{q}\uparrow} + h.c. \qquad \text{(C.11)}$$

The corresponding diagrammatics would then take the form:
Evaluation of the interaction vertex gives:

$$\begin{aligned}
-V_{tr}(\mathbf{k},\mathbf{k}',\mathbf{q}) &= (-U)^2 \sum_{\mathbf{p}} G_\uparrow(\mathbf{k}'-\mathbf{p},\tau) G_\downarrow(-\mathbf{k}-\mathbf{p},-\tau) \\
&= U^2 \sum_{\mathbf{p}} G_\uparrow(\mathbf{p}+\mathbf{k}',\tau) G_\downarrow(\mathbf{p}-\mathbf{k},-\tau) \\
&= -U^2 [-\sum_{\mathbf{p}} G_\uparrow(\mathbf{p}+(\mathbf{k}+\mathbf{k}'),\tau) G_\downarrow(\mathbf{p},-\tau)] \\
&= -U^2 \chi^0_{+-}(\mathbf{k}+\mathbf{k}') \qquad \text{(C.12)}
\end{aligned}$$

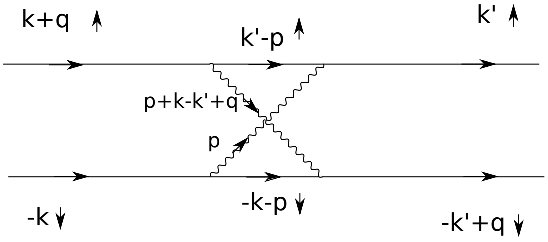

Figure C.4: Ladder interaction diagram second order. Labelling of interaction vertices corresponds to the form of the interaction Hamiltonian stated in Eqn. (C.11).

In this case we end up with the final interaction Hamiltonian to second order:

$$H_{tr} = \frac{1}{2N} \sum_{\mathbf{k},\mathbf{k}',\mathbf{q}} U^2 \chi^0_{+-}(\mathbf{k}+\mathbf{k}') c^\dagger_{\mathbf{k}'\uparrow} c^\dagger_{-\mathbf{k}'+\mathbf{q}\downarrow} c_{-\mathbf{k}\downarrow} c_{\mathbf{k}+\mathbf{q}\uparrow} + h.c. \tag{C.13}$$

The effort of this section was done to resolve an apparent discrepancy in the momentum index – is it $V(\mathbf{k}-\mathbf{k}')$ or $V(\mathbf{k}+\mathbf{k}')$?– of the pairing through transverse fluctuations. In brief, the only thing we have been doing is playing around with labeling of the interaction Hamiltonians. This should not change anything for the real spin-fluctuation mediated pairing between electrons and the symmetry of the pairing state which is achieved by this pairing interaction. And it does not! The reason is connected to the fact that the spin ordering of the c-operators are different in each representation of the interaction Hamiltonian. Both forms turn out to give the same superconducting gap solutions in the singlet and triplet channel, but the interaction must by symmetrized/antisymmetrized properly. This is the remedy for the apparent discrepancy.

C.2 Interaction Hamiltonian in the SDW phase

Here we derive the interaction Hamiltonians due to spin-fluctuated mediated pairing expressed in terms of the eigenstates of the SDW phase. We show the details of the derivation for the transverse interaction Hamiltonian. The longitudinal interaction Hamiltonian is derived in the same way. First we start with the form spin-flip formulation of the transverse interaction Hamiltonian given in Eq. C.3:

$$\begin{aligned}
H^{tr} &= -\frac{1}{2N}\sum_{k,k',q}\sum_{\sigma} V_{+-}(k-k')c^{\dagger}_{k'\sigma}c^{\dagger}_{-k'+q\overline{\sigma}}c_{-k+q\sigma}c_{k\overline{\sigma}} && \text{(transform } k \text{ and } k' \text{ sum to the primed sum of rBZ)}\\
&= -\frac{1}{2N}\sum_{k,k'}^{\prime}\sum_{q}\sum_{\sigma}\Big[V_{+-}(k-k')c^{\dagger}_{k'\sigma}c^{\dagger}_{-k'+q\overline{\sigma}}c_{-k+q\sigma}c_{k\overline{\sigma}} && \text{for } (k,k')\\
&\qquad +V_{+-}(k-k'+Q)c^{\dagger}_{k'+Q\sigma}c^{\dagger}_{-k'+Q+q\overline{\sigma}}c_{-k+q\sigma}c_{k\overline{\sigma}} && \text{for } (k,k'+Q)\\
&\qquad +V_{+-}(k-k'+Q)c^{\dagger}_{k'\sigma}c^{\dagger}_{-k'+q\overline{\sigma}}c_{-k+Q+q\sigma}c_{k+Q\overline{\sigma}} && \text{for } (k+Q,k')\\
&\qquad +V_{+-}(k-k')c^{\dagger}_{k'+Q\sigma}c^{\dagger}_{-k'+Q+q\overline{\sigma}}c_{-k+Q+q\sigma}c_{k+Q\overline{\sigma}}\Big] && \text{for } (k+Q,k')\\
&= -\frac{1}{2N}\sum_{k,k'}^{\prime}\sum_{\sigma}\Big[V_{+-}(k-k')c^{\dagger}_{k'\sigma}c^{\dagger}_{-k'\overline{\sigma}}c_{-k\sigma}c_{k\overline{\sigma}} && \text{(restrict q-sum to only } q=0 \text{ and } q=Q)\\
&\qquad +V_{+-}(k-k'+Q)c^{\dagger}_{k'+Q\sigma}c^{\dagger}_{-k'+Q\overline{\sigma}}c_{-k\sigma}c_{k\overline{\sigma}}\\
&\qquad +V_{+-}(k-k'+Q)c^{\dagger}_{k'\sigma}c^{\dagger}_{-k'\overline{\sigma}}c_{-k+Q\sigma}c_{k+Q\overline{\sigma}}\\
&\qquad +V_{+-}(k-k')c^{\dagger}_{k'+Q\sigma}c^{\dagger}_{-k'+Q\overline{\sigma}}c_{-k+Q\sigma}c_{k+Q\overline{\sigma}}\\
&\qquad +V_{+-}(k-k')c^{\dagger}_{k'\sigma}c^{\dagger}_{-k'+Q\overline{\sigma}}c_{-k+Q\sigma}c_{k\overline{\sigma}}\\
&\qquad +V_{+-}(k-k'+Q)c^{\dagger}_{k'+Q\sigma}c^{\dagger}_{-k'\overline{\sigma}}c_{-k+Q\sigma}c_{k\overline{\sigma}}\\
&\qquad +V_{+-}(k-k'+Q)c^{\dagger}_{k'\sigma}c^{\dagger}_{-k'+Q\overline{\sigma}}c_{-k\sigma}c_{k+Q\overline{\sigma}}\\
&\qquad +V_{+-}(k-k')c^{\dagger}_{k'+Q\sigma}c^{\dagger}_{-k'\overline{\sigma}}c_{-k\sigma}c_{k+Q\overline{\sigma}}\Big]
\end{aligned} \tag{C.14}$$

$$\begin{aligned}
H^{tr} = -\frac{1}{2N}\sum_{k,k'}^{\prime}\sum_{\sigma}\Big[&V_{+-}(k-k')\Big\{(u_{k'}\alpha^{\dagger}_{k'\sigma}+v_{k'}\beta^{\dagger}_{k'\sigma})(u_{k'}\alpha^{\dagger}_{-k'\overline{\sigma}}+v_{k'}\beta^{\dagger}_{-k'\overline{\sigma}})(u_k\alpha_{-k\sigma}+v_k\beta_{-k\sigma})(u_k\alpha_{k\overline{\sigma}}+v_k\beta_{k\overline{\sigma}})\\
&+(v_{k'}\alpha^{\dagger}_{k'\sigma}-u_{k'}\beta^{\dagger}_{k'\sigma})(v_{k'}\alpha^{\dagger}_{-k'\overline{\sigma}}-u_{k'}\beta^{\dagger}_{-k'\overline{\sigma}})(v_k\alpha_{-k\sigma}-u_k\beta_{-k\sigma})(v_k\alpha_{k\overline{\sigma}}-u_k\beta_{k\overline{\sigma}})\\
&-(u_{k'}\alpha^{\dagger}_{k'\sigma}+v_{k'}\beta^{\dagger}_{k'\sigma})(v_{k'}\alpha^{\dagger}_{-k'\overline{\sigma}}-u_{k'}\beta^{\dagger}_{-k'\overline{\sigma}})(v_k\alpha_{-k\sigma}-u_k\beta_{-k\sigma})(u_k\alpha_{k\overline{\sigma}}+v_k\beta_{k\overline{\sigma}})\\
&-(v_{k'}\alpha^{\dagger}_{k'\sigma}-u_{k'}\beta^{\dagger}_{k'\sigma})(u_{k'}\alpha^{\dagger}_{-k'\overline{\sigma}}+v_{k'}\beta^{\dagger}_{-k'\overline{\sigma}})(u_k\alpha_{-k\sigma}+v_k\beta_{-k\sigma})(v_k\alpha_{k\overline{\sigma}}-u_k\beta_{k\overline{\sigma}})\Big\}\\
+V_{+-}(k-k'+Q)\Big\{&-(v_{k'}\alpha^{\dagger}_{k'\sigma}-u_{k'}\beta^{\dagger}_{k'\sigma})(v_{k'}\alpha^{\dagger}_{-k'\overline{\sigma}}-u_{k'}\beta^{\dagger}_{-k'\overline{\sigma}})(u_k\alpha_{-k\sigma}+v_k\beta_{-k\sigma})(u_k\alpha_{k\overline{\sigma}}+v_k\beta_{k\overline{\sigma}})\\
&-(u_{k'}\alpha^{\dagger}_{k'\sigma}+v_{k'}\beta^{\dagger}_{k'\sigma})(u_{k'}\alpha^{\dagger}_{-k'\overline{\sigma}}+v_{k'}\beta^{\dagger}_{-k'\overline{\sigma}})(v_k\alpha_{-k\sigma}-u_k\beta_{-k\sigma})(v_k\alpha_{k\overline{\sigma}}-u_k\beta_{k\overline{\sigma}})\\
&+(v_{k'}\alpha^{\dagger}_{k'\sigma}-u_{k'}\beta^{\dagger}_{k'\sigma})(u_{k'}\alpha^{\dagger}_{-k'\overline{\sigma}}+v_{k'}\beta^{\dagger}_{-k'\overline{\sigma}})(v_k\alpha_{-k\sigma}-u_k\beta_{-k\sigma})(u_k\alpha_{k\overline{\sigma}}+v_k\beta_{k\overline{\sigma}})\\
&+(u_{k'}\alpha^{\dagger}_{k'\sigma}+v_{k'}\beta^{\dagger}_{k'\sigma})(v_{k'}\alpha^{\dagger}_{-k'\overline{\sigma}}-u_{k'}\beta^{\dagger}_{-k'\overline{\sigma}})(u_k\alpha_{-k\sigma}+v_k\beta_{-k\sigma})(v_k\alpha_{k\overline{\sigma}}-u_k\beta_{k\overline{\sigma}})\Big\}\Big]
\end{aligned} \tag{C.15}$$

Restricting to intrapocket Cooper pairs only:

$$
\begin{aligned}
H^{tr} = & -\frac{1}{2N}\sideset{}{'}\sum_{k,k'}\sum_{\sigma}\Big[V_{+-}(k-k')\Big\{(u_{k'}^2\alpha^\dagger_{k'\sigma}\alpha^\dagger_{-k'\overline{\sigma}}+v_{k'}^2\beta^\dagger_{k'\sigma}\beta^\dagger_{-k'\overline{\sigma}})(u_k^2\alpha_{-k\sigma}\alpha_{k\overline{\sigma}}+v_k^2\beta_{-k\sigma}\beta_{k\overline{\sigma}})\\
&+(v_{k'}^2\alpha^\dagger_{k'\sigma}\alpha^\dagger_{-k'\overline{\sigma}}+u_{k'}^2\beta^\dagger_{k'\sigma}\beta^\dagger_{-k'\overline{\sigma}})(v_k^2\alpha_{-k\sigma}\alpha_{k\overline{\sigma}}+u_k^2\beta_{-k\sigma}\beta_{k\overline{\sigma}})\\
&-(u_{k'}v_{k'}\alpha^\dagger_{k'\sigma}\alpha^\dagger_{-k'\overline{\sigma}}-u_{k'}v_{k'}\beta^\dagger_{k'\sigma}\beta^\dagger_{-k'\overline{\sigma}})(u_kv_k\alpha_{-k\sigma}\alpha_{k\overline{\sigma}}-u_kv_k\beta_{-k\sigma}\beta_{k\overline{\sigma}})\\
&-(u_{k'}v_{k'}\alpha^\dagger_{k'\sigma}\alpha^\dagger_{-k'\overline{\sigma}}-u_{k'}v_{k'}\beta^\dagger_{k'\sigma}\beta^\dagger_{-k'\overline{\sigma}})(u_kv_k\alpha_{-k\sigma}\alpha_{k\overline{\sigma}}-u_kv_k\beta_{-k\sigma}\beta_{k\overline{\sigma}})\Big\}\\
&+V_{+-}(k-k'+Q)\Big\{-(v_{k'}^2\alpha^\dagger_{k'\sigma}\alpha^\dagger_{-k'\overline{\sigma}}+u_{k'}^2\beta^\dagger_{k'\sigma}\beta^\dagger_{-k'\overline{\sigma}})(u_k^2\alpha_{-k\sigma}\alpha_{k\overline{\sigma}}+v_k^2\beta_{-k\sigma}\beta_{k\overline{\sigma}})\\
&-(u_{k'}^2\alpha^\dagger_{k'\sigma}\alpha^\dagger_{-k'\overline{\sigma}}+v_{k'}^2\beta^\dagger_{k'\sigma}\beta^\dagger_{-k'\overline{\sigma}})(v_k^2\alpha_{-k\sigma}\alpha_{k\overline{\sigma}}+u_k^2\beta_{-k\sigma}\beta_{k\overline{\sigma}})\\
&+(u_{k'}v_{k'}\alpha^\dagger_{k'\sigma}\alpha^\dagger_{-k'\overline{\sigma}}-u_{k'}v_{k'}\beta^\dagger_{k'\sigma}\beta^\dagger_{-k'\overline{\sigma}})(u_kv_k\alpha_{-k\sigma}\alpha_{k\overline{\sigma}}-u_kv_k\beta_{-k\sigma}\beta_{k\overline{\sigma}})\\
&+(u_{k'}v_{k'}\alpha^\dagger_{k'\sigma}\alpha^\dagger_{-k'\overline{\sigma}}-u_{k'}v_{k'}\beta^\dagger_{k'\sigma}\beta^\dagger_{-k'\overline{\sigma}})(u_kv_k\alpha_{-k\sigma}\alpha_{k\overline{\sigma}}-u_kv_k\beta_{-k\sigma}\beta_{k\overline{\sigma}})\Big\}\Big]
\end{aligned}
$$

In conclusion, the interaction Hamiltonian for transverse interactions take the form:

$$
\begin{aligned}
H^{tr} = & -\frac{1}{2N}\sideset{}{'}\sum_{k,k'}\sum_{\sigma}\Big[V_{+-}(k-k')\Big\{\underbrace{(u_k^2u_{k'}^2+v_k^2v_{k'}^2-2u_ku_{k'}v_kv_{k'})}_{n^2(k,k')}(\alpha^\dagger_{k'\sigma}\alpha^\dagger_{-k'\overline{\sigma}}\alpha_{-k\sigma}\alpha_{k\overline{\sigma}}+\beta^\dagger_{k'\sigma}\beta^\dagger_{-k'\overline{\sigma}}\beta_{-k\sigma}\beta_{k\overline{\sigma}})\\
&+\underbrace{(u_k^2v_{k'}^2+u_{k'}^2v_k^2+2u_ku_{k'}v_kv_{k'})}_{m^2(k,k')}(\alpha^\dagger_{k'\sigma}\alpha^\dagger_{-k'\overline{\sigma}}\beta_{-k\sigma}\beta_{k\overline{\sigma}}+\beta^\dagger_{k'\sigma}\beta^\dagger_{-k'\overline{\sigma}}\alpha_{-k\sigma}\alpha_{k\overline{\sigma}})\Big\}\\
&+V_{+-}(k-k'+Q)\Big\{-\underbrace{(u_k^2v_{k'}^2+u_{k'}^2v_k^2-2u_ku_{k'}v_kv_{k'})}_{p^2(k,k')}(\alpha^\dagger_{k'\sigma}\alpha^\dagger_{-k'\overline{\sigma}}\alpha_{-k\sigma}\alpha_{k\overline{\sigma}}+\beta^\dagger_{k'\sigma}\beta^\dagger_{-k'\overline{\sigma}}\beta_{-k\sigma}\beta_{k\overline{\sigma}})\\
&-\underbrace{(u_k^2u_{k'}^2+v_k^2v_{k'}^2+2u_ku_{k'}v_kv_{k'})}_{l^2(k,k')}(\alpha^\dagger_{k'\sigma}\alpha^\dagger_{-k'\overline{\sigma}}\beta_{-k\sigma}\beta_{k\overline{\sigma}}+\beta^\dagger_{k'\sigma}\beta^\dagger_{-k'\overline{\sigma}}\alpha_{-k\sigma}\alpha_{k\overline{\sigma}})\Big\}\Big]\\
= & -\frac{1}{2N}\sideset{}{'}\sum_{k,k'}\sum_{\sigma}\Big[[V_{+-}(k-k')n_{k,k'}^2-V_{+-}(k-k'+Q)p_{k,k'}^2](\alpha^\dagger_{k'\sigma}\alpha^\dagger_{-k'\overline{\sigma}}\alpha_{-k\sigma}\alpha_{k\overline{\sigma}}+\beta^\dagger_{k'\sigma}\beta^\dagger_{-k'\overline{\sigma}}\beta_{-k\sigma}\beta_{k\overline{\sigma}})\\
&+[V_{+-}(k-k')m_{k,k'}^2-V_{+-}(k-k'+Q)l_{k,k'}^2](\alpha^\dagger_{k'\sigma}\alpha^\dagger_{-k'\overline{\sigma}}\beta_{-k\sigma}\beta_{k\overline{\sigma}}+\beta^\dagger_{k'\sigma}\beta^\dagger_{-k'\overline{\sigma}}\alpha_{-k\sigma}\alpha_{k\overline{\sigma}})\Big]
\end{aligned}
\tag{C.16}
$$

The derivation of the interaction Hamiltonian in the longitudinal channel is performed in the same way and yields:

$$
\begin{aligned}
H^{lo/ch} &= \frac{1}{2}\sum_{i,j}(U+V_{\text{bub}}(i,j))c^\dagger_{i\uparrow}c^\dagger_{j\downarrow}c_{j\downarrow}c_{i\uparrow}\\
&= \frac{1}{4N}\sum_{\mathbf{q},\mathbf{k},\mathbf{k}'}\sum_{\sigma}\Big[2U+V_z(\mathbf{k}-\mathbf{k}')-V_c(\mathbf{k}-\mathbf{k}')\Big]c^\dagger_{\mathbf{k}'\sigma}c^\dagger_{-\mathbf{k}'+\mathbf{q}\overline{\sigma}}c_{-\mathbf{k}+\mathbf{q}\overline{\sigma}}c_{\mathbf{k}\sigma}
\end{aligned}
\tag{C.17}
$$

Appendix D

Calculation of the anisotropy gap

Here we show the derivation of the dispersion relation of a Heisenberg model including exchange anisotropies, DM interaction and an external magnetic field. The magnetic field is applied along the c axis. The DM anisotropy and magnetic field both acts to cant the spins out of the $\mathrm{CuO_2}$ planes. The exchange Hamiltonian is given by:

$$H = \sum_{\langle i,j \rangle} S_i \cdot \hat{J} \cdot S_j \tag{D.1}$$

with

$$\hat{J} = \begin{pmatrix} J_{aa} & 0 & 0 \\ 0 & J_{bb} & J_{bc} \\ 0 & -J_{bc} & J_{cc} \end{pmatrix} \tag{D.2}$$

where the exchange energy J_{bc} is due to the DM anisotropy. We write out the Hamiltonian containing anisotropies and external field in a common global coordinate systems. Let S_i denote spins on one sublattice and S_j denote spins on the other sublattice.

$$\begin{aligned} H &= \sum_{\langle i,j \rangle} J_{aa} S_i^x S_j^x + (J_{bb} S_j^y + J_{bc} S_j^z) S_i^y + (-J_{bc} S_j^y + J_{cc} S_j^z) S_i^z - g\mu_B H [\sum_i S_i^z + \sum_j S_j^z] \\ &= \sum_{\langle i,j \rangle} J_{aa} S_i^x S_j^x + J_{bb} S_i^y S_j^y + J_{cc} S_i^z S_j^z + J_{bc}(S_i^y S_j^z - S_i^z S_j^y) - g\mu_B H [\sum_i S_i^z + \sum_j S_j^z] \end{aligned} \tag{D.3}$$

Next step is to introduce a local coordinate system for each sublattice. We introduce a local coordinate system for the first sublattice which is canted out of the plane by an angle θ around the a axis.

$$\begin{aligned} \begin{pmatrix} S_x \\ S_y \\ S_z \end{pmatrix} &= \begin{pmatrix} 1 & 0 & 0 \\ 0 & \cos\theta & -\sin\theta \\ 0 & \sin\theta & \cos\theta \end{pmatrix} \begin{pmatrix} S_i^x \\ S_i^y \\ S_i^z \end{pmatrix} \\ &= \begin{pmatrix} S_i^x \\ \cos\theta S_i^y - \sin\theta S_i^z \\ \sin\theta S_i^y + \cos\theta S_i^z \end{pmatrix} \end{aligned} \tag{D.4}$$

For the second sublattice the local coordinate system is canted out of the plane by an angle of $\pi - \theta$ around the a axis.

$$\begin{aligned} \begin{pmatrix} S_x \\ S_y \\ S_z \end{pmatrix} &= \begin{pmatrix} 1 & 0 & 0 \\ 0 & -\cos\theta & -\sin\theta \\ 0 & \sin\theta & -\cos\theta \end{pmatrix} \begin{pmatrix} S_j^x \\ S_j^y \\ S_j^z \end{pmatrix} \\ &= \begin{pmatrix} S_i^x \\ -\cos\theta S_j^y - \sin\theta S_j^z \\ \sin\theta S_j^y - \cos\theta S_j^z \end{pmatrix} \end{aligned} \tag{D.5}$$

We rewrite the Hamiltonian in Eq. (D.3) in terms of local coordinates for each sublattice. Note that in the equation below the spins are represented in each of their local coordinate systems.

$$
\begin{aligned}
H \;=\; & \sum_{\langle i,j\rangle} J_{aa} S_i^x S_j^x + \underbrace{\{J_{cc}\sin^2\theta - J_{bb}\cos^2\theta + 2J_{bc}\cos\theta\sin\theta\}}_{h_y} S_i^y S_j^y \\
& + \underbrace{\{J_{bb}\sin^2\theta - J_{cc}\cos^2\theta + 2J_{bc}\cos\theta\sin\theta\}}_{h_z} S_i^z S_j^z \\
& + \underbrace{\{-J_{bb}\cos\theta\sin\theta - J_{cc}\cos\theta\sin\theta + J_{bc}(\sin^2\theta - \cos^2\theta\}}_{h_{yz}} S_i^y S_j^z \\
& + \underbrace{\{J_{bb}\cos\theta\sin\theta + J_{cc}\cos\theta\sin\theta - J_{bc}(\sin^2\theta - \cos^2\theta\}}_{-h_{yz}} S_i^z S_j^y \\
& - g\mu_B H[\sum_i (\sin\theta S_i^y + \cos\theta S_i^z) + \sum_j (\sin\theta S_j^y - \cos\theta S_j^z)]
\end{aligned}
\tag{D.6}
$$

Now we will diagonalize the spin Hamiltonian by first replacing the spin operators by the first order approximations in second quantization formalism, using the approach of Holstein-Primakoff:

$$
\begin{aligned}
S_x &\simeq \sqrt{\frac{S}{2}}(a + a^\dagger) \\
S_y &\simeq S - a^\dagger a \\
S_z &\simeq \frac{1}{i}\sqrt{\frac{S}{2}}(a - a^\dagger)
\end{aligned}
\tag{D.7}
$$

The Hamiltonian expressed in second quantization is:

$$
\begin{aligned}
H \;=\; & \sum_{\langle i,j\rangle} \Big[J_{aa}\frac{S}{2}(a_i + a_i^\dagger)(b_j + b_j^\dagger) + h_y(S - a_i^\dagger a_i)(S - b_j^\dagger b_j) - h_z\frac{S}{2}(a_i - a_i^\dagger)(b_j - b_j^\dagger) \\
& + h_{yz}(S - a_i^\dagger a_i)\frac{1}{i}\sqrt{\frac{S}{2}}(b_j - b_j^\dagger) - h_{yz}\frac{1}{i}\sqrt{\frac{S}{2}}(a_i - a_i^\dagger)(S - b_j^\dagger b_j)\Big] \\
& - g\mu_B H\sum_i[\sin\theta(S - a_i^\dagger a_i) + \cos\theta\frac{1}{i}\sqrt{\frac{S}{2}}(a_i - a_i^\dagger)] - g\mu_B H\sum_j[\sin\theta(S - b_j^\dagger b_j) - \cos\theta\frac{1}{i}\sqrt{\frac{S}{2}}(b_j - b_j^\dagger)] \\
= \;& H_0 + \sum_i[-Szh_y - g\mu_B H\sin\theta]a_i^\dagger a_i + \frac{1}{i}\Big[\sqrt{\frac{S}{2}}Szh_{yz} + g\mu_B H\sqrt{\frac{S}{2}}\cos\theta\Big]a_i^\dagger \\
& \qquad + \frac{1}{i}\Big[-\sqrt{\frac{S}{2}}Szh_{yz} - g\mu_B H\sqrt{\frac{S}{2}}\cos\theta\Big]a_i \\
& + \sum_j[-Szh_y - g\mu_B H\sin\theta]b_j^\dagger b_j + \frac{1}{i}\Big[-\sqrt{\frac{S}{2}}Szh_{yz} - g\mu_B H\sqrt{\frac{S}{2}}\cos\theta\Big]b_j^\dagger \\
& \qquad + \frac{1}{i}\Big[\sqrt{\frac{S}{2}}Szh_{yz} + g\mu_B H\sqrt{\frac{S}{2}}\cos\theta\Big]b_j \\
& + \sum_{\langle i,j\rangle}[\frac{S}{2}J_{aa} - \frac{S}{2}h_z]a_i b_j + [\frac{S}{2}J_{aa} - \frac{S}{2}h_z]a_i^\dagger b_j^\dagger + [\frac{S}{2}J_{aa} + \frac{S}{2}h_z]a_i b_j^\dagger + [\frac{S}{2}J_{aa} + \frac{S}{2}h_z]a_i^\dagger b_j
\end{aligned}
\tag{D.8}
$$

Note that since the coefficients are real and the operators of each sublattice commute, the Hamiltonian is Hermitian. First we consider the linear terms, which cancel out due to the canting of the spins out of plane in the equilibrium configuration. All four linear terms have the same coefficient. Setting this term to zero gives:

$$\begin{aligned}
0 &= \sqrt{\frac{S}{2}}Szh_{yz} + g\mu_B H\sqrt{\frac{S}{2}}\cos\theta \Leftrightarrow \\
0 &= Sz\{-J_{bb}\cos\theta\sin\theta - J_{cc}\cos\theta\sin\theta + J_{bc}(\sin^2\theta - \cos^2\theta\} + g\mu_B H\cos\theta \Leftrightarrow \\
\sin\theta &= \frac{-J_{bc}}{J_{bb}+J_{cc}}\frac{\cos 2\theta}{\cos\theta} + \frac{1}{J_{bb}+J_{cc}}(g\mu_B H)/(Sz)
\end{aligned} \tag{D.9}$$

Dependent on the sign of J_{bc}, the DM-term and the external field draw the spins in the same or opposite directions. In undoped La_2CuO_4 the spins cant in opposite directions in alternate layers [162]. Note that in the case of $J_{bb} = J_{cc} = J = 1$ and $J_{bc} = -D \cdot J = -D$ the canting angle given in Eqn. (D.9) is identical to the expression derived in Ref. [161], Eqn. (5).

The Hamiltonian takes a simpler form now when the linear terms are zero:

$$\begin{aligned}
H &= H_0 + \sum_i[-Szh_y - g\mu_B H\sin\theta]a_i^\dagger a_i + \sum_j[-Szh_y - g\mu_B H\sin\theta]b_j^\dagger b_j \\
&\quad + \sum_{\langle i,j\rangle}\left[\frac{S}{2}J_{aa} - \frac{S}{2}h_z\right](a_i b_j + a_i^\dagger b_j^\dagger) + \left[\frac{S}{2}J_{aa} + \frac{S}{2}h_z\right](a_i b_j^\dagger + a_i^\dagger b_j)
\end{aligned} \tag{D.10}$$

Fourier transforming we get:

$$\begin{aligned}
H &= H_0 + \sum_q h_1[a_q^\dagger a_q + b_q^\dagger b_q] \\
&\quad + \sum_{q,\delta} h_2[e^{iq\cdot\delta}a_q^\dagger b_{-q}^\dagger + e^{-iq\cdot\delta}a_q b_{-q}] + h_3[e^{iq\cdot\delta}a_q^\dagger b_q + e^{-iq\cdot\delta}a_q b_q^\dagger] \\
&= H_0 + \sum_q h_1[a_q^\dagger a_q + b_q^\dagger b_q] + h_2 z\gamma_q[a_q^\dagger b_{-q}^\dagger + a_q b_{-q}] + h_3 z\gamma_q[a_q^\dagger b_q + a_q b_q^\dagger]
\end{aligned} \tag{D.11}$$

with

$$\begin{aligned}
h_1 &= SzJ_{bb} - (2zSJ_{bc} + g\mu_B H)\theta \\
h_2 &= \frac{S}{2}(J_{aa} + J_{cc}) - SJ_{bc}\theta \\
h_3 &= \frac{S}{2}(J_{aa} - J_{cc}) - SJ_{bc}\theta \\
\gamma_q &= \frac{1}{z}\sum_\delta e^{iq\cdot\delta} = \frac{1}{2}(\cos q_x + \cos q_y)
\end{aligned} \tag{D.12}$$

where z is the number of nearest neighbours and we have used that the angle θ is small. The Hamiltonian is diagonalized by using the general method of Lindgård [176]. We get the dispersion relation, valid for small tilting angles θ:

$$\begin{aligned}
(E_q^{f,g})^2 &= h_1^2 + z^2\gamma_q^2[h_3^2 - h_2^2] \pm 2z\gamma_q h_1 h_3 \\
&= S^2z^2[J_{bb}^2 - \gamma_q^2 J_{aa}J_{cc} \pm \gamma_q(J_{aa} - J_{cc})J_{bb}] \\
&\quad -S^2z^2[4J_{bb}J_{bc} + 2\gamma_q^2 J_{aa}J_{bc} \pm 2\gamma_q(J_{aa} + J_{bb} - J_{cc})J_{bc})]\theta \\
&\quad -S^2z^2[2J_{bb} \pm \gamma_q(J_{aa} - J_{cc})]\theta(g\mu_B H)/(Sz)
\end{aligned} \tag{D.13}$$

where $|J_{bb}| > |J_{aa}| > |J_{cc}|$, $\gamma_q = \frac{1}{z}\sum_\delta e^{iq\cdot\delta}$ and $\theta \simeq \frac{-J_{bc}+(g\mu_B H)/(Sz)}{J_{bb}+J_{cc}}$.

We can also generalize the expression to larger values of θ, using again the general result of Ref. [176]. The dispersion is given by:

$$E^2 = E_1^2 + E_2^2 \pm E_3^2 \tag{D.14}$$

where $E_1^2 = h_1^2$, $E_2^2 = z^2\gamma_q^2[h_3^2 - h_2^2]$, and $E_3^2 = 2z\gamma_q h_1 h_3$. The general expressions for h_1, h_2 and h_3 are given by:

$$\begin{aligned}
h_1 &= Sz(J_{bb}\cos^2\theta - J_{cc}\sin^2\theta - 2J_{bc}\cos\theta\sin\theta) - g\mu_B H\sin\theta \\
h_2 &= \frac{S}{2}(J_{aa} - J_{bb}\sin^2\theta + J_{cc}\cos^2\theta - 2J_{bc}\cos\theta\sin\theta) \\
h_3 &= \frac{S}{2}(J_{aa} + J_{bb}\sin^2\theta - J_{cc}\cos^2\theta + 2J_{bc}\cos\theta\sin\theta)
\end{aligned} \tag{D.15}$$

and thus

$$\begin{aligned}
E_1^2/(z^2S^2) &= [J_{bb}\cos^2\theta - J_{cc}\sin^2\theta - 2J_{bc}\cos\theta\sin\theta]^2 + \big(\frac{g\mu_B H}{zS}\big)^2\sin^2\theta \\
&\quad -2(J_{bb}\cos^2\theta - J_{cc}\sin^2\theta - 2J_{bc}\cos\theta\sin\theta)\frac{g\mu_B H}{zS}\sin\theta \\
&\simeq [J_{bb}(1-\theta^2) - J_{cc}\theta^2 - 2J_{bc}\theta]^2 + (\frac{g\mu_B H}{zS})^2\theta^2 \\
&\quad -2(J_{bb}(1-\theta^2) - J_{cc}\theta^2 - 2J_{bc}\theta)\frac{g\mu_B H}{zS}\theta
\end{aligned} \tag{D.16}$$

$$\begin{aligned}
E_2^2/(z^2S^2) &= \gamma_q^2[J_{aa}J_{bb}\sin^2\theta + 2J_{cc}J_{bc}\cos^3\theta\sin\theta - (J_{aa}J_{cc}\cos^2\theta + 2J_{bb}J_{bc}\cos\theta\sin^3\theta)] \\
&\simeq \gamma_q^2[J_{aa}J_{bb}\theta^2 + 2J_{cc}J_{bc}\theta - J_{aa}J_{cc}(1-\theta^2)]
\end{aligned}$$

$$\begin{aligned}
E_3^2/(z^2S^2) &= \gamma_q\Big[J_{aa}J_{bb}\cos^2\theta + J_{bb}^2\cos^2\theta\sin^2\theta - J_{bb}J_{cc}\cos^4\theta + 2J_{bb}J_{bc}\cos^3\theta\sin\theta \\
&\quad -J_{aa}J_{cc}\sin^2\theta - J_{bb}J_{cc}\sin^4\theta + J_{cc}^2\cos^2\theta\sin^2\theta - 2J_{cc}J_{bc}\cos\theta\sin^3\theta \\
&\quad -2J_{aa}J_{bc}\cos\theta\sin\theta - 2J_{bb}J_{bc}\cos\theta\sin^3\theta + 4J_{cc}J_{bc}\cos^3\theta\sin\theta - 4J_{bc}^2\cos^2\theta\sin^2\theta \\
&\quad -(J_{aa} + J_{bb}\sin^2\theta - J_{cc}\cos^2\theta + J_{bc}\cos\theta\sin\theta)\frac{g\mu_B H\sin\theta}{zS}\Big] \\
&\simeq \gamma_q\Big[J_{aa}J_{bb}(1-\theta^2) + J_{bb}^2\theta^2 - J_{bb}J_{cc}(1-2\theta^2) + 2J_{bb}J_{bc}\theta \\
&\quad -J_{aa}J_{cc}\theta^2 + J_{cc}^2\theta^2 \\
&\quad -2J_{aa}J_{bc}\theta + 4J_{cc}J_{bc}\theta - 4J_{bc}^2\theta^2 \\
&\quad -(J_{aa} + J_{bb}\theta^2 - J_{cc}(1-\theta^2) + J_{bc}\theta)\frac{g\mu_B H\theta}{zS}\Big]
\end{aligned} \tag{D.17}$$

In the approximation we keep only terms to second order in θ.

<ins>Limiting case: $J_{bc} = 0$ and $H = 0$</ins>

If we consider the case of no DM interaction as well as no external field, the expression in Eqn. (D.13) reduces to:

$$(E_q^{f,g})^2 = S^2z^2[(J_{bb} \pm J_{aa}\gamma_q)(J_{bb} \mp J_{cc}\gamma_q)] \tag{D.18}$$

Limiting case: $J_{bc} = 0$ and $J_{aa} = J_{bb} = J_{cc} = J$
In this case the expression in Eqn. D.13 (and Eqn. D.18) reduces to:

$$\begin{aligned}(E_q^{f,g})^2 = {} & S^2z^2\Big[J^2(1-2\theta^2)^2 - 2J(1-2\theta^2)\frac{g\mu_B H}{zS}\theta + \Big(\frac{g\mu_B H}{zS}\Big)^2\theta^2 \\ & +\gamma_q^2 J^2(2\theta^2-1) + \gamma_q\Big(2J^2\theta^2 - 2J\theta^2\frac{g\mu_B H}{zS}\Big)\Big]\end{aligned} \tag{D.19}$$

with $\theta = \sin^{-1}(\frac{g\mu_B H/zS}{2J})$.

Bibliography

[1] N. P. Armitage, P. Fournier, and R. L. Greene, Rev. Mod. Phys. **82**, 2421 (2010).

[2] Y. Krockenberger, H. Irie, O. Matsumoto, K. Yamagami, M. Mitsuhashi, A. Tsukada, M. Naito and H. Yamamoto, Scientific Rep. **3**, 2235 (2013). Y. Krockenberger, H. Irie, J. Yan, L. Waterston, B. Eleazer, Keita Sakuma, and H. Yamamoto, Applied Physics Express **7**, 063101 (2014).

[3] C. E. Gough, M. S. Colclough, E. M. Forgan, R. G. Jordan, M. Keene, C. M. Muirhead, A. I. M. Rae, N. Thomas, J. S. Abell, and S. Sutton, Nature **326**, 855 (1987).

[4] J. F. Annett, Superconductivity, Superfluids and Condensates, Oxford University Press (2004).

[5] W. L. McMillan, Phys. Rev. **167**, 331 (1968).

[6] A.P. Drozdov, M. I. Eremets, I. A. Troyan, V. Ksenofontov, and S. I. Shylin, preprint available at arXiv:1506.08190.

[7] Z.-X. Shen, D. S. Dessau, B. O. Wells, D. M. King, W. E. Spicer, D. Marshall, L. W. Lombardo, A. Kapitulnik, P. Dickinson, S. Doniach, J. A. G. Loeser, and C. H. Park, Phys. Rev. Lett. **70**, 1553 (1993).

[8] A. Damascelli, Z. Hussain, and Zhi-Xun Shen, Rev. Mod. Phys. **75** (2003).

[9] W. Kohn, and J. M. Luttinger, Phys. Rev. Lett. **15**, 524 (1965).

[10] N. F. Berk and J. R. Schrieffer, Phys. Rev. Lett. **17**, 433 (1966).

[11] M. T. Beal-Monod, C. Bourbonnais, and V. J. Emery, Phys. Rev. B **34**, 7716 (1986).

[12] D. J. Scalapino, E. Loh, Jr., and J. E. Hirsch, Phys. Rev. B **34**, 8190 (1986).

[13] A. J. Leggett, Rev. Mod. Phys **47**, 332 (1975).

[14] K. Miyake S. Schmitt-Rink, and C. M. Varma, Phys. Rev. B **34**, 6554 (R) (1986).

[15] N. P. Armitage, P. Fournier, and R. L. Greene,Rev. Mod. Phys. **82**, 2421 (2010)

[16] M. Hashimoto, I. M. Vishik, R.-H. He, T. P. Devereaux, and Z.-X. Shen, Nature Phys. **10**, 483 (2014).

[17] I.M. Vishik, W.S. Lee, F. Schmitt, B. Moritz, T. Sasagawa, S. Uchida, K. Fujita, S. Ishida, C. Zhang, T.P. Devereaux, and Z.X. Shen Phys. Rev. Lett. bf 104, 207002 (2010).

[18] H. Matsui, K. Terashima, T. Sato, T. Takahashi, S.-C. Wang, H.-B. Yang, H. Ding, T. Uefuji, and K. Yamada, Phys. Rev. Lett. **94**, 047005 (2005).

[19] G. Blumberg, A. Koitzsch, A. Gozar, B. S. Dennis, C. A. Kendziora, P. Fournier, and R. L. Greene, Phys. Rev. Lett. **88**, 107002 (2002).

[20] D. Parker and A. V. Balatsky, Phys. Rev. B **78**, 214502 (2008).

[21] K. Terashima, H. Matsui, T. Sato, T. Takahashi, M. Kofu, and K. Hirota, Phys. Rev. Lett. **99**, 017003 (2007).

[22] V. A. Khodel, V. M. Yakovenko, M. V. Zverev, and H. Kang, Phys. Rev. B **69**, 144501 (2004).

[23] R. Hlubina, Phys. Rev. B **59**, 9600 (1999).

[24] F. Guinea, R. S. Markiewicz, and M. A. H. Vozmediano, Phys. Rev. B **69**, 054509 (2004).

[25] S. Raghu, S.A. Kivelson, and D.J. Scalapino, Phys. Rev. B **81**, 224505 (2010).

[26] D. J. Scalapino, *The case for* $d_{x^2-y^2}$ *pairing in the cuprate superconductors.*, Physics Reports **250**, 329-365 (1995).

[27] I. Eremin, D. Manske, C. Joas, K.H. Bennemann Europhys. Lett. **58**, 871 (2002).

[28] D.M. Newns, C.C. Tsuei, and P.C. Pattnaik, Phys. Rev. B **52**, 13611 (1995).

[29] M. Sigrist and K. Ueda, Rev. Mod. Phys. **63**, 239 (1991).

[30] Y. Deng, E. Kozik, N. V. Prokof'ev, and B. V. Svistunov, ArXiv:1408.2088.

[31] I. Eremin, E. Tsoncheva, and A. V. Chubukov, Phys. Rev. B **77**, 024508 (2008).

[32] A. V. Chubukov and J. P. Lu, Phys. Rev. B **46**, 11163 (1992)

[33] G.Esirgen and N. E. Bickers, Phys. Rev. B **55**, 2122 (1997).

[34] S. Onari, R. Arita, K. Kuroki, and H. Aoki, Phys. Rev. B **70**, 094523 (2004).

[35] H. Aoki, Physica C **437-438**, 11-16 (2006).

[36] Ø. Fischer, M. Kugler, I. Maggio-Aprile, C. Berthod, and C. Renner, Rev. Mod. Phys. **79**, 353 (2007).

[37] T. Cren, D. Roditchev, W. Sacks, and J. Klein, Europhys. Lett. **54**, 84 (2001).

[38] C. Howald, P. Fournier, and A. Kapitulnik, Phys. Rev. B **64**, 100504(R) (2001).

[39] S. H. Pan *et al.*, Nature **413**, 282 (2001).

[40] K. M. Lang, V. Madhavan, J. E. Hoffman, E. W. Hudson, H. Eisaki, S. Uchida, and J. C. Davis, Nature (London) **415**, 412 (2002).

[41] Y. Kohsaka, C. Taylor, K. Fujita, A. Schmidt, C. Lupien, T. Hanaguri, M. Azuma, M. Takano, H. Eisaki, H. Takagi, S. Uchida, J. C. Davis, Science **315**, 1380-1385 (2007).

[42] K. K. Gomes, A. N. Pasupathy, A. Pushp, S. Ono, Y. Ando, A. Yazdani, Nature **447**, 569 (2007)

[43] A. N. Pasupathy, A. Pushp, K. K. Gomes, C. V. Parker, J. Wen, Z. Xu, G. Gu, S. Ono, Y. Ando, A. Yazdani, Science **320**, 196 (2008)

[44] K. McElroy, J. Lee, J. A. Slezak, D.-H. Lee, H. Eisaki, S. Uchida, and J. C. Davis, Science **309**, 1048 (2005).

[45] T. S. Nunner, B. M. Andersen, A. Melikyan, and P. J. Hirschfeld, Phys. Rev. Lett. **95**, 177003 (2005).

[46] T. S. Nunner, P. J. Hirschfeld, B. M. Andersen, A. Melikyan, and K. McElroy, Physica C **460-462**, 446 (2007).

[47] T. S. Nunner, W. Chen, B. M. Andersen, A. Melikyan, and P. J. Hirschfeld, Phys. Rev. B **73**, 104511 (2006).

[48] B. M. Andersen, A. Melikyan, T. S. Nunner, and P. J. Hirschfeld, Phys. Rev. Lett. **96**, 097004 (2006).

[49] B. M. Andersen, A. Melikyan, T. S. Nunner, and P. J. Hirschfeld, Phys. Rev. B **74**, 060501(R) (2006).

[50] B. M. Andersen, P. J. Hirschfeld, and J. A. Slezak, Phys. Rev. B **76**, 020507(R) (2007).

[51] J. A. Slezak, Jinho Lee, M. Wang, K. McElroy, K. Fujita, B. M. Andersen, P. J. Hirschfeld, H. Eisaki, S. Uchida, and J. C. Davis, Proc. Natl. Acad. Sci. USA **105**, 3203 (2008).

[52] H. Suhl, D. R. Fredkin, J. S. Langer, and B. T. Matthias Phys. Rev. Lett. **9**, 63 (1962); A. I. Larkin, Sov. Phys. JETP **31**, 784 (1970); A. Weinkauf and J. Zittartz, Z. Phys. B **21**, 135 (1975); K. Chattopadhyay, R. A. Klemm and D. Sa, J. Phys.: Cond. Matt. **14**, L577 (2002).

[53] Y. He, T. S. Nunner, P. J. Hirschfeld, and H.-P. Cheng, Phys. Rev. Lett. **96**, 197002 (2006).

[54] A. E. Ruckenstein, P. J. Hirschfeld, and J. Appel, Phys. Rev. B **36**, 857 (1987).

[55] G. Baskaran, Z. Zou, and P.W. Anderson, Solid State Comm. **63**, 973 (1987).

[56] Z. Wang, J. R. Engelbrecht, S. Wang, H. Ding, and S. H. Pan, Phys. Rev. B **65**, 064509 (2002).

[57] J.-X. Zhu, cond-mat/0508646.

[58] W. Chen, M. Gabay, and P. J. Hirschfeld, New J. Phys. **14**, 033004 (2012).

[59] M. M. Maśka, Ź. Śledź, K. Czajka, and M. Mierzejewski, Phys. Rev. Lett. **99**, 147006 (2007).

[60] S. Johnston, F. Vernay, B. Moritz, Z.-X. Shen, N. Nagaosa, J. Zaanen, and T. P. Devereaux, Phys. Rev. B **82**, 064513 (2010).

[61] K. Foyevtsova, R. Valentí, and P. J. Hirschfeld, Phys. Rev. B **79**, 144424(2009).

[62] G. Khaliullin, M. Mori, T. Tohyama, and S. Maekawa, Phys. Rev. Lett. **105**, 257005 (2010).

[63] R. B. Christensen, P. J. Hirschfeld, and B. M. Andersen, Phys. Rev. B **84**, 184511 (2011).

[64] K. Foyevtsova, H. C. Kandpal, H. O. Jeschke, S. Graser, H.-P. Cheng, R.Valentí and P. J. Hirschfeld, Phys. Rev. B **82**, 054514 (2010).

[65] D. J. Scalapino, Phys. Rep. **250**, 329 (1995).

[66] J. W. Harter, B. M. Andersen, J. Bobroff, M. Gabay, and P. J. Hirschfeld, Phys. Rev. B **75**, 054520 (2007).

[67] B. M. Andersen, P. J. Hirschfeld, A. P. Kampf, and M. Schmid, Phys. Rev. Lett. **99**, 147002 (2007).

[68] B. M. Andersen and P. J. Hirschfeld, Phys. Rev. Lett. **100**, 257003 (2008).

[69] B. M. Andersen, S. Graser, and P. J. Hirschfeld, Phys. Rev. Lett. **105**, 147002 (2010).

[70] Y. Ohashi, Phys. Rev. B **60**, 15388 (1999); Phys. Rev. B **66**, 054522 (2002).

[71] J. R. Schrieffer, J. Low Temp. Phys., **99**, 314 (1995).

[72] A. V. Chubukov, D. Pines, and J. Schmalian, ‘The Physics of Conventional and Unconventional Superconductors’ edited by K.H. Bennemann and J.B. Ketterson (Springer-Verlag 2004).

[73] B. M. Andersen, S. Graser, and P. J. Hirschfeld, Phys. Rev. B **78**, 134502 (2008).

[74] A. T. Rømer, S. Graser, P. J. Hirschfeld, and B. M. Andersen, submitted to J. Supercond. Novel Magn. (2012).

[75] S. Graser, P. J. Hirschfeld, L.-Y. Zhu, and T. Dahm, Rev. B **76**, 054516 (2007).

[76] I. Martin, D. Podolsky, and S. A. Kivelson, Phys. Rev. B **72**, 060502 (2005).

[77] Chien-Hua Pao and N. E. Bickers, Phys. Rev. B **44** 10270 (1991).

[78] P. Monthoux and D. J. Scalapino, Phys. Rev. Lett. **72**, 1874 (1994).

[79] S. Graser, T. A. Maier, P. J. Hirschfeld and D. J. Scalapino, New J. Phys. **11**, 025016 (2009).

[80] J. R. Schrieffer, X. G. Wen, and S. C. Zhang, Phys. Rev. B **39**, 11663 (1989).

[81] David M. Frenkel and W. Hanke, Phys. Rev. B **42**, 6711 (1990).

[82] B. I. Shraiman and E. D. Siggia, Phys. Rev. Lett. **62**, 1564 (1989).

[83] T. Uefuji, T. Kubo, K. Yamada, M. Fujita, K. Kurahashi, I. Watanabe, K. Nagamine, Physica C **357**, 208 (2001).

[84] M. Fujita, M. Matsuda, S.-H. Lee, M. Nakagawa, and K. Yamada, Phys. Rev. Lett. **101**, 107003 (2008).

[85] Armitage N. P., *et al.*, Phys. Rev. Lett. **88**, 257001 (2002).

[86] M. Brinkmann, T. Rex, H. Bach, and K. Westerholt, Phys. Rev. Lett **74**, 4927 (1995).

[87] S. D. Wilson, S. Li, P. Dai, W. Bao, J.-H. Chung, H. J. Kang, S.-H. Lee, S. Komiya, Y. Ando, and Q. Si, Phys. Rev. B **74**, 144514 (2006).

[88] H. J. Kang, P. Dai, H. A. Mook, D. N. Argyriou, V. Sikolenko, J. W. Lynn, Y. Kurita, S. Komiya, and Y. Ando Phys. Rev. B **71**, 214512 (2005).

[89] N. P. Armitage, D. H. Lu, D. L. Feng, C. Kim, A. Damascelli, K. M. Shen, F. Ronning, Z.-X. Shen, Y. Onose, Y. Taguchi, and Y. Tokura, Phys. Rev. Lett. **86** 1126 (2001).

[90] T. Sato, T. Kamiyama, T. Takahashi, K. Kurahashi, K. Yamada, Science **291**, 1517 (2001).

[91] Y. Dagan, M. M. Qazilbash, C. P. Hill, V. N. Kulkarni, and R. L. Greene, Phys. Rev. Lett. **92** 167001 (2004).

[92] S. D. Wilson, P. Dai, S. Li, S. Chi, H. J. Kang, and J. W. Lynn, Nature **442**, 59 (2006).

[93] J. Zhao, P. Dai, S. Li, P. G. Freeman, Y. Onose, and Y. Tokura, Phys. Rev. Lett. **99**, 017001 (2007).

[94] W. Rowe, J. Knolle, I. Eremin, and P. Hirschfeld, Phys. Rev. B **86**, 134513 (2012).

[95] D. Manske, I. Eremin, and K. H. Bennemann, Phys. Rev. B **63**, 054517 (2001).

[96] A. V. Chubukov and D. M. Frenkel Phys. Rev. B **46**, 11884 (1992).

[97] M. Yu. Kuchiev and O.P. Sushkov, Physica C **218**, 197 (1993); V.V. Flambaum, M.Yu. Kuchiev, and O.P. Sushkov, Physica C **227**, 267 (1994).

[98] W. Rowe, I. Eremin, A. T. Rømer, B. M. Andersen and P. J. Hirschfeld, *Doping asymmetry of superconductivity coexisting with antiferromagnetism in spin fluctuation theory*, New J. Phys. **17**, 023022 (2015).

[99] S. Maiti, M. M. Korshunov, T.A. Maier, P.J. Hirschfeld, and A.V. Chubukov, *Evolution of the Superconducting State of Fe-Based Compounds with Doping* Phys. Rev. Lett. **107**, 147002 (2011).

[100] Wenya W. Rowe *Spin fluctuation theory for unconventional superconductivity in Antiferromagnetic metals*, Dissertation University of Florida (2014).

[101] E. Razzoli *et al.*, Phys. Rev. Lett. **110**, 047004 (2013).

[102] Y. Peng *et al.*, Nature Comm. **3459** (2013).

[103] W. A. Atkinson, J. David Bazak, and B. M. Andersen, Phys. Rev. Lett. **109**, 267004 (2012).

[104] Y.-M. Lu, T. Xiang, and D.-H. Lee, Nature Physics **10**, 634 (2014).

[105] M.Yu. Kuchiev and O.P. Sushkov, Physica C **218** 197-207 (1993).

[106] V.V. Flambaum, M. Yu. Kuchiev, and O.P. Sushkov, Physica C **227** 267-278 (1994).

[107] G. L. Squires, *Introduction to the Theory of Thermal Neutron Scattering*, Dover Publications (1997).

[108] Gen Shirane, Stephen M. Shapiro, and John M. Tranquada, *Neutron Scattering with a Triple-Axis Spectrometer*, Cambrigde University Press (2002).

[109] Kim Lefmann, *Neutron Scattering: Theory, Instrumentation, and Simulation*, University of Copenhagen (2014).

[110] A. Zheludev, *Reslib* 3.4, *3-axis resolution library for MatLab*, Neutron Science Scattering Division, Oak Ridge National Laboratory, (2007)

[111] http://www.mcstas.org/

[112] K. Yosida, *Theory of Magnetism*, Springer (1996).

[113] J. Larsen, B. Mencia Uranga, G. Stieper, S. L. Holm, C. Bernhard, T. Wolf, K. Lefmann, B. M. Andersen, and C. Niedermayer, Phys. Rev. B **91**, 024504 (2015).

[114] E. Fradkin, S. A. Kivelson, J. M. Tranquada, Rev. Mod. Phys. **87**, 457 (2015).

[115] P. Materne, S. Kamusella, R. Sarkar, T. Goltz, J. Spehling, H. Maeter, L. Harnagea, S. Wurmehl, B. Büchner, H. Luetkens, C. Timm, H.-H. Klauss, preprint available at arXiv:1505.00962.

[116] J. M. Tranquada, B. J. Sternlieb, J. D. Axe, Y. Nakamura, and S. Uchida, Nature **375**, 561 (1995).

[117] M. Fujita, H. Goka, K. Yamada, J. M. Tranquada and L. P. Regnault, Phys. Rev. B **70**, 104517 (2004).

[118] M. Hücker, M. v. Zimmermann, G. D. Gu, Z. J. Zu, J. S. Wen, G. Xu, H. J. Kang, A. Zheludev and J. M. Tranquada, Phys. Rev. B **83**, 104506 (2011).

[119] H.-H. Klauss, W. Wagener, M. Hillberg, W. Kopmann, H. Walf, F. J. Litterst, M. Hücker, and B. Büchner, Phys. Rev. Lett. **85**, 4590 (2000).

[120] J. Fink, E. Schierle, E. Weschke, J. Geck, D. Hawthorn, V. Soltwisch, H. Wadati, H.-H. Wu, H. A. Dürr, N. Wizent, B. Büchner, and G. A. Sawatzky, Phys. Rev. B **79**, 100502(R) (2009).

[121] G. Ghiringhelli, M. Le Tacon, M. Minola, S. Blanco-Canosa, C. Mazzoli, N.B. Brookes, G.M. De Luca, A. Frano, D. G. Hawthorn, F. He, T. Loew, M. Moretti Sala, D.C. Peets, M. Salluzzo, E. Schierle, R. Sutarto, G. A. Sawatzky, E. Weschke, B. Keimer and L. Braicovich, Science **337**, 821 (2012).

[122] J. Chang, E. Blackburn, A. T. Holmes, N. B. Christensen, J. Larsen, J. Mesot, Ruixing Liang, D. A. Bonn, W. N. Hardy, A. Watenphul, M. v. Zimmermann, E. M. Forgan, S. M. Hayden, Nature Physics **8**, 871 (2012).

[123] N. B. Christensen, J. Chang, J. Larsen, M. Fujita, M. Oda, M. Ido, N. Momono, E. M. Forgan, A. T. Holmes, J. Mesot, M. Huecker, and M. v. Zimmermann, arXiv:1404.3192.

[124] V. Thampy, M. P. M. Dean, N. B. Christensen, L. Steinke, Z. Islam, M. Oda, M. Ido, N. Momono, S. B. Wilkins, and J. P. Hill, Phys. Rev. B **90**, 100510(R) (2014).

[125] T. P. Croft, C. Lester, M. S. Senn, A. Bombardi, and S. M. Hayden, Phys. Rev. B **89**, 224513 (2014).

[126] M.-H. Julien, Physica B **329-333**, 693 (2003).

[127] Q. Li, M. Hücker, G. D. Gu, A. M. Tsvelik, J. M. Tranquada, Phys. Rev. Lett. 99, 067001 (2007).

[128] J. M. Tranquada, G. D. Gu, M. Hü cker, Q. Jie, H.-J. Kang, R. Klingeler, Q. Li, N. Tristan, J. S. Wen, G. Y. Xu, Z. J. Xu, J. Zhou, M. v. Zimmermann, Phys. Rev. B 78, 174529 (2008).

[129] M. Hücker, M. v. Zimmermann, G. D. Gu, Z. J. Xu, J. S. Wen, G. Xu, H. J. Kang, A. Zheludev, J. M. Tranquada, Phys. Rev. B 83, 104506 (2011).

[130] R. J. Birgeneau, D. R. Gabbe, H. P. Jenssen, M. A. Kastner, P. J. Picone, T. R. Thurston, G. Shirane, Y. Endoh, M. Sato, K. Yamada, Y. Hidaka, M. Oda, Y. Enomoto, M. Suzuki, and T. Murakami, Phys. Rev. B **38** 6614 (1988).

[131] R. J. Birgeneau, Y. Endoh, Y. Hidaka, K. Kakurai, M. A. Kastner, T. Murakami, G. Shirane, T. R. Thurston, and K. Yamada, Phys. Rev. B **39**, 2868 (1989).

[132] T. Suzuki, T. Goto, K. Chiba, T. Shinoda, T. Fukase, H. Kimura, K. Yamada, M. Ohashi and Y. Yamaguchi, Phys. Rev. B **57**, R3229 (1998).

[133] H. Kimura, H. Matsushita, K. Hirota, Y. Endoh, K. Yamada, G. Shirane, Y. S. Lee, M. A. Kastner, and R. J. Birgeneau, Phys. Rev. B **61**, 14366 (2000).

[134] J. M. Tranquada, in Handbook of High-Temperature Superconductivity Theory and Experiment, edited by J. R. Schrieffer, (Springer, New York, 2007).

[135] R. J. Birgeneau, C. Stock, J. M. Tranquada and K. Yamada, J. Phys. Soc. Jpn. **75**, 111003 (2006).

[136] K. Yamada, C. H. Lee, K. Kurahashi, J. Wada, S. Wakimoto, S. Ueki, H. Kimura, Y. Endoh, S. Hosoya, G. Shirane, R. J. Birgeneau, M. Greven, M. A. Kastner, and Y. J. Kim, Phys. Rev. B **57**, 6165 (1998).

[137] S. Katano, M. Sato, K. Yamada, T. Suzuki, and T. Fukase, Phys. Rev. B **62**, R14677 (2000).

[138] B. Lake, H. M. Rønnow, N. B. Christensen, G. Aeppli, K. Lefmann, D. F. McMorrow, P. Vorderwisch, P. Smeibidl, N. Mangkorntong, T. Sasagawa, M. Nohara, H. Takagi, and T. E. Mason, Nature **415**, 299-302 (2002).

[139] J. Chang, Ch. Niedermayer, R. Gilardi, N. B. Christensen, H. M. Rønnow, D. F. McMorrow, M. Ay, J. Stahn, O. Sobolev, A. Hiess, S. Pailhes, C. Baines, N. Momono, M. Oda, M. Ido, and J. Mesot, Phys. Rev. B **78**, 104525 (2008).

[140] M. Kofu, S.-H. Lee, M. Fujita, H.-J. Kang, H. Eisaki, and K. Yamada, Phys. Rev. Lett. **102**, 047001 (2009).

[141] B. M. Andersen, S. Graser, M. Schmid, A. P. Kampf, and P. J. Hirschfeld, J. Phys. Chem. Solids **72**, 358 (2011).

[142] J. Chang, N. B. Christensen, Ch. Niedermayer, K. Lefmann, H. M. Rønnow, D. F. McMorrow, A. Schneidewind, P. Link, A. Hiess, M. Boehm, R. Mottl, S. Pailhés, N. Momono, M. Oda, M. Ido, and J. Mesot, Phys. Rev. Lett. **102**, 177006 (2009).

[143] B. Khaykovich, S. Wakimoto, R. J. Birgeneau, M. A. Kastner, Y. S. Lee, P. Smeibidl, P. Vorderwisch, and K. Yamada, Phys. Rev. B **71**, 220508(R) (2005).

[144] B. Lake, K. Lefmann, N. B. Christensen, G. Aeppli, D. F. McMorrow, H.M. Rønnow, P. Vorderwisch, P. Smeibidl, N. Mangkorntong, T. Sasagawa, M. Nohara, H. Takagi, Nature Materials, **4**, 658 (2005).

[145] D. Vaknin, S. K. Sinha, D. E. Moncton, D. C. Johnston, J. M. Newsam, C. R. Safinya, and H. E. King, Jr., Phys. Rev. Lett. **58**, 2802 (1987).

[146] T. Freltoft, J. E. Fischer, G. Shirane, D. E. Moncton, S. K. Sinha, D. Vaknin, J. P. Remeika, A. S. Cooper, D. Harshman, Phys. Rev. B **36** 826 (1987).

[147] Y. Endoh, K. Yamada, R. J. Birgeneau, D. R. Gabbe, H. P. Jenssen, M. A. Kastner, C. J. Peters, P. J. Picone, T. R. Thurston, J. M. Tranquada, G. Shirane, Y. Hidaka, M. Oda, Y. Enomoto, M. Suzuki, and T. Murakami,Phys Rev B **37**,7443 (1988).

[148] Y. S. Lee, R. J. Birgeneau, M. A. Kastner, Y. Endoh, S. Wakimoto, K. Yamada, R. W. Erwin, S.-H. Lee, G. Shirane, Phys. Rev. B, **60**, 3643 (1999).

[149] J. Chang, A. P. Schnyder, R. Gilardi, H. M. Rønnow, S. Pailhes, N. B. Christensen, Ch. Niedermayer, D. F. McMorrow, A. Hiess, A. Stunault, M. Enderle, B. Lake, O. Sobolev, N. Momono, M. Oda, M. Ido, C. Mudry, and J. Mesot, Phys. Rev. Lett. **98**, 077004 (2007).

[150] Astrid T. Rømer, Master Thesis *Magnetic correlations in the high-temperature superconductor* $La_{1.88}Sr_{0.12}CuO_4$, Niels Bohr Institute, University of Copenhagen (2009).

[151] E. H. da Silva Neto, R. Comin, F. He, R. Sutarto, Y. Jiang, R. L. Greene, G. A. Sawatzky, and Damascelli, Science **347**, 282 (2015).

[152] T. E. Mason, G. Aeppli and H. A. Mook, Phys. Rev. Lett. **68**, 1414 (1992).

[153] N. B. Christensen, J. Chang, E. Razzoli, M. Bator, Ch. Niedermayer, K. Lefmann, H. M. Ronnow, D. F. Mcmorrow, A. Schneidewind, P. Link, A. Hiess, M. Boehm, R. Mottl, S. Pailhès, M. Oda, M. Ido, N. Momono, J. Mesot, J. Phys. Soc. Jpn. **80** Supplement B SB030 (2011).

[154] K. Yamada, S. Wakimoto, G. Shirane, C. H. Lee, M. A. Kastner, S. Hosoya, M. Greven, Y. Endoh, and R. J. Birgeneau, Phys. Rev. Lett. **75**, 1626 (1995).

[155] B. Lake, G. Aeppli, K. N. Clausen, D. F. McMorrow, K. Lefmann, N. E. Hussey, N. Mangkorntong, M. Nohara, H. Takagi, T. E. Mason, and A. Schröder, Science **291**, 1759 (2001).

[156] B. Keimer, N. Belk, R. J. Birgeneau, A. Cassanho, C. Y. Chen, M. Greven, M. A. Kastner, A. Aharony, Y. Endoh, R. W. Erwin, and G. Shirane, Phys. Rev. B **46**, 14034 (1992).

[157] F. C. Chou, N. R. Belk, M. A. Kastner, R. J. Birgeneau, and A. Aharony, Phys. Rev. Lett. **75**, 2204 (1995).

[158] S. Wakimoto, S. Ueki, Y. Endoh, and K. Yamada, Phys. Rev. B **62**, 3547 (2000).

[159] P. J. Peters, R. J. Birgeneau, M. A. Kastner, H. Yoshizawa, Y. Endoh, J. Tranquada, G. Shirane, Y. Hidaka, M. Oda, M. Suzuki, and T. Murakami, Phys. Rev. B **37** 9761 (1988).

[160] S. Wakimoto, R. J. Birgeneau, Y. S. Lee, and G. Shirane, Phys. Rev. B **63**, 172501 (2001).

[161] A. L. Chernyshev, Phys. Rev. B **72**, 174414 (2005).

[162] T. Thio, T. R. Thurston, N. W. Preyer, P. J. Picone, M. A. Kastner, H. P. Jenssen, D. R. Gabbe, C. Y. Chen, R. J. Birgeneau, and Amnon Aharony, Phys. Rev. B **38** 905 (1988).

[163] J. M. Tranquada, G. D. Gu, M. Hücker, Q. Jie, H.-J. Kang, R. Klingeler, Q. Li, N. Tristan, J. S. Wen, G. Y. Xu, Z. J. Xu, J. Zhou, and M. v. Zimmermann, Phys. Rev. B **78**, 174529 (2008).

[164] J. Wen, Z. Xu, G. Xu, J. M. Tranquada, G. Gu, S. Chang, and H. J. Kang, Phys. Rev. B **78**, 212506 (2008).

[165] J. M. Tranquada, C. H. Lee, K. Yamada, Y. S. Lee, L. P. Regnault and H. M. Ronnow, Phys. Rev. B **69**, 174507 (2004).

[166] N. B. Christensen, D. F. McMorrow, H. M. Rønnow, B. Lake, S. M. Hayden, G. Aeppli, T. G. Perring, M. Mangkorntong, M. Nohara and H. Takagi, Phys. Rev. Lett. **93**, 147002 (2004).

[167] A. T. Boothroyd, P. Babkevich, D. Prabhakaran and P. G. Freeman, Nature **471**, 341 (2011).

[168] A. T. Boothroyd, D. Prabhakaran, P. G. Freeman, S. J. S. Lister, M. Enderle, A. Hiess, and J. Kulda, Phys. Rev. B **67**, 100407 (R) (2003).

[169] A.T. Boothroyd, P.G. Freeman, D. Prabhakaran, M. Enderle, and J. Kulda, Physica B **345**, 1 (2004).

[170] K. Nakajima, K. Yamada, S. Hosoya, T. Omata, and Y. Endoh, J. Phys. Soc. Jpn **62**, 4438 (1993).

[171] Paul G. Freeman, personal communication (2013).

[172] R. Gilardi, A. Hiess, N. Momono, M. Oda, M. Ido and J. Mesot, Europhys. Lett. **66**, 840 (2004).

[173] H. Takagi, T Ido, S. Ishibashi, M Uota, S. Uchida and Y. Tokura, Phys. Rev. B **40**, 2254 (1989).

[174] T. Nakano, N. Momono, M. Oda and M. Ido, J. Phys. Soc. Jpn. **67**, 2622 (1998).

[175] J. Larsen, Ph.D. Dissertation, *Quantum Phase Transitions in* $CoCl_2$ *salts, and the Nature of the Co-existence of Magnetism and Superconductivity in* Y_9Co_7 *and* $La_{2-x}Sr_xCuO_{4+y}$, Technical University of Denmark, (2013).

[176] P. A. Lindgård *et al.* J. Phys. Chem. Solids, **28** 1357 (1966).

[177] M. Braden, G. Heger, P. Schweiss, Z. Fisk, K. Gamayunov, I. Tanaka, and H. Kojima, Physica C **191**, 455 (1992).

[178] A. T. Rømer, J. Chang, N. B. Christensen, B. M. Andersen, K. Lefmann, L. Mähler, J. Gavilano, R. Gilardi, Ch. Niedermayer, H. M. Rønnow, A. Schneidewind, P. Link, M. Oda, M. Ido, N. Momono, and J. Mesot, Phys. Rev. B **87**, 144513 (2013).

[179] Y. S. Lee, F. C. Chou, A. Tewary, M. A. Kastner, S. H. Lee, and R. J. Birgeneau, Phys. Rev. B **69** 020502(R) (2004).

[180] Linda Udby, Ph.D. Dissertation *Superoxygenated* $La_{2-x}Sr_xCuO_{4+y}$ *– virtual and physical experiments*, Niels Bohr Institute, University of Copenhagen (2009).

[181] R. Gilardi, Ph.D. Dissertation 15780, *Inelastic and small-angle neutron scattering study of the* $La_{2-x}Sr_xCuO_4$ *high-Tc superconductor in a magnetic field*, ETH Zürich (2004).